Charge transport in amorphous silicon

A study by electrically detected magnetic resonance

Am Fachbereich Physik der Freien Universität Berlin
zur Erlangung der Würde eines
Doktors der Naturwissenschaften (Dr. rer. nat.)
eingereichte Dissertation

vorgelegt von

Jannik Möser

Institut für Experimentalphysik
Freie Universität Berlin
März 2019

Erstgutachter: Prof. Dr. K. Lips
Zweitgutachter: Prof. Dr. J. Behrends

Datum der Disputation: 20.05.2019

Abstract

This thesis presents a systematic study of charge-transport and -recombination mechanisms via paramagnetic states in hydrogenated amorphous silicon (a-Si:H). The structural disorder of this prototypical amorphous semiconductor induces localized states within the band gap that act as traps and recombination centers for charge carriers, detrimentally influencing the electronic material properties. Gaining insight into the nature of such loss mechanisms is thus crucial to develop a better understanding of the relation between structural and electronic properties of amorphous semiconductors in general, and of the functioning of a-Si-based technological applications like photovoltaic devices in particular.

The tool of choice to study the influence of localized states on the electronic material properties is electrically detected magnetic resonance (EDMR). This technique combines the power of electron paramagnetic resonance (EPR) to identify and characterize paramagnetic species on a microscopic level with current detection, providing selectivity to those species involved in electronic transitions. Due to its high sensitivity, EDMR further allows to probe current-limiting spin-dependent processes in fully processed devices. This capability will be exploited to conduct EDMR experiments on both the bulk a-Si:H film samples and operating a-Si:H solar cells.

Using a combinination of EDMR and EPR techniques, we directly probe the fundamental charge-separation mechanism in a-Si:H. For the first time, we conclusively prove the existence of both EDMR and EPR fingerprints of strongly localized light-generated excitonic states in a-Si:H. We will investigate their impact on electronic properties and provide evidence for their key role in the separation process of light-generated charge carriers, which is of central importance for the operation of photovoltaic devices.

In the scope of this work, we also describe and develop EDMR methodology, which is not only limited to a-Si:H, but can be applied to all kinds of organic and inorganic materials that exhibit spin-dependent conductivity. In particular, we present a novel EDMR detection scheme that can be used to separate the resonances of different paramagnetic species based on their spin state.

This work has to be seen in the context of a vast amount of previous research in the field of disordered solids in general and a-Si:H in particular. We will review results of earlier studies in light of our new findings and thereby will be able to give answers to long-standing questions concerning the microscopic nature of transport and recombination channels in a-Si:H. Since many of the structural and electronic properties of a-Si:H are universal features of disordered solids, our results do not only concern technological applications of a-Si:H, but are also of basic scientific interest regarding current-limiting processes in amorphous semiconductors.

Kurzfassung

Die vorliegende Arbeit untersucht Ladungstransport- und -rekombinationsprozesse in hydrogenisiertem amorphen Silizium (a-Si:H). Als Prototyp eines ungeordneten Halbleiters sind die strukturellen und elektronischen Eigenschaften von a-Si:H maßgeblich durch das Fehlen kristalliner Ordnung bestimmt. Dies führt zur Ausbildung lokalisierter Zustände, die als Elektronenfallen und Rekombinationszentren den Ladungstransport stark beeinträchtigen können. Um die Auswirkung struktureller Unordnung auf elektronische Materialeigenschaften im Detail zu verstehen, ist es unablässig, Transportmechanismen auf nanoskopischer Ebene zu untersuchen.

Die dafür ideale Methode ist elektrisch detektierte Magnetresonanz (EDMR). Diese auf Elektronenspinresonanz (EPR, engl.: *electron paramagnetic resonance*) beruhende Spektroskopiemethode vereint die Möglichkeit, paramagnetische Zentren zu identifizieren und auf atomarer Ebene zu charakterisieren, mit elektrischer Detektion. Dadurch misst EDMR gezielt paramagnetische Zustände, die an elektronischen Transport- oder Rekombinationsprozessen beteiligt sind. Da EDMR zudem hochempfindlich ist, können Experimente sogar an vollständig prozessierten optoelektronischen Bauelementen, wie etwa Solarzellen, durchgeführt werden.

Sowohl EDMR als auch EPR wurden in dieser Arbeit eingesetzt, um direkten experimentellen Zugang zum Ladungstrennungsmechanismus lichtinduzierter Elektronen-Loch-Paare in a-Si:H zu erhalten. Erstmalig konnte so eindeutig die Existenz von stark gekoppelten, lokalisierten Exzitonen nachgewiesen und ihr Einfluss auf elektronische Transporteigenschaften untersucht werden. Die Ergebnisse zeigen, dass Exzitonen eine Schlüsselrolle in der Trennung lichtinduzierter Ladungsträger einnehmen, die für die Funktionsweise von Solarzellen von zentraler Bedeutung ist.

Im Rahmen dieser Arbeit wurden außerdem Methodiken entwickelt, die auch für die Untersuchung anderer Halbleitermaterialen angewendet werden können, die spinabhängige Leitfähigkeit aufweisen. Insbesondere wird eine neue EDMR-Detektionsmethode präsentiert, die eine Identifizierung verschiedener paramagnetischer Zentren auf Basis des zugrundeliegenden Spinzustands ermöglicht.

Diese Arbeit steht im Kontext einer umfangreichen Forschungshistorie an a-Si:H. Frühere Ergebnisse konnten auf Basis dieser Arbeit neu bewertet werden, wobei Antworten auf lange bestehende Fragestellungen in Bezug auf die nanoskopische Beschaffenheit elektronischer Transportprozesse in a-Si:H gefunden werden konnten. Da viele strukturelle und elektronische Eigenschaften von a-Si:H ungeordnete Festkörper im Allgemeinen betreffen, sind die Ergebnisse nicht auf technische Anwendungen von a-Si:H beschränkt, sondern auch von grundlegendem wissenschaftlichen Interesse für das Verständnis elektronischer Prozesse in amorphen Halbleitern.

Contents

Symbols

Values of fundamental constants refer to the recommendations by the Committee on Data for Science and Technology (CODATA), taken from the most recent version [1].

Δ	Spin-pair symmetry change (eq. 2.62)
Ω	Rabi-nutation frequency in SI units (eq. 2.73)
$\mathfrak{R}, \mathfrak{I}$	Real and imaginary part of a complex number
α	Normalized nutation-frequency coefficient (eq. 2.75)
β	Flip angle of a microwave pulse (eq. 2.18)
χ	Magnetic susceptibility
η	Resonator filling factor
γ	Gyromagnetic ratio, $\gamma = g\mu_\mathrm{B}/\hbar$
λ	Spin-orbit coupling constant
δ_{ij}	Kronecker delta
$\boldsymbol{\mu}$	Magnetic dipole moment
μ, μ_r	Absolute and relative magnetic permeability
$\mu_{e,h}$	Charge-carrier mobility of electrons and holes
μ_0	Magnetic constant, $\mu_0 = 4\pi \cdot 10^{-7}\,\mathrm{N/A^2}$
μ_B	Bohr magneton, $\mu_\mathrm{B} = 927.400\,999\,4(57) \cdot 10^{-26}\,\mathrm{J/T}$
μ_N	Nuclear magneton, $\mu_\mathrm{N} = 5.050\,783\,699(31) \cdot 10^{-27}\,\mathrm{J/T}$
ν	(Microwave) photon frequency
ν_Δ, ζ	Abbreviations used for description of EDMR (eq. 2.50)
ν_0	Larmor frequency, $\nu_0 = g\mu_\mathrm{B}B_0/h$
ν_1	Microwave-field strength in frequency units, $\nu_1 = g\mu_\mathrm{B}B_1/h$
$\Delta\nu$	Larmor-frequency separation
$\delta\nu_0$	Resonance-frequency offset, $\delta\nu_0 = \nu_0 - \nu$
$\boldsymbol{\omega}$	Angular frequency vector, $\lvert\omega\rvert = 2\pi\nu$
ϕ	Spin-mixing angle (eq. 2.48)
$\boldsymbol{\psi}$	Wavefunction
σ	Conductivity
τ	Time constant, dephasing time
τ_L	Charge-carrier lifetime
$\varepsilon, \varepsilon_\mathrm{r}$	Absolute and relative permittivity
ε_0	Electric constant, $\varepsilon_0 = 8.854\,187\,817\,\ldots \cdot 10^{-12}\,\mathrm{F/m}$
ξ	Localization length of an electronic state
$\boldsymbol{A}$	Hyperfine-coupling tensor (section 2.3)
$A_x, A_y, A_z, A_\parallel, A_\perp$	Principal values of $\boldsymbol{A}$ for rhombic and axial symmetry
a_iso	Isotropic hyperfine-coupling constant (eq. 2.34)

$\boldsymbol{B}_0$	Static magnetic-field vector
$\boldsymbol{B}_1$	Microwave magnetic-field vector
$\boldsymbol{B}_{\mathrm{eff}}$	Effective magnetic-field vector in the rotating frame (eq. 2.15)
B_{m}	Modulation amplitude
$B_{\mathrm{min}}, B_{\mathrm{max}}$	Half-field resonance positions (eq. 2.40)
ΔB_0	Spectral line width (FWHM)
ΔB_{pp}	Peak-to-peak line width
$\boldsymbol{D}$	Zero-field splitting/dipolar interaction tensor (sections 2.3.3 and 2.3.4)
d	Dissociation rate
D, E	Axial and rhombic dipolar hyperfine coupling
D^0, D^-, D^+	Energy states of an amphoteric (dangling-bond) defect
D_x, D_y, D_z	Principal values of $\boldsymbol{D}$
e	Elementary charge, $e = 1.602\,176\,620\,8(98) \cdot 10^{-19}$ C
$\boldsymbol{e}_x, \boldsymbol{e}_y, \boldsymbol{e}_z$	Cartesian-coordinate unit vectors
E_i	Energy level of a state $\lvert i\rangle$
E_{ij}	Transition energy between states $\lvert i\rangle$ and $\lvert j\rangle$
$E_{\mathrm{C}}, E_{\mathrm{V}}$	Conduction- and valence-band mobility edges
$E_{\mathrm{F}}, E_{\mathrm{F},n}, E_{\mathrm{F},p}$	Fermi-level, quasi-Fermi levels for electrons and holes
f_{m}	Modulation frequency
G	Generation rate of photo-excited charge carriers
$\boldsymbol{g}$	Landé g-tensor (section 2.3.1)
g	Isotropic Landé g-value
$g_x, g_y, g_z, g_\parallel, g_\perp$	Principal values of $\boldsymbol{g}$ for rhombic and axial symmetry
g_e	Free-electron g-value, $g_e = 2.002\,319\,304\,361\,82(52)$
g_{N}	Nuclear g-value
$h, \hbar$	Planck constant, $h = 2\pi\hbar = 6.626\,070\,040(81) \cdot 10^{-34}$ J s
$\boldsymbol{\mathcal{H}}_0, \boldsymbol{\mathcal{H}}_1$	Static and oscillatory spin Hamiltonians
I	Electric current
$\boldsymbol{I}$	Nuclear-spin vector
i	Imaginary unit, $i^2 = -1$
I, m_I	Nuclear-spin quantum numbers
$I_\alpha(x)\,, K_\alpha(x)$	Modified Bessel functions of the first and second kind
ΔI	EDMR current change
J	Exchange coupling between electron spins (section 2.3.4)
k	Boltzmann constant, $k = 1.380\,648\,52(79) \cdot 10^{-23}$ J/K
$\boldsymbol{L}$	Orbital angular momentum
m	Mass
$\boldsymbol{M}, M_x, M_y, M_z$	Spin-magnetization vector, $\boldsymbol{M} = (M_x,\ M_y,\ M_z)$
m_e	Electron rest mass, $m_e = 9.109\,383\,56(11) \cdot 10^{-31}$ kg
$\boldsymbol{M}_0$	Thermal-equilibrium magnetization (eq. 2.7)
$\boldsymbol{n}$	Orientation vector
n_S, N_S	Spin density and absolute number of spins
P	(Microwave) power
p_S, p_T, p_D, p_Q	Singlet/triplet and doublet/quartet transition probabilities
Q	Resonator quality
ΔQ	Integrated charge of the EDMR current $\Delta I/I$

R	Gas-flow ratio
$\boldsymbol{\mathcal{R}}$	Redfield relaxation operator (eq. 2.55)
$\boldsymbol{r}$	Position or distance vector
r, θ, ϕ	Spherical polar coordinates
$\boldsymbol{R}(\alpha, \beta, \gamma)$	Euler rotation matrix with Euler angles α, β, γ
S, m_S	Electron-spin quantum numbers
$\boldsymbol{S}, S_x, S_y, S_z$	Electron-spin vector, $\boldsymbol{S} = (S_x, S_y, S_z)$
$\boldsymbol{\mathcal{S}}, \boldsymbol{\mathcal{S}}_{\mathrm{cr}}, \boldsymbol{\mathcal{S}}_{\mathrm{an}}$	Stochastic spin-pair creation and annihilition operators (eq. 2.55)
$\boldsymbol{T}$	Dipolar hyperfine-coupling tensor (section 2.3.2)
T	Temperature
t	Time
T, ρ	Axial and rhombic dipolar hyperfine coupling (eq. 2.36)
T_x, T_y, T_z	Principal values of $\boldsymbol{T}$
T_1, T_2	Longitudinal and transversal spin-relaxation times
t_{P}	Microwave-pulse length
U	Correlation energy
$\boldsymbol{U}_0, \boldsymbol{U}_1$	Unitary transformation matrices (eqs. 2.47 and 2.70)
U_{C}	Coulomb-interaction energy
V	Electric voltage, volume
V_{B}	Bias voltage applied to an EDMR sample
W	Lattice-relaxation energy
w	Weighting factor
x, y, z	Cartesian coordinates
Z	Impedance

Abbreviations

a-Si:D	Deuterated amorphous silicon
a-Si:H	Hydrogenated amorphous silicon
AC	Alternating current
AFC	Automatic frequency control
c-Si	Crystalline silicon
CBT	Conduction-band tail
CRN	Continuous random network
CT	Charge-transfer (state)
CW	Continuous wave
DB	Dangling bond
DB-PAS	Doppler-broadening positron-annihilation spectroscopy
DC	Direct current
DEER	Double electron-electron resonance
DFT	Density-functional theory
DPPH	2,2-diphenyl-1-picrylhydrazyl
EDMR	Electrically detected magnetic resonance
ELDOR	Electron-electron double resonance
ENDOR	Electron-nuclear double resonance
EPR	Electron paramagnetic resonance
eq.	Equation
ESEEM	Electron-spin echo-envelope modulation
FFT	Fast Fourier transform
FID	Free induction decay
fig.	Figure
FTIR	Fourier-transform infrared (spectroscopy)
FWHM	Full width at half maximum
GI-PAW	Gauge-including projector-augmented plane wave
HFI	Hyperfine interaction
HIT	Heterojunction with intrinsic thin layer
HTA	High turning angle
HWHM	Half width at half maximum
ISC	Intersystem crossing
KSM	Kaplan-Solomon-Mott (spin-pair model)
LCAO	Linear combination of atomic orbitals
LEPR	Light-induced electron paramagnetic resonance
MPFU	Multi-channel pulse-forming unit

MW	Microwave
NMR	Nuclear magnetic resonance
ODMR	Optically detected magnetic resonance
OLED	Organic light-emitting diodes
PC	Photoconductivity
PEANUT	Phase-inverted echo-amplitude-detected nutation
PECVD	Plasma-enhanced chemical vapour deposition
PEDMR	Pulsed electrically detected magnetic resonance
PEPR	Pulsed electron paramagnetic resonance
pin	*P*-type/intrinsic/*n*-type
PL	Photoluminescence
QFRS	Quadrature frequency-resolved spectroscopy
RDF	Radial distribution function
ref.	Reference
RF	Radio frequency
RMS	Root mean square
RT	Radiative tunneling
SE	Singlet exciton
SNR	Signal-to-noise ratio
SRT	Shot-repetition time
SWE	Staebler-Wronski effect
tab.	Table
TCO	Transparent conductive oxide
TE	Triplet exciton
TEP	Triplet-exciton/polaron (complex)
TFT	Thin-film transistor
TIA	Transimpedance amplifier
TWT	Travelling-wave tube
VBT	Valence-band tail
ZFS	Zero-field splitting
μc-Si	Microcrystalline silicon

CHAPTER 1

Introduction

Hydrogenated amorphous silicon (a-Si:H) is one of the most thoroughly studied semiconducting materials in recent decades. This extensive research on a-Si:H has been driven not only by technological applications, but also by basic scientific interest in the structural and electronic properties of disordered solids. In this respect, a-Si:H can today be considered as the prototypical disordered covalent system. Amorphous silicon is also amongst the most important materials for electronic applications, ranging from TFT displays in modern multimedia devices [2] to state-of-the-art solar-cell panels [3].

Considering the huge technological success and the vast amount of research, a surprisingly large number of unanswered questions remain concerning the microscopic structure and the nature of fundamental electronic properties of a-Si:H. A prominent example with major impact on the performance of a-Si-based optoelectronic devices is the Staebler-Wronski effect (SWE) [4, 5], which causes light-induced degradation of the electric conductivity. Despite more than 40 years of active research, the detailed physical origin of the effect remains a puzzle. Controversial discussions even concern the fundamental structure of a-Si:H. In particular, the widely accepted model of a continuous random network for the structural topology of a-Si has recently been questioned [6].

Many of the properties of a-Si:H turn out to extend far beyond this particular material and apply to disorded solids in a more general sense. This concerns especially the impact of disorder-induced localized states on electronic transport. The structural disorder causes a number of localized states within the energy gap of a-Si:H. However, this property is not specific to a-Si:H, but is a universal feature of disordered semiconductors [7]. Localized electronic states can act as electronic traps and provide recombination pathways for charge carriers, thereby determining most of the electronic material properties. Understanding the microscopic physical mechanisms at work is thus of crucial importance not only regarding a-Si:H, but concerning disordered solids in general.

An ideally suited tool for the investigation of localized electronic states is electron paramagnetic resonance (EPR) spectroscopy. If singly occupied by a trapped charge carrier, localized states become paramagnetic and the electron spin can be utilized as a probe in magnetic-resonance experiments. A particular strength of EPR is that it is not only able to identify paramagnetic species based on their characteristic g-value, but is also sensitive to local interactions of the electron spin with, for instance, other electrons or nuclei. Thereby, EPR can also provide valuable information regarding the microscopic structure of localized electronic states. In fact, much of today's knowledge about disorder-induced localized states is based on a broad range of EPR investigations.

The most prominent paramagnetic state in a-Si:H is the dangling-bond (DB) defect. After being first detected by EPR in the late 1960s [8, 9], the DB defect has probably been

the most extensively studied paramagnetic center in any disordered solid. EPR studies on a-Si:H were able to unambiguously link the above-mentioned SWE to an increased DB density [10, 11], illustrating the impact of paramagnetic defect states on the material properties of a-Si:H. The structural model for the DB defect is a three-fold undercoordinated bonding site in the amorphous network and has evolved mainly based on a number of detailed EPR investigations. Nevertheless, it took almost 30 years of controversial discussion [12–15] until this model became established. With this in mind, it is apparent why the understanding of other types of defects and many of the electronic transport mechanisms associated with localized states is still much more rudimentary.

In their role as trap states and recombination centers for excess charge carriers, localized gap states detrimentally affect the electronic transport properties of amorphous semiconductors. Even more specific insight into the nature of such loss mechanisms can be gathered from electrically detected magnetic resonance (EDMR). This technique directly probes spin-dependent charge-carrier transport and recombination channels via paramagnetic states. EDMR is thus selective to those paramagnetic species that actually influence electronic transport. Since the first observation of spin-dependent conductivity changes in a-Si:H by Solomon *et al.* [16] in 1977, many studies have utilized EDMR to investigate the nature of disorder-induced transport and recombination processes [17]. Due to its high sensitivity (by orders of magnitude higher than conventional EPR), EDMR can even be applied to fully processed devices like thin-film solar cells.

A major step that further promoted the application range of EDMR spectroscopy was the development of pulsed EDMR (PEDMR) detection schemes by Boehme and Lips [18, 19] in 2002. With modern EPR spectrometers, the full arsenal of pulsed-EPR techniques today can be translated into electrical detection sequences. Employing electrical readout of coherent spin effects provides much more specific information concerning the nature of spin-dependent electronic transport and recombination processes. Such experiments include PEDMR nutation measurements, capable of disentangling processes involving different spin species [20, 21], or double-resonance techniques, which can identify electron spin-spin couplings [22–24] or interactions with surrounding nuclei [25].

In this work, we will employ modern PEDMR techniques to gain new insights into electronic transport and loss channels in a-Si:H. We will thereby not only reevaluate prevailing models for spin-dependent conductivity, but also identify new transport channels via paramagnetic states that influence the fundamental charge-separation mechanism in a-Si:H. Our results will be set into the perspective of previous research, attempting to answer a small share of the multitude of unanswered questions that remain for this technologically and scientifically important material. In the following, the structure of this thesis will be briefly outlined.

Chapter 2 summarizes the fundamental principles of EPR and EDMR spectroscopy. This includes the basic description of paramagnetic states in terms of the spin Hamiltonian as well as the theoretical principles of PEDMR experiments. A special emphasis will be put on the relation between pulsed EPR and EDMR detection schemes, laying the basis for the different PEDMR experiments employed within this work.

Chapter 3 gives an overview of structural and electronic properties of a-Si:H. In particular, we will focus on the role of disorder-induced localized states and summarize the

results obtained from previous magnetic-resonance studies. Moreover, we will discuss evidence for transport and recombination channels that has emerged from other experimental techniques, such as photoconductivity and -luminescence measurements. This short review will facilitate the interpretation of the experimental results presented in the following chapters.

Chapter 4 discusses the types of samples and experimental procedures employed in this work. We will describe both the design and preparation of a-Si:H film, powder and fully processed solar-cell samples and the experimental setups used for EPR and EDMR experiments. In addition, we will describe common data-acquisition and -processing techniques that have been employed to measure and analyze the experimental data.

Chapter 5 presents multifrequency PEDMR experiments on undoped a-Si:H films carried out at X-band frequencies (9.6 GHz) and a recently developed high-field/-frequency EDMR setup operating at 263 GHz/9.4 T [26]. By employing such a multifrequency approach, we were able to disentangle paramagnetic species based on their different magnetic-field-dependent and -independent resonant fingerprints. We further present the results of temperature-dependent PEDMR experiments, which illustrate the presence of distinctly different spin-dependent transport and recombination channels in different temperature regimes.

Chapter 6 contains the largest share of experimental results obtained in the course of this work and forms the heart of this thesis. Here, we will present a comprehensive PEDMR study that provides detailed insight into the transport processes in a-Si:H at low temperatures ($T = 10$ K). In particular, we will, for the first time, show unambiguous evidence for the presence of strongly coupled excitonic states in a-Si:H. Such triplet excitons (TEs) have been claimed to be involved in charge-tranport mechanisms in a-Si:H already in the 1990s [27, 244]. However, conclusive evidence has as yet been missing. We will give answers to this long-standing issue by unraveling the nature of a spin-dependent recombination channel mediated by TEs. By combining PEDMR with transient-EPR experiments, we will further show that TEs play a central role for charge separation in a-Si:H and are thus of crucial importance for technological applications like photovoltaic devices. In the course of this study, we employed a number of advanced PEDMR techniques and developed a novel electrical detection scheme that allows to separate EDMR signatures of different spin states. The methodology used in this chapter is not limited to a-Si:H, but is applicable to all kinds of semiconductors and may thus be of wider use.

Chapter 7 takes a deeper look into the nature of the non-radiative recombination channel via dangling-bond defects. Pulsed EDMR techniques will be utilized to elucidate the detailed physical recombination mechanism, which is known to be the major current-limiting loss channel in a-Si:H under ambient conditions and thus significantly influences the performance of a-Si:H-based electronic devices.

Chapter 8 summarizes the results obtained from different types of a-Si:H EDMR and EPR samples and assesses them in the context of previous results in the large research field of a-Si:H. Moreover, future research strategies to resolve remaining questions that emerged in the course of this thesis will be discussed.

CHAPTER 2

Basic principles of EPR and EDMR

The heart of this work is the analysis role of defect states in amorphous silicon on charge-transport properties of the material. The tools of choice for this study are magnetic-resonance techniques, in particular, electron paramagnetic resonance (EPR) and electrically detected magnetic resonance (EDMR). While EPR is already capable of providing detailed insights into the electronic and atomic structure of paramagnetic states on a microscopic level, EDMR even allows to directly probe spin-dependent charge-transport pathways via paramagnetic states in real devices, such as silicon-based solar cells. This chapter reviews the fundamental principles of these methods and thereby lays the basis for the experiments presented in subsequent chapters.

2.1 ELECTRON PARAMAGNETIC RESONANCE

Electrons carry an instrinsic angular momentum, the electron spin $\boldsymbol{S}$, and an electric charge $-e$, giving rise to a magnetic dipole moment[1]

$$\boldsymbol{\mu} = \gamma\hbar\boldsymbol{S} = g\frac{-e\hbar}{2m_e}\boldsymbol{S} = -g\mu_\mathrm{B}\boldsymbol{S}. \tag{2.1}$$

The proportionality factor $\gamma = g\mu_\mathrm{B}/\hbar$ is the gyromagnetic ratio, with the Planck constant $\hbar = h/2\pi$, the Bohr magneton $\mu_\mathrm{B} = e\hbar/2m_e$, the electron rest mass m_e, and the Landé g-factor. The latter can be understood as a quantum-mechanical correction factor accounting for the electron behaving differently from a classical charged particle. For an isolated, non-interacting electron, referred to as the *free electron*, $g_e \approx 2.002\,319$. If the electron is bound to an atomic orbital, its g-factor is shifted from the free-electron value due the additional orbital angular momentum (see section 2.3.1).

Carrying a magnetic moment, the free electron is paramagnetic. In presence of an external magnetic field, $\boldsymbol{\mu}$ aligns to the field vector $\boldsymbol{B}_0$. Since the electron spin is quantized, with $S = 1/2$ and the two possible spin states expressed by the magnetic quantum number $m_S = \pm 1/2$, only two orientations are possible: $\boldsymbol{\mu}$ can either align parallel ($m_S = -1/2$) or antiparallel ($m_S = +1/2$) to $\boldsymbol{B}_0$. While these two spin states are energetically degenerate in absence of a magnetic field, the interaction with $\boldsymbol{B}_0$ will lift this degeneracy. The energy associated with this *Zeeman interaction* is given by the Hamiltonian

$$\boldsymbol{\mathcal{H}}_\mathrm{EZ} = -\boldsymbol{\mu}^\mathrm{T}\boldsymbol{B}_0 = g\mu_\mathrm{B}\boldsymbol{S}^\mathrm{T}\boldsymbol{B}_0 = g\mu_\mathrm{B}S_zB_0 = m_S g\mu_\mathrm{B}B_0, \tag{2.2}$$

where S_z is the electron-spin component along the z-direction, which is (arbitrarily) defined along the magnetic-field vector $\boldsymbol{B}_0 = B_0\boldsymbol{e}_z$. The presence of a magnetic field thus

[1] Note that we follow the common convention of EPR literature and define spin operators as dimensionless multiples of the Pauli matrices, differing from the quantum-mechanical definitions by a factor of $\hbar$.

TABLE 2.1 Common microwave bands and associated frequency ranges used in EPR spectroscopy. The EPR frequencies listed relate to common resonance frequencies of commercial EPR spectrometers. Resonance fields are calculated based on eq. 2.3 for the free electron ($g = g_e$). Spin polarizations are calculated according to eq. 2.4 for the listed resonance frequencies/magnetic fields at room temperature ($T = 300$ K) and liquid-helium temperature ($T = 4$ K).

Waveband designator[a)]	Frequency range (GHz)	Typical EPR frequency (GHz)	Resonace field (mT)	Polarization at 300 K (%)	Polarization at 4 K (%)
L	1–2	1.0	36	0.008	0.6
S	2–4	3.5	120	0.03	2
X	8–12	9.6	340	0.08	6
Q	33–50	34	1200	0.3	20
W	75–110	94	3400	0.8	51
mm	110–300	263	9400	2.1	92

[a)] Waveband designators and frequency ranges are according to the IEEE standard letter designations for radar-frequency bands [28].

leads to an energy splitting $\Delta E = g\mu_B B_0 = \nu_0/h$ between the two spin states, where ν_0 is referred to as the *Larmor frequency*. Between these two Zeeman levels, magnetic dipole transitions with $\Delta m_S = \pm 1$ can be induced through absorption (or emission) of electromagnetic radiation of frequency ν if the photon energy $h\nu$ matches the energy-level splitting, that is, if

$$\Delta E = g\mu_B B_0 = h\nu, \quad \text{(that is, } \nu = \nu_0\text{)}. \tag{2.3}$$

At a given irradiation frequency and magnetic field, the appearance of EPR is hence determined by the Landé g-factor. As described above, this value deviates from the free-electron value g_e for real-world samples depending of the microscopic environment of the paramagnetic state. In EPR spectroscopy, the g-factor acts as a fingerprint that is used to identify different paramagnetic states by their resonance positions.

A typical EPR experiment uses microwave (MW) irradiation at a fixed frequency and the magnetic field B_0 is swept to match the resonance condition if $\nu_0 = \nu$. The MW spectrum ranges from about 1 GHz to 300 GHz and is subdivided into different frequency bands. The most common microwave bands used in EPR spectroscopy are listed in tab. 2.1 together with the resonant magnetic fields for the free electron. The vast majority of EPR experiments are conducted at X-band ($\nu \approx 9.6$ GHz), while the highest commerically available frequency is at 263 GHz, where superconducting magnets are required to reach to required resonant field of more than 9 T.

The intensity of an EPR line is governed by the probability of a transition between the Zeeman levels induced by absorption of a MW photon. This transition probability depends on the population difference $\Delta N = N_\downarrow - N_\uparrow$ between the two spin states. At thermal equilibrium, energy-level populations obey Boltzmann statistics, and the population difference is determined by the energy splitting and the thermal energy kT,

$$\frac{\Delta N}{N_S} = \frac{N_\downarrow - N_\uparrow}{N_\downarrow + N_\uparrow} = \frac{1 - \exp(-\Delta E/kT)}{1 + \exp(-\Delta E/kT)}, \tag{2.4}$$

where k denotes the Boltzmann constant and N_S the total number of spins occupying both Zeeman levels. The relative population difference expressed in eq. 2.4, often referred to as *spin polarization*, depends on two experimental parameters: (i) temperature and (ii) the Zeeman splitting ΔE at resonance, which is determined by the MW frequency. For

the free electron, at X band ($\nu = 9.6\,\mathrm{GHz}$, $B_0 = 340\,\mathrm{mT}$), the polarization is only about 0.08 % at room temperature ($T = 300\,\mathrm{K}$). This means that the two spin states are almost equally populated. The spin polarization, and thus the MW-absorption probability, can be substantially increased by conducting the experiment at cryogenic temperature and/or higher frequency and magnetic field: at liquid-helium temperature ($T = 4\,\mathrm{K}$), the polarization rises to almost 6 %, while at $\nu = 263\,\mathrm{GHz}$ and $B_0 = 9.4\,\mathrm{T}$, it is already around 2 % at room temperature and increases to more than 90 % at $T = 4\,\mathrm{K}$. This illustrates, how the sensitivity of EPR, which is already a highly sensitive method by itself, can be further pushed by choosing the experimental conditions.

Equation 2.4 contains information about another key property of EPR: As the intensity of an EPR signal is proportional to ΔN, it is also proportional to N_S, the total number of paramagnetic states,

$$\Delta N = \frac{1 - \exp(-\Delta E/kT)}{1 + \exp(-\Delta E/kT)} N_S \approx \frac{\Delta E}{2kT} N_S \quad (\text{for } \Delta E \ll kT). \tag{2.5}$$

Thus, EPR is not only able to identify paramagnetic species by their g-value, but is also capable to quantitatively measure the concentration of these species within the sample volume. Together with its high sensitivity and its destruction-free nature, this renders EPR a unique characterization tool, employed in various branches of both science and industry.

2.2 EPR DETECTION SCHEMES

Different excitation schemes exist for the measurement of EPR. The majority of EPR experiments are carried out by applying continuous low-power MW irradiation and detecting the EPR-induced absorption of MW energy. To record EPR spectra, the resonance condition (eq. 2.3) is changed by adiabatically sweeping[1] either the MW frequency or the magnetic field, while the respective other parameter is held constant. This type of EPR experiment is referred to as *continuous-wave EPR (CWEPR)*. Alternatively, the spin system is imposed to a short (ns to µs) high-power MW burst inducing a strongly non-thermal spin magnetization due to the coherent excitation of the spin ensemble. After the MW pulse, the spin system will freely evolve while emitting MW photons, which are detected as an EPR signal. This class of experiments is referred to as *pulsed EPR (PEPR)*. In the following, we will briefly discuss the detection principle of CW and PEPR, which also apply to many of the EDMR experiments presented throughout this thesis.

2.2.1 Continuous-wave EPR

The spin polarization in presence of an applied magnetic field (eq. 2.5) gives rise to a net equilibrium magnetization

$$\boldsymbol{M}_0 = \frac{1}{V} \sum_{i=1}^{N_S} \boldsymbol{\mu}_i = M_0 \boldsymbol{e}_z \approx -N_S \frac{g\mu_B B_0}{2kT} \boldsymbol{e}_z, \tag{2.6}$$

[1] Non-adiabatic passage conditions, resulting in passage effects, which are exploited for EPR detection schemes such as rapid-scan EPR [29], are not discussed in the scope of this work.

oriented along the magnetic-field vector $\boldsymbol{B}_0$. Resonant MW excitation induces transitions between spin states and thereby leads to a change of the bulk magnetization. Under continuous MW irradiation and steady-state conditions (adiabatic changes of B_0 or ν), this magnetization change is expressed by [1]

$$M_x = \frac{\delta\nu_0 \nu_1 T_2^2}{1 + \delta\nu_0^2 T_2^2 + \nu_1^2 T_1 T_2} M_0, \tag{2.7a}$$

$$M_y = \frac{\nu_1 T_2}{1 + \delta\nu_0^2 T_2^2 + \nu_1^2 T_1 T_2} M_0, \tag{2.7b}$$

$$M_z = \frac{1 + \delta\nu_0^2 T_2^2}{1 + \delta\nu_0^2 T_2^2 + \nu_1^2 T_1 T_2} M_0, \tag{2.7c}$$

where $\delta\nu_0 = \nu_0 - \nu$ is the resonance offset between the Larmor frequency ν_0 and the MW frequency ν and $\nu_1 = g\mu_B B_1/h$ denotes the amplitude of the MW magnetic field $\boldsymbol{B}_1$ in frequency units.

The time constants T_1 and T_2 denote the longitudinal and transversal relaxation times, describing the return of the non-equilibrium magnetization $\boldsymbol{M}$ to its thermal equilibrium state $\boldsymbol{M}_0$. The longitudinal relaxation or *spin-lattice* time T_1 describes the relaxation of M_z due to locally fluctuating magnetic fields causing energy transitions between the spin states. Such fluctuations arises due to energy exchange between the electron spins and the lattice by absorption or stimulated emission of phonons [30]. The transversal or *spin-spin* relaxation time T_2 describes the loss of coherence between the spin magnetic moments due to local interactions between individual spins (spin flip-flops). If the MW excitation is weak with respect to spin relaxation ($\nu_1 \ll 1/\sqrt{T_1 T_2}$), eq. 2.7 reduces to

$$M_x = \frac{\delta\nu_0 \nu_1 T_2^2}{1 + \delta\nu_0^2 T_2^2} M_0, \tag{2.8a}$$

$$M_y = \frac{\nu_1 T_2}{1 + \delta\nu_0^2 T_2^2} M_0, \tag{2.8b}$$

$$M_z = M_0. \tag{2.8c}$$

In this case, the magnetization vector $\boldsymbol{M}$ is only slightly deflected from its equilibrium state $\boldsymbol{M}_0 = M_0 \boldsymbol{e}_z$, with the components $M_{x,y}$ being proportional to both the spin polarization (M_0) and the incident MW-field strength B_1. Due to the linearity to B_1, the regime $\nu_1 \ll 1/\sqrt{T_1 T_2}$ is also called the *linear-power regime*. In the opposite case ($\nu_1 \gg 1/\sqrt{T_1 T_2}$), the steady-state magnetization vanishes ($M_x, M_z, M_z \to 0$) and the EPR signal is quenched. This is referred to as *saturation*.

The magnetization components M_x and M_y created by resonant MW absorption, give rise to a change of the sample susceptibility χ, expressed by the complex transverse susceptibility

$$\chi = \frac{\mu}{B_1}\left(M_x - iM_y\right), \tag{2.9}$$

[1] Equation 2.7 represents the steady-state solution of the Bloch equations (eq. 2.19), which are discussed in the following section.

where $\mu = \mu_r \mu_0$ denotes the magnetic permeability. The change of the sample susceptibility is detected as the EPR signal. Technically, this is usually accomplished by placing the EPR sample into a MW cavity (also referred to as *MW resonator*), which is resonant at the MW frequency ν. Microwaves are coupled into the cavity by matching the impedance of the MW transmission line to the impedance of the resonator (*critical coupling*). A change of the sample susceptibility results in a change of the resonator impedance, spoiling the coupling to the MW transmission line. As a result, MW power is reflected from the cavity, which is converted into a signal voltage using a MW diode.

The real (*dispersive*) part of χ ($\Re(\chi) \propto M_x$) changes the inductance of the cavity, which results in a shift of the resonator frequency. In a typical EPR spectrometer, this frequency shift is, however, componensated by an automatic frequency-control (AFC) device. The imaginary (*absorptive*) susceptibility ($\Im(\chi) \propto M_y$) causes the impedance change detected as the EPR signal. The resulting signal voltage is given by [31]

$$V_S = \eta Q \Im(\chi) \sqrt{Z_0 P}, \tag{2.10}$$

where P is the MW power ($\sqrt{P} \propto B_1$), Z_0 is the impedance of the MW transmission line, and Q and η denote the resonator quality and filling factor.

To enhance the sensitivity of a CWEPR experiment, usually phase-sensitive detection is employed. Therefor, a small modulation B_m is superimposed onto the external magnetic field, oscillating at frequency f_m (typically in the kHz range). For small modulation amplitudes and frequencies that are slow with respect to relaxation ($f_m \ll 1/T_1$), the spin ensemble can be estimated as a linear system and the EPR signal will be modulated at the same frequency f_m. The signal is then processed by a lock-in amplifier, which acts as a narrow band-pass filter at frequency f_m. A byproduct of lock-in detection is that the EPR spectral line shape is transformed to its first derivative. The same phase-sensitive detection scheme is also employed for CWEDMR experiments.

2.2.2 Pulsed EPR

Pulsed EPR comprises a large variety of experiments, which allow to specifically address certain interactions of the spin system with its surrounding and disentangle overlapping EPR signals stemming from different paramagnetic centers by introduced additional parameter dimensions. Examples of such experiments include pulsed ENDOR [32] or ESEEM [33], which probe the interactions between electron and nuclear spins, double-resonance techniques like DEER [34], sensitive to couplings between different electron spins, or two-dimensional nutation experiments, which can be utilized to separate the EPR signatures of different spin centers by their characteristic nutation frequency [35]. Many of the available PEPR experiments have been translated into electrical and optical detection schemes. The basic principles of PEPR thus also form the basis for many PEDMR experiments, which make up the core of this work.

The common ground of all PEPR techniques is the excitation of the spin ensemble with a series of short high-power MW pulses. This pulse sequence is followed by a free evolution of the spin magnetization, giving rise to coherent emission of MW irradition, which can be observed on a nanosecond time scale. Strongly non-equilibrium spin magnetizations are obtained, such that a description of these experiments in terms of eq. 2.8 is clearly not possible. However, a basic understand of the effects of a MW pulse on the spin

ensemble can be gained by classically describing the motion of $\boldsymbol{M}$ under the influence of a strong $\boldsymbol{B}_1$ MW field.

The motion of the magnetization vector in presence of an arbitrary (potentially time-dependent) magnetic field $\boldsymbol{B}(t)$ is described by the classical torque equation

$$\frac{\mathrm{d}\boldsymbol{M}}{\mathrm{d}t} = \gamma \boldsymbol{B}(t) \times \boldsymbol{M}. \tag{2.11}$$

This equation of motion describes a counter-clockwise precessión of $\boldsymbol{M}$ about the magnetic-field axis at frequency $\gamma B(t)$. In presence of MW irradiation, the effective magnetic field is $\boldsymbol{B}(t) = \boldsymbol{B}_0 + \boldsymbol{B}_1(t)$, where $\boldsymbol{B}_0 = B_0 \boldsymbol{e}_z$ is the externally applied static magnetic field and $\boldsymbol{B}_1(t)$ is the MW field, oscillating at frequency $\omega = 2\pi\nu$. For the moment, let us assume a circularly polarized MW field, rotating counter-clockwise within the xy-plane, that is,

$$\boldsymbol{B}_1(t) = B_1 \left[\cos(\omega t) \cdot \boldsymbol{e}_x + \sin(\omega t) \cdot \boldsymbol{e}_y\right]. \tag{2.12}$$

Due to the rotation of $\boldsymbol{B}_1$, the magnetization vector will follow a complex three-dimensional nutation trajectory. It is therefor convenient to describe the motion of $\boldsymbol{M}$ in a reference frame, where $\boldsymbol{B}_1$ is time-independent, that is, a frame rotating about the z-axis at frequency ω in the same direction as $\boldsymbol{M}$ and $\boldsymbol{B}_1$. This coordinate transformation into the *rotating frame* is illustrated in fig. 2.1. Mathematically, the transformation is obtained from the relation

$$\mathrm{d}\boldsymbol{M} = \mathrm{d}\boldsymbol{M}\big|_{\mathrm{rot}} + \boldsymbol{\omega}\,\mathrm{d}t \times \boldsymbol{M} \quad \Leftrightarrow \quad \left.\frac{\mathrm{d}\boldsymbol{M}}{\mathrm{d}t}\right|_{\mathrm{rot}} = \frac{\mathrm{d}\boldsymbol{M}}{\mathrm{d}t} - \boldsymbol{\omega} \times \boldsymbol{M}, \tag{2.13}$$

where $\boldsymbol{\omega} = \omega \boldsymbol{e}_z$ denotes the angular frequency vector describing the rotation of the new reference frame. To obtain the equation of motion of $\boldsymbol{M}$ in the rotating frame, we plug eq. 2.11 into eq. 2.13, yielding,[1]

$$\frac{\mathrm{d}\boldsymbol{M}}{\mathrm{d}t} = \left(\boldsymbol{\omega}_0 - \boldsymbol{\omega} + \boldsymbol{\omega}_1\right) \times \boldsymbol{M}, \quad \text{where} \quad \boldsymbol{\omega}_0 = \gamma B_0\, \boldsymbol{e}_z \quad \text{and} \quad \boldsymbol{\omega}_1 = \gamma B_1\, \boldsymbol{e}_x. \tag{2.14}$$

This describes a so-called *Rabi nutation* about an effective magnetic field

$$\boldsymbol{B}_{\mathrm{eff}} = \boldsymbol{B}_0 - \boldsymbol{\omega}/\gamma + \boldsymbol{B}_1, \tag{2.15}$$

tilted from the z-axis by an angle

$$\theta = \arctan\left(\frac{\nu_1}{\delta\nu_0}\right), \tag{2.16}$$

where $\nu_1 = g\mu_{\mathrm{B}} B_1/h$ is the precession frequency about $\boldsymbol{B}_1$ and $\delta\nu_0 = \nu_0 - \nu$ denotes the resonance offset between the Larmor-precession frequency about $\boldsymbol{B}_0$ and the MW frequency. The frequency of this nutation (*Rabi frequency*) is given by

$$\Omega = \sqrt{\nu_1^2 + \delta\nu_0^2}. \tag{2.17}$$

[1] From now on, we will omit the explicit label of the reference frame, and refer to the rotating frame, when describing pulsed EPR and EDMR experiments in the classical vector picture.

For resonant MW excitation ($\delta\nu_0 = 0$), the magnetization vector nutates about $\boldsymbol{B}_1$ at frequency $\Omega = \nu_1$. During a MW pulse of length t_P, the magnetization is thus rotated about the x-axis by a *flip angle*

$$\beta = 2\pi\Omega t_\mathrm{P} = 2\pi\nu_1 t_\mathrm{P}. \tag{2.18}$$

If the magnetization is in thermal equilibrium before the pulse ($\boldsymbol{M} = \boldsymbol{M}_0 = M_0\boldsymbol{e}_z$), a flip angle $\beta = \pi/2$ fully rotates the magnetization into the xy-plane. After the MW pulse, the spins will freely evolve, according to eq. 2.14 ($\boldsymbol{\omega}_1 = 0$). If, in addition, longitudinal (T_1) and transversal (T_2) relaxation are taken into account, expressing eq. 2.14 in terms of the magnetization components $M_{x,y,z}$ yields the *Bloch equations*

$$\frac{\mathrm{d}M_x}{\mathrm{d}t} = -\delta\omega M_y - \frac{M_x}{T_2}, \tag{2.19a}$$

$$\frac{\mathrm{d}M_y}{\mathrm{d}t} = \delta\omega M_x - \omega_1 M_z - \frac{M_y}{T_2}, \tag{2.19b}$$

$$\frac{\mathrm{d}M_z}{\mathrm{d}t} = \omega_1 M_y - \frac{M_y - M_0}{T_1}, \tag{2.19c}$$

which fully describe the dynamics of a two-level system, such as the free electron [30]. The signal arising from the complex transversal susceptibility $\chi = M_x - iM_y$ during free evolution takes the form

$$V_S \propto \exp(i\delta\omega t)\exp\left(-t/T_2\right) \tag{2.20}$$

and is referred to as the *free induction decay (FID)*. For $\delta\omega = 2\pi\delta\nu_0 = 0$, the FID follows a simple exponential decay (see fig. 2.2), from which the relaxation time T_2 can be determined. This relaxation time, measured from an FID, is often denoted as T_2^*. This is due to the fact that transversal relaxation not only occurs due to spin-spin relaxation (T_2), but

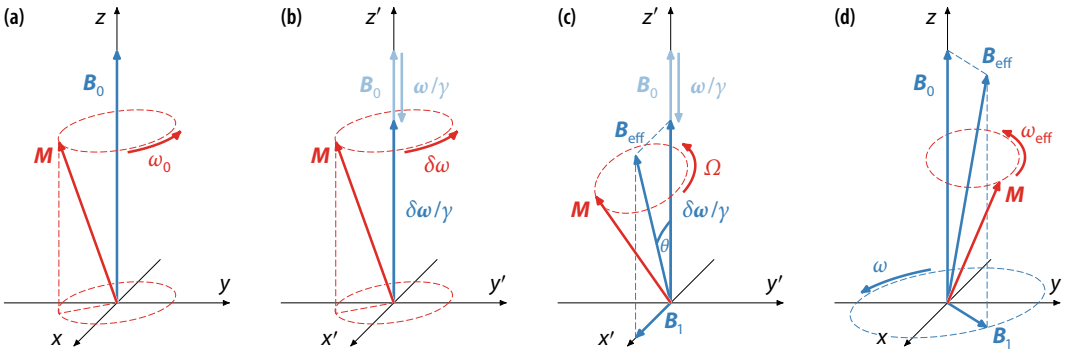

FIGURE 2.1 Schematic illustration of the motion of the spin-magnetization vector $\boldsymbol{M}$ in the laboratory and the rotating frame. (a) In presence of a static external magnetic field $\boldsymbol{B}_0$, the magnetization precesses about $\boldsymbol{B}_0$ at the Larmor frequency $\omega_0 = 2\pi\nu_0$. (b) In a coordinate frame (x', y', z') that rotates about the z-axis at frequency $\omega = 2\pi\nu$, the precession frequency is given by the frequency offset $\delta\omega = \omega_0 - \omega$. (c) A circularly polarized MW field $\boldsymbol{B}_1(t)$, oscillating at the MW frequency ν, becomes time-invariant in the rotating frame. The magnetization precesses about an effective magnetic field $\boldsymbol{B}_\mathrm{eff}$, tilted from the z-axis by an angle θ, at the Rabi-nutation frequency Ω. (d) In the laboratory frame, the motion of $\boldsymbol{M}$ is a complex three-dimensional nutation, which can be visualized as a precession about $\boldsymbol{B}_\mathrm{eff}$ at frequency $\omega_\mathrm{eff} = \left(\nu_0^2 + \nu_1^2\right)^{1/2}$, superimposed by the precession of $\boldsymbol{B}_\mathrm{eff}$ about the z-axis at frequency $\omega = 2\pi\nu$.

also due to magnetic-field inhomogeneity and Larmor-frequency distributions (*g*-strain section 2.4. The actual spin-spin relaxation time T_2 can be determined from a spin-echo decay measurement (see below).

Recording the FID as a function of the pulse lengths t_p can also be used to measure the Rabi frequency Ω. Such a Rabi-nutation experiment can be used to identify different paramagnetic species with different spin-quantum numbers. This is because the Rabi frequency of higher spin states ($S > 1/2$) will deviate from eq. 2.17, according to [36]

$$\Omega_{m_S,m_S+1} = \sqrt{[S(S+1) - m_S(m_S+1)]\nu_1^2 + \delta\nu_0^2}, \tag{2.21}$$

for an EPR transition $|S, m_S\rangle \leftrightarrow |S, m_S+1\rangle$. In this work, we will only deal with $S = 1/2$ and $S = 1$ species. For the allowed EPR transitions ($\Delta m_S = \pm 1$), one obtains the on-resonant Rabi frequencies ($\delta\nu_0 = 0$)

$$\Omega_{S=1/2} = \nu_1 \quad \text{and} \tag{2.22a}$$

$$\Omega_{S=1} = \sqrt{2}\,\nu_1. \tag{2.22b}$$

We will follow this approach in chapter 6 to distinguish between EDMR signals stemming from $S = 1/2$ and $S = 1$ species. If the spin state and *g*-value of the paramagnetic species is known (*e. g.*, when using a $S = 1/2$ reference sample), the observed Rabi frequency can also be used to calibrate $B_1 = h\nu_1/g\mu_\mathrm{B}$.

The rotating-frame vector picture provides a convenient framework to illustrate the evolution of the spin magnetization during and after a series of MW pulses. We will use this below to illustrate a final important concept, referred to as *electron-spin echo*, which forms the basis of many PEPR and EDMR experiments. Before, however, we need to reconsider the MW field $\boldsymbol{B}_1$, which we assumed to be circularly polarized for the derivation of the rotating frame. In pratice, linearly polarized MW fields are used in most EPR setups. The validity of the rotating-frame picture can be shown by treating the linearly polarized of amplitude $2B_1$ as a superposition of two opposingly directed circularly polarized fields $\boldsymbol{B}_1^{\circlearrowleft}$ and $\boldsymbol{B}_1^{\circlearrowright}$,

$$\boldsymbol{B}_1(t) = 2B_1\cos(\omega t) = \boldsymbol{B}_1^{\circlearrowleft}(t) + \boldsymbol{B}_1^{\circlearrowright}(t), \tag{2.23a}$$

where

$$\boldsymbol{B}_1^{\circlearrowleft,\circlearrowright}(t) = B_1\left[\cos(\omega t)\cdot\boldsymbol{e}_x \pm \sin(\omega t)\cdot\boldsymbol{e}_y\right]. \tag{2.23b}$$

After transformation into the rotating frame the counter-clockwise component $\boldsymbol{B}_1^{\circlearrowleft}$ will be time-invariant, while $\boldsymbol{B}_1^{\circlearrowright}$ will now rotate at frequency 2ω. The double-frequency component is thus off-resonant by approximately $\boldsymbol{B}_1^{\circlearrowleft}$ and can be treated as a perturbation. Considering the time-averaged Hamiltonian, it will lead to a shift of the resonance frequency by a few kHz (referred to as the *Bloch-Siegert shift* [37]), which is usually negligible compared compared to the GHz resonance frequencies. The linearly polarized MW field can thus be replaced by a circularly polarized field of half the amplitude, known as the *rotating-wave approximation*, and the motion of $\boldsymbol{M}$ can be described in the rotating frame.

The rotating-frame transformation does not only serve illustrative purposes. It also represents the actual detection frame of the PEPR signal. This is due to the employment of

a so-called *quadrature-detection scheme*, which uses a double-balanced mixer that mixes the MW output from the resonator with two reference signals. The two references are decoupled from the MW and phase-shifted by 90° with respect to each other. The resulting signal voltage can be expressed as

$$V_S \propto M_x - iM_y, \tag{2.24}$$

that is, the transversal magnetization (or susceptibility) in the rotating frame. Other than in CWEPR, the PEPR signal voltage is directly detected, with the use of a lock-in amplifier. Moreover, both the real (dispersive) and the imaginary (absorptive) signal are detected by means of the quadrature scheme.

While the detection of an FID represents the most simple PEPR experiment, most PEPR detection schemes involve a sequence of multiple pulses. Most of these pulse sequences are based on the detection of electron-spin echoes. The basic excitation scheme for the observation of a spin echo is the so-called *Hahn-echo sequence* [38] and consists of two pulses with flip angles $\pi/2$ and π, separated by a *dephasing time* τ, as illustrated in fig. 2.2. The first $\pi/2$ pulse rotates the magnetization from its thermal-equilibrium state (fig. 2.2b) into the xy-plane (fig. 2.2c). During the free-evolution period τ, spin packets precess with their respective resonance-offset frequencies $\delta\boldsymbol{\omega}$ about $\boldsymbol{B}_0$. Due to field inhomogeneities and a distribution of g-values, spin packets precess at different frequencies, such that phase coherence is lost (fig. 2.2d). The second pulse flips the fan of spin-magnetization vectors from $+y$ to $-y$ (fig. 2.2e). This effectively inverts the precession direction: spin packets with higher precession frequencies $\delta\boldsymbol{\omega}$ will now lag in phase behind those with lower precession frequencies. As a result, all spin packets will refocus at time τ after the second pulse and form an *echo* of the original spin coherence, flipped by an angle of π. Coherent emission gives rise an EPR signal, which is referred to as the electron-spin or Hahn echo.

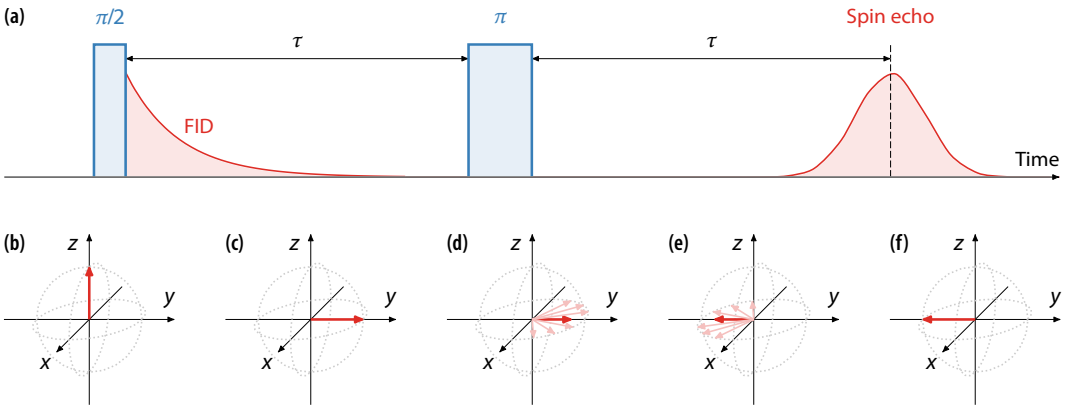

FIGURE 2.2 Illustration of the evolution of the spin magnetization and the detected EPR signals during a two-pulse Hahn-echo experiment. (a) Pulse sequence and EPR response as a function of time. (b–f) Evolution of the spin-magnetization vector $\boldsymbol{M}$ (red) in the rotating frame. (b) Before the first pulse, the spin system is in thermal equilibrium ($\boldsymbol{M} = \boldsymbol{M}_0 = M_0\boldsymbol{e}_z$). (c) The first $\pi/2$ pulse ($\boldsymbol{B}_1 = B_1\boldsymbol{e}_x$) flips the magnetization into the xy-plane, giving rise to an EPR signal. (d) During the time interval τ, individual spin packets due to a distribution of Larmor frequencies. The resulting EPR signal is an exponential FID. (e) A second π pulse flips the dephased magnetization packets, inverting the dephasing direction. (f) After the second time interval τ, the dephased spin packets have refocussed, which is detected as a coherent spin echo.

The illustration in fig. 2.2 neglects relaxation effects. During the evolution periods τ, spin-spin and spin-lattice relaxation will occur. Spin-spin relaxation contributes to the dephasing of spin packets, however, due to spontaneous spin flip-flops instead of precession-frequency differences. Thus, coherence loss due to spin-spin relaxation cannot be refocussed by the second pulse. Recording the spin-echo intensity as a function of τ thus allows to measure the spin-spin relaxation time T_2.

The Hahn-echo sequence forms the basis of many PEPR and EDMR experiments. It is beyound the scope of this work to give an overview of the wide range of available PEPR detection. Comprehensive reviews can be found in the literature (*e. g.*, ref. [30]). A summary of the practical aspects of PEPR experiments has recently been given by Stoll [39]. In section 2.5, we will establish the connection between the basic PEPR concepts discussed in this section and the translation into EDMR detection schemes. Before, however, we will introduce the different interactions of paramagnetic centers with their surrounding, affecting the resonance frequencies observed in an EPR or EDMR experiment.

2.3 SPIN HAMILTONIAN

The previous section described the idealized situation of a free electron, whose sole magnetic interaction is with an externally applied magnetic field. The energies of the spin states were given by the Hamiltonian in eq. 2.2, leading to a single resonance line at $g\mu_B B_0 = h\nu$. For real-world paramagnetic species, however, EPR spectra are in general more complex as electrons in atoms or molecules are subject to a variety of magnetic interactions with their local environment, such as interactions between multiple electrons (*fine structure*) or with nearby nuclear dipole moments (*hyperfine structure*). The resulting energy states can lead to a large set of allowed EPR transitions, producing spectra with a multitude of line components.

The energies of all possible states within the ground state of a paramagnetic species are described by the *static spin Hamiltonian*. For a system with an effective electron spin S and m nuclei with spins I_i, this can be written as [40]

$$\boldsymbol{\mathcal{H}}_0 = \boldsymbol{\mathcal{H}}_{\mathrm{EZ}} + \boldsymbol{\mathcal{H}}_{\mathrm{ZFS}} + \boldsymbol{\mathcal{H}}_{\mathrm{HFI}}. \tag{2.25}$$

The three terms in eq. 2.25 describe the electron Zeeman interaction ($\boldsymbol{\mathcal{H}}_{\mathrm{EZ}}$), which has already been introduced in section 2.1, the zero-field splitting ($\boldsymbol{\mathcal{H}}_{\mathrm{ZFS}}$) and the hyperfine interactions between the electronand nuclear spins ($\boldsymbol{\mathcal{H}}_{\mathrm{HFI}}$). Further contributions to the spin Hamiltonian, such as nuclear Zeeman and quadrupole interactions, have been neglected in eq. 2.25, as those contributions are of minor significance for this work. A comprehensive treatise of all possible contributions to the static spin Hamiltonian is to be found in the literature (see refs. [30, 41, 42]). In addition, eq. 2.25 is limited to a single-spin system, such that additional terms due to exchange or dipolar couplings with other electron spins have been omitted. These contributions will, however, be discussed in section 2.5, when we will deal with pairs of spins for the description of EDMR.

In the following, we briefly address the different interaction terms in eq. 2.25 individually and discuss the EPR parameters associated with them. The theoretical principles presented in this section form the basis for all EPR and EDMR experiments presented within this work.

2.3.1 Electron Zeeman interaction

In section 2.1, we derived the Zeeman interaction term, $\mathcal{H}_{\mathrm{EZ}} = g_e \mu_{\mathrm{B}} \boldsymbol{S}^{\mathrm{T}} \boldsymbol{B}_0$, for the case of the free electron, where g_e is the isotropic g-value of the free electron. In general, however, the interaction of a paramagnetic centers with an external magnetic can dependent on the relative orientation of $\boldsymbol{S}$ and $\boldsymbol{B}_0$ due to asymmetries in the wavefunction or the surrounding crystal field. Such anisotropies are taken into account by replacing the scalar g-value with a 3×3 interaction matrix $\boldsymbol{g}$. The general expression for the electron Zeeman term then becomes

$$\mathcal{H}_{\mathrm{EZ}} = \mu_{\mathrm{B}} \boldsymbol{S}^{\mathrm{T}} \boldsymbol{g} \boldsymbol{B}_0. \tag{2.26}$$

The interaction matrix $\boldsymbol{g}$ is commonly referred to as the *g-tensor*, although, strictly speaking, $\boldsymbol{g}$ itself is not a tensor in the physical sense. However, the experimentally observed g-value for a given orientation $\boldsymbol{n} = \boldsymbol{B}_0 / B_0$ is [41]

$$g(\boldsymbol{n}) = \sqrt{\boldsymbol{n}^{\mathrm{T}} (\boldsymbol{g}^{\mathrm{T}} \boldsymbol{g}) \boldsymbol{n}}, \tag{2.27}$$

and this measurable quantity $\sqrt{\boldsymbol{g}^{\mathrm{T}} \boldsymbol{g}}$ is a symmetric second-rank tensor. In the following, we will refer to this quantity as the g-tensor. The symmetric g-tensor, while not being diagonal in general, can be diagonalized via a rotational transformation $\boldsymbol{R}(\alpha, \beta, \gamma)$ to its principal axis system:

$$\boldsymbol{g}_{\mathrm{diag}} = \boldsymbol{R}^{\mathrm{T}}(\alpha, \beta, \gamma)\, \boldsymbol{g} \boldsymbol{R}(\alpha, \beta, \gamma) = \begin{pmatrix} g_x & & \\ & g_y & \\ & & g_z \end{pmatrix} \tag{2.28}$$

The g-tensor can thus be fully characterized be its three real principal values $g_{x,y,z}$ and the three so-called *Euler angles* α, β, γ that define the orientation of its principal axis system. In EPR, the latter is usually regarded as the *molecular frame* and all interaction tensors are referred to this frame.

The orientation of $\boldsymbol{B}_0$ with respect to the molecular frame can be expressed with two polar angles θ and ϕ, such that $\boldsymbol{B}_0 = B_0\,(\sin\theta\cos\phi,\ \sin\theta\sin\phi,\ \cos\theta)$. The observed effective g-valueis then given by

$$g(\theta,\ \phi) = \sqrt{(g_x \sin\theta\cos\phi)^2 + (g_y \sin\theta\sin\phi)^2 + (g_z \cos\theta)^2}. \tag{2.29}$$

Based on the symmetry of the paramagnetic center, three types of g-tensor anisotropies can be distinguished: (i) For *cubic* symmetry, g is isotropic with $g = g_x = g_y = g_z$ and the same EPR spectrum is observed for all orientations. (ii) For *axial* symmetry, two principal g-values $g_\perp = g_x = g_y$ and $g_\parallel = g_z$ are observed for perpendicular and parallel orientation of $\boldsymbol{B}_0$ with respect to the symmetry axis. The experimentally observed effective g-value in this case is determined by the angle θ between $\boldsymbol{B}_0$ and the symmetry axis: $g(\theta) = \left(g_\perp^2 \sin^2\theta + g_\parallel^2 \cos^2\theta\right)^{1/2}$. (iii) A more complex structures of the paramagnetic center, where the axial symmetry is lifted, is referred to as *rhombic* symmetry. In this case, the three principal values $g_{x,y,z}$ are non-degenerate and the observed g-value depends on both polar angles θ and ϕ as described by eq. 2.29.

For a crystalline sample, where all paramagnetic sites exhibits the same orientation, the g-tensor anisotropy can be directly measured by rotating the sample and recording

the effective g-value as a function of θ and ϕ. If a sample, however, is present in the form of a powder or when dealing with disordered materials such as a-Si, the orientation of an individual paramagnetic center is random. For truely disordered samples, all orientations occur with equal probability and a distribution of all possible orientations is observed at once. Examples of the resulting characteristic EPR spectra, referred to as *powder patterns*, are shown in fig. 2.3 for the three cases of an isotropic g-value (fig. 2.3a) and a g-tensor with axial (fig. 2.3b) and rhombic (fig. 2.3c) anisotropy.

The principal g-values of real paramagnetic centers, for example, defect states in silicon, deviate from the free-electron value g_e. This is due to an interaction of the electron-spin magnetic moment with the orbital angular momentum of the charge carrier by means of spin-orbit coupling. Although, for a non-degenerate electronic ground state, the orbital angular momentum is quenched ($L = 0$), a perturbation arises from the ground state being mixed with excited states, such that an orbital momentum $\boldsymbol{L}$ is admixed into the ground state. The Hamiltonian given in eq. 2.26 can then also be written as

$$\boldsymbol{\mathcal{H}}_{\mathrm{EZ}} = \mu_{\mathrm{B}} \left(\boldsymbol{L}^{\mathrm{T}} + g_e \boldsymbol{S}^{\mathrm{T}} \right) \boldsymbol{B}_0 + \lambda \boldsymbol{L}^{\mathrm{T}} \boldsymbol{S}. \tag{2.30}$$

The first part is the electron Zeeman term including the admixed orbital angular momentum, and $\boldsymbol{\mathcal{H}}_{\mathrm{SO}} = \lambda \boldsymbol{L}^{\mathrm{T}} \boldsymbol{S}$ is the spin-orbit interaction, where λ is the spin-orbit coupling constant. By means of second-order perturbation theory and comparison with eq. 2.26, an expression for g_{ij}, the elements of $\boldsymbol{g}$, can be derived [42]:

$$g_{ij} = g_e \delta_{ij} + 2\lambda \sum_{n \neq 0} \frac{\langle 0|L_i|n\rangle \langle n|L_j|0\rangle}{E_0 - E_n}, \tag{2.31}$$

where $|0\rangle$ and $|n\rangle$ denote the wavefunctions of the ground state and the nth excited state with energies E_0 and E_n, respectively. Thus, the smaller the energy gap between the ground state and the excited states, and the larger the spin-orbit coupling, the larger the deviation of the principal values of $\boldsymbol{g}$ from the free-electron value g_e. For all paramagnetic centers discussed within this work, only small g-value are observed ($\Delta g < 0.01$). However,

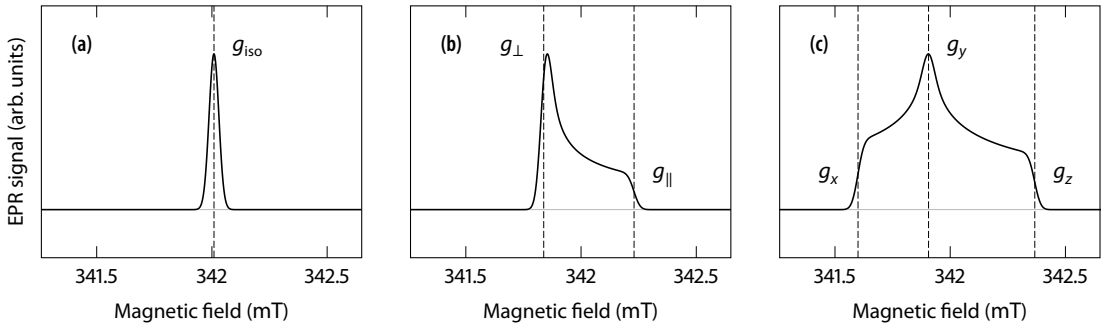

FIGURE 2.3 Simulated X-band ($\nu = 9.6$ GHz) EPR powder spectra for different g-tensor symmetries. Absorption spectra are shown for (a) an isotropic g-tensor with $g = 2.0055$, (b) an axially symmetric g-tensor with $g_\perp = 2.0065$ and $g_\parallel = 2.0042$, and (c) a rhombic g-tensor with principal values $g_x = 2.0079$, $g_y = 2.0061$ and $g_z = 2.0034$. These g-values correspond to the principal values found for the dangling-bond defect in a-Si:H [148]. Note that g-strain has been neglected for the simulations, such that the simulated spectra do not resemble the actual EPR signature of DB defects. Instead, the spectra have been convolved with a field-independent Gaussian line width of 0.05 mT. Simulations have been carried out using the EasySpin [43] MATLAB toolbox.

for sufficiently strong doping and large λ, it is possible to obtain strong g-value shifts for paramagnetic states in amorphous silicon [44].

For disordered materials such as amorphous silicon (see chapter 3 for details), g-values are not sharply defined, as indicated by fig. 2.3. Owing to the disorder, variations of the local structural and electronic environment of paramagnetic states result in a distribution of g-tensors, commonly referred to as *g-strain* (Δg). Due to the magnetic-field dependence of the Zeeman interaction, g-strain leads to a broadening of the EPR spectrum that is proportional to B_0. Thereby, field-dependent g-strain broadening counteracts the resolution enhancement obtained by carrying out EPR experiments at high MW frequencies and magnetic fields. On the other hand, multifrequency/-field experiments can be used to distinguish between g-strain and other field-independent broadening mechanisms (see also section 2.4). We will employ this strategy in chapter 5, where multifrequency EDMR is used to separated signals stemming from different paramagnetic states by the field dependencies of the respective spectral line widths.

2.3.2 Hyperfine interaction

The hyperfine interaction (HFI) between an electron spin $\boldsymbol{S}$ and a nuclear spin $\boldsymbol{I}$ is described by the Hamiltonian

$$\boldsymbol{\mathcal{H}}_{\mathrm{HFI}}/h = \boldsymbol{S}^{\mathrm{T}}\boldsymbol{A}\boldsymbol{I}, \tag{2.32}$$

where $\boldsymbol{A}$ denotes the *hyperfine-coupling tensor*. Note that, as for the g-tensor discussed in the previous section, $\boldsymbol{A}$ itself is only a 3×3 matrix, but the observable $\sqrt{\boldsymbol{A}^{\mathrm{T}}\boldsymbol{A}}$ is a symmetric second-rank tensor, which we will refer to as the tensor $\boldsymbol{A}$ (see also ref. [41]).

The HFI can be split apart into the isotropic *Fermi contact interaction* and the *electron-nuclear dipolar interaction*, such that

$$\boldsymbol{A} = a_{\mathrm{iso}}\boldsymbol{I}_3 + \boldsymbol{T}, \tag{2.33}$$

where $\boldsymbol{I}_3$ denotes the 3×3 identity matrix, a_{iso} is the isotropic hyperfine-coupling constant and $\boldsymbol{T}$ the anisotropic dipolar coupling tensor. The former is given by [45]

$$a_{\mathrm{iso}} = \frac{2}{3}\mu_0 g_e \mu_{\mathrm{B}} g_{\mathrm{N}} \mu_{\mathrm{N}} \left|\psi_0(0)\right|^2, \tag{2.34}$$

where μ_0 is the magnetic constant, g_{N} and μ_{N} denote the nuclear g value and the nuclear magneton, respectively, and $|\psi_0(0)|^2$ is the electron spin density at the position of the nucleus ($r = 0$). For the simplest case, of an electron spin with $S = 1/2$ coupled to a single nuclear spin $I = 1/2$, HFI results in a splitting of each of the two Zeeman levels ($m_S = \pm 1/2$) into two levels that belong to the two nuclear-spin states ($m_I = \pm 1/2$). This leads to two allowed EPR transitions with $\Delta m_S = \pm 1$ and $\Delta m_I = 0$, separated by a_{iso}.

The electron-nuclear dipolar coupling tensor $\boldsymbol{T}$ is a traceless, symmetric 3×3 matrix with the elements [45]

$$T_{ij} = \frac{\mu_0}{4\pi} g_e \mu_{\mathrm{B}} g_{\mathrm{N}} \mu_{\mathrm{N}} \left\langle \psi_0 \left| \frac{3 r_i r_j - \delta_{ij} r^2}{r^5} \right| \psi_0 \right\rangle, \tag{2.35}$$

where $\boldsymbol{r}$ is the distance vector between the nucleus and the electron. As for the g-tensor

in eq. 2.28, the symmetric tensor $\boldsymbol{T}$ can be diagonalized by a rotational transformation $\boldsymbol{R}(\alpha, \beta, \gamma)$ to its principal axis system:

$$\boldsymbol{T}_{\text{diag}} = \boldsymbol{R}^{\text{T}}(\alpha, \beta, \gamma)\, \boldsymbol{T}\boldsymbol{R}(\alpha, \beta, \gamma) = \begin{pmatrix} T_x & & \\ & T_y & \\ & & T_z \end{pmatrix} = \begin{pmatrix} -T+\rho & & \\ & -T-\rho & \\ & & 2T \end{pmatrix}. \tag{2.36}$$

In this expression, the three principal values $T_{x,y,z}$ have been replaced by an axial component $T = T_z/2$ and a rhombic component $\rho = (T_x - T_y)/2$. This substitution is valid since $\boldsymbol{T}$ is traceless ($\text{tr}\,\boldsymbol{A} = a_{\text{iso}}$). Within this work, we will only consider isotropic or axially symmetric HFIs ($\rho = 0$). Axial symmetry is, for example, found in amorphous silicon for the HFI of dangling-bond defects with ^{29}Si nuclei ($I = 1/2$) [46]. In this case, the hyperfine tensor consists of only two principal values $A_\perp = A_x = A_y$ and $A_\parallel = A_z$ with

$$\begin{aligned} A_\perp &= a_{\text{iso}} - T, \\ A_\parallel &= a_{\text{iso}} + 2T. \end{aligned} \tag{2.37}$$

Within this work, we will not perform detailed analysis of HFIs. However, hyperfine terms will be used, when simulating EPR and EDMR spectra, stemming from paramagnetic species such as the dangling-bond defect, that are known to exhibit HFIs. Further theoretical details and summaries of spectroscopic techniques to disentangle HFIs in EPR spectra can be found in recent EPR literature [32, 33, 45, 47].

2.3.3 Zero-field splitting

In the previous sections, we have limited the discussion to electron spins with $S = 1/2$. In this work, however, we will also deal with higher spin systems, in particular with strongly coupled $S = 1/2$ spins forming a triplet state ($S = 1$). In such a case, the dipolar coupling between the electron spins lifts the degeneracy of the ground state. This field-independent interaction is refered to as *zero-field splitting (ZFS)* and leads to a fine-structure term

$$\boldsymbol{\mathcal{H}}_{\text{ZFS}}/h = \boldsymbol{S}^{\text{T}}\boldsymbol{D}\boldsymbol{S}, \tag{2.38}$$

where $\boldsymbol{D}$ is the traceless, symmetric ZFS tensor. Similar to the tensors $\boldsymbol{g}$ and $\boldsymbol{A}$ discussed in the previous sections, $\boldsymbol{D}$ can be diagonalized to its principal axis system, such that

$$\boldsymbol{D}^{\text{diag}} = \begin{pmatrix} D_x & & \\ & D_y & \\ & & D_z \end{pmatrix} = \begin{pmatrix} -D/3+E & & \\ & -D/3-E & \\ & & 2D/3 \end{pmatrix}. \tag{2.39}$$

As in the previous section for the hyperfine-coupling tensor, the three principal values $D_{x,y,z}$ have been substituted by an axial ZFS parameter D and a rhombic ZFS parameter E that reflect the symmetry of the spin system. For cubic symmetry, $D = E = 0$; for axial symmetry, $D \neq 0$ and $E = 0$; and for rhombic symmetry, both $D \neq 0$ and $E \neq 0$. The effect of ZFS on the Zeeman levels is shown in fig. 2.4a for an $S = 1$ system, assuming axial symmetry ($E = 0$). The diagram shows the energy levels as a function of magnetic field for both perpendicular (black) and parallel (red) orientation of the magnetic-field vector with respect to the ZFS z-axis. Averaging over all possible orientation leads to the characteristic powder spectrum shown in fig. 2.4b, referred to as *Pake pattern*, which arises due to the

orientation-dependent resonance fields of the $\Delta m_S = \pm 1$ transitions (marked by the black and red arrows in fig. 2.4a).

The simulated spectrum in fig. 2.4b shows an additional small contribution at lower magnetic field. The presence of this line is due an EPR transition between the $m_S = \pm 1$ states of the triplet manifold (dashed arrows in fig. 2.4a). Such forbidden $\Delta m_S = \pm 2$ transitions become weakly allowed in the presence of ZFS, as the dipolar interactions between the spins lead to off-diagonal elements in the Hamiltonian that mix the $m_S = \pm 1$ states [48]. The position and shape of this resonance is described by the two magnetic-field values B_{min} and B_{max}, corresponding to the resonance fields at perpendicular and parallel orientation between $\boldsymbol{B}_0$ and the principal axes of $\boldsymbol{D}$, as illustrated in fig. 2.4c. These field values are given by [48]

$$B_{\text{min}} = \frac{h\nu}{2g\mu_{\text{B}}}\sqrt{1 - \frac{4}{3}\left(\frac{D^*}{\nu}\right)^2}, \text{ where } D^* = \sqrt{D^2 + 3E^2}, \text{ and} \tag{2.40a}$$

$$B_{\text{max}} = \frac{h\nu}{2g\mu_{\text{B}}}\sqrt{1 - \left(\frac{D}{\nu}\right)^2}. \tag{2.40b}$$

Since the resonance position is close to $h\nu/2g\mu_{\text{B}}$ for $D, E \ll \nu$, this transitions is often referred to as *half-field resonance*. From fig. 2.4 it is evident that the half-field resonance is much less affected by anisotropy than the full-field Pake pattern, resulting in a much narrower line shape. In addition, field-dependent line-broadening effects (g-strain) are

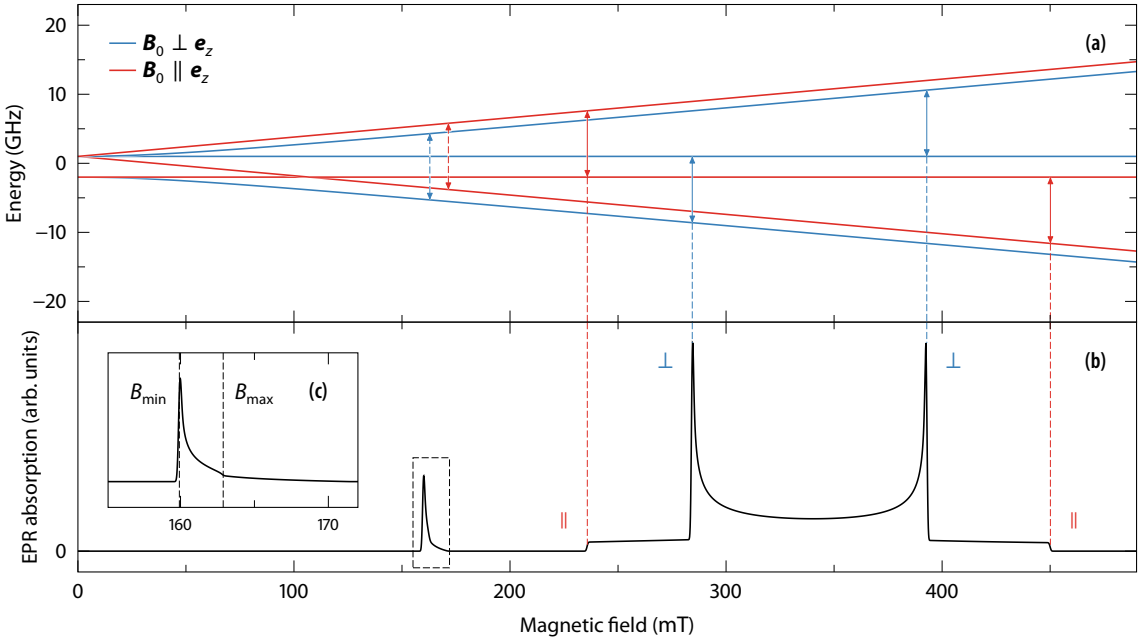

FIGURE 2.4 (a) Energy-level diagram of an $S = 1$ triplet state with an axially symmetric D-tensor ($D = 3000$ MHz, $E = 0$, $g = 2$) for perpendicular (blue) and parallel (red) orientation of the D-tensor principal axes with respect to the external magnetic field. Vertical arrows mark the allowed ($\Delta m_S = \pm 1$) resonant EPR transitions at a MW frequency of 9.6 GHz. The dashed arrows indicate weakly allowed $\Delta m_S = \pm 2$ transitions. (b) Simulated powder EPR absorption spectrum, obtained for the energy-level distribution shown in fig. a by averaging over all orientations. The characteristic spectral shape is referred to as Pake pattern. (c) Enlarged view of the half-field resonance resulting from the $\Delta m_S = \pm 2$ transitions.

significantly smaller at lower magnetic field. Therefore, B_{min} can often be determined accurately in order to estimate the D-value based on eq. 2.40. In chapter 6, we report the first-time observation of an electrically detected half-field resonance in amorpous silicon, and use the line shape, determined by B_{min} and B_{max}, to estimate the D-value of the associated $S = 1$ triplet state.

2.3.4 Weak coupling between electron spins

In the previous section, we discussed the spin Hamiltonian of strongly coupled spins that are treated in a total-spin basis (*e. g.*, $S = 1$ for two coupled $S = 1/2$ spins). Spin-dependent transport and recombination processes giving rise to EDMR occur between weakly coupled paramagnetic states (see section 2.5), which are still described by their individual spins. In general, the interaction between two coupled spins $\boldsymbol{S}_{\mathrm{A}}$ and $\boldsymbol{S}_{\mathrm{B}}$ is described by the Hamiltonian

$$\boldsymbol{\mathcal{H}}_{\mathrm{AB}}/h = -J\boldsymbol{S}_{\mathrm{A}}^{\mathrm{T}}\boldsymbol{S}_{\mathrm{B}} + \boldsymbol{S}_{\mathrm{A}}^{\mathrm{T}}\boldsymbol{D}_{\mathrm{AB}}\boldsymbol{S}_{\mathrm{B}}. \tag{2.41}$$

The first term describes the *isotropic exchange interaction*, which results from an orbital overlap of the paired spins. Typically, exchange interaction becomes relevant for spin-spin distances below about 15 Å [49]. Exchange interaction splits the formerly degenerate total-spin states of the coupled pair by an energy J. If the ground state is the higher spin state ($S = 1$ for $S_{\mathrm{A}} = S_{\mathrm{B}} = 1/2$), the coupling is referred to as *ferromagnetic* ($J > 0$), while the opposite case of a low-spin ($S = 0$) ground state and an excited high-spin state is referred to as *antiferromagnetic* ($J < 0$) [50].[1]

The second term in eq. 2.41 denotes the dipolar coupling, which has already been discussed in the previous section for the case of strongly coupled spins described as a single total-spin state $S > 1/2$. Considering the case of two $S = 1/2$ states, the description as a single isolated $S = 1$ state (eq. 2.38), and the dipolar-coupling term of the individual spins (eq. 2.41) are related by $\boldsymbol{S}^{\mathrm{T}}\boldsymbol{D}\boldsymbol{S} = 2\boldsymbol{S}_{\mathrm{A}}^{\mathrm{T}}\boldsymbol{D}\boldsymbol{S}_{\mathrm{B}}$, that is $\boldsymbol{D}_{\mathrm{AB}} = 2\boldsymbol{D}$ [50]. Under high-field conditions ($D \ll g\mu_{\mathrm{B}}B_0/h$) and using point-dipole approximation for the two spins, the dipolar coupling term can also be written as

$$\boldsymbol{S}_{\mathrm{A}}^{\mathrm{T}}\boldsymbol{D}_{\mathrm{AB}}\boldsymbol{S}_{\mathrm{B}} = -D\left(3\boldsymbol{S}_{\mathrm{A}}^{z}\boldsymbol{S}_{\mathrm{B}}^{z} - \boldsymbol{S}_{\mathrm{A}}^{\mathrm{T}}\boldsymbol{S}_{\mathrm{B}}\right) = -D\left(3\cos^2\theta - 1\right), \tag{2.42}$$

where θ denotes the angle between $\boldsymbol{B}_0$ and the interspin-distance vector $\boldsymbol{r}_{\mathrm{AB}}$. In its principal axes frame, $\boldsymbol{D}_{\mathrm{AB}}$ can then be written as [30]

$$\boldsymbol{D}_{\mathrm{AB}}^{\mathrm{diag}} = \begin{pmatrix} -D & & \\ & -D & \\ & & 2D \end{pmatrix}. \tag{2.43}$$

In this case, the dipolar coupling strength D serves as a measure of r_{AB}, according to [49]

$$D = \frac{\mu_0 g_{\mathrm{A}} g_{\mathrm{B}} \mu_{\mathrm{B}}^2}{4\pi h} r_{\mathrm{AB}}^{-3} \qquad \text{(weak coupling, } |J - D| \ll \Delta\nu\text{)}. \tag{2.44a}$$

[1] Different conventions exist for the exchange interaction in eq. 2.41. Amongst physicists, the notations $+J\boldsymbol{S}_{\mathrm{A}}^{\mathrm{T}}\boldsymbol{S}_{\mathrm{B}}$ or $-J\boldsymbol{S}_{\mathrm{A}}^{\mathrm{T}}\boldsymbol{S}_{\mathrm{B}}$ is typically used, while the notation $+2J\boldsymbol{S}_{\mathrm{A}}^{\mathrm{T}}\boldsymbol{S}_{\mathrm{B}}$ or $-2J\boldsymbol{S}_{\mathrm{A}}^{\mathrm{T}}\boldsymbol{S}_{\mathrm{B}}$ is more common in the chemistry community.

As indicated, this expression is only valid in the limit of weak coupling, much smaller than the Larmor separation $\Delta\nu = |\nu_A - \nu_B|$. In the strong coupling limit ($|J - D| \gg \Delta\nu$), an additional factor of 3/2 has to be included, such that [49]

$$D = \frac{3}{2} \cdot \frac{\mu_0 g_A g_B \mu_B^2}{4\pi h} r_{AB}^{-3} \qquad \text{(strong coupling, } |J - D| \gg \Delta\nu\text{).} \tag{2.44b}$$

The prefactor arises when describing dipolar coupling in with a total spin $\boldsymbol{S} = \boldsymbol{S}_A + \boldsymbol{S}_B$, that is, $\boldsymbol{S}^T \boldsymbol{D} \boldsymbol{S}$, instead using of the single-spin notation $\boldsymbol{S}_A^T \boldsymbol{D} \boldsymbol{S}_B$. In the strong coupling case, the observed D-value is by a factor 3/2 larger than in the weak coupling case (compare eqs. 2.39 and 2.43).[1]

In the course of this work, we will use the relation between the dipolar coupling strength and the spin-spin distance will given by eq. 2.44 to determine the distance distribution of strongly coupled excitonic states discovered to play a key role in the charge-separation mechanism in amorphous silicon (see chapter 6).

2.4 BROADENING OF EPR LINES

The spin Hamiltonian described in the previous section determines the transition frequencies of an ensemble of identical electron and nuclear spins, also referred to as a *spin packet*. Resonance lines observed in an EPR (or EDMR) spectrum, however, do not appear at sharp frequency/field positions but exhibit a line width determined by *homogeneous* and *inhomogeneous broadening*. As already mentioned above, these broadening mechanisms (g-strain) can also dependent on the amplitude of the external magnetic field. The field dependency of the spectral line width can thus provide valuable information about the microscopic nature of the spin system.

Homogeneous broadening determines the line width of an individual spin packet and results from the Heisenberg uncertainty principle ($\Delta E \Delta t \geq \hbar$). The lifetime of a spin packet is determined by the spin-lattice relaxation time T_1, such that the minimum observable line width is given by $\Delta\boldsymbol{\omega} \geq 1/T_1$. This type of homogeneous broadening is also referred to as *lifetime broadening*.

In many cases, homogeneous broadening is determined not only by the lifetime, but also by the spin-coherence, or spin-spin relaxation time T_2. Spin-spin relaxation arises due to local magnetic-field fluctuations, originating from, *e. g.*, thermal motion and spin flips of surrounding electron and nuclear spins. In this case, T_2 restricts the homogeneous line width. The resulting EPR line shape a single spin packet is then a Lorentzian with a line width of $2/T_2$. Further details concerning spin-relaxation mechanisms that lead to homogeneous broadening can be found in standard EPR textbooks (see, for example, refs. [30, 41]).

Inhomogeneous broadening refers to the superposition of resonances stemming from *different* spin packets with a distribution of Larmor frequencies. The resulting EPR line shape is the sum of the (homogeneously broadened) lines of all individual spin packets, such that the inhomogeneous line width depends on the underlying distribution of Larmor frequencies.

[1] This will also become evident in section 2.5.6, where we give explicit expressions for the eigenvalues and transition energies of a coupled pair, both in the weak- and in the strong-coupling limit.

The most dominant source of inhomogeneous broadening, especially in disordered materials like amorhous silicon, is a distribution of the spin-Hamiltonian parameters. This includes anisotropies of the interaction tensors ($\boldsymbol{g}$, $\boldsymbol{A}$, $\boldsymbol{D}$), as illustrated in fig. 2.3, and so-called *strain effects*, that is, a distribution of the principal interaction values due to local disorder. Amorphous silicon is a prime example for this kind of inhomogeneous broadening, as the structural disorder leads to a variation of bond lengths and angles inducing a broad distribution of g-values (see chapter 3). For a normal strain distribution, as it is often the case, a Gaussian line shape is observed.

Another common type of inhomogeneous broadening, referred to as *unresolved HFI*, is observed if the electron spin interacts with many distant nuclear spin (for example, ^{1}H or ^{29}Si in a-Si:H). The large number of HFI is not resolved in the EPR spectrum and leads to an inhomogeneous broadening of the resonance.

The field dependency of the broadening mechanism is determined by the underlying spin-Hamiltonian interaction. Since the electron Zeeman interaction is proportional to B_0, inhomogeneous g-strain broadening increases with B_0, as opposed to inhomogeneous broadening of $\boldsymbol{A}$ (A-strain, unresolved HFI) or $\boldsymbol{D}$ (D-strain) or homogeneous broadening, which are field-independent. Multifrequency/-field experiments thus provide a viable tool to separate different line-shape components based on the type of broadening.

2.5 ELECTRICALLY DETECTED MAGNETIC RESONANCE

Electron paramagnetic resonance is a powerful tool to identify paramagnetic species and study their electronic structure. While in section 6.7 we will employ (transient) EPR to elucidate the role of localized paramagnetic states in the charge-separation mechanism of a-Si:H, the main focus of this work is the investigation of the microscopic nature of electronic transport and recombination channels. The tool of choice is therefor electrically detected magnetic resonance (EDMR), which selectively probes those paramagnetic centers that are involved in current-limiting processes. Moreover, the sensitivity of EDMR is by orders of magnitude higher than that of conventional EPR, reaching even towards single-spin sensitivity [51, 52]. In this section, we will summarize the basic theoretical concepts, laying the basis for the description of EDMR experiments.

The influence of EPR on the photoconductivity was first explored in 1966 by Schmidt and Salomon [53], Maxwell and Honig [54] as well as Hirose *et al.* [55]. In the early 1970s, Lépine and Prejean [56] detected spin-dependent recombination in silicon. They also proposed a model that explained the spin-dependent recombination channel by an increased capture cross section based on a change of the spin polarization. Lépine's model, as well as subsequent model that attempted to explain the observed resonant photocurrent changes [16, 57, 58], however, failed to predict the experimentally observed signal magnitudes as well as temperature and magnetic-field dependencies. Finally, in 1978, Kaplan, Solomon and Mott [59] (KSM) described spin-dependent recombination based on the formation of intermediate weakly coupled spin pairs, which could explain the experimentally obtained results. Following these early studies, EDMR was employed to investigate recombination mechanisms in various types of inorganic [16, 17, 60–63] and organic [64–66] semiconductors as well as fully processed devices such as solar cells [57, 67–69], diodes [70, 71] or transistors [72].

For more than two decades, EDMR was limited to field-swept continuous wave (CW) experiments. It was only in 1999, when Hiromitsu *et al.* [66] reported the first time-domain EDMR experiments, succeeded by the work of Boehme and Lips [18, 73, 74], who studied the transient recombination dynamics after application of a resonant MW pulse. This finally paved the way towards electrical readout of spin coherence by means of pulsed EDMR (PEDMR) [19, 75, 76]. The model developed by Boehme and Lips for the theoretical description of PEDMR experiments was based on the original KSM intermediate-pair model and treated both the cases of spin-dependent recombination [19] and hopping transport [77]. It layed the basis for the development of broad range of electrical readout techniques, such as electrically detected Rabi nutations [20], spin echoes [78], hyperfine spectroscopy like ESEEM [23] and ENDOR [25], or pump-probe ED-ELDOR [22] and -DEER [24] experiments. In addition, numerical and analytical methods were developed, predicting the PEDMR signals of spin pairs under different coupling strengths [79–84]. Recently, Keevers *et al.* [85] further extended the theoretical description to spin pairs comprising $S = 1$ triplet states.

The large pool of PEDMR techniques available today renders PEDMR the ideally suited for the analysis of the microscopic nature of spin-dependent transport and recombination processes. Moreover, the development of new readout sequences, based on experiments known from PEPR, is straightforward, as we will show in chapter 6 by the developments of an electrical detection scheme of the so-called phase-inverted echo-amplitude-detected nutation (PEANUT) experiment [35]. Pulsed EDMR is thus the tool of choice and primarily employed technique thoughout this work. In the following, we will briefly summarize the basic theoretical principles, based on the spin-pair models mentioned above and the spin-interaction Hamiltonians discussed in section 2.3.

2.5.1 Spin-dependent electronic transitions

Electrically detected magnetic resonance probes transport and recombination channels via localized paramagnetic states by their spin dependency. In general, transport of elec-

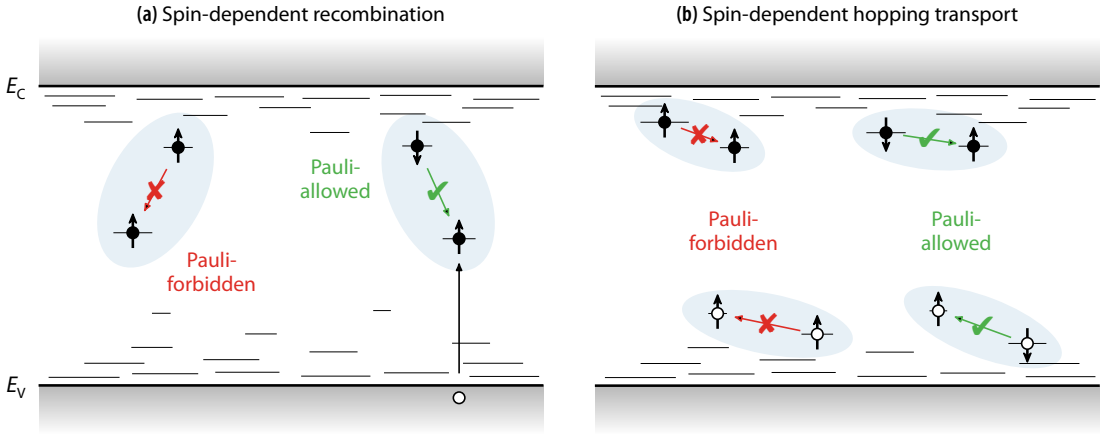

FIGURE 2.5 Schematic illustration of spin-dependent pair processes via localized states in a-Si:H. (a) Spin-dependent recombination of trapped electrons via mid-gap defect states. Transitions are Pauli-blocked for parallel spin orientation (left) and become allowed if either one of the paired spins is flipped (right). (b) Spin-dependent hopping transport of electrons (upper) and holes (lower) via localized band-tail states (see text for further discussion).

trons and holes occurs in the extended conduction and valence band states, where the spin state of an individual charge carriers is is not conserved for a long time and has little influence on the conductivity. However, in disordered materials like amorphous silicon, a large density of localized states exist that act as charge-carrier traps and recombination centers (see chapter 3). These states can be occupied by either one or two charge carriers according to the Pauli-exclusion principle. Tunneling transport and recombination paths between nearby localized states thus become spin-dependent if both states are singly occupied. This is schematically illustrated in fig. 2.5 for the two prominent examples of recombination and hopping transport via localized band-tail and mid-gap defect states in amorphous silicon. When the spins of the neighbouring charge carriers are parallel to each other, the transition is blocked, whereas it becomes allowed for antiparallel alignment.

Singly occupied localized states are paramagnetic and their spin states can therefor be manipulated by means of EPR. Resonantly flipping either one of the two spins will affect the transition probability between the adjacent states. This results in a resonant conductivity change, which is detected as the EDMR signal. Spin-dependent recombination in amorphous silicon occurs between trapped electrons and mid-gap defect states (dangling bonds, see section 3.2.1), followed by the capture of a hole, as shown in fig. 2.5a. This leads to a decrease of the charge-carrier density and, as a result, to a quenching of the conductivity. For the case of spin-dependent hopping conduction (fig. 2.5b), an increased transition probability results in an enhanced charge-carrier mobility, which will be detected by an increase of the conductivity.

As discussed in detail in chapter 3, transport and recombination via defects and band-tail states plays a crucial role for the electronic properties of disordered semiconductors like amorphous silicon. By means of EDMR, these microscopic transport channels can be directly probed and assigned to defect states based on the EPR signature. This makes EDMR the ideal tool to study and elucidate the impact of defect states on electronic transport. In the following, we will summarize the theoretical concepts for describing EDMR signal observed for spin-dependent recombination and hopping-transport channels. The basis for this is the KSM spin-pair model [59] and the subsequent theory of PEDMR developed by Boehme and Lips [19, 76].

2.5.2 Spin-pair Hamiltonian

The essence of the KSM model [59], which also form the basis for the theoretical description of PEDMR by Boehme and Lips [19], is the localization of charge carriers into intermediate coupled spin pairs prior to a spin-dependent transition. After being trapped, recombination or transport processes are exclusive between the coupled spins, that is, dissociation of the pair is required before interactions with other charge carriers can occur. In presence of an external magnetic field $\boldsymbol{B}_0$, the static spin Hamiltonian of the pair of spins A and B, with $S_A = S_B = 1/2$,[1] is described by

$$\boldsymbol{\mathcal{H}}_0/h = \mu_B \left(\boldsymbol{S}_A^T \boldsymbol{g}_A + \boldsymbol{S}_B^T \boldsymbol{g}_B\right) \boldsymbol{B}_0/h - J \boldsymbol{S}_A^T \boldsymbol{S}_B - D\left(3 S_A^z S_B^z - \boldsymbol{S}_A^T \boldsymbol{S}_B\right). \tag{2.45}$$

The first term describes the electron Zeeman interactions of the individual spins A and B (section 2.3.1), while the other two terms denote the exchange and dipolar coupling be-

[1] Spin pairs comprising higher spin states are discussed in section 2.5.8.

tween the two spins (section 2.3.4). For the sake of simplicity, we omitted HFIs, although these can easily be incorporated, using the expressions given in section 2.3.2. In the following, we will further neglect g-tensor anisotropy to simplify the expressions using the Larmor frequencies $\nu_{A,B} = g_{A,B}\mu_B B_0/h$. The matrix representation in the product base $|\psi\rangle = (|\uparrow\uparrow\rangle, |\uparrow\downarrow\rangle, |\downarrow\uparrow\rangle, |\downarrow\downarrow\rangle)$ reads

$$\boldsymbol{\mathcal{H}}_0 = \frac{h}{2}\begin{pmatrix} 2\nu_0 - J/2 - D & 0 & 0 & 0 \\ 0 & \Delta\nu + J/2 + D & -J + D & 0 \\ 0 & -J + D & -\Delta\nu + J/2 + D & 0 \\ 0 & 0 & 0 & -2\nu_0 - J/2 - D \end{pmatrix}, \tag{2.46}$$

where $\nu_0 = (\nu_A + \nu_B)/2$ is the mean Larmor frequency and $\Delta\nu = \nu_A - \nu_B$ the separation of Larmor frequencies of spins A and B. For a coupled pair ($|J - D| > 0$), the Hamiltonian is non-diagonal in the product base, but can be diagonalized into its energy eigenbasis by a matrix rotation

$$\boldsymbol{\mathcal{H}}_0^{\mathrm{en}} = \boldsymbol{U}_0^{\dagger}\boldsymbol{\mathcal{H}}_0\boldsymbol{U}_0, \quad \text{where} \quad \boldsymbol{U}_0 = \begin{pmatrix} 1 & 0 & 0 & 0 \\ 0 & \cos\phi & \sin\phi & 0 \\ 0 & -\sin\phi & \cos\phi & 0 \\ 0 & 0 & 0 & 1 \end{pmatrix} \tag{2.47}$$

and ϕ is the *spin-mixing angle*,

$$\phi = \frac{1}{2}\arctan\frac{J - D}{\Delta\nu}. \tag{2.48}$$

The energy eigenvalues can be read from

$$\boldsymbol{\mathcal{H}}_0^{\mathrm{en}} = \frac{h}{2}\begin{pmatrix} 2\nu_0 - \zeta & 0 & 0 & 0 \\ 0 & \nu_\Delta + \zeta & 0 & 0 \\ 0 & 0 & -\nu_\Delta + \zeta & 0 \\ 0 & 0 & 0 & -2\nu_0 - \zeta \end{pmatrix}, \tag{2.49}$$

where we introduced the abbreviations

$$\nu_\Delta = \sqrt{(J - D)^2 + \Delta\nu^2} \quad \text{and} \quad \zeta = J/2 + D. \tag{2.50}$$

The corresponding energy eigenstates $|\psi^{\mathrm{en}}\rangle = \boldsymbol{U}_0{}^{\dagger}\,|\psi\rangle$ are given by

$$|\psi^{\mathrm{en}}\rangle = \begin{pmatrix} |T_+\rangle \\ |2\rangle \\ |3\rangle \\ |T_-\rangle \end{pmatrix} = \begin{pmatrix} |\uparrow\uparrow\rangle \\ \cos\phi\ |\uparrow\downarrow\rangle - \sin\phi\ |\downarrow\uparrow\rangle \\ \sin\phi\ |\uparrow\downarrow\rangle + \cos\phi\ |\downarrow\uparrow\rangle \\ |\downarrow\downarrow\rangle \end{pmatrix} \tag{2.51}$$

With increasing coupling strength ($|J - D| \gg \Delta\nu$ and $\phi \to \pm\pi/4$), the mixed states $|2\rangle$ and $|3\rangle$ approach the pure triplet and singlet states

$$|S\rangle = (|\uparrow\downarrow\rangle - |\downarrow\uparrow\rangle)/\sqrt{2} \tag{2.52a}$$

$$|T_0\rangle = (|\uparrow\downarrow\rangle + |\downarrow\uparrow\rangle)/\sqrt{2} \tag{2.52b}$$

In the weak coupling limit ($|J - D| \ll \Delta\nu$ and $\phi \to 0$), $|2\rangle$ and $|3\rangle$ simply represent the product states $|\uparrow\downarrow\rangle$ and $|\downarrow\uparrow\rangle$, respectively. At intermediate coupling strengths, the states exhibit a mixture of singlet and triplet content, depending on the amplitudes of J and D.

2.5.3 Spin-to-charge conversion

Above, we have derived the energy eigenstates and -values of a weakly coupled pair of $S = 1/2$ spins. As qualitatively discussed in section 2.5.1, the spin dependency of an electronic transition giving rise to an EDMR signal is based on the Pauli-exclusion principle. Therefor, the observable in EDMR is the *spin-pair symmetry*, in terms of singlet and triplet content, other than in conventional EPR, where *spin polarization* is measured. Since the basic assumption of the KSM model is that transitions can exclusively occur between the coupled spin pair, the transition probability p_i solely depends on the singlet and triplet content of the pair's eigenstate $|i\rangle$,

$$p_i = p_S \, |\langle i|S\rangle|^2 + p_T \, |\langle i|T\rangle|^2, \tag{2.53}$$

where p_S and p_T are the different transition probabilities of pure singlet (pairs with permutation antisymmetry) and pure triplet (pairs with permutation symmetry) states ($p_S \gg p_T$). By inserting eqs. 2.51 and 2.52, one obtains for the four eigenstates:

$$p_{T_+,T_-} = p_T \quad \text{and} \quad p_{2,3} = \frac{p_S}{2}\left(1 \mp \frac{J-D}{\nu_\Delta}\right) + \frac{p_T}{2}\left(1 \pm \frac{J-D}{\nu_\Delta}\right). \tag{2.54}$$

Note that we have not yet specified the nature of the spin-dependent transition. Equation 2.53 rather makes the general assumption that the transition probability is governed by the permutation symmetry of the intermediate pair. Accordingly, the dynamics of a spin-dependent transition is solely determined by the dynamics of the spin-pair ensemble. The state of the pair ensemble is described by the density matrix $\boldsymbol{\rho}$. Its time evolution can be expressed by the *stochastic Liouville equation*, developed for the model of spin-dependent recombination by Haberkorn and Dietz [86],

$$\frac{\mathrm{d}}{\mathrm{d}t}\boldsymbol{\rho}(t) = -\frac{i}{\hbar}\left[\boldsymbol{\mathcal{H}}, \boldsymbol{\rho}(t)\right] + \boldsymbol{\mathcal{S}}\left[\boldsymbol{\rho}(t)\right] + \boldsymbol{\mathcal{R}}\left[\boldsymbol{\rho}(t) - \boldsymbol{\rho}^0\right]. \tag{2.55}$$

The first terms corresponds to the well known Liouville-von-Neumann equation, describing the quantum-mechanical state evolution in the Schrödinger picture. The stochastic operator $\boldsymbol{\mathcal{S}} = \boldsymbol{\mathcal{S}}_{\mathrm{cr}} + \boldsymbol{\mathcal{S}}_{\mathrm{an}}$ describes external changes changes of the ensemble by creation and annihilation of spin pairs. The third term, with the Redfield operator $\boldsymbol{\mathcal{R}}$, takes account the loss of spin coherence due to relaxation, as described by the Redfield relaxation theory [87] (see, for instance, ref. [41] for details). In terms of the density matrix, the total transition probability $P(t)$ can be written as

$$P(t) = p_S \,\mathrm{tr}\left[|S\rangle\langle S| \, \boldsymbol{\rho}(t)\right] + p_T \sum_{i=-1}^{1} \mathrm{tr}\left[|T_i\rangle\langle T_i| \, \boldsymbol{\rho}(t)\right]. \tag{2.56}$$

Using the formalism provided by eqs. 2.55 and 2.56 together with the static spin Hamiltonian derived in the previous section, we are now able to describe the dynamics of the spin-pair ensemble and the resulting spin-dependent change of $P(t)$. The final step is

to translate the change of $P(t)$ into a change of the measured conductivity. The latter is determined by the density and the mobility of free charge carriers,

$$\sigma = e\left(n_e\mu_e + n_h\mu_h\right), \tag{2.57}$$

where $n_{e,h}$ and $\mu_{e,h}$ denote the electron and hole densities and mobilities, respectively. Depending on the type of the transition (*e. g.*, recombination or hopping transport), a spin-dependent increase of the transition probability may either result in a change of $n_{e,h}$ (spin-dependent recombination) or $\mu_{e,h}$ (spin-dependent hopping) causing the conductivity change.

2.5.4 Spin-dependent recombination

Based on eq. 2.57, the conductivity change $\Delta\sigma(t) = \sigma(t) - \sigma^0$ due to spin-dependent recombination can be expressed by the change of electron and hole densities $\Delta n_{e,h}(t)$,

$$\Delta\sigma(t) = e\left[\Delta n_e(t)\mu_e + \Delta n_h(t)\mu_h\right]. \tag{2.58}$$

The free electron density n_e can only change by dissociation of the intermediate pair. The dissociation probability d is assumed to be spin-independent ($d = d_S = d_T$). The hole density, however, decreases after recombination of the spin pair. Accordingly, based on eqs. 2.53 and 2.56, we can express $\Delta n_{e,h}(t)$ as

$$\Delta n_e(t) = \tau_{\mathrm{L}} d \sum_{i=1}^{4} \Delta\rho_{ii}(t) \quad \text{and} \quad \Delta n_h(t) = -\tau_{\mathrm{L}} \sum_{i=1}^{4} r_i \Delta\rho_{ii}(t), \tag{2.59}$$

where r_i denotes the recombination rates of the spin-pair eigenstates given by eq. 2.53, $\Delta\rho_{ii}(t) = \rho_{ii}(t) - \rho_{ii}^0$ is the eigenstate density change and τ_{L} the charge-carrier lifetime, which is assumed to be equal for electrons and holes.[1] Further, τ_{L} as well as the pair generation rate G are considered to be constant and spin-independent. Inserting eq. 2.59 into eq. 2.58 yields the transient conductivity change

$$\Delta\sigma(t) = e\tau_{\mathrm{L}} d\mu_e \sum_{i=1}^{4} \Delta\rho_{ii}(t) \left(1 - \frac{r_i}{d}\frac{\mu_h}{\mu_e}\right). \tag{2.60}$$

The above expression provides the link between the observed conductivity change during an EDMR experiment and the time evolution of the underlying spin-pair ensemble, expressed by eq. 2.55. Boehme and Lips [19, 76] explicitly solved eq. 2.60 under the assumption of spin-independent charge-carrier generation ($\{\boldsymbol{S}_{\mathrm{cr}}\}_{ii} = G/4$) and spin-spin relaxation (T_2) being the fastest time scale. The resulting transient conductivity follows a multi-exponential decay, according to

$$\begin{aligned}\Delta\sigma(t) = \frac{e\tau_{\mathrm{L}} d\mu_e G}{2r_T} \Bigg\{ & 2\left[\frac{r_T}{d}\frac{\mu_h}{\mu_e} - 1\right] \exp\left[-\left(r_T + d\right)t\right] \\ & - \left[\frac{r_2}{d}\frac{\mu_h}{\mu_e} - 1\right]\left[1 + \frac{J-D}{\nu_\Delta}\right] \exp\left[-\left(\frac{r_2}{2} + d + \frac{1}{T_2}\right)t\right] \\ & - \frac{r_3}{d}\frac{\mu_h}{\mu_e}\left[1 - \frac{J-D}{\nu_\Delta}\right] \exp\left[-r_3 t\right] \Bigg\} \Delta(t=0),\end{aligned} \tag{2.61}$$

[1] Equal electron and hole lifetime are used to simplify the equations. In reality, however, they may differ significantly.

where $r_{2,3}$ are linear combinations of r_S and r_T, as defined by eq. 2.54. The quantity

$$\Delta(t=0) = -\frac{\Delta\rho_{11,44}(t=0)}{\mathrm{tr}\,\boldsymbol{\rho}^0} = \frac{\Delta\rho_{22,33}(t=0)}{\mathrm{tr}\,\boldsymbol{\rho}^0}\frac{\nu_\Delta}{\nu_\Delta \pm (J-D)}. \qquad 2.62$$

describes the spin density that has been shifted from the pure triplet states $|T_+\rangle$ and $|T_-\rangle$ into the mixed states $|2\rangle$ and $|3\rangle$, or in other words, the initial manipulation of the spin-pair permutation symmetry. This manipulation is achieved by MW-induced transitions between the spin states (see section 2.5.6). This direct dependency of the measured transient conductivity change on $\Delta(t=0)$ forms the basis of all PEDMR experiments.

2.5.5 Spin-dependent hopping transport

Hopping transport refers to tunneling transitions between localized states. In amorphous silicon, hopping conduction through localized band-tail states in an energy range kT around the (quasi-)Fermi level is the dominant charge-transport mechanism at low temperature ($T < 60$ K). At higher temperature, the increased thermal energy shifts the transport path into the extended band states and hopping transport becomes insignificant (see chapter 3). A hopping transition between two states can become spin-dependent based on the Pauli-exclusion principle if both states are singly occupied. Therefor, EDMR can probe such hopping-transport channels. The model for spin-dependent recombination, described above, has been extended to spin-dependent hopping conduction by Boehme and Lips [76]. The model follows the same scheme by assuming different transition rates p_S and p_T for singlet and triplet states, leading to different transition probabilities for the eigenstates of the spin pair (eq. 2.54).

The model proposed by Boehme and Lips is based a *pair site* consisting of the nearby states A and B, as illustrated in fig. 2.6. The intermediate spin pair is formed when both states are singly occupied. Spin pairs are thus created by (spin-independent) hopping transitions of charge carriers trapped in localized states in direct vicinity of the pair site (fig. 2.6a) into the unoccupied pair state (fig. 2.6b). The associated pair-creation probability is p_0. After formation, the weakly coupled pair is in a state $|\psi\rangle$, as described in section 2.5.2, and the spin-pair symmetry can be manipulated by EPR. To complete the hopping process, either on of the two paired spins must dissociate into a second localized

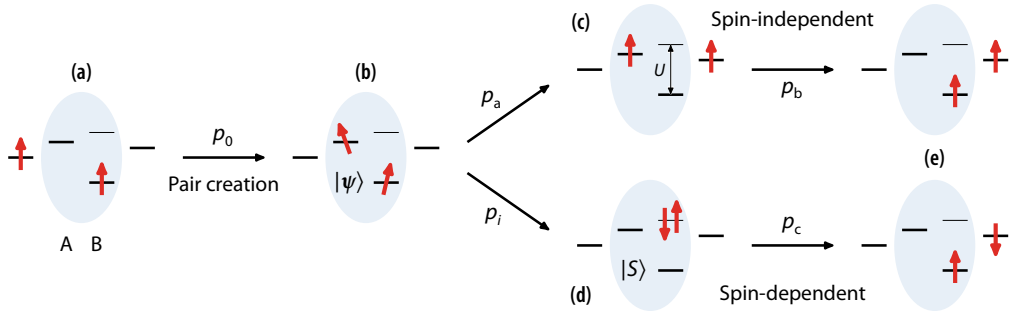

FIGURE 2.6 Hopping transport through a spin-pair site (shaded blue area), based on the intermediate-pair model for spin-dependent hopping conduction proposed by Boehme and Lips [76]. Two alternative hoppings paths exist resulting in the same final state. Only the lower hopping path (fig. d) is spin-dependent (see text for further discussion). Illustration adapted from refs. [76] and [88].

state outside the pair site (fig. 2.6e). Two possible scenarios arise to reach this final state (figs. 2.6c and d): In the upper path (fig. 2.6c), transport is Pauli-blocked for spin A, but spin B can tunnel to the nearby state, followed by transition of spin A into the now unoccupied state B. The associated probabilities are p_a and p_b, respectively, both being *spin-independent*. The lower path (fig. 2.6d) refers to the case where the spin-pair symmetry is manipulated by EPR into a state with increased single content. A transition of the spin trapped in state A into state B will then occur at the *spin-dependent* probability p_i (eq. 2.53). The hopping process is completed by a final spin-independent transition of either one of the two spins into the external localized state (fig. 2.6e). Note that the doubly occupied state formed after the spin-dependent transition (fig. 2.6d) is higher in energy by the correlation energy U, arising from the Coulomb repulsion between the two electrons (see section 3.2.1). A prerequisite for spin-dependent hopping thus is that the average energy gap between the localized exceeds U [89]. This is certainly the case in amorphous silicon, where band-tail states extended for into the mobility gap, whereas the correlation energy of conduction-band-tail electrons and valence-band-tail holes is on the order of 10 meV and 100 meV, respectively [90].

Considering the two possible channels for a hopping transition, the combined dissociation probability after pair formation of the intermediate pair is given by [76]

$$d_i = \frac{p_\mathrm{a} p_\mathrm{b}}{p_\mathrm{a} + p_\mathrm{b}} + \frac{p_i p_\mathrm{c}}{p_i + p_\mathrm{c}}, \quad \text{where} \quad p_i = p_S \left|\langle i|S\rangle\right|^2 + p_T \left|\langle i|T\rangle\right|^2. \tag{2.63}$$

Other than spin-dependent recombination, a hopping transition does not affect the charge-carrier density. The conductivity change instead is due to a change of the electron and hole mobilities μ_e and μ_h,

$$\Delta\sigma(t) = e\left[n_e \Delta\mu_e(t) + n_h \Delta\mu_h(t)\right]. \tag{2.64}$$

In the following, we will only consider the electron term. Similar expressions are obtained for spin-dependent hopping of holes.

The charge-carrier mobilities change as a function of the total spin-dependent transition-rate change $\Delta R = \sum_i \Delta\rho_{ii} d_i$. Since the resulting mobility changes $\Delta\mu_e$ will be small with respect to the steady-state mobilities μ_e^0, one can approximate $\Delta\mu_e$ by a first-order change $\mu_e(\Delta R) = \mu_e^0 + \partial\mu_e/\partial R$. In analogy to eq. 2.60, we can thus express the conductivity change in terms of the density matrix,

$$\Delta\sigma(t) = e n_e \frac{\partial\mu_e}{\partial R} \sum_{i=1}^{4} \Delta\rho_{ii}(t)\, d_i. \tag{2.65}$$

The resulting conductivity transient takes the form [76]

$$\begin{aligned}\Delta\sigma(t) = e n_e \frac{\partial\mu_e}{\partial R} \mathrm{tr}\,\boldsymbol{\rho}^0 \Bigg\{ &-2\exp\left[-d_T t\right] \\ &+ \left[1 + \frac{J-D}{\nu_\Delta}\right] \exp\left[-\left(\frac{d_2}{2} + \frac{1}{T_2}\right) t\right] \\ &+ \left[1 - \frac{J-D}{\nu_\Delta}\right] \exp\left[-d_3 t\right] \Bigg\} \Delta(t=0),\end{aligned} \tag{2.66}$$

where the EPR-induced permutation-symmetry change $\Delta(t=0)$ is given by eq. 2.62. As for the case of spin-dependent recombination, the transient conductivity change follows a triple-exponential decay, proportional to $\Delta(t=0)$. Comparison of eqs. 2.61 and 2.66 further shows that opposite signs are obtained for spin-dependent hopping and recombination. The sign of the PEDMR signal can thus be used to distinguish between transport and recombination channels.

2.5.6 Electrical detection of spin coherence

So far, we have discussed the time evolution of the spin-pair ensemble in terms of the static spin Hamiltonian derived in section 2.5.2. Based on stochastic Liouville equation, the dynamics of the ensemble and the spin-dependent change in conductivity can be described. The starting point for the evolution is an initial non-steady-state density matrix, obtained by coherent manipulation of the spin ensemble under MW irradiation. In PEDMR experiments, this is done by applying either one or a sequence of short MW pulses, which induce resonant transitions between the spin states. After this pulse sequence ($t=0$), the ensemble is left with a state density $\boldsymbol{\rho}(t=0) \neq \boldsymbol{\rho}^0$ and a an associated permutation-symmetry change $\Delta(t=0)$. As we have seen in section 2.5.4, the subsequent transient conductivity change is directly proportional to this EPR-induced manipulation of the pair ensemble.

To include coherent MW excitation into the description, we need to consider to presence of the time-dependent MW field, oscillating at the MW frequency ν,

$$\boldsymbol{B}_1(t) = B_1 \boldsymbol{e}_x \exp(-i\omega t), \quad \text{where} \quad \omega = 2\pi\nu. \tag{2.67}$$

The Zeeman interaction between spins A and B and the magnetic field $\boldsymbol{B}_1$ gives rise to an oscillatory spin Hamiltonian[1]

$$\boldsymbol{\mathcal{H}}_1(t)/h = \nu_1 \left(\boldsymbol{S}_\mathrm{A}^x + \boldsymbol{S}_\mathrm{B}^x\right) \exp(-i\omega t), \quad \text{where} \quad \nu_1 = \gamma B_1/2\pi. \tag{2.68}$$

After transformation of $\boldsymbol{\mathcal{H}}_1(t)$ into the energy eigenbasis (eq. 2.47), the total spin Hamiltonian reads

$$\boldsymbol{\mathcal{H}}^\mathrm{en}(t) = \boldsymbol{\mathcal{H}}_0^\mathrm{en} + \boldsymbol{\mathcal{H}}_1^\mathrm{en}(t), \quad \text{where} \quad \boldsymbol{\mathcal{H}}_1^\mathrm{en}(t) = \boldsymbol{U}_0^\dagger \boldsymbol{\mathcal{H}}_1(t)\, \boldsymbol{U}_0. \tag{2.69}$$

The time-dependency of the Hamiltonian can be removed by a coordinate transformation into the rotating frame, which precesses at frequency ν about the z-axis (see section 2.2.2). Mathematically, this transformation can be expressed as [30]

$$\boldsymbol{\mathcal{H}}^\mathrm{rot} = \boldsymbol{U}_1^\dagger \boldsymbol{\mathcal{H}}^\mathrm{en} \boldsymbol{U}_1 - \boldsymbol{U}_1^\dagger \frac{\mathrm{d}\boldsymbol{\mathcal{H}}^\mathrm{en}}{\mathrm{d}t} \boldsymbol{U}_1, \quad \text{where} \quad \boldsymbol{U}_1(t) = \exp\left[-i\omega\left(\boldsymbol{S}_\mathrm{A}^z + \boldsymbol{S}_\mathrm{B}^z\right) t\right]. \tag{2.70}$$

The resulting spin Hamiltonion $\boldsymbol{\mathcal{H}}^\mathrm{rot} = \boldsymbol{\mathcal{H}}_0^\mathrm{rot} + \boldsymbol{\mathcal{H}}_1^\mathrm{rot}$ in the rotating frame is time-invariant (rotating-wave approximation, see section 2.2.2). The static Hamiltonian will be shifted in energy, according to

$$\boldsymbol{\mathcal{H}}_0^\mathrm{rot} = \boldsymbol{\mathcal{H}}_0^\mathrm{en} - h\nu \left(\boldsymbol{S}_\mathrm{A}^z + \boldsymbol{S}_\mathrm{B}^z\right), \tag{2.71}$$

[1]The g-value difference between spins A and B can be neglected since $B_1 \ll B_0$. In eq. 2.68, we thus assume $g = (g_\mathrm{A} + g_\mathrm{B})/2 \approx g_\mathrm{A} \approx g_\mathrm{B}$.

whereas the time-independent driving-field Hamiltonian $\boldsymbol{\mathcal{H}}_1^{\mathrm{rot}}$ is given by

$$\boldsymbol{\mathcal{H}}_1^{\mathrm{rot}} = \frac{h\nu_1}{2}\begin{pmatrix} 0 & \cos\phi - \sin\phi & \cos\phi + \sin\phi & 0 \\ \cos\phi - \sin\phi & 0 & 0 & \cos\phi - \sin\phi \\ \cos\phi + \sin\phi & 0 & 0 & \cos\phi + \sin\phi \\ 0 & \cos\phi - \sin\phi & \cos\phi + \sin\phi & 0 \end{pmatrix}, \tag{2.72}$$

The diagonal elements of $\boldsymbol{\mathcal{H}}_0$ in the energy eigenbasis, $E_i = \{\boldsymbol{\mathcal{H}}_0^{\mathrm{en}}\}_{ii}$, represent the energies associated with the different spin states, whereas the off-diagonal elements of the rotating-frame driving term, $\{\boldsymbol{\mathcal{H}}_1^{\mathrm{rot}}\}_{ij}$, correspond to the transition amplitudes, which indicate the probability of a transition $|i\rangle \rightarrow |j\rangle$ with energy difference $E_{ij} = E_j - E_i$.

As shown in section 2.2.2, the presence of a $\boldsymbol{B}_1$-field leads to a spin precession about the effective field $\boldsymbol{B}_{\mathrm{eff}} = \boldsymbol{B}_1 + 2\pi\,(\nu_0 - \nu)\boldsymbol{e}_z/\gamma$ at the Rabi-nutation frequency Ω. The Rabi frequency is determined by the transition amplitude and takes the form

$$\Omega_{ij} = \sqrt{(\alpha_{ij}\nu_1)^2 + (\nu_{ij} - \nu)^2}, \tag{2.73}$$

where

$$\nu_{ij} = (E_j - E_i)/h \tag{2.74}$$

denotes the transition frequency between states $|i\rangle$ and $|j\rangle$, and α_{ij} can be read off from the off-diagonal entries of $\boldsymbol{\mathcal{H}}_1^{\mathrm{rot}}$ in eq. 2.72,

$$\alpha_{ij}^2 = \left(\cos\phi \pm \sin\phi\right)^2 = 1 \pm \sin 2\phi. \tag{2.75}$$

To give explicit expression for transition frequencies and amplitudes, we will in the following distinguish the two cases of weak ($|J - D| \ll \Delta\nu$) and strong ($|J - D| \gg \Delta\nu$) coupling of the spin pair.

Weak coupling For $|J - D| \ll \Delta\nu$, one obtains a spin-mixing angle $\phi \rightarrow 0$, and the pair's eigenstates are simply the product states

$$|\psi^{\mathrm{en}}\rangle = \begin{pmatrix} |1\rangle \\ |2\rangle \\ |3\rangle \\ |4\rangle \end{pmatrix} = \begin{pmatrix} |\uparrow\uparrow\rangle \\ |\uparrow\downarrow\rangle \\ |\downarrow\uparrow\rangle \\ |\downarrow\downarrow\rangle \end{pmatrix} \tag{2.76}$$

and the rotating-frame Hamiltonian becomes

$$\boldsymbol{\mathcal{H}}^{\mathrm{rot}} = \frac{h}{2}\begin{pmatrix} 2\left(\nu_0 - \nu\right) - \zeta & \nu_1 & \nu_1 & 0 \\ \nu_1 & \Delta\nu + \zeta & 0 & \nu_1 \\ \nu_1 & 0 & -\Delta\nu + \zeta & \nu_1 \\ 0 & \nu_1 & \nu_1 & -2\left(\nu_0 - \nu\right) - \zeta \end{pmatrix}. \tag{2.77}$$

The allowed EPR transitions ($\Delta m_S = \pm 1$) excite either spin A or B and are given by

$$|\uparrow\uparrow\rangle \leftrightarrow |\downarrow\uparrow\rangle, \qquad \nu_{13} = \nu_A - J/2 - D, \tag{2.78a}$$
$$|\uparrow\downarrow\rangle \leftrightarrow |\downarrow\downarrow\rangle, \qquad \nu_{24} = \nu_A + J/2 + D, \tag{2.78b}$$
$$|\uparrow\uparrow\rangle \leftrightarrow |\uparrow\downarrow\rangle, \qquad \nu_{12} = \nu_B - J/2 - D, \tag{2.78c}$$
$$|\downarrow\uparrow\rangle \leftrightarrow |\downarrow\downarrow\rangle, \qquad \nu_{34} = \nu_B + J/2 + D. \tag{2.78d}$$

One thus obtains two resonances for each paired spin, centered at ν_A and ν_B and split by $2D + J$. For weakly coupled pairs in EDMR, this splitting is usually negligible, such that simply the separate resonances of spins A and B are observed.

The Rabi-nutation frequencies are obtained from the off-diagonal entries and are equal for all transitions,

$$\Omega_{ij} = \sqrt{\nu_1^2 + (\nu_{ij} - \nu)^2} \quad (\alpha_{ij} = 1), \tag{2.79}$$

which correspoinds to the expected nutation frequency for an EPR transition of $S = 1/2$ states. During a MW pulse of length t_P, the excited spin will accordingly precess at frequency Ω_{ij}. This directly translates into a Rabi nutation of the spin-pair permutation symmetry Δ. As a function of t_P, the spin-pair state will be a linear combination of the parallel, pure triplet states ($|\uparrow\uparrow\rangle$, $|\downarrow\downarrow\rangle$) and the anti-parallel states with mixed singlet and triplet content ($|\uparrow\downarrow\rangle$, $|\downarrow\uparrow\rangle$). Boehme and Lips [19] have shown that the results pair symmetry $\Delta(t_P)$ is given by

$$\Delta(t_P) = \frac{1}{2}\left(\frac{\nu_1}{\Omega}\right)^2 \left[1 - \cos(2\pi\Omega t)\right] \qquad (\Delta\nu \gg \nu_1). \tag{2.80}$$

Recording the transient conductivity change as a function of the MW-pulse length thus allows to measure *electrically detected Rabi (ED-Rabi)* nutations. The experimental procedure to record ED-Rabi nutations will be illustrated in chapter 6.

Equation 2.80 describes the ED-Rabi nutation in case of *selective* excitation of either one of the two paired spins A and B. A special case arises for *non-selective* excitation, where both spins nutate simultaneously. This occurs if the Larmor separation is less than the MW excitation width, typically expressed by the criterion $\Delta\nu \ll \nu_1$.[1] The nutation of $\Delta(t_P)$ is then described by [88]

$$\Delta(t_P) = \frac{1}{4}\left(\frac{\nu_1}{\Omega}\right)^2 \left[3 - \cos(4\pi\Omega t)\right] \qquad (\Delta\nu \ll \nu_1). \tag{2.81}$$

The observed ED-Rabi nutation frequency is thus 2Ω. This doubling of the nutation frequency under non-selective spin-pair excitation is also referred to as *spin locking* or *spin beating*. The observation of spin locking has been used to identify spin-dependent transport and recombination channels via weakly coupled pair in inorganic and organic semiconductors [91] and device such as solar cells [92, 93] or organic light-emitting diodess (OLEDs) [21, 94]. Analytical expressions for the ED-Rabi spectra of weakly coupled spin pairs, which also cover the onset of spin locking, have been given by Glenn *et al.* [82].

[1] Note that the excitation bandwidth of a MW pulse is determined by its length ($\approx 1/t_P$). Since the pulse length is changed during an ED-Rabi experiment, the bandwidth is not well defined and thus expressed in terms of B_1. In this thesis, we propose an alternative detection scheme, which allows to control the excitation bandwidth during an electrically detected nutation experiment (see section 6.4 for details).

Strong coupling For strong exchange or dipolar coupling ($|J - D| \gg \Delta\nu$ and $\phi \to \pm\pi/4$), the eigenbasis of the coupled pair is the pure triplet-singlet basis

$$|\psi^{\mathrm{en}}\rangle = \begin{pmatrix} |1\rangle \\ |2\rangle \\ |3\rangle \\ |4\rangle \end{pmatrix} = \begin{pmatrix} |T_+\rangle \\ |S\rangle \\ |T_0\rangle \\ |T_-\rangle \end{pmatrix} \tag{2.82}$$

and the spin Hamiltonian is given by

$$\mathcal{H}^{\mathrm{rot}} = \frac{h}{2} \begin{pmatrix} 2(\nu_0 - \nu) - J/2 - D & 0 & \sqrt{2}\nu_1 & 0 \\ 0 & 3J/2 & 0 & 0 \\ \sqrt{2}\nu_1 & 0 & -J/2 + 2D & \sqrt{2}\nu_1 \\ 0 & 0 & \sqrt{2}\nu_1 & -2(\nu_0 - \nu) - J/2 - D \end{pmatrix}. \tag{2.83}$$

Due to spin conservation, transitions are now limited to the triplet manifold. As expected from the selection rule $\Delta m_S = \pm 1$, only two non-zero transition moments found between the $|T_+\rangle$ and $|T_-\rangle$ sublevels ($m_S = \pm 1$) and the $|T_0\rangle$ state ($m_S = 0$),

$$|T_+\rangle \leftrightarrow |T_0\rangle, \qquad \nu_{13} = (\nu_A + \nu_B)/2 - 3D/2, \tag{2.84a}$$

$$|T_-\rangle \leftrightarrow |T_0\rangle, \qquad \nu_{34} = (\nu_A + \nu_B)/2 + 3D/2. \tag{2.84b}$$

In the strong-coupling limit, thus only one set of resonance, centered about the average Larmor frequency ν_0 and split by $3D$ is observed, instead of the separate resonances of spins A and B in the weak-coupling limit. Note also the factor of 3/2, indicating the larger effective D-value of a strongly coupled pair (see also discussion in section 2.3.4). Averaging over all orientations θ yields a Pake pattern, as shown in section 2.3.3.

The Rabi frequencies of both transitions, given by eq. 2.73 and the off-diagonal entries in eq. 2.83, are

$$\Omega_{ij} = \sqrt{2\nu_1^2 + (\nu_{ij} - \nu)^2} \quad (\alpha_{ij} = \sqrt{2}), \tag{2.85}$$

corresponding to EPR nutation frequency expected for strongly coupled pairs forming an effective $S = 1$ state (compare eqs. 2.21 and 2.22 in section 2.2.2).

As can be seen from eq. 2.84, EPR transitions between the eigenstates of a strongly coupled pair will only shift density between the triplet sublevels. Therefor, the pair permutation symmetry in terms of singlet and triplet content remains unchanged no spin-dependent transport or recombination can be observed.[1] The two cases of weak and strong coupling can therefor be considered as boundaries, in between of which transition frequencies and amplitudes of the coupled pair are observed. Intermediate regimes, where $|2\rangle$ and $|3\rangle$ are states with mixed singlet and triplet content have been treated both analytically and numerically by Limes *et al.* [84].

An important case arises in the presence of strong exchange coupling ($J \gg \Delta\nu$) but vanishing dipolar interaction ($D = 0$). In this case, one obtaines transition frequencies

[1] An indirect resonant singlet population can be obtained via intersystem crossing (ISC). This is, for instance, then case of HFIs between the paired spins and surrounding nuclei mixes the $|T_0\rangle$ and $|S\rangle$ states and allows for a population shift [88]. Alternatively, an additional spin could be coupled to the pair, allowing for additional spin-dependent transitions (see section 2.5.8).

for the four transitions

$$|T_{\pm}\rangle \leftrightarrow |2\rangle, \qquad \nu_{\pm,2} \approx \nu_0 \pm \left(J + \Delta\nu^2/4J\right), \tag{2.86a}$$

$$|T_{\pm}\rangle \leftrightarrow |3\rangle, \qquad \nu_{\pm,3} \approx \nu_0 \pm \Delta\nu^2/4J, \tag{2.86b}$$

and the single-transition $\sqrt{2}\nu_1$ Rabi frequency given by eq. 2.85. However, for $J \gg \Delta\nu$, the splitting between the $|T_{\pm}\rangle \leftrightarrow |3\rangle$ transitions becomes negligibly small and the transitions are effectively driven under spin-locking conditions, independently of the B_1 strength. A multiple-transition analysis yields an on-resonant Rabi frequency of $2\nu_1$ [83, 84]. Numerical simulations predict this exchange-coupling induced $2\nu_1$ component also in the presence of dipolar coupling, when $J > D$ and a Pake distribution of D-values is assumed [84]. As discussed above, a $2\nu_1$ nutation frequency is also observed for weakly coupled pairs under spin-locking conditions due to high B_1 fields. Experimentally, double-frequency components stemming from strongly exchange coupled or weakly coupled spins can be distinguished by carrying out ED-Rabi measurements at low B_1 strengths. Spin locking of weakly coupled pairs will only be observed if the excitation window exceeds the Larmor separation, whereas strong exchange coupling will always produce a $2\nu_1$ component. This fact has been exploited to disentangle spin-dependent processes involving weakly coupled polaron pairs and strongly exchange-coupled triplet-exciton states in organic semiconductors [21, 94]. In section 6.4, we will also follow this approach to distinguish between transport channels involving weakly and strongly coupled pairs in a-Si:H solar cells.

2.5.7 Electrically detected spin echoes

Above we have shown how spin coherence reflects in the spin-pair permutation symmetry. This allows to record ED-Rabi nutations, which forms the basis of all PEDMR experiments. The PEDMR toolbox is, however, not limited to single-pulse experiments. Over the past decade, a diverse range of PEPR experiments, such as ESEEM [23], ENDOR [25] or -DEER [24], have been translated into the respective EDMR equivalents. The common pulse-sequence component of these PEPR experiments is the Hahn spin-echo sequence, introduced in section 2.2.2. Electrically detected spin echoes have first been demonstrated by Huebl *et al.* [78] in 2008, providing the key building block to translate PEPR sequences into electrical-detection schemes.

The modified EDMR spin-echo sequence is schematically shown in fig. 2.7a. The first two pulses constitute the EPR Hahn-echo sequence, as shown in fig. 2.2. The corresponding evolution of the spin-pair magnetization vectors in the rotating frame is shown in figs. 2.7b–f, where we assume that the MW pulses are on-resonant for spins A (red) and off-resonant for spins B (green). Spin-A packets will accordingly dephase and refocus during the evolution periods τ_1 and τ_2 to form a spin echo in $-y$ direction at time $\tau_2 = \tau_1$ after the π pulse. The magnetization of spin B is unaffected and remains at its thermal-equilibrium position. In PEPR experiments, the spin-echo is observed due to the transversal susceptibility change giving rise to coherent emission of MWs (see section 2.2.2). In EDMR, the observable is the change in singlet and triplet content of the spin-pair state. One thus needs to transform the xy-magnetization of spins A into singlet-triplet symmetry of the spin pair. This is achieved by the final $-\pi/2$ read-out pulse, which projects the magnetization vector of spins A from the xy-plane onto the z-axis (fig. 2.7g). The effective flip angle during the entire three-pulse sequence is π, giving rise to an EDMR transient as it

would have been after a single resonant MW pulse. However, only the efficiency of flipping spins A is proportional to the spin coherence before at the time of the read-out pulse. The permutation symmetry $\Delta(t = 0)$ at the end of the read-out pulse is thus proportional to the spin-echo amplitude at time τ_2.

The record the entire spin-echo electrically, the EDMR transient is recorded as a function of the read-out-pulse position τ_2. Maximum signal intensity is observed for $\tau_2 = \tau_1$, where the maximum echo intensity is observed. For $\tau_2 < \tau_1$, spins A have not fully refocussed, and for $\tau_2 > \tau_1$ spin packets have dephased again. In both cases the a lower singlet-state content is observed after the read-out pulse, quenching the EDMR signal. Recording the integrated charge ΔQ after the final pulse as a function of τ_2 thus yields the electrically detected spin echo. This method of stepwise scanning the echo amplitude is also referred to as *echo tomography* [78, 95].

Electrically detected spin echoes are the basis for setting up new PEDMR detection schemes. After creating spin coherence for either one of the paired spins, the spin ensemble can be manipulated in the same way as in PEPR. The final spin coherence is then read out by adding a final projection pulse. Using this recipe, basically any PEPR sequence can be translated into a respective EDMR experiment. In section 6.4.3, we will demonstrate this concept by recording nutation-frequency-resolved EDMR spectra using the so-called *phase-inverted echo-amplitude-detected nutation (PEANUT)* sequence [35], which is a well-establish PEPR technique, but has not yet been employed for electrical detection.

2.5.8 Spin-pair complexes involving more than two spins

For the theoretical description of EDMR, we have assumed a coupled pair of two $S = 1/2$ states. In this course of this work, however, we will also discuss spin-dependent electronic transitions that involve three instead of two coupled spins. An example is a three-particle process via a doublet-triplet complex, that is coupled pair of a single $S = 1/2$ particle and a strongly bound $S = 1$ state formed by another pair of $S = 1/2$ spins. Spin-dependent trans-

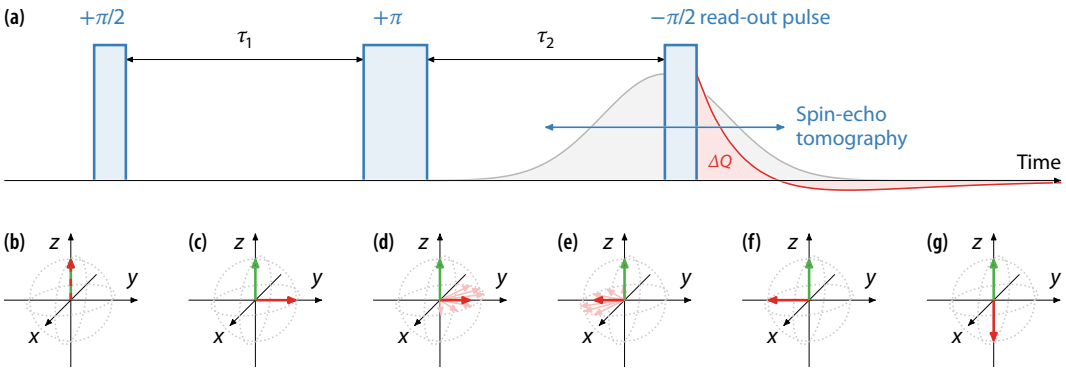

FIGURE 2.7 Modified three-pulse sequence for the electrical detection of Hahn echoes. (a) Pulse sequence and exemplary EDMR transient as a function of time. (b–f) Evolution of the spin-magnetization vectors of spins A (red) and B (green), forming the KSM spin pair, during the two-pulse EPR Hahn-echo sequence. The MW pulses are assumed to be on resonance only for spins A. (g) Magnetization vectors after the final $-\pi/2$ read-out pulse, which projects *xy*-magnetization into spin-pair symmetry. By measuring the integrated charge ΔQ of the EDMR transient $\Delta I(t)$ as a function of τ_2, the entire electrically detected spin echo can be recorded ("echo tomography").

port and recombination processes via such three-particle complexes have been reported for both organic [21, 91, 96] and inorganic [97, 98] semiconductors. The theoretical model for PEDMR developed by Boehme and Lips, summarized in sections 2.5.2 to 2.5.6, has recently been extended to coupled pairs of $S = 1/2$ and $S = 1$ states by Keevers *et al.* [85]. Here, we will only briefly review the basic concept of this model and refer to the original article for a comprehensive treatise.

The spin dependency of electronic transitions between a doublet-triplet spin-pair complex is schematically illustrated in fig. 2.8 for three spin configurations in presence of an external magnetic field. Independent from the type of the electronic transition (*e. g.*, hopping transport or recombination), transitions between the *S*1 spins and the weakly coupled $S = 1/2$ spin are Pauli-forbidden if all spins are aligned parallel, that is, if the total spin state is an *S*3/2 quartet (fig. 2.8a). For anti-parallel alignment of the *S*1 spin with respect to the *S*1 pair, a total-spin-1/2 doublet state is formed and electronic transitions become Pauli-allowed. Such a transition could, for instance, be a tunneling hop of either one of the strongly coupled spins into the singly occupied $S = 1/2$ state. The transition probability thus depends on the doublet ($|D\rangle$) and quartet ($|Q\rangle$) content of the total spin complex.

This already indicates the pathway for a theoretical description in analogy to the model for weakly coupled $S = 1/2$ states: Instead of considering different transition probabilites p_S and p_T for singlet and triplet content of the spin-pair, the spin-state dependent transition probabilites are given by

$$p_i = p_D \left|\langle i|D\rangle\right|^2 + p_Q \left|\langle i|Q\rangle\right|^2, \tag{2.87}$$

where p_D and p_Q are the doublet and quartet transition rates ($p_D \gg p_Q$). Accordingly, the total transition probibility can be expressed in terms of the density matrix,

$$P(t) = p_D \sum_{i=-1/2}^{1/2} \mathrm{tr}\left[|D_i\rangle\langle D_i|\,\boldsymbol{\rho}(t)\right] + p_Q \sum_{i=-3/2}^{3/2} \mathrm{tr}\left[|Q_i\rangle\langle Q_i|\,\boldsymbol{\rho}(t)\right]. \tag{2.88}$$

The evolution of $\boldsymbol{\rho}(t)$ can then be derived from the stochastic Liouville equation (eq. 2.55),

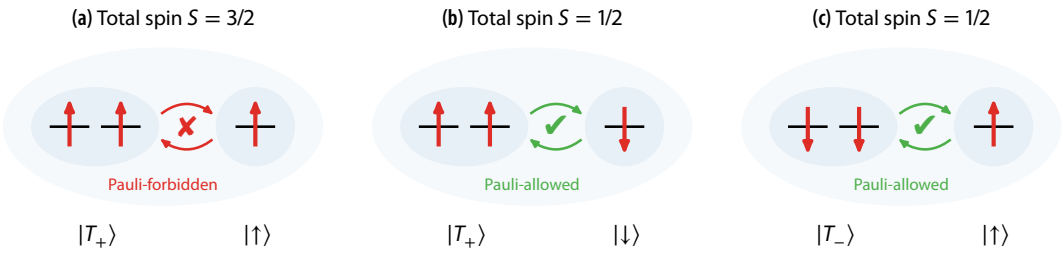

FIGURE 2.8 Illustration of spin-dependent electronic transitions between a weakly coupled spin pair consisting of a strongly coupled triplet ($S = 1$) state and a third $S = 1/2$ spin. Three possible spin configurations are shown: (a) If all spins are aligned parallel ($|T_+\uparrow\rangle$ or $|T_-\downarrow\rangle$), transitions between the spin-pair states are forbidden due to the Pauli exclusion principle. To total spin state is a quartet1 ($|Q\rangle$, total spin $S = 3/2$). Flipping either the (b) $S = 1/2$ or the (c) $S = 1$ spin results in spin configurations $|T_+\downarrow\rangle$ and $|T_-\uparrow\rangle$, respectively, forming a total doublet state ($|D\rangle$, total spin $S = 1/2$). Transitions between the paired electronic states become Pauli-allowed. Configurations where $m_S = 0$ for the triplet manifold ($|T_0\uparrow\rangle$ and $|T_0\downarrow\rangle$, not shown) exhibit mixed doublet and quartet content.

based on the static spin Hamiltonian, which is given by

$$\mathcal{H}_0/h = \mu_B \left(\boldsymbol{S}_A^T \boldsymbol{g}_A + \boldsymbol{S}_B^T \boldsymbol{g}_B\right) \boldsymbol{B}_0/h + \boldsymbol{S}_A^T \boldsymbol{D}_A \boldsymbol{S}_A - J_{AB} \boldsymbol{S}_A^T \boldsymbol{S}_B + \boldsymbol{S}_A^T \boldsymbol{D}_{AB} \boldsymbol{S}_B \tag{2.89}$$

for $S_A = 1$ and $S_B = 1/2$. The first two terms correspond to the electron-Zeeman interactions, the second term is the ZFS of the triplet state and the last two terms denote the exchange and dipolar interaction between the two spin states. The matrix representation of this Hamiltonian in the product base is a 6×6 matrix. In analogy to section 2.5.2 the spin Hamiltonian can be diagonalized into its energy eigenbasis by a unitary matrix transformation. After including the oscillatory Hamiltonian accounting for the MW field $\boldsymbol{B}_1$, transition frequencies and amplitudes can be read from the diagonal and off-diagonal matrix elements. Explicit expressions and a transition analysis for different coupling regimes can be found in ref. [85].

The model sketched above was originally developed in view of spin-dependent recombination mediated by *triplet-exciton/polaron (TEP)* complexes, observed in organic semiconductors and devices like OLEDs and solar cells [21, 91, 96]. However, it applies to spin-dependent transport and recombination processes via three-spin complexes also in inorganic semiconductors like amorphous silicon. Recently, a similar spin-dependent Auger-like recombination process has been reported microcrystalline-silicon thin-film solar cells [98]. In the scope of this work we will identify a comparable spin-dependent transport channel also in the EDMR signatures of amorphous silicon, which can be described based on the theoretical model developed by Keevers *et al.*

2.6 SUMMARY AND CONCLUSION

In this chapter, we have summarized the basic principles of EPR and EDMR spectroscopy, thereby laying the foundation for the experimental results presented throughout this work. In particular, we discussed the model for spin-dependent transport and recombination processes that give rise to conductivity changes probed by EDMR. We further established the link between coherent spin manipulation and electrical read-out, which allows to convert the wide variety of existing PEPR detection schemes into EDMR experiments. This will be of particular use in chapter 6, where we employ a toolkit of PEDMR techniques to disentangle electronic transport channels in amorphous-silicon solar cells.

CHAPTER 3

Amorphous silicon: a brief survey

This thesis is focussed on understanding spin-dependent transport processes in amorphous silicon (a-Si). However, research on a-Si dates back until the middle of the last century. In this chapter, we will give a brief overview on the development and properties of the material. In particular, we will emphasize the impact of defect states on the electronic quality of a-Si and summarize the information gained from magnetic-resonance, photoluminescence and photoconductivity studies to understand the microscopic origin of electronic transport and recombination processes. This chapter thus lay the foundation to set the experimental results presented later on into the context of previous research.

3.1 HYDROGENATED AMORPHOUS SILICON

Amorphous silicon (a-Si) is amongst one of the most extensively studied materials of the last decades and can today be regarded as the prototypical amorphous semiconductors. Despite its low production costs, however, pure a-Si is a virtually useless material for technological applications owing to its poor electronic quality [99–101]. The reason is a high density of electronic defects, caused by the structural disorder that distinguishes a-Si from crystalline silicon (c-Si). A major breakthrough was the discovery that the incorporation of hydrogen during the a-Si growth produces a material with strongly improved properties, thereafter referred to as *hydrogenated a-Si (a-Si:H)*. This finding initiated a huge amount of research leading to a broad range of device technologies based on a-Si:H, such as solar cells, thin-film transistors, sensors, detectors or displays [101].

The principal difference of a-Si with respect to c-Si is the lack of long-range order. On a short range, a-Si preserves the four-fold coordinated, tetrahedal order of c-Si. Experimental evidence for this similar local structure is provided from the radial distribution function (RDF), obtained from X-ray diffraction data, which describes the local density distribution as a function of distance from a reference atomic site. In the RDF of pure a-Si, the first peak is found at a distance of 2.35 Å, almost identical to the crystalline value of 2.4 Å [102]. However, it is a common feature of RDF data of a-Si that subsequent peaks become more and more broadened and deviate from those obtained for c-Si, until the RDF becomes completely smeared out for atomic distances larger than about 6–10 Å. This shows that for larger length scales, the atomic structure of a-Si can be considered as entirely disordered.

The simplest and commonly used structural model that fits the a-Si RDF data of short-range order and long-range disorder is that of a *continuous random network (CRN)*, originally introduced for the description of glasses such as silica [103]. In a CRN model for a-Si, the periodic crystalline, four-fold coordinated structure of c-Si is replaced by a ran-

dom network of atoms, where each atomic site has a specific coordination number than varies from site to site [104], as schematically illustrated in fig. 3.1a. While the preservation of short-range order results in similar bulk electronic properties of a-Si compared to its crystalline counterpart (most notably, both being semiconductors), the long-range disorder described by the CRN model at the same time leads to fundamental differences. For instance, the structural disorder produces a variation of bond lengths and angles between different atomic sites. This results in weak Si−Si bonds giving rise to so-called *band tails* of localized electronic states (*Anderson localization* [7]) extending from both the conduction and the valence band deep into the otherwise forbidden band gap [105], as depicted in fig. 3.1b. Thus, the concept of sharp band edges and band gaps used for crystals is inappropriate for amorphous semiconductors and instead replaced by the *mobility edges* E_C and E_V, which define the *mobility gap*, respectively (about 1.9 eV for a-Si:H [99]). The term "mobility edge" is due to the fact that the energies E_C and E_V mark the transition from the extended states forming the conduction and valence band, respectively, to the localized band-tail states, where the charge-carrier mobility drops by orders of magnitude [106]. Band-tail states play a crucial role in a-Si since electronic transport in a semiconductor occurs at the band (or mobility) edges.

The most critical disorder-induced characteristic of a-Si, however, is a high density of structural defects. In crystals, defects are local interruptions of the crystalline lattice (for example, vacancies, interstitials or dislocations). In a disordered random-network structure, however, the mere structural feature is the atomic coordination. The principal type of defect in an amorphous solid thus is a coordination defect. As illustrated in fig. 3.1a, the CRN allows to easily incorporate atoms with different coordination numbers [99], which may induce over- or under-coordinated atomic sites. In a-Si, the fundamental structural defect is the so-called *dangling bond (DB)*, referring to an under-coordinated site in the a-Si network, where one of the four Si valence electrons cannot form a covalent bond with a neighbouring Si atom and is left unbound ("dangling"). In fig. 3.1a, a DB thus corresponds to a three-fold coordinated atomic site (red). Dangling bonds appears as localized elec-

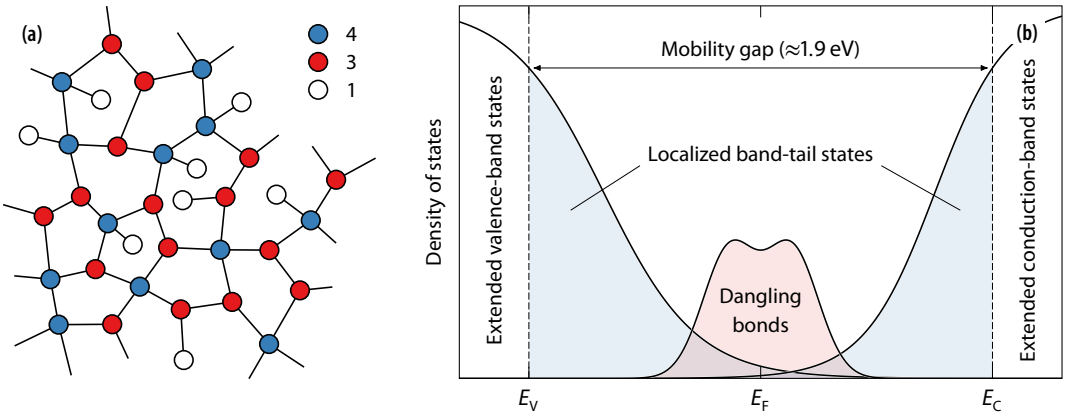

FIGURE 3.1 **(a)** Example of a continuous-random-network structure with atomic sites of different bonding coordination, as indicated by the different colors. Adapted from ref. [99]. **(b)** Schematic distribution of the density of states as a function of energy in the band gap of amorphous silicon, including localized band-tail states and dangling bond (DB) defects. The energies E_V and E_C denote the valence-band and conduction-band mobility edges, respectively, and E_F the Fermi level. The two peaks of the DB distribution qualitatively reflect the amphoteric nature of DB defects and are separated by the correlation energy U (see section 3.2). Adapted from ref. [101].

tronic states close to the middle of the band gap, leading to an additional distribution of states in the energy gap (see fig. 3.1b). In pure a-Si, the DB density can be as high as 10^{20} 1/cm^3 [107]. Together with the band-tail states, the consequent density of gap states is sufficiently high to effectively pin the Fermi level in the middle of the band gap [101]. This not only results in a very low conductivity, but also prevents any desirable property of a semiconductor, such as photoconductivity or the ability to manipulate electron and hole conductivities by doping. Therefor, the structural defects in a-Si are the fundamental reason for the poor electronic quality of the material.

The situation of a-Si fortunately improved in the late 1960s, when new deposition techniques, such as plasma-enhanced chemical vapour deposition (PECVD) [108], were established, which allowed to prepare a-Si films of higher electronic quality. It was soon discovered that the improved quality was a result of the incorporation of hydrogen during growth [109], by both increasing the photoconductivity [188] and enabling substitutional doping of a-Si films [110]. In the following decades, extensive research activities evolved in the field of a-Si:H [99, 101]. In addition, a-Si:H was soon successfully employed for technological applications, including solar cells [111] and thin-film transistors [112].

The improved electronic quality of a-Si:H was attributed to a reduced density of gap states, in particular, a lower density of DB defects. In 1974, Lewis *et al.* [109] showed that incorporating hydrogen into amorphous germanium films reduced the defect density by orders of magnitude and proposed the same origin for the electronic improvement of a-Si:H. They interpreted their results in terms of a compensation of DBs by hydrogen. By forming a strong Si−H bond instead of a DB, the localized midgap state would be dismissed deep into the valence band [107], thereby reducing the density of gap states. The vast amount of subsequent research clearly solidified this picture [99]. Modern device-grade a-Si:H, typically deposited at a hydrogen concentrations of about 10 at. %, reaches DB densities of a few 10^{14} 1/cm^3 [101], orders of magnitude below the defect density in unhydrogenated a-Si.

While the reduced defect density in a-Si:H drastically improves the material quality, the remaining gap states are still a determining factor for the electronic transport properties. Tail states and DBs act as traps and recombination centers for charge carriers, thereby reducing the conductivity. In state-of-the-art devices that employ a-Si:H (for instance, heterojunction c-Si/a-Si:H solar cells) transport and loss mechanisms at defect sites play a crucial role for the device efficiency. Understanding the microscopic nature of defects and their impact on charge-carrier transport has therefor been the major driving force for numerous studies carried out on a-Si:H over the last decades. Despite this extensive amount of research and the huge success of a-Si:H in technological applications, however, a plethora of fundamental questions regarding the detailed physical mechanisms in a-Si:H remain unanswered. Prime examples include the origin of light-induced degradation of a-Si:H by means of the so-called Staebler-Wronski effect (see section 3.2), the microscopic defect structure in a-Si:H and at interfaces with other silicon phases such as c-Si [113, 114], or even the description of the atomic structure by a CRN, which has recently been questioned [6]. This shows that further effort is required to achieve a better understanding of amorphous semiconductors and a-Si:H, in particular.

This work focusses on transport and recombination processes via disorder-induced defects such as band-tail states or DBs. Since these states can be paramagnetic if occupied by a single electron or hole, magnetic-resonance techniques are ideally suited tools

for their identification and structural characterization. Compared to other experimental techniques, such as optical absorption, photoemission spectroscopy, capacitance or field-effect measurements, or tunneling spectroscopy, EPR is the only method that allows the microscopic identification of defect states by their *g*-value and additionally provides insights into the local atomic structure by means of the hyperfine interaction. Even more specific information is obtained from EDMR, which directly probes those paramagnetic states involved in electronic transport and recombination processes. Both EPR and EDMR have been successfully applied to a-Si:H in the past. In the following sections, the results of this research are briefly summarized, with a special emphasis on the open questions adressed in this work concerning the defect-related electronic transport properties of a-Si:H.

3.2 PARAMAGNETIC STATES IN AMORPHOUS SILICON

The first EPR experiments on a-Si date back until 1969, when Brodsky and Title [8] as well as Ditina *et al.* [9] observed a single resonance line at a *g*-value of 2.0055, which was attributed to the DB defect. In the following, numerous EPR investigations of a-Si have been conducted, such that today the DB defect in a-Si is certainly amongst the most thoroughly studied paramagnetic center in disordered solids. In addition, further resonances were found in the EPR signals of doped a-Si:H [115–118] and also by light-induced EPR on both doped and undoped a-Si:H [119–122]. These resonances, appearing at *g*-values of about 2.004 and 2.01, were assigned to electrons and holes trapped in band-tail states of the conduction and valence band, respectively [123], respectively. This section provides a short overview of the experimental evidence obtained from EPR studies on these paramagnetic centers.

3.2.1 Dangling bonds

In their original EPR study on a-Si, Brodsky and Title found a Lorentzian-shaped line at a *g*-value of 2.0055 and a spin density of 10^{20} 1/cm^3 [8]. Their interpretation of the resonance in terms of DB defects was more or less intuitive due to the similarity to signals of DBs observed at artificially disordered c-Si surfaces [124, 125]. Despite the lack of conclusive evidence, this assignment was accepted by the scientific community for the following twenty years. In 1986, Pantelides fundamentally challengend the DB hypothesis by proposing a model of over-coordinated atomic sites with five covalent bonds, which he termed *floating bonds*, as the origin of the EPR line [12]. This subsequently gave rise to controversial discussion [13, 14] and led to the conclusion that solely based on *g*-value and line-width information, unambiguously assigning the origin of the EPR resonance to either the floating- or the dangling-bond model was not possible.

Experimental evidence that favored the DB assignment instead of the opposing floating-bond model was given by Stutzmann and Biegelsen [126, 127] by a more detailed study of the ^{29}Si hyperfine structure. They analyzed the experimentally obtained hyperfine tensor in terms of a model introduced by Watkins and Corbett [128] that approximates the wavefunction by a linear combination of atomic orbitals (LCAO). Thereby, they could show that 45–65 % of the underlying defect wavefunction is localized on a single Si atom [127]. This observation contradicts the floating-bond proposal, where a much higher degree of

delocalization would be expected [129, 130]. In addition, the LCAO analysis revealed that the defect wavefunction can be described by an sp^3 hybrid, with about 10 % *s*-type and 90 % *s*-type contributions. An sp^3 hybridization had been similarly found for the P_b center at the interface between c-Si and SiO_2 [131], the most prominent example of a silicon DB defect, which further advocated the DB model. Later LCAO calculations by Ishii and Shimizu [132], as well as multifrequency-EPR experiments by Umeda *et al.* [15] gave similar results and confirmed the similarities to the P_b center, such that the DB assignment became firmly established.

Being an under-coordinated bonding site, the neutral DB defect is occupied by a single electron. However, DBs are *amphoteric*, that is, by a shift of the Fermi level (*e. g.*, by doping), neutral DBs can be either populated with a second electron or depolutated to create negatively or positively charged DBs. The energy states associated with neutral and charged DBs are denoted D^0, D^- and D^+. Depending on its charge state, the transition energy to populate or depopulate a DB shifts by the *correlation energy* [99]

$$U = U_C - W = \frac{e^2}{4\pi\varepsilon_r\varepsilon_0 r} - W. \tag{3.1}$$

The first term, U_C, describes the Coulomb repulsion between two electrons separated by a distance r, which is only present in the doubly occupied D^- state. The second term, W, is the energy gain due to a change of the local bonding configuration by the addition of an electron to the DB state (*lattice relaxation*, see ref. [99]). The correlation energy can thus be either positive or negative. For positive U ($U_C > W$), the singly occupied D^0 state is lowest in energy, such that all defects are paramagnetic at thermal equilibrium (assuming $U \ll kT$). However, if the lattice-relaxation energy exceeds the Coulomb repulsion ($U_C < W$), one obtains a negative-U defect, a concept first introduced by Anderson [133]. In this case, the neutral D^0 state is unstable and the equilibrium state comprises an equal density of charged D^- and D^+ states [99, 134]. Such negative-U defects are observed in chalcogenide glasses [135, 136]. Since both D^- and D^+ are diamagnetic ($S = 0$), they do not show an EPR signal at thermal equilibrium. Dangling bonds thus have a positive correlation energy, which has been estimated at about 0.2–0.3 eV from depletion-width-modulated EPR [137] and the deviations from Curie-law behavior in temperature-dependent EPR measurements [138]. Nevertheless, several studies assumed a coexisting distribution of negative-U DBs as the potential origin of LEPR signals [139–144] or as precursor states for the Staebler-Wronski effect [140, 145] (see following sections).

Concerning the microscopic structure of DB defects, further information was obtained from EPR studies that compared a-Si:H with deuterated a-Si (a-Si:D), where hydrogen was replaced with deuterium (D) during the deposition process [126, 146, 147]. Although the magnetic moment of D is smaller than that of H, no spectral change was observed between the DB signals of a-Si:H and a-Si:D. This led to the conclusion that hydrogen is absent in the direct vicinity of DB defects and only unresolved HFIs with more distant ^{1}H nuclei are present and lead to broadening of the line width. The observation that no hydrogen is back-backbonded to atomic sites carrying DBs seems surprising at first glance, when comparing the natural abundancy of ^{29}Si (4.7 at. %) to the hydrogen content (around 10 at. %). From pure statistics, one might thus expect a number of back-bonded ^{1}H nuclei at DB sites similar that is of the same order as the number of back-bonded ^{29}Si nuclei. Nevertheless, as pointed out by Biegelsen and Stutzmann [126], the anticorrelation

TABLE 3.1 Summary of experimentally and theoretically obtained spin-Hamiltonian parameters of paramagnetic states in a-Si:H, obtained by different groups. Only the principal values of the *g*-tensor and the isotropic (a_{iso}) and axial component (T) of the *A*-tensor are shown. Further parameters such as strains or field-independent broadening function can be found in the listed references.

	Reference	g_x (or $g_\perp$)	g_y (or $g_\perp$)	g_z (or $g_\parallel$)	a_{iso} (MHz)	T (MHz)
DB	Stutzmann, Biegelsen [127]	2.008	2.008	2.004	205	50
	Umeda *et al.* [15]	2.0065	2.0065	2.0039	206	63
	Ishii, Shimizu (DFT) [148]	-	-	-	–220	–70
	Fehr *et al.* [148]	2.0079	2.0061	2.0034	190	39
	Fehr *et al.* (DFT) [148]	2.0093	2.0064	2.0035	–252	–37
CBT	Umeda *et al.* [149, 150]	2.004	2.004	2.004	200	-
	Ishii, Shimizu (DFT) [151]	-	-	-	–270	–39
VBT	Umeda *et al.* [149, 150]	2.019	2.012	2.005	<80	-
	Ishii, Shimizu (DFT) [151]	-	-	-	–38	–36
	Akhtar *et al.* (EDMR) [26]	2.015	2.009	2.006	-	-

of DBs with hydrogen simply confirms the picture of both the formation of DBs and the incorporation of hydrogen is due to a reduction of local strain in the amorphous network. Hydrogen thus compensates for DBs defects, which is the principal benefit of a-Si:H with respect to pure a-Si, as discussed in the previous section.

The above-mentioned studies by Stutzmann and Biegelsen [127] and Umeda *et al.* [15] both found axial anisotropies for both the *g*- and the *A*-tensor (see tab. 3.1). In addition, an orientation-dependent line width due to strain in the spin-Hamiltonian parameters caused by the structural disorder was observed in both studies. However, the MW frequencies used in their EPR experiments were limited to either only X-band [127] or to frequencies below Q-band [15]. Since strain-induced line widths are of the same order as anisotropies, the spectra obtained in these studies thus only partly allowed a clear separation of field-dependent (*g*-tensor) and field-indepedent (*A*-tensor) spectral contributions. A more recent multifrequency EPR study by Fehr *et al.* extendend the range of frequencies from S- to W-band [148]. In addition, they combined their experiments with a theoretical analysis by means of density-functional theory (DFT), allowing for a more profound determination and interpretation of the DB spin-Hamiltonian parameters. Other than the earlier studies, Fehr *et al.* found rhombic *g*-tensor anisotropy, both experimentally and from DFT calculations (see tab. 3.1). Although, concerning the *g*-tensor, Fehr *et al.* found good agreement between experimental results and DFT calculations, they likewise observed a mismatch between the calculated—both from their study and from earlier DFT calculations [151]—and the experimentally obtained HFI parameters (see tab. 3.1). From this, they concluded that the DB defect is in reality far more delocalized than assumed in the DFT models and than it was concluded in the earlier studies. These findings again questioned integral aspects of the DB model and thereby illustrate that, even after fifty years of extensive research, fundamental questions concerning the microscopic defect structure in a-Si:H remain unanswered.

3.2.2 Metastable defects and light-induced degradation

An important driver for research on defect states in a-Si:H has been their relation to light-induced degradation by means of the *Staebler-Wronski effect (SWE)*. In 1977, Staebler and Wronski [4] discovered that upon light exposure both the photo- and the dark conduc-

tivity of unpoed a-Si:H was decreased by several orders of magnitude. Although they also found that the effect is reversible through annealing at temperatures around 150–200 °C, the SWE severly limits the use a-Si:H for photovoltaic applications [152].

Staebler and Wronski observed that the conductivity decrease is the result of a Fermi-level shift towards midgap and a reduced charge-carrier lifetime, and proposed the generation of a light-induced metastable defect density in the band gap, increasing the recombination cross section for charge carriers, as a potential origin of the effect [5]. Subsequent studies by Dersch *et al.* [10] and Stutzmann *et al.* [11] then provided experimental evidence relating the SWE to DB defects, as they observed a light-induced, reversible increase of the DB EPR signal. In the following, a multitude of microscopic models to explains the creation of metastable DB defects have been proposed [11, 140, 145, 153–160]. These models include the recombination-induced breaking of weak Si−Si bonds [11, 157], the formation of metastable hydrogen complexes [154, 156], the dissociation of Si−H bonds [158], or the creation of metastable neutral DBs from formerly charged negative-*U* states [140, 145].[1] Many of these models predict the creation of DB defects that are spatially correlated to hydrogen atoms, yet no experimental evidence exists for such a correlation. In fact, investigations probing the presence of hydrogen in the vicinity of metastable DBs resulted in almost identical EPR spectra of native and light-induced defects [147]. Thus, despite the variety of models, the microscopic process leading the creation of metastable DB defects until today remains unclear.

Recently, Fehr *et al.* [162] reinvestigated one of the early models by Carlson [153] that related metastable defect creation to microvoids in the amorphous structure. By employing PEPR relaxation measurements, they found that metastable DBs can be separated into two types: Accordingly, the majority of light-induced DBs are isolated DBs (about 80 %), while a portion of DBs exists (about 20 %) that is clustered and could be associated to microvoids, as originally proposed by Carlson. These conclusions are support by recent results of Melskens *et al.* [163], who found that reduction of the density of nanosized voids results in enhanced electronic stability of a-Si:H. Local structures such as microvoids may thus play an important role for the SWE.

While the investigation of the light-induced defects is not the central aim of this work, the SWE is yet another example that illustrates the plethora of open questions that still exist, not only regarding light-induced degradation, but also concerning the entire structure an, in particular, the microcopic nature of defects in a-Si:H.

3.2.3 Conduction- and valence-band tail states

As discussed in section 3.1, the electronic properties of a-Si:H are not only affected by midgap defect states but also by the localized band-tail states close to the conduction-band and valence-band mobility edges. While these states do not exhibit an EPR signal in undoped a-Si:H, the conduction-band (CBT) and valence-band tail (VBT) states can be made paramagnetic by shifting of the (quasi-)Fermi level. This can be accomplished either by substitutional doping or by generating excess charge carriers, for instance, by optical excitation (LEPR) or charge-carrier injection.

The first LEPR investigations on a-Si:H were carried out in the late 1970s [119–122]. These experiments revealed two new resonances in undoped a-Si:H in addition to the

[1] A comprehensive discussion of microscopic models fot the origin of the SWE is beyond the scope of this work, but reviews can be found in the literature (for instance, see refs. [152, 161]).

DB signal: (i) a narrow resonance ($\Delta B_{pp} \approx 6$ G) at $g = 2.0043$–2.0048 and (ii) a broad resonance ($\Delta B_{pp} \approx 20$ G) at $g = 2.010$–2.013. Street and Biegelsen [123] attributed these signals to electrons and holes trapped at CBT and VBT states, respectively. This assignment was substantiated by the observation of the same resonances by EPR on *n*-type phosphorus- and *p*-type boron-doped a-Si:H [115–118]. Phosphorus-doping of a-Si:H shifts the Fermi level E_F towards the conduction-band mobility edge E_C, boron doping towards the valence-band mobility edge E_V. Thereby the occupancy of tail states is changed: Unoccupied CBT states are populated or doubly occupied VBT states are depopulated into singly occupied and thus paramagnetic states, which is consistent with the observation of either one of the two EPR lines for *n*- and *p*-type a-Si:H. In undoped a-Si:H, light excitation shifts the quasi-Fermi levels $E_{F,n}$ and $E_{F,p}$ for electrons and holes towards E_C and E_V, respectively, explaining the presence of both lines in LEPR spectra.

An alternative explanation of the $g = 2.004$ and $g = 2.01$ resonances in LEPR spectra was the trapping of light-generated electrons and holes at negatively charged DBs [139–144]. This model requires a high density of DBs with a negative correlation energy U coexisting with the positive-U defects responsible for the dark-EPR signal (see section 3.2.1). A summary of experimental evidence favoring this model can be found in ref. [164].

As for the DB defect, additional information stemming from the HFI with ^{29}Si was required to decide between the two models: While initial studies did not succeed in identifying clearly discernible ^{29}Si hyperfine structures [143, 165], a later, more detailed study by Umeda *et al.* [149, 150], which employed pulsed LEPR relaxation measurements on undoped a-Si:H with varying ^{29}Si concentration, unambigously resolve hyperfine shoulders of the CBT resonance that increased according to the ^{29}Si concentration. Umeda *et al.* further analyzed the relative intensity of this shoulder and found that the HFI with ^{29}Si is about twice as large for the $g = 2.004$ line than for the DB signal. From this result, they concluded that the wavefunction associated with this signal is spread over two Si atoms, which clearly advocates the assignment to a CBT state caused by a weak Si−Si bond. Although, Umeda *et al.* were not able to resolve HFI for the $g = 2.01$ resonance, also owing to the broader and anisotropic line shape (see below), they assigned the line to holes trapped at VBT states by analógy and thereby confirmed the initial explanation by Street and Biegelsen [123] in preference to the charged-DB model.

From the absence of hyperfine structure, Umeda *et al.* concluded an upper bound for the isotropic HFI of VBT states given by the line width (3 mT or about 80 MHz). They explained this lower HFI—with respect to that observed for the CBT line (7 mT or about 200 MHz)—with a more *p*-like wavefunction for holes trapped in VBT states, as compared to electrons in CBT states. This interpretation is supported by earlier DFT calculations [151, 166] that predicted HFIs in agreement with the experimental results (see tab. 3.1). Besides the HFI parameters, Umeda *et al.* also analyzed the field-dependency broadening of the LEPR line shape with respect to *g*-tensor anisotropy by carrying out multifrequency experiments. While they found an isotropic *g*-value for the CBT resonance, they observed pronounced rhombic anisotropy for the VBT line (see tab. 3.1). Recent multifrequency EDMR measurements by Akhtar *et al.* [26] also found a good fit assuming rhombic anisotropy, although it is to be noted that due to strongly overlapping signals and a potentially over-parameterized fit this report can only partly confirm the results by Umeda *et al.*.

3.3 RECOMBINATION OF EXCESS CHARGE CARRIERS

While EPR has proved to be a powerful tool for the analysis of defect states in a-Si:H, the early research on a-Si:H also employed optical and electrical measurements to gain information concerning the structure of gap states and their impact on electronic transport properties [99, 101, 107]. In particular, *photoluminescence* and *photoconductivity* measurements have been employed intensively to understand charge-carrier transport and recombination pathways. Combining these experiments with magnetic resonance finally led to the development of EDMR and ODMR, allowing to specifically probe the involvement of paramagnetic defects, such as DBs and band-tail states, in the microscopic transport processes.

3.3.1 Photoluminescence and photoconductivity

The observation of photoluminescence (PL) in a-Si:H by Engemann and Fischer [167] in 1974 triggered a series of studies by different groups [168–175], aiming to identify the microscopic recombination mechanism responsible for the observed photoemission. Photoluminescence occurs when an excited pair of charge carriers, that is, an electron at energy E_n and a hole at energy E_p, recombines radiatively to emit a photon of energy $h\nu = E_n - E_p$. Different PL peaks were reported in the energy range of 0.7–1.5 eV, depending on the deposition conditions and the doping level.[1] A common feature, however, was the observation of a broad single broad emission band centered at 1.25–1.4 eV in undoped a-Si:H of low defect density, and another transition at 0.8–0.9 eV for either defect-rich, low-quality samples or in case of phosphorus- or boron-doped a-Si:H [176]. The former is often called *intrinsic* or *principal luminescence*, the latter is referred to as *defect luminescence* and is assigned to a radiative recombination between an electron trapped in a doubly occupied DB defect (D^-) and a VBT hole [175]. The first model for the instrinisc PL, present in all a-Si:H samples, was suggested by Tsang and Street [177], who interpreted the emission band in terms of a *radiative tunneling (RT)* recombination between electron and holes trapped in CBT and VBT states.

The RT model was based on the observation of disparate PL kinetics between different groups: The reported PL lifetimes spread over a wide range from a few nanoseconds [168] up to milliseconds [172]. To explain this behavior, Tsang and Street adapted a model that had been previously used for the description of donor-acceptor pairs in crystalline semiconductors [178].[2] In a-Si:H, charge carriers that have been excited into the extended band states will relax down to their respective tail states through rapid thermalization on a picosecond time scale [180, 181]. This allows the conclusion that all recombination (radiative or non-radiative) happens after the excited electrons and holes have been trapped in CBT and VBT states, respectively. In the RT model, recombination thus happens between electrons and holes localized on CBT and VBT sites separated by a distance r. The lifetime τ then depends solely on r, as given by

$$\tau = \tau_0 \exp\left(2r/\xi\right), \tag{3.2}$$

where ξ is the largest localization length of the two states and τ_0 is a time constant that

[1] A comprehensive review summarizing the early PL studies can be found in ref. [176].

[2] For a detailed description of the radiative-tunneling model for the recombination in a-Si:H, refer to the original articles [176–178] as well as recent reviews, *e. g.*, in refs. [101, 179].

was estimated to about 10 ns [177]. As, in eq. 3.2, the lifetime τ solely depends on the separation r between excited electrons and holes trapped in tail states, which is expected to vary randomly, the RT model was successful in explaining the wide range of PL lifetimes.

A fundamental question concerning the nature of a recombination process is whether the recombining charge carriers stem from a *geminate* or a *non-geminate* pair [182]. In a geminate process, the electron and the hole are created by the same photon, *i. e.*, the charge carriers are not able to diffuse apart during thermalization, before being trapped and recombining. Opposingly, a non-degeminate (or *distant-pair*) process refers to electrons and holes that diffused apart after excitation and recombine with the nearest available partner that has been excited in a another absorption event. Both geminate [176, 183, 184] and distant-pair recombination [185] were proposed as the origin of PL and the decision between the two models has been under controversial debate since then. Preliminary conclusions were drawn from photoconductivity (PC) measurements that complemented the early PL studies [186–190]. Comparing PL and PC allows to distinguish between geminate and non-geminate recombination: While both can cause PL, only non-geminate recombination influences the photocurrent since since geminate pairs that are not separated do not contribute to electronic transport.

Studies of both PL and PC of a-Si:H have shown that their temperature dependencies are auto-correlated [169, 174, 177, 188, 190], as depicted in fig. 3.2a: At low temperatures ($T < 60$ K), the PL intensity is maximal with quantum efficicies above 30 %, whereas the PC is very low with a value of about $\sigma_P / eG = 10^{-11}$ cm^2/V (normalized by charge e and

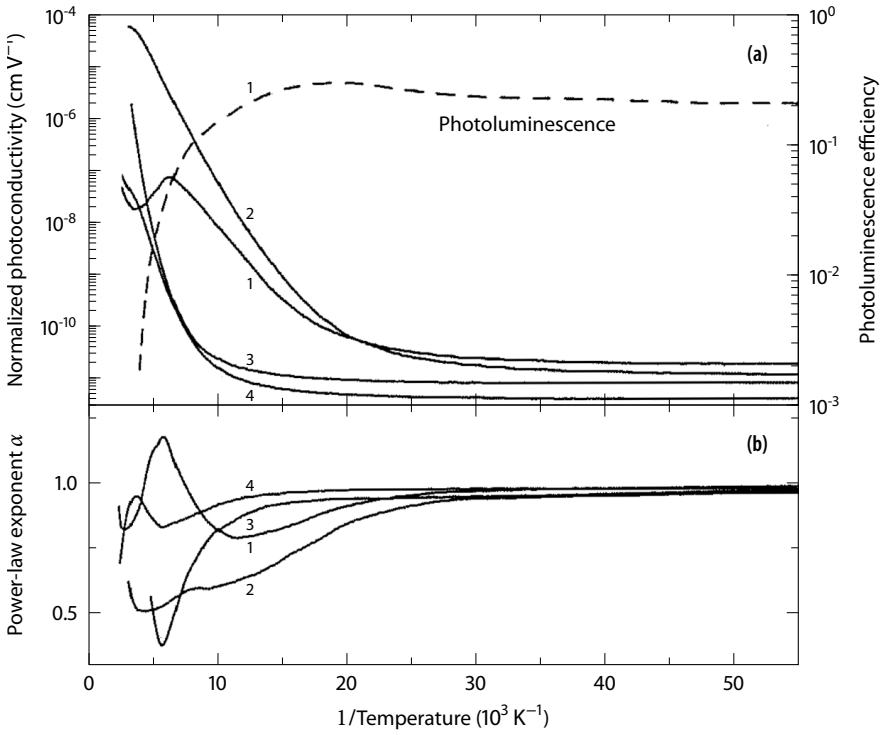

FIGURE 3.2 Temperature dependency of (a) the photoluminescence and the normalized photoconductivity σ_P / eG and (b) the exponent α of the power-law relation $\sigma_P \propto G^\alpha$ of four different a-Si:H films: 1) PECVD undoped, 2) phosphorus-doped (100 ppm PH_3), 3) boron-doped (1000 ppm B_2H_6), and 4) sputtered undoped. Reproduced from ref. [190].

generation rate G). With increasing temperature, the PC strongly increases, while the PL intensity decreases until it is entirely quenched for $T \gtrsim 200\,\mathrm{K}$. Thus, PL and PC appear to be competing processes. In the early literature, this observation was interpreted as radiative geminate-pair recombination being the dominant recombination mechanism at low temperature, outweighted by non-radiative recombination with increasing PC at higher temperatures [176, 191]. By combining PL measurements with quantitative EPR, it was further found that the PL intensity decreases with increasing DB density [192]. This led to the conclusion that the primary (non-radiative) recombination path in the high-temperature regime ($T > 60\,\mathrm{K}$) is provided by DBs, acting as recombination centers for excess charge carriers [176, 191]. This recombination channel was later confirmed and extensively studied by EDMR (see section 3.4.1).

Both PL and PC intensities were almost independent of temperature in the $T < 60\,\mathrm{K}$ regime. Nevertheless, at high excitation densities (generation rates $G > 10^{20}\,1/\mathrm{cm}^3\,\mathrm{s}$), the PL efficiency reached a peak at about 50 K and slightly decreases for lower temperatures [190, 191], indicating the existence of another non-radiative recombination channel that competes with radiative recombination at low temperature. This channel has been ascribed to Auger recombination [173, 191], that is, a three-particle process were the energy released during recombination of an electron-hole pair is transfered to a nearby third charge carrier instead of leading to the emission of a photon. This assignment was supported by a later study by Ambros *et al.* [193], who found that the dependence of the low-temperature PL intensity and lifetime on the carrier generation rate were well in agreement with what would be expected for a competing non-radiative Auger process.

Figure 3.2b shows the dependence of the PC on the charge-carrier generation rate G, expressed as a power law $\sigma_\mathrm{p} \propto G^\alpha$, for a-Si:H films of different electronic quality and doping. At higher temperatures, both the dependence on G and the PC magnitude and kinetics are strongly determined by the Fermi-level position and the density of gap states. However, at low temperatures ($T < 60\,\mathrm{K}$), σ_p depends linearly on G ($\alpha \approx 1$) and has a similar magnitude for all samples, indicating a more universal PC mechanism. In fact, a similar behavior has been observed for a broad range of amorphous semiconductors [194, 195]. This characteristic low-temperature PC has been associated with hopping conduction of electrons and holes in the band tails [194, 196–200]. In absence of thermal energy ($T = 0\,\mathrm{K}$), hopping transport can only occur to states that are lower in energy (*energy-loss hopping*), and σ_p arises from charge carriers that escape during thermalization before recombining as a geminate pair. Calculated values for σ_p based on this model led to values that are in good agreement with the observed experimental values [198, 199, 201, 202]. With increasing temperature (or under the influence of an electric field), hopping is enabled also to states that are higher in energy. Calculations predict a resulting hopping-transport path that is moved more and more towards the mobility edge, until it shifts into the extended band states for $T \gtrsim 100\,\mathrm{K}$ [199, 201, 202]. This is in good agreement with the experimental observations of a strongly increasing and material-dependent PC at higher temperatures (see fig. 3.2).

3.3.2 Frequency-resolved spectroscopy

To further elucidate the origin of recombination, the impact of the charge-carrier density on both the PL intensity and the lifetime distribution was studied by varying the generation rate G. This led to a novel PL method, introduced by Dunstan *et al.* [203, 204] and

referred to as *(quadrature) frequency-resolved spectroscopy (QFRS)*, which measures the in- and out-of-phase components of the PL signal in quadrature and thereby is capable of directly probing the lifetime distribution. Bort *et al.* [205] measured QFRS spectra as a function of the generation rate and observed a transition in the PL kinetics at a generation rate $G_0 \approx 10^{19}\,1/\mathrm{cm}^3\,\mathrm{s}$. For $G < G_0$, the lifetime distribution was independent of G, whereas for $G > G_0$, Bort *et al.* observed a shift to shorter lifetimes with a sublinear dependence on G ($\tau \propto G^{-0.9}$). At first glance, this result can be interpreted in terms of the RT model as a transition between geminate and distant-pair recombination as the predominant process. According to eq. 3.2, the lifetime τ in the RT model solely depends on the electron-hole-pair separation r. For geminate pairs, r is independent of the charge-carrier density, and thus τ is expected to be independent of G. For distant pairs, however, an increase of G leads to a lower separation of recombining pairs, resulting in a predicted G-dependence of τ that is in good agreement with the experimental data [185].

Until this point, the RT model provided a satisfactory description of the experimental data. However, it failed to explain the lifetime distributions obtained from subsequent QFRS experiments: Boulitrop and Dunstan [207] were the first to observe two distinct peaks instead of the broad lifetime distribution deduced from the early PL measurements

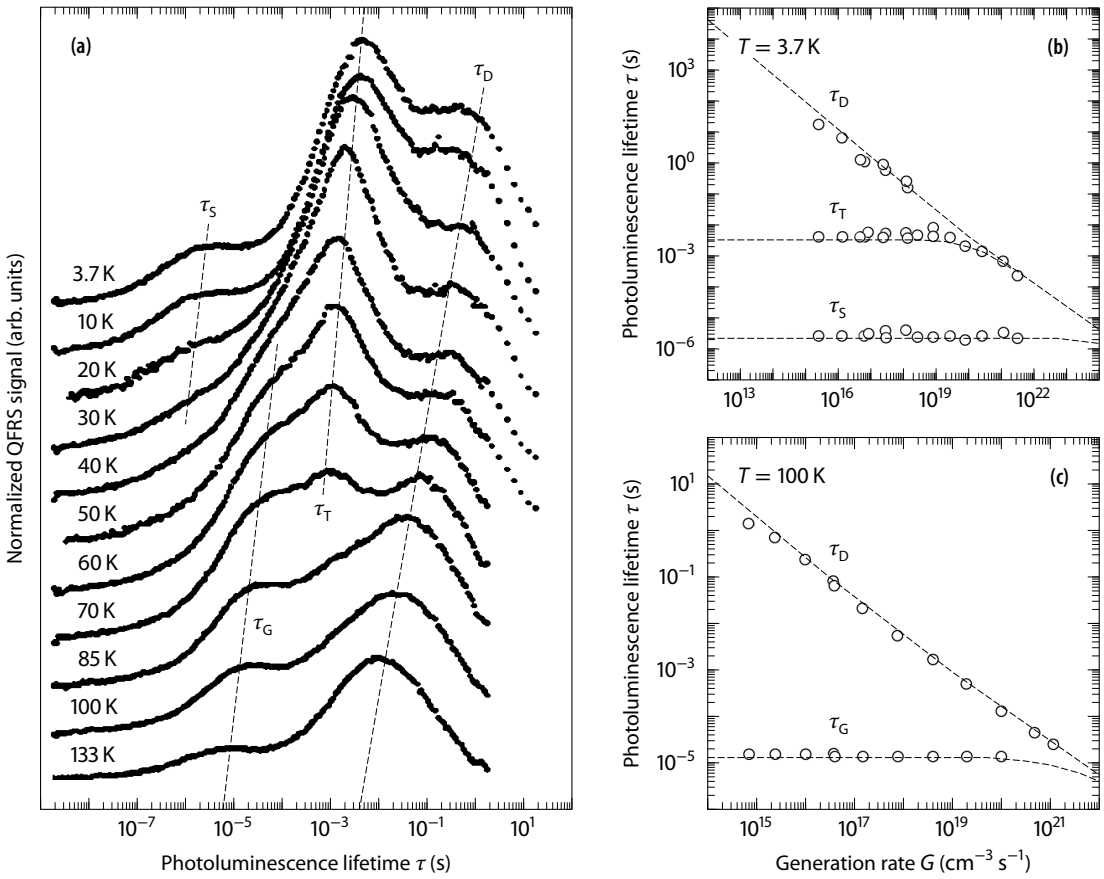

FIGURE 3.3 Quadrature frequency-resolved spectroscopy (QFRS) data of a-Si:H from Aoki *et al.* [206], measured at an excitation energy of 2.33 eV. (a) QFRS spectra of a-Si:H, recorded as a function of temperature at a constant generation rate ($G \approx 1.0 \cdot 10^{17}\,1/\mathrm{cm}^3\,\mathrm{s}$). (b) Peak lifetimes at constant temperature $T = 3.7$ K and (c) $T = 100$ K as a function of the generation rate G. Reproduced from ref. [206].

and predicted by the RT model. Several groups confirmed this finding, reporting a short-lifetime peak at $\tau_S \approx 3\,\mu s$ and a long-lifetime peak at $\tau_T \approx 1\,ms$ [193, 208–212]. Later QFRS measurements by Aoki *et al.* [206, 213–215] (see fig. 3.3), which benefited from an improved wide-band experimental setup, exhibited a third, long-living component with lifetimes $\tau_D = 0.1$–$160\,s$. These results provide clear evidence that distinct recombination channels exist in a-Si:H, with lifetimes that are well separated from each other. It becomes immediately obvious that these different channels cannot be explained based on a distribution of electron-hole-pair separations, as in the RT model. Similar peaks have been found in the lifetime distributions of amorpous silicon nitride [208, 215], amorphous germanium [211–213, 216] and chalcogenide glasses [217, 218], indicating the recombination channels observed in a-Si:H to be a universal property of amorphous semiconductors.

The τ_S and τ_T peaks were observed in QFRS spectra and low temperatures ($T < 50\,K$) and for low generation rates ($G < G_0 = 10^{19}\,1/cm^3\,s$), with peak positions independent on G (see figs. 3.3a and 3.3b). This is characteristic for geminate-pair recombination, as described above and observed before at low excitation densities [205]. The different lifetimes τ_S and τ_T were assigned to geminate recombination of singlet and triplet excitons [206, 210], due to the different kinetics of spin-allowed and spin-forbidden singlet and triplet transitions. This assignment had already been done before by Stachowitz *et al.* [210]. With increasing temperature, τ_S and τ_T merge into a single peak at about $\tau_G = 10$–$100\,\mu s$, also exhibiting geminate, that is, G-independent behavior [206, 213] (see fig. 3.3c). This was explained to originate from the recombination of geminate pairs that are prevented to form a strongly bound exciton by thermal disturbance [206]. The τ_D peak was observed over the entire temperature range (4–130 K) [206, 213–215]. This peak showed a similar dependence on G as observed before by Bort *et al.* [205] ($\tau_D \propto G^{-0.8}$). In addition, Aoki *et al.* [213] compared their QFRS results to earlier LEPR studies by Street

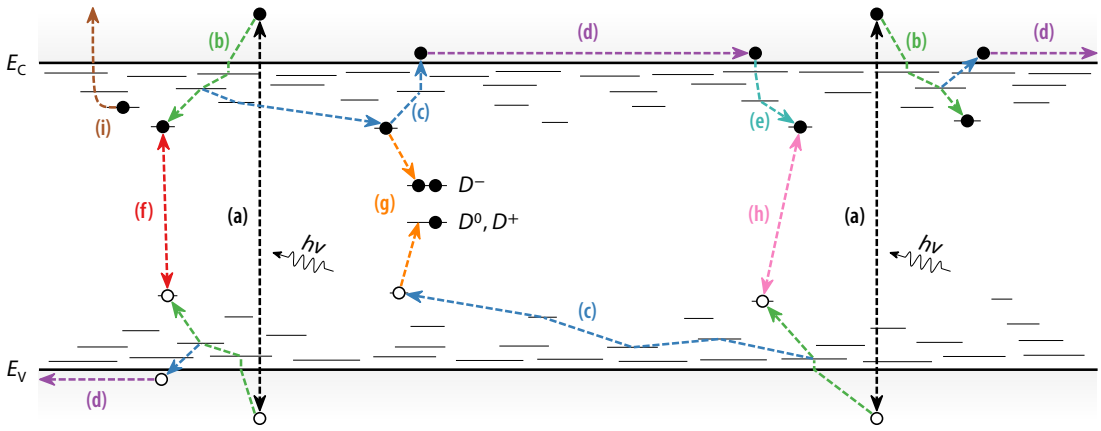

FIGURE 3.4 Schematic illustration of transport and recombination channels for light-generated charge carriers in a-Si:H. E_C and E_V denote the conduction- and valence-band mobility edges and D^+, D^0, D^- the differently charged states of a DB defect, separated by the correlation energy U. (For simplicity, only a single DB is included in the diagram.) The arrows indicate different transport and recombination pathways of light-generated electron-hole pairs (see text for further discussion): (a) generation of electron-hole pairs by light excitation, (b) relaxation of excited charge carriers via rapid thermalization, (c) charge-carrier transport by hopping through tail states or (d) above the mobility edge, (e) re-trapping of mobile charge carriers into tail states, (f) radiative recombination of geminate pairs, (g) non-radiative recombination via DB defects, (h) non-geminate, radiative distant-pair recombination, and (i) non-radiative Auger recombination.

and Biegelsen [122] and Yamasaki *et al.* [143] and found the spin density n_S to exhibit a sublinear dependence on G ($n_S \propto G^{-0.17}$) that was in good agreement with the QFRS results and with the predictions made for distant-pair recombination [185]. This led to the conclusion that geminate and distant-pair recombination coexist over the entire temperature range. In fact, this had already been proposed before as the result of theoretical calculations [198, 219], and due to the observation of low-temperature hopping conductivity, which should also allow for non-geminate recombination [196].

To summarize the picture that emerged from PC, PL and QFRS studies, fig. 3.4 shows the schematic band diagram of a-Si:H illustrating the different transport and recombination channels for photo-excited charge carriers. Excited electron-hole pairs are generated by absorption of photons of energy $h\nu$ (fig. 3.4a). After excitation into the extended band states, charge carriers relax down towards the mobility edge through rapid thermalization (fig. 3.4b). During further thermalization into the tail states, the charge-carrier can either stay spatially correlated and finally recombine as a geminate pair either radiatively (fig. 3.4f) or in a non-radiative Auger recombination process (fig. 3.4i), or escape the geminate pair by diffusion (fig. 3.4c), thereby contributing to σ_P. At low temperatures, diffusion through the tail states can only occur by energy-loss hopping, while with increasing thermal energy hopping transitions to states higher in energy become possible, leading to an enhanced charge-carrier mobility and a quenching of geminate recombination. At $T \gtrsim 100$ K, the transport path shifts into the extended band states (fig. 3.4d). Non-radiative recombination via dangling-bond defects (fig. 3.4g) becomes the dominant loss mechanism, either by direct capture of charge carriers from the extended states, or after charge carriers have been retrapped into localized tail states in close proximity to the DB site (fig. 3.4e).

This picture of electronic transport and recombination channels in a-Si:H has been developed on the basis of PC and PL studies. Further insight into the validity of these models can be obtained by probing specific transport chennels based on their spin-dependency using ODMR and EDMR spectroscopy.

3.4 SPIN-DEPENDENT TRANSPORT AND RECOMBINATION

The analysis of PL and PC intensities and kinetics successfully identified different recombination and transport channels in a-Si:H. An unambiguous assignment to microscopic processes or defect states solely based on this data is, however, not possible. More specific information can be obtained from ODMR and EDMR experiments, as these methods directly probe the paramagnetic states involved in recombination and transport processes. In particular, the combination of both techniques allows to address different recombination channels. By EDMR, current-quenching recombination processes and current-enhancing transport mechanisms (*e. g.*, hopping transport or charge-carrier detrapping) can be distinguished, while ODMR allows to seperate radiative and non-radiative recombination pathways, which lead to an increasing or decreasing signals. Applications of EDMR and ODMR to a-Si:H emerged in parallel to the development of PL and QFRS studies: Solomon *et al.* [16] reported the first spin dependency of PC in 1977, followed shortly thereafter by the first observation of spin-dependent PL by Biegelsen *et al.* [220] as well as Morigaki *et al.* [221]. Subsequently, several groups used EDMR [60, 61, 67,

72, 222–226] and ODMR [227–235] to study the microscopic nature of transport and recombination processes in a-Si:H. In view of the results obtained from PC, PL and QFRS spectroscopy, this section summarizes the additional information gained from ODMR and EDMR leading to the present picture of transport and recombination in a-Si:H.

3.4.1 Spin-dependent recombination via dangling bonds

EDMR has been applied not only the a-Si:H films, but also to fully processed devices such as a-Si:H homo- [67, 68, 236–238] and a-Si/c-Si heterojunction solar cells [69, 77, 239, 240], a-Si-based thin-film transistors (TFTs) [72] or Schottky-barrier diodes [71]. All types of samples and devices exhibited a characterisitic current-quenching EDMR signal at temperatures $T = 100$–300 K, where most of the early EDMR experiments were carried out. This signals was immediately assigned to non-radiative recombination via DB defects, which had already been proposed before as the predominant recombination channel [192] due to the anticorrelation between PL efficiency and DB defects (see section 3.3.1). Deconvolution of the observed EDMR signal by altering the modulation phase (see fig. 3.5a) revealed of two features that contain the characteristic signatures of all paramagnetic states known in undoped a-Si:H:

- All samples showed a line at $g = 2.0050$ ($\Delta B_{pp} \approx 1$ mT), consistent with the superpositon of the resonances of a singly occupied CBT state ($g = 2.0044$) and a neutral DB defect ($g = 2.0055$).
- In samples of low defect density, an additional line appeared at $g = 2.01$ ($\Delta B_{pp} \approx 2$ mT), identical to the resonance of a hole trapped in a VBT state. The relative intensity of the hole line increased with decreasing defect density [60].

Dersch *et al.* [60] were the first to associate these two signal components with a two-step recombination process, schematically depicted in fig. 3.5b: They interpreted the appearance of the $g = 2.0050$ in the EDMR spectra of all a-Si:H samples as a spin-dependent

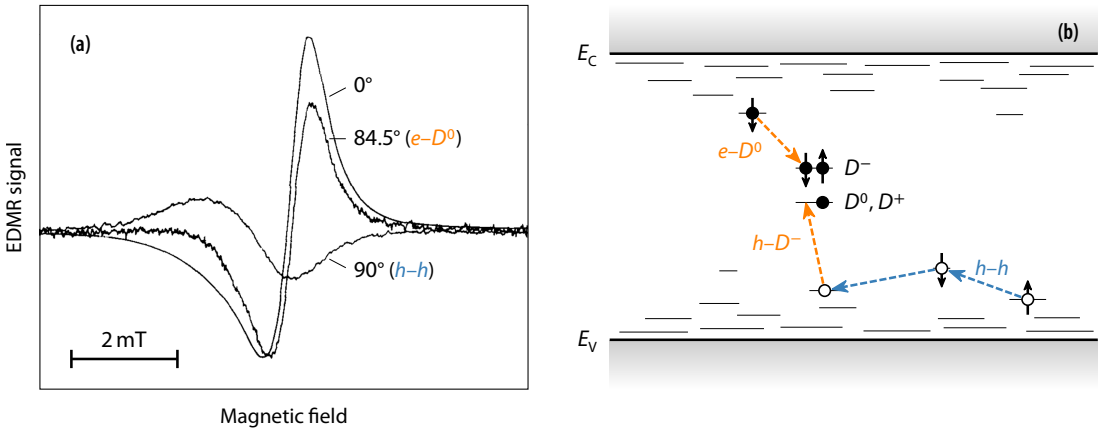

FIGURE 3.5 (a) Field-modulated CWEDMR spectra of undoped a-Si:H at $T = 160$ K. Recorded with a modulation frequency of 5 kHz and different modulation phases as indicated, to decompose the signal. Reproduced from ref. [27]. (b) Recombination scheme for spin-dependent recombination via DBs as proposed by Dersch *et al.* [60]. Dashed arrows mark tunneling transitions of electrons and holes. Arrows on electrons and holes indicate spin-dependent transitions (see text for further details).

tunneling transition of an electron trapped in a CBT state into a neutral DB defect (e–D^0). The recombination cycle is completed by a the capture of a hole into the intermediately negatively charged DB (h–D^-). A direct tunneling transition of a hole into the doubly occupied D^- state is not spin-dependent. Thus, Dersch *et al.* explained the appearance of a current-quenching VBT resonance for low-defect samples with diffusion of holes by hopping through VBT states towards the DB site, thereby increasing the recombination rate. The hopping transitions can be spin-dependent if two neighbouring VBT states are singly occupied (h–h transition in fig. 3.5b). For samples of high defect density, a single direct transition to a defect state becomes more probable than diffusion through the tail states, which explains the decreasing relative intensity of the hole resonance.

A similar resonance has also been found in ODMR spectra of undoped a-Si:H [231–233]. As expected for a non-radiative recombination process, the e–D^0 resonance appeared as a quenching signal in ODMR. For samples of low defect density, also the hole resonance has been observed as a quenching ODMR signal [231].

Although the picture proposed by Dersch *et al.* explains the experimentally observed EDMR and ODMR signals and has been widely accepted in the literature, it is to be noted that the microscopic recombination mechanism appears to change when changing the excitation energy. Brandt and Stutzmann [241] found that for sub-bandgap illumination, the g-value of the e–D^0 resonance shifts from $g = 2.0050$ to $g = 2.0062$. Later, Stutzmann *et al.* [17] explained this behavior with a change of the dominant recombination mechanism from tunneling of an electron into the DB followed by the capture of a hole, to tunneling of hole into DB followed by the capture of an electron. In fact, ODMR experiments using the defect luminescence band (0.9 eV) show an enhancing signal at $g \approx 2.0065$, which has been assigned to a radiative recombination between VBT holes and neutral DBs [221, 229, 233]. This shows the microscopic process behind the dominant recombination mechanism in a-Si:H is still subject to debate.

3.4.2 Spin-dependent hopping conduction

At low temperatures ($T \lesssim 100$ K), reported EDMR spectra of a-Si:H exhibit resonances at $g = 2.0040$–2.0045 and $g \approx 2.01$ [17], resembling the EPR signatures of CBT- and VBT-trapped electrons and holes. This assignment is supported by the fact the $g = 2.004$ resonance appears in n-type phosphorus-doped a-Si:H [27, 69, 77, 225], whereas the $g = 2.01$ signal is found in p-type boron-doped samples [27, 60, 225]. Both resonances have been identified as current-enhancing signals, which has recently been confirmed by means of PEDMR [26]. Since hopping transport via tail states is the dominant transport process at low temperatures (see section 3.3.1), both signals have been assigned to spin-dependent hopping conduction of electrons and holes in their respective tail states (see also section 2.5.5).

In doped a-Si:H, the observation of spin-dependent hopping within the tail states is consistent with the doping-induced shift of the Fermi level. Spin-dependent hopping has, however, also been observed in undoped a-Si:H, for instance in a-Si:H TFTs under conditions of strong electron accumulation [72], or in a-Si:H solar cells under illumination or strong forward-bias conditions [26, 69, 226]. In these non-equilibrium cases, the quasi-Fermi levels of electrons and holes are shifted from mid-gap into the tail states.

While spin-dependent recombination in a-Si:H has been extensively investigated in previous research, spin-dependent transport at low temperatures has gained much less

attention yet. This is also a result of the much lower photoconductivity of a-Si:H at cryogenic temperatures. In fact, most CWEDMR experiments on a-Si:H have been conducted at temperatures above 100 K, where transport predominantly occurs within the extended band states, and spin-dependent recombination via DB defects is the major spin-dependent transition probed by EDMR. With improved experimental setups and sample designs, low-temperature EDMR have come into reach. In chapter 6, we will present a comprehensive low-temperature PEDMR study, which will also reevaluate the assignment of the observed signals the spin-dependent tail-state hopping conduction.

3.4.3 Excitonic states

Besides the EDMR and ODMR signals assigned to spin-dependent recombination and transport channels via defects and localized tail states, both methods have revealed a distinctively different resonance at $g \approx 2.008$, characterized by an unusually broad X-band line width of about 20 mT. This line has been observed in CWODMR spectra of undoped a-Si:H at low temperatures ($T \leq 30$ K) [233, 242, 243] as well as in CWEDMR spectra at temperatures of about 150 K [27, 244].

The origin of this resonance has been controversially discussed throughout the literature. Brandt and Stutzmann [244] assigned the line to strongly dipolar-coupled triplet excitons and explained the broad line width with a distribution of exciton radii and coupling strengths. Such a distribution would lead to a line shape that consists of a superposition of Pake patterns (see section 2.3.3), adding up to form an approximate Gaussian line shape. This is consistent with the observed EDMR line shape. From the line width, they estimate an average exciton radius of 5 Å. The argument is, however, solely based on the line width. An alternative explanation was also based on excitonic states, but explained the signal with strongly exchange-coupled electron-hole pairs trappied in CBT and VBT states [27, 233, 235]. This interpretation is supported by the observed g-value, which is close to the arithmetic mean of the CBT and VBT resonances.

In the case of ODMR, unambiguous proof for the presence of spin-dependent processes via excitonic states is provided by the observation of a half-field resonance ($g \approx 4$), which can be assigned to the $\Delta m_S = \pm 2$ transitions between the $|T_+\rangle$ and $|T_-\rangle$ states of an $S = 1$ triplet manifold [242, 243, 245]. In addition, later pulsed-ODMR studies identified the $S = 1$ character by means of field-resolved ED-Rabi nutation experiments [246–248]. Such evidence is, however, as yet missing for the EDMR resonance.

To date, it is unclear whether the same excitonic species give rise to the ODMR and EDMR signals. In addition, the nature of the underlying spin-dependent process is entirely unknown. Spin-dependent radiative recombination of the excitons could explain the ODMR signal. This is supported by the observation of radiative recombination channels via geminate excitons by means of photoluminescence, as discussed in section 3.3.2. However, such a spin-dependent recombination channel via geminate triplet excitons cannot cause an EDMR signal, since geminate pairs do not contribute to photoconductivity. Possible alternative explanation include spin-dependent dissociation or a three-particle Auger-like recombination mechanism. Such processes have been identified in organic semiconductors [21, 96] and recently also in μc-Si:H [98]. Answers to these open questions cannot be found from the EDMR and ODMR spectra alone. Modern PEDMR techniques, however, allow to probe the origin of this resonance in much more detail. In chapter 6, we will address this issue and present a combined EDMR/EPR study that not

only proves the excitonic origin of the EDMR resonance, but also allows to conclude on the microscopic nature of the underlying transport process.

3.5 SUMMARY

This chapter has given a brief overview of the characteristics of a-Si:H, especially focussing on the electronic-transport properties that arise from the structural disorder. This thesis lays particular emphasis on the microscopic nature of transport and recombination processes that are of fundamental importance for the efficiency of a-Si:H-based devices such as, *e. g.*, solar cells. The immense research history on a-Si:H—part of which presented in this chapter—lays the basis for this work. In particular, the models developed for transport and recombination channels via defect states will be probed with the help of modern PEDMR techniques. We will use this chapter as a starting point and reference in order to set the results obtained in the course of this thesis into context.

Finally, it is to be noted that many of the mechanisms present in a-Si:H have proven to be universal properties of amorphous semiconductors. Therefor, both earlier studies and the results of this thesis are not necessarily limited to a-Si:H or the specific situation in a-Si:H-based solar cells, but can be of more general relevance, considering a-Si:H as a prototype material for disorded solids.

CHAPTER 4

Materials and methods

This chapter summarizes the procedures summarizes sample-preparation procedures and describes the experimental setups for carrying out EDMR and EPR experiments. We further introduce common measurement techniques and post-acquisition data-processing strategies, which will be employed in the subsequent chapters. Finally, we discuss numerical simulation and fitting routines that will be used to identify and characterize paramagnetic species based on their EDMR and EPR fingerprints.

4.1 SAMPLE DESIGN AND PREPARATION

With a global production share of about 95 %, todays photovoltaics market is vastly dominated by crystalline-silicon (c-Si) wafer-based solar cells [249]. Record conversion efficiencies have reached 26.7 % on a laboratory scale and 24.4 % for module sizes [250], approaching the physical limit of single-junction c-Si cells (29 %). Alternative second-generation technologies such as a-Si or µc-Si thin-film cells suffer from significantly lower conversion efficiencies (10–12 %). Their relative market share has drastically decreased over the last decade, even though these thin-film concepts offer much lower production costs owing to the reduced material consumption. Also third-generation technologies like organic or dye-sensitized solar cells have not yet reached commercial relevance and often suffer from the lack of long-term stability [251].

The comparably low efficiencies of a-Si or µc-Si thin-film devices are a result of the inferior electronic material quality. Disorder-induced localized states within the band gap act as traps and recombination centers, reducing photoconductivity (see previous chapter). Nevertheless, these materials play a crucial role also in wafer-based c-Si cells. Todays record-efficiency cells are designed in a so-called *heterojunction with intrinsic thin layer (HIT™)* structure [252]. This cell design uses ultra-thin *n*- and *p*-doped a-Si layers as front- and back-contacts (typically about 10 nm thick), to form charge-selective *pn*- an nn^+-heterojunctions with the *n*-type c-Si absorber that allow for efficient separation of photoexcited electrons and holes. A major breakthrough, which paved the way towards high-efficiency devices, was achieved by introducing additional thin intrinsic a-Si layers between the c-Si wafer and the doped contact layers. The effect is a drastical reduction of charge-carrier recombination at the surface of the c-Si absorber and the interface to the contact layers. The physical origin is believed to be passivation of c-Si surface DBs. However, the microscopic nature of charge separation, transport and recombination, in particular in the a-Si/c-Si interface region, is to a large extent unknown.

Due to its selectivity to transport and recombination pathways via paramagnetic states, such as, *e. g.*, surface and interface defects, EDMR is the tool of choice to find answers to the vast amount of open question concerning the physical mechanisms in HIT solar cells.

Previous studies applied EDMR to a-Si/c-Si heterojunction solar cells [77, 239, 240] and identified spin-dependent transport and recombination channels that could be assigned to c-Si surface DBs and localized tail states within the amorphous layer. In particular, these studies revealed a significant influence of the amorphous layer on the electronic transport properties of the heterostructures, even for layer thicknesses of anly a few nm. However, the proximity of *g*-values leads to a strong overlap between different resonances and thus prevents an unambiguous disentanglement of the associated transport channels in HIT devices. In this work, we thus take a step back and isolate the intrinsic a-Si layer using specific sample designs. This both serves to address fundamental properties of a-Si and lays to basis for future experiments on fully processed device structures. For this purpose, we will investigate both bulk intrisic a-Si film samples (chapter 5) and operating *pin* solar cells, which use an *i*-a-Si:H absorber and *p*- and *n*-doped µc-Si:H contact layers (chapters 6 and 7). In the following, we summarize the design and preparation procedure of these sample structures. In addition, we discuss the preparation of a-Si:H powder samples that will be used for transient-EPR experiments in chapter 6.

4.1.1 Amorphous-silicon film samples and *pin* solar cells

The layer structure of a-Si:H film and *pin* solar-cell samples is shown in figs. 4.1a and b. Both types of samples were deposited on Corning borosilicate-glass substrates by means of radio-frequency plasma-enhanced chemical vapour deposition (RF-PECVD) at Forschungszentrum Jülich. Details concerning the deposition procedure can be found in ref. [253]. Films and *pin* structures were grown on aluminum-doped ZnO transparent conductive oxide (TCO), serving as front contact. For both film and solar-cell samples,

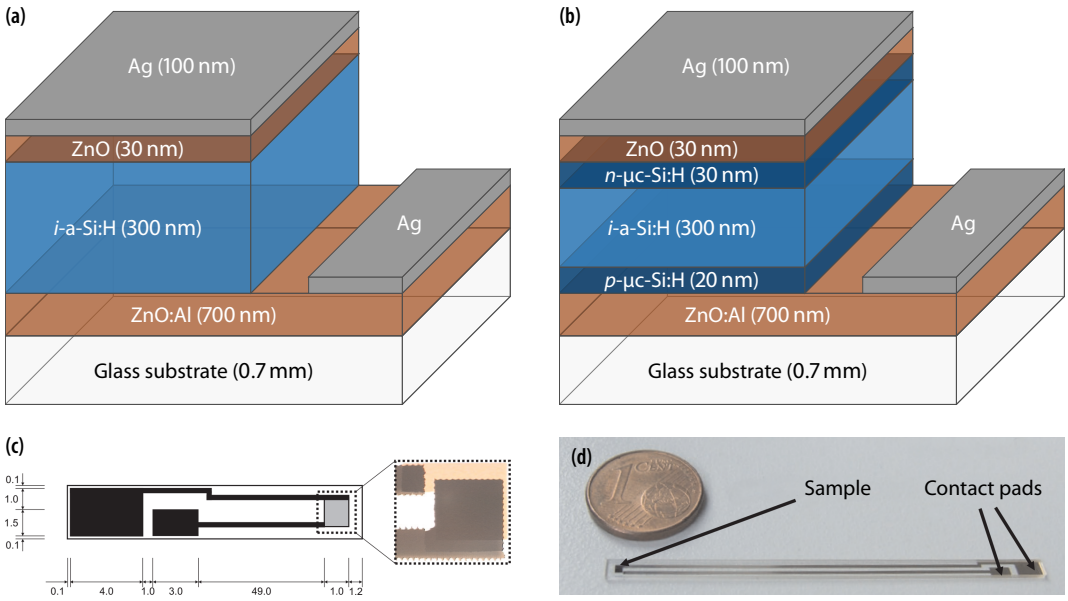

FIGURE 4.1 Structure and sample design of intrinsic a-Si:H film and *pin* solar-cell EDMR samples. (a) Schematic cross-section through film and (b) *pin* solar cells deposited by PECVD on glass substrates (see text for details). Note that the drawn layer thicknesses are chosen arbitrarily for presentation purposes. (c) Sample geometry and (d) photograph of a fully processed EDMR sample. The insert in fig. c shows a micrograph of the active sample area ($1 \times 1\,mm^2$). Figures c and d are reprinted from ref. [88], showing a sample of the same size and contact geometry.

intrinsic a-Si:H layers with a thickness of 300 nm were used. The *pin* structures were obtained by sandwiching the intrinsic layer with two thin *p*-type, boron-doped (≈0.2 at. %) and *n*-type, phosphorus-doped (≈1.5 at. %) μc-Si:H layers with thicknesses of 20 nm and 30 nm, respectively. A final ZnO/silver stack serves as back contact and light reflector.

The layered structures were deposited on $50 \times 100\,mm^2$ substrates. To fit the EDMR samples into the available sample space and provide electrical contacts to the detection system, a special EDMR contact structure has been developed (fig. 4.1c), which were realized by laser scribing (see ref. [254] for details). The sample area is confined to $1 \times 1\,mm^2$, which is in the range of homogeneous MW- and magnetic-field distribution within the EDMR setups. Electrical contacts are provided by 100 nm thin and 50 mm long silver strips. This design has been chosen to minimize the amount of conductive material inside the EPR resonator. Conductors in general distort the MW field and thereby produce B_1 inhomogeneity. To minimize these distortions, the thickness of the contact strips should be lower than the penetration depth of the MW irradiation, which is about 0.6 μm for silver at 9.6 GHz (X-band). The length of the strip lines is long enough to feed the contact pads outside of the active resonator area. Electrical contacts to the detection system can than be established using silver paste without affecting the MW field. After laser scribing, a set of 10–20 EDMR sample structure are obtained as one batch, which are separated with a diamond saw. A photograph of such an EDMR sample is shown in fig. 4.1d. A micrograph of the active device area is shown in the insert of fig. 4.1c.

4.1.2 Amorphous-silicon EPR samples

In chapter 6, we will compare the EDMR signature of a-Si:H *pin* solar cells to transient-EPR spectra obtained from intrinsic a-Si:H powder samples. These samples were prepared at Forschungszentrum Jülich and Delft Technical University from thin films deposited by RF-PECVD, as described in detail in refs. [253] and [163], respectively. Thin a-Si:H films were deposited from a mixture of silane (SiH_4) and hydrogen (H_2) gas on aluminum-foil substrates at temperatures of about 200 °C. The hydrogen/silane gas-flow-rate ratio $R = [H_2]/[SiH_4]$, as well as the deposition conditions (pressure, deposition rate), were varied to produce a-Si:H of varying electronic quality (details will be discussed in section 6.7.4). After film deposition, the aluminium substrate was etched off using HCl acid. The remaining a-Si:H flakes were filtered from the suspension, dried at ambient conditions and sealed into standard EPR quartz tubes.

In section 6.7.4, we will also compare the EPR signatures of as-deposited and light-soaked a-Si:H samples to probe potential relations of the observed paramagnetic states to the Staebler-Wronski effect (see previous chapter). Therefor the deposited film samples were split into two pieces, one of which was light-soaked for 400 h under an AM1.5 sun simulator at an ambient temperature of 50 °C.

Structural and electronic differences between samples prepared at different deposition and light-soaking conditions were analyzed by Fourier-transform infrared (FTIR) and Doppler-broadening positron-annihilation spectroscopy (DB-PAS) combined with quantitative EPR measurements (see ref. [163] for details). FTIR and DB-PAS probe the structural material quality and identify open-volume deficiencies such as nanovoids [255, 256]. Quantitative EPR was used to measure the spin density of DB defects, serving as an indicator for the electronic material quality. Results of these measurements for the investigated samples, will be summarized in section 6.7.4.

4.2 EDMR AND EPR INSTRUMENTATION

Within this work, we present X-band (9.6 GHz) and mm-waveband (263 GHz) CW and PEDMR results. The experiments were carried out using commercial Bruker BioSpin EPR spectrometers located at the Helmholtz-Zentrum Berlin für Materialien und Energie (HZB). In addition, we performed transient EPR experiments, using a laboratory-built X-band spectrometer at the Freie Universität Berlin. This section describes these experimental setups and outlines the required hardware changes to implement electrial detection schemes. Note that we will not discuss the basic working principle of an EPR spectrometer. Comprehensive descriptions can be found in standard EPR textbooks.

4.2.1 X-band pulsed EDMR

Figure 4.2 depicts the X-band EDMR setup, which is based on a Bruker ELEXSYS E580 CW and PEPR spectrometer. The upper part (fig. 4.2a) shows the MW and magnetic-field setup, consisting of a 10″ iron magnet (Bruker ER 073, maximum field 1.45 T) and an X-band CW and pulsed MW bridge (Bruker E580-1010). The sample is mounted inside a dielectric-ring MW resonator (Bruker ER 4118X-MD-5), which is placed into a continuous-flow helium cryostat (Bruker ER 4118CF). The temperature is adjusted at constant helium-flow using heating resistors, which are controlled by a temperature-control unit (Oxford Mercury iTC or Oxford ITC503). Temperature stabilities of about 0.1 K are obtained with this setup. The magnetic field is measured with an FT-NMR teslameter (Bruker ER 036TM), placed outside of the cryostat. Magnetic-field offsets with respect to the sample position need to be determined by EPR calibration measurements of standard samples with known g-values. Typical standard samples are, for instance, DPPH or

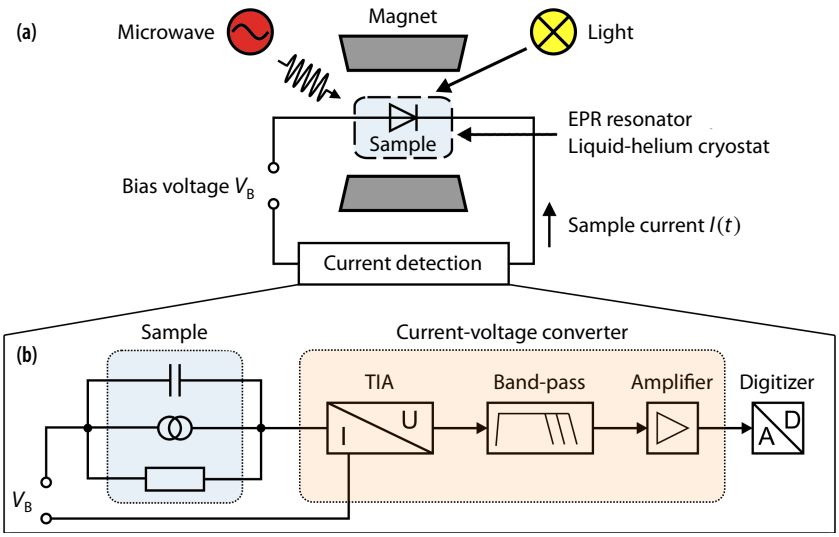

FIGURE 4.2 Sketch of the X-band PEDMR setup. (a) Microwave and magnetic-field setup based on a commercial Bruker ELEXSYS E580 spectrometer. The sample is mounted inside of an EPR resonator and electrically connected to the detection system. (b) Electrical detection scheme using a dedicated EDMR current/voltage converter (Elektronik-Manufaktur Mahlsdorf). The sample is depicted by an equivalent circuit that consists of a parallel connection of a current source, a resistor and a capacitor. After filtering and amplification, the signal voltage, corresponding the the EDMR current change $\Delta I(t)$, is fed into the digitizer integrated into the EPR spectrometer. Reprinted with modifications from ref. [88].

$N@C_{60}$.

For high-power MW pulses, the system is equipped with a 1 kW travelling-wave-tube (TWT) amplifier (Applied Systems Engineering 117X). Pulse sequences are generated by a multi-channel pulse-forming unit (MPFU) (Bruker PatternJet) with up to eight different pulse channels. The amplitudes phases of the pulse channels were calibrated to have two sets of four equal-amplitude phases, $\pm x/\pm y$ and $\pm\langle x\rangle/\pm\langle y\rangle$, available. The four different phases are used for setting up phase-cycling schemes [30]. The second set of phase channels is calibrated at a different amplitude, allowing for experiments with MW pulses of different B_1 strength (details will be discussed in the experimental chapters). The MW bridge is further equipped with an addition MW source for ELDOR experiments (Bruker E580-400U), which will be used in section 6.8 to set up electrically detected electron-electron double resonance (ELDOR) experiments.

Illumination of the EDMR sample with white light is provided by a halogen cold light source (Schott KL 2500 LCD) and guided towards the sample through the optical windows of the cryostat and resonator using a gooseneck light guide. The light source is stabilized by an external DC power supply (Thurlby Thandar TSX1820P) in constant-voltage mode, yielding lamp powers of about 95 W (lamp-power stability ≈ 2 W).

The EDMR sample is mounted on a customly designed sample holder and placed inside an EPR quartz tube to avoid contact with the resonator assembly. Electrical wires are connected to the contact pads (see figs. 4.1c and d) using silver conductive paste. The wires are led out of the cryostat through a vacuum-tight feedthrough and connected to the electrical detection system.

The most critical part of an EDMR experiment is the sensitive detection of the resonant current changes. While the absolute current obtained from the samples under investigation is on the order of μA, the EPR-induced current changes are only in the range of pA to nA. To accurately record these small current changes, we used a low-noise current/voltage converter and amplifier (Elektronik-Manufaktur Mahlsdorf, EMM), which was specifically developed for EDMR experiments [88]. The resulting current-detection scheme is depicted in fig. 4.2b. The EMM device contains a constant-voltage source, which is used to apply a bias voltage V_B to the EDMR sample (voltage range ± 3 V). The sample current is measured symmetrically between the two voltage output $\pm V_B/2$. This symmetrical configuration suppresses interferences with electromagnetic background signal (*e. g.*, originating from the TWT amplifier). The current input $I(t)$ is converted into a signal voltage by a differential transimpedance amplifier (TIA) with a conversion factor of 10^4 V/A. This signal, corresponding to the absolute sample current, is monitored by with a digital voltmeter (Stanford Research Systems SIM970). To separate the current change induced by EDMR, the converted voltage signal is passed through a band-pass filter with adjustable bandwidth. The high-pass cutoff frequency can be varied between 1 Hz and 1000 Hz and removes the DC component, which corresponds to the constant sample current. The low-pass cutoff can be varied between 0.2 MHz and ≈ 1.5 MHz and determines the time resolution of the detection setup. After filtering, the remaining AC component—that is, the EDMR current change $\Delta I(t)$—is further amplified (amplification factor A_F adjustable between 5 and 2000) and fed to an 8 bit digitizer integrated into the EPR spectrometer (Bruker SpecJet-II, time resolution 1 ns).

4.2.2 High-field/-frequency EDMR

To realize multifrequency EDMR experiments, we complemented our X-band EDMR setup with a high-field/-frequency mm-waveband setup, which is based on a commercial Bruker ELEXSYS E780 CW and PEPR spectrometer [257], operating at 263 GHz and magnetic fields between 0 T and 12 T. The setup and the implemented extensions for electrical detection have been described in detail by Akhtar *et al.* [26].

The spectrometer is equipped with a heterodyne MW bridge and a cryogen-free superconductive magnet. Microwaves are generated at an intermediate X-band frequency (9.65 ± 0.04 GHz) and up-converted to 263 GHz over multiple mixing stages. In a quasi-optical front-end, the up-converted MW signal is propagated as a Gaussian beam and coupled into a corrugated waveguide (see ref. [257] for details). The magnet system consists of two coils: The main coil can produce homogeneous magnetic fields ranging from 0 T to 12 T. It can either be used for broad field sweeps, or can be stabilized at a certain magnetic field using a persistent switch. The sweep coil produces fields of ± 0.15 T on top of the main field. In sweep mode, the spectrometer features a calibrated linearized-field mode, allowing to keep field nonlinearities below 10 ppm [257]. Experiments carried out in this work will always be carried out in linearized sweep mode, with the main field stabilized at 9.4 T. Field inhomogeneities over the entire sample space have been measured and are below 0.2 mT.

The E780 spectrometer has available a TE_{011} MW resonator. However, the available sample space (inner tube diamater 0.2 mm) is not sufficient for EDMR experiments. Therefor, the EDMR sample is placed into a non-resonant probehead, which is shown in figs. 4.3a and b. The sample is mounted on top of a Rexolite sample holder (fig. 4.3c), allowing for a maximum sample diameter of about 5 mm. The X-band sample structures thus had to be cut to an appropriated length, leaving only about 1–2 mm of the contact strip lines. Electrical connections were realized using thin gold wires attached to the remaining contact lines with silver paste. The gold wires were soldered to coaxial cables, which were led out of the probehead and connected to the EMM current/voltage converter (see previous section). The resulting signal voltage was then fed into the SpecJet-II digitizer of the spectrometer. Illumination was provided by the white light source described in the previous

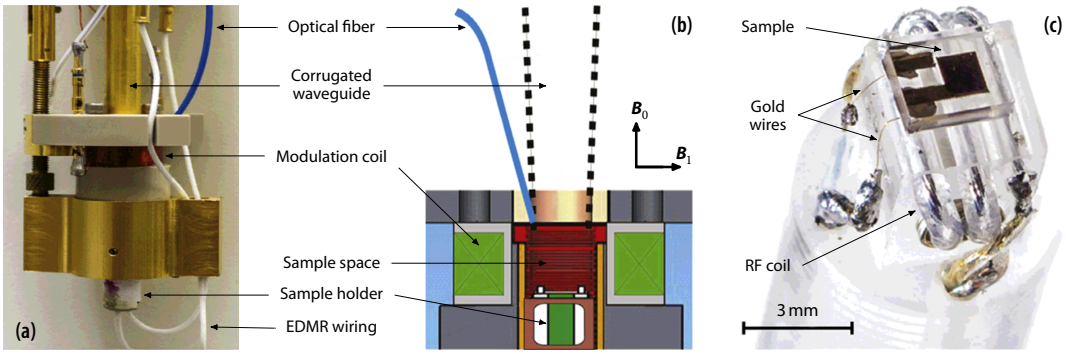

FIGURE 4.3 (a) Photograph and (b) schematic cross-section of the 263 GHz EDMR probehead. (c) Photograph of the EDMR sample holder with a mounted a-Si:H *pin* solar-cell sample. Note that during the time of the experiments presented in chapter 5, an RF coil was attached to the sample holder, which was used for MHz excitation in other experiments (see text for discussion). Figures reprinted from ref. [26].

section and guided towards the sample with an optical fiber (diameter 1.22 mm).

The sample holder, which was used during the 263 GHz experiment presented in chapter 5, was equipped with a custom-built RF coil (see fig. 4.3c). This coil had no function for the experiments presented in this work, but was used to provide MHz excitation for other EDMR experiments carried out using the same sample. Only after recording the data set discussed in chapter 5, it turned out that this RF coil had been accidentally made from wires containing ferromagnetic materials. Due to the proximity to the coil, the EDMR sample was thus exposed to a constant magnetic-field offset of about 8 mT.[1] The field offset was not measured during data acquisition and the measurement series could not be reproduced in the time frame of this work. Therefor, we will have to consider the field axis as uncalibrated and take into account the field offset as an unknown parameter for the data analysis in chapter 5.

Other than in the X-band spectrometer, no MW amplifier is available in the 263 GHz setup. The MW power is thus limited to a maximum of 15 mW. With optimal alignment of the MW beam with respect to the corrugated waveguide, maximum B_1 amplitudes of about 10 µT can be achieved at the sample position (corresponding to a π-pulse length of about 2 µs). However, for the given sample and setup geometry (see figs. 4.1 and 4.3), MW irradiation needs to pass the glass substrate of the EDMR sample. Test experiments revealed that this leads to an additional loss of MW power by about 10 dB. Typical π-pulse lengths for 263 GHz PEDMR experiments were thus in the range of 4–6 µs. This limits the set of PEDMR experiments that could be conducted, since pulse sequences comprising multiple MW pulses are hardly to realize for such long pulse lengths. Recently, the spectrometer has been equipped with a MW-power upgrade, increasing the maximum power to 100 mW. For future high-frequency EDMR experiment, the available B_1-strength will thus be increased by a factor of about 2.5. Further enhancements could be achieved by building resonant Fabry-Perot-type structures to amplify the B_1-field at the sample position. However, not much effort has been put into such optimizations yet, also due to signicant downtimes of the instrument within the time frame of this work. The high-frequency EDMR experiments were thus limited to single-pulse experiments.

4.2.3 Continuous-wave EDMR

The majority of EDMR experiments presented in this work use pulse excitation schemes. Nevertheless, we will also discuss some few CWEDMR measurements. In a CWEDMR experiment, the sample is exposed to continuous MW irradation at a fixed frequency, while adiabatically sweeping the magnetic field. As in CWEPR, magnetic-field modulation and phase-sensitive detection by means of a lock-in amplifier is employed (see section 2.2.1). At X-band, the modulation coils integrated into the resonator assembly are used for this purpose, which can allows for peak-to-peak modulation amplitudes of up to 2 mT at frequencies between 0.1 kHz and 100 kHz. At 263 GHz, a single modulation coil is integrated into the non-resonant probehead (see fig. 4.3), which can provide up to 5 mT peak-to-peak modulation fields.

Continuous-wave EDMR usually offers a higher sensitivity than PEDMR, mainly due to the use of lock-in detection. However, this benefit can be outweighted by strong background signals superimposed onto the EDMR signal. This is especially an issue in the

[1] This offset was measured later by means of EPR measurements of standard samples with known g-values.

263 GHz setup, where electrical contacts have to be located in close proximity to the sample and inside of the modulation field. The oscillating modulation field induce background current that are not filtered out by phase-sensitive detection. When sweeping the external magnetic field, these background signals produce non-constant baselines, which can often not be unambiguously removed from the EDMR signal. This is especially true for broad signals, as observed in a-Si:H.

An important drawback of CWEDMR is that it does provide information on the signal dynamics. This is a result of the phase-sensitive detection, which sets a narrow-band detection window, centered about the modulation frequency. As shown in section 2.5, the EDMR transient signal contains both positive and negative contributions, independent of the underlying transport process. In PEDMR, the signal sign can be determined by recording the entire transient. On the contrary, the choice of the modulation frequency in relation to the different rate coefficients determines which signal components will be detected in a CWEDMR spectrum. As shown by Lee *et al.* [258], the interpretation of CWEDMR spectra and in particular the determination of the signal sign can be very ambiguous.

4.2.4 Transient EPR

In chapter 6, we will complement PEDMR experiments on a-Si:H *pin* solar cells with transient EPR (TREPR) measurements on a-Si:H powder samples. In essence, TREPR is a time-resolved technique that directly detects the transient CWEPR signal after a light-pulse excitation. Experimental details and a summary of typical applications of TREPR can be found elsewhere (see, for instance, a recent review by Weber [259]). Herein, we will only briefly summarize the experimental setup used for the measurements presented in section 6.7.

Transient-EPR spectra were acquired on a laboratory-built spectrometer [260], located at Freie Universität Berlin (AG Bittl). The EPR setup consists of an electromagnet (Varian V-7301), a Bruker ER 056 QRVM microwave bridge and a Bruker ER 4118X-MD-5 dielectric-ring resonator. Optical excitation was provided by a laser flash at a wavelength of 670 nm using a Nd:YAG laser (Spectra Physics GCR-11) in combination with an optical parametric oscillator (OPTA OPO BBO-355-vis/IR). The EPR signal after the laser pulse was directly recorded under continuous MW irradiation by a digital oscilloscope (LeCroy WaveRunner 104MXi). The magnetic-field axis was calibrated using an NMR teslameter (Bruker ER 035M). As for X-band EDMR measurements, the field offset between the positions of the teslameter and the sample was calibrated with a reference sample ($N@C_{60}$). Cooling of the sample was achieved using a laboratory-built continuous-flow helium cryostat.

Time-domain TREPR signals are usually superimposed by strong background signals following the laser flash. These background signals result from dielectric heating of both EPR sample and the resonator assembly, given rise to a change of the resonator impedance and hence increased MW reflection. Since TREPR signals are generally recorded as two-dimensional signal maps, these background signals can easily be subtracted, as outlined in section 4.3.2. Since dielectric-heating effects depend on electrical conductivities, the background signals can also be useful to conclude on the sample conductivity, as will be shown in section 4.2.4.

4.3 PULSED EDMR MEASUREMENTS

Most of this work is based on PEDMR experiments. Chapter 5 is limited to field-swept single-pulse experiments conducted at different MW frequencies. In chapters 6 and 7, we will extend to set of experiments to electrically detected nutation experiments (ED-Rabi, ED-PEANUT) and multi-pulse experiments such as ED-ELDOR. Details concerning these PEDMR techniques will be discussed in the experimental chapters. In the following, we summarize the basic idea of a single-pulse EDMR experiment, which forms the basis for all PEDMR detection schemes.

4.3.1 Principle of a pulsed EDMR experiment

As discussed in section 2.5, the transient current after a pulsed MW excitation is governed by the spin-pair state density at the end of the MW pulse. After exciting resonant transitions between states of the spin-pair ensemble, the current change $\Delta I(t)$ is proportional the change of singlet- and triplet-state density induced by the resonant transitions. The basic principle of a PEDMR experiment is thus the measurement of either the entire transient current response $\Delta I(t)$ or the integrated net charge ΔQ after the excitation of the spin-pair ensemble by a MW pulse of length t_P. Recording ΔQ as a function of the external magnetic field yields the field-domain PEDMR spectrum. By measuring ΔQ for different pulse lengths, ED-Rabi nutation traces are obtained. Replacing the single pulse by a three-pulse sequence, allows to detect electrically detected Hahn echoes (see section 2.5.7).

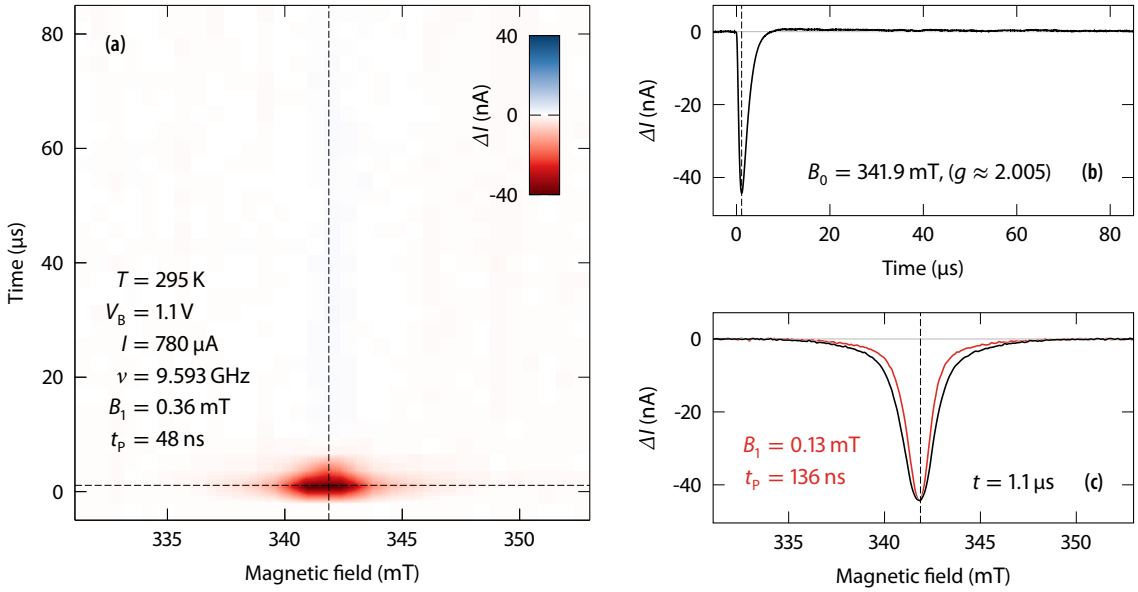

FIGURE 4.4 Exemplary X-band PEDMR spectrum of an a-Si:H *pin* solar cell, recorded at room temperature under dark, forward-bias conditions. (a) Two-dimensional signal map obtained by measuring the transient current response after the MW pulse as a function of the applied magnetic field. (b, c) Single time- and field-domain slices, corresponding to cross sections through fig. a, as indicated by the dashed lines. The red trace in fig. c shows the maximum field-domain spectrum recorded at a lower B_1 and correspondingly longer π-pulse length (normalized to equal amplitude), illustrating the effect of MW-power broadening.

Single-pulse EDMR spectra will generally not be measured by recording ΔQ, which would yield one-dimensional field-domain spectra. Instead, we will exploit the capability of PEDMR to probe the signal dynamics by recording the entire time-domain EDMR signal after a pulse. Field-swept PEDMR spectra thus produce two-dimensional field/time signal maps, as exemplarily shown in fig. 4.4a. Time- and field-domain spectra are obtained either as single-slice cross sections, as shown in figs. 4.4b and c, or by boxcar-integrated over a certain magnetic-field or time range, respectively.

The pulse length in a field-swept PEDMR experiment will typically be set to match a flip angle $\beta = 2\pi\nu_1 t_P = \pi$, where $\nu_1 = g\mu_B B_1/h$ is the on-resonant Rabi-nutation frequency (for $S = 1/2$). The choice of t_P and B_1 depends on the acceptable amount of spectral broadening due to the excitation bandwidth of the MW pulse. For rectangular pulses, the bandwidth is given by $1/t_P$ [30], corresponding to the region of homogeneous MW excitation. For the spectrum shown in fig. 4.4, a pulse length of 48 ns was used, corresponding to a bandwidth of about 21 MHz (or 0.75 mT). With a spectral line width of about 2 mT, this is already at limits. The resulting broadening effect is illustrated by comparison to the red trace in fig. 4.4c, which corresponds to the PEDMR spectrum recorded with a bandwidth of about 7 MHz (or 0.25 mT).

4.3.2 Post-acquistion data processing

Pulsed EDMR experiments involve a considerable amount of post-acquisition processing steps. This comprises baseline corrections, data normalization, Fourier transformations (exempli gratia (*e. g.*), for nutation experiments) or least-squares fits. All data-processing routines have been implemented in MATLAB© (Release 2015b, The MathWorks, Inc., Natick (MA), United States). Most post-processing steps will be discussed in detail in the experimental chapters. Common to all PEDMR measurements, however, is the necessity for background correction and appropriate data normalization, which we will thus discuss already at this point.

The strong MW radiation applied during PEDMR experiments induces non-resonant currents, both in the EDMR sample and in the contact lines. These currents appear as background signals that are superimposed onto the resonant EDMR transients, and can be of the same order of magnitude, or even stronger than the actual signal. Such MW-induced backgrounds thus have to be subtracted from the raw EDMR transients. Figure 4.5 illustrates the background-correction procedure for two PEDMR signals recorded at X-band (left column) and 263 GHz (right column) of an a-Si:H *pin* solar cell. The availability of two-dimensional data sets allows for accurate separation of signal and background currents by means of a two-step baseline removal along the time and field dimension. In a first step a constant baseline is fitted and subtracted from all time-domain traces of the raw data (figs. 4.5a and f). For this purpose, data acquisition is started already a few µs prior to the MW pulse to allow for a non-signal baseline region.[1] Subtraction of a *constant* baseline along the time dimension removes any *non-constant* baseline in the field domain, induced, for instance, by a drift of the constant current. The second step is the subtraction of a constant baseline from all field-domain slices. The field axis thus has to be chosen sufficiently wide to comprise non-signal regions. This step conversely

[1] A prerequisite for this background subtraction is the choice of a shot-repetition time (SRT) that allows for complete equilibration of the current. Otherwise, signal components that have not fully decayed would be subtracted. Especially at low temperatures, this may require SRTs of a few ms.

removes any non-constant time-domain baseline, that is, the MW-induced background currents. The resulting total two-dimensional background signals are shown in figs. 4.5b and g. Subtraction from the raw data maps yields the background-corrected EDMR signals (figs. 4.5c and h).

The illustration in fig. 4.5 shows that background correction is crucial, especially for 263 GHz PEDMR spectra. Here, the background signals are much stronger as compared

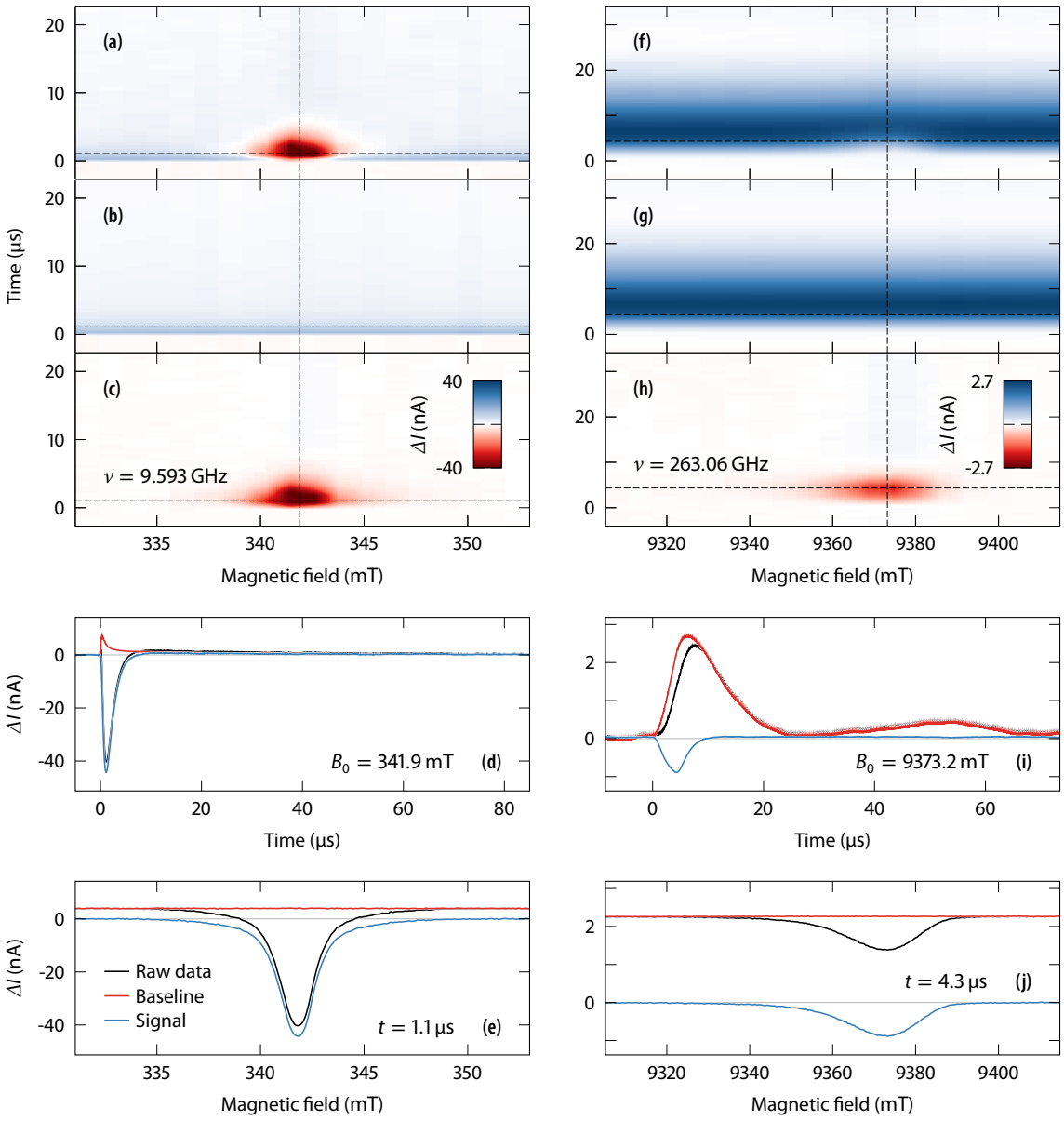

FIGURE 4.5 Background-correction procedure for two-dimensional PEDMR spectra, illustrated for X-band (left) and 263 GHz (right) spectra of an a-Si:H *pin* solar cell, recorded at room temperature under dark, forward-bias conditions ($V_B = 1.1$ V). (a) Raw signal, (b) two-dimensional baseline and (c) baseline-corrected X-band PEDMR signal. (d, e) Time- and field-domain cross sections through figs. a–c, as indicated by the dashed lines. (f–j) Equivalent spectra at 263 GHz. Note the much stronger relative amplitude of the background signal, which is a result of the electrical contacts being located in the MW field.

to X-band. This is a result of the setup geometry (see section 4.2.2), which requires to locate the electrical contacts in direct proximity to the sample and hence within the MW field. Non-resonant MW-induced currents are thus much stronger than at X-band, where the contact pads can be placed outside of the EPR cavity.

The baseline-correction procedure sketched above is not limited to field-swept PEDMR spectra, but applies in general for two-dimensional data sets. Accordingly, we will follow the same recipe for, *e. g.*, field-resolved nutation experiments (ED-Rabi, ED-PEANUT), echo-detected experiments (ED-ELDOR) or two-dimensional TREPR spectra. Details will be discussed in the particular experimental sections.

A final comment should be made concerning the data-normalization nomenclatures used within this work. Field-swept EPR and EDMR spectra will in general be displayed on a magnetic-field axis in units of mT (instead of, for example, a g-value axis). However, this makes direct comparison of different spectra difficult, since the MW frequencies slightly vary in between experiments (9.5–9.8 GHz at X-band, 262–264 GHz for high-field/-frequency experiments). Therefor, if not stated otherwise, field axes will be normalized to 9.6 GHz and 263 GHz, respectively.[1] Resonant current changes are either given as absolute values in units of nA or pA, or relative current changes $\Delta I/I$, taking into account the constant current I.

4.4 NUMERICAL SIMULATIONS AND FITTING ROUTINES

Extracting quantitative information about paramagnetic species and spin-dependent transport channels from EPR or EDMR measurements often requires comparison to simulations in conjunction with least-squares fitting techniques. Basic fitting and regression routines based on, *e. g.*, linear, exponential, sinusoidal or polynomial models are implemented using the MATLAB Optimization Toolbox™ Field-domain spectral simulations and least-squares fits are carried out using the EasySpin [43] toolbox, as described in section 4.4.1. If quantitative parameters are extracted by fitting procedures, it is indispensable to also evaluate uncertainty ranges, taking into account both experimental and fitting errors. For simple linear-regression models, analytical expressions exist to calculate fitting uncertainties. For complex non-linear models (for instance, spectral simulations), error estimation can either be achieved by manual variation of fitting parameters, or with the help of numerical Monte-Carlo approaches, as shown in section 4.4.2.

4.4.1 Simulations of EPR and EDMR spectra

Field-swept pulsed and CWEDMR spectra typically are a superposition of the EPR signatures of the paramagnetic species involved in the spin-dependent pair process. Field-domain EDMR and EPR spectra can thus be simulated and least-squares fitted in the same manner. Within this work, all spectral simulations will be carried out using the EasySpin [43] MATLAB library, which has become the most widely used simulation tool in the EPR community. For disordered solid-state systems like a-Si:H, EasySpin offers the so-called `pepper` function, which calculates powder-average spectra.

[1] This normalization induces small errors for field-independent spectral components. The normalization is thus only applied for data visualization, while data-processing (*e. g.*, least-squares fitting) is based on the actual magnetic-field axis.

It is to be noted that the EasySpin package is not capable of simulating PEDMR experiments in general. This is due to the fact that PEPR and PEDMR measurements are based on different observables. Pulsed EPR probe directly probes the spin magnetization (see section 2.2.2), whereas PEDMR signals are proportional to the spin-pair permutation symmetry. For weakly coupled $S = 1/2$, field-domain spectra can still be modelled as the superposition of the individual EPR spectra. For stronger couplings, this approximation, however, breaks down and the contribution of individual EPR transitions depends on the associated permutation-symmetry change. Accurate simulations of PEDMR signals require the time evolution of the stochastic Liouville equation (section 2.5.3). Various numerical procedures have been developed over the course of the last decade that address this issue for spin-pair processes in different coupling regimes [79–81, 84, 85, 88]. These methods, however, are computationally intense, especially for disordered systems like a-Si:H. If multiple parameter distributions (g-strain, A-strain, D-strain) have to be taken into account—which will be often the case for the processes investigated in this work—, the required computation times soon approach a regime, where least-squares fitting becomes impossible. In the scope of this work, we did not adress this issue. We will, however, compare our experimental results to numerical calculations reported in recent literature, which, for instance, allows to qualitatively conclude on relative dipolar- and exchange-coupling strengths.

4.4.2 Bootstrapping

When fitting experimental data with calculated functions based on a theoretical model, it is a common challenge to estimate confidence intervals of the parameters obtained from a fit. While the determination of statistical uncertainties follows a straightforward approach for simple linear-regression models, numerical methods are required for nonlinear least-squares fits (for example, a spectral fit of an EPR or EDMR spectrum). A solution would be to record a sample of N data sets and perform least-square fits an each signal y_k to derive a statistical distribution of fit parameters μ_k. Confidence intervals could then be easily determined from the mean values and standard deviations of the resulting μ_k distributions. Obviously, this approach is in practice not feasible due to the vast amount of experimental data required.

Bootstrap resampling [261, 262] is a widely used numerical approach that allows to derive statistical estimates of a single sample. In essence, bootstrapping mimics a sample population by randomly resampling from the original sample y to obtain a synthetic distribution of N samples y^*_k. Statistics of a parameter μ obtained from least-squares regression of y are then estimated from the distribution of the respective bootstrap results μ^*_i determined from y^*_k. The mathematical background that proofs the validity of the approach is described elsewhere (see, for instance, ref. [262]), Herein, we will only briefly describe the procedure used for least-squares fits with bootstrap resampling.

Assume an observed signal $y_i(x_i)$ at n points x_i, where $i = 1, \ldots, n$. Best-fit parameters μ are estimated from a nonlinear least-squares regression based on the given model, resulting in a fit spectrum $f_i(x_i)$ and residuals $\varepsilon_i = y_i - f_i$. At each bootstrap iteration k, the least-squares fit is repeated using a generated sample $y^*_{i,k}$, based on the following steps.

(1) The original fit residuals ε_i are randomly resampled, resulting in a new set of residuals $\varepsilon_{j,k}$, picked from ε_i at random indices j. In other words, each value of the new

set of n residuals $\varepsilon_{j,k}$ is one of the original values ε_i chosen at equal probability.

(2) A bootstrap data set $y^*_{i,k}$ is generated by adding the resampled residuals to the original fit result, that is, $y^*_{i,k} = f_i + \varepsilon_{j,k}$. The bootstrap data set is treated as an independent population sample, independent from the original signal y_i. However, it still contain the signal information encoded in the resampled residuals. The deviation of $y^*_{i,k}$ from y_i depends on the size of the fit residuals ε_i, determined by the experimental SNR and the quality of the least-squares fit.

(3) The least-squares regression is repeated based on the bootstrap data set $y^*_{i,k}$, resulting in a fit spectrum $f^*_{i,k}$ and parameter estimates μ^*_k. To allow for least-squares fit results that are unbiased of the choice of the initial set of fit parameters μ_0, each bootstrap iteration step uses initial values μ_0 that are randomly selected within the pre-defined parameter boundaries.

(4) Steps 1–3 are repeated N times (*e. g.*, $N = 1000$), resulting in a distribution of N parameter estimates μ^*_k. The standard deviation $\Delta\mu^*$ of the bootstrap population, referred to as the *bootstrap standard error*, yields an estimate for the statistical error $\Delta\mu$ of the original parameter. Proportional confidence intervals of the fit spectrum f_i can be estimated from percentiles of the the bootstrap distribution $f^*_{i,k}$ (eq. 4.2).

For calculating standard deviations and percentiles of the bootstrap populations, the individual bootstrap iterations k are weighted, based on the goodness of the bootstrap fits with respect to the original data. Therefor, weights w_k are calculated from the residual sum of squares,

$$w_k = \left[\sum_i (\varepsilon^*_{i,k})^2\right] = \left[\sum_i (y_i - f^*_{i,k})^2\right]. \tag{4.1}$$

Weighted standard deviations and percentiles are then calculated based on standard mathematical formulas.

Note that the term "percentile" refers to the cutoff value of a that is larger or equal then a certain percentage of the distribution. Using percentiles, $100\,(1-\alpha)\,\%$ confidences intervals, *e. g.*, of the fit spectrum f_i, can be estimated from the bootstrap population, according to

$$f_{CI} = \left(f^*_{\alpha/2}, f^*_{1-\alpha/2}\right), \tag{4.2}$$

where $f^*_{\alpha/2}$ denotes the $\alpha/2$ (weighted) percentile of the $f^*_{i,k}$ bootstrap distribution. Typically, 95 % confidence intervals ($\alpha = 0.05$), corresponding to to a $\pm 2\sigma$ interval, will be used as an indicator for the confidence level of a fit result.

Bootstrapping is a computationally intensive method, since least-squares fits need to be performed at each iteration step and the bootstrap population size N needs to be sufficiently large to provide statistically meaningful results. The computation time can be significantly reduced by employing parallel-computing on multiple CPUs (based on the MATLAB Parallel Computing Toolbox™). Nevertheless, bootstrapping is not feasible for time-consuming multiparameter fits, where the least-squares regression of a single data set can easily take several hours—an example is the global multifrequency fit of a-Si:H EDMR spectra presented in section 5.4. In these cases, errors can only be estimated by manual variation of fitting parameters and observation of the resulting model function.

CHAPTER 5

Multifrequency EDMR on amorphous-silicon

This chapter presents pulsed-EDMR experiments on undoped a-Si:H films, conducted at X-band (9.6 GHz/0.34 T) and mm-waveband (263 GHz/9.4 T). Based on this multifrequency approach, we were able to disentangle the different resonance contributions by means of a global least-squares spectral fit. By measuring temperature-dependent EDMR spectra, we demonstrate the transition between a current-quenchning spin-dependent recombination process at room temperature towards a current-enhancing process at cryogenic temperatures.

5.1 INTRODUCTION

The results of previous research, summarized in chapter 3, revealed a number of recombination and transport pathways that are present in a-Si:H and predominate the electronic material properties under different conditions. For instance, a complex temperature dependency of the photoconductivity was found: At low temperatures, charge-carrier transport is governed by hopping through the localized band-tail states, whereas at higher temperatures, the transport path is shifted into the extended band states and recombination via DB defects becomes the dominant current-limiting loss mechanism. The goal of this thesis is to gain a better understanding of the microscopic nature of electronic transport processes present in the different temperature regimes, using EDMR to selectively probe transport and recombination pathways via localized paramagnetic states. This chapter aims to give an overview of the spin-dependent processes present in a-Si:H. For this purpose, multifrequency EDMR spectra of undoped a-Si:H films have been measured at temperatures ranging from 10 K to room temperature. From these experiments, it will become evident that the EDMR signals observed at low temperatures are distinctly different from those at room temperature. While this chapter focusses an the transition between these two distinct regimes, chapters 6 and 7 will then take a deeper look into the processes at low temperature and room temperature, respectively.

The spectra presented in this chapter have been recorded by means of pulsed EDMR. As opposed to the conventional CW approach, PEDMR provides not only the magnetic-field-domain EDMR spectrum, but also the time evolution after the MW pulse. The signal dynamics can often be utilized to deconvolve overlapping resonances [263, 264]. In addition, PEDMR allows to directly differentiate between current-quenching and -enhancing processes from the signal sign, other than in CWEDMR, where magnetic-field (or microwave) modulation is used, leading to a complex dependency of the signal sign on the modulation frequency [258].Coherent spin manipulation in PEDMR experiments further allow to adapt pulse sequences known from PEPR, in order to perform experiments based on electrically detected Rabi nutations or electron-spin echoes. Such experiments

will be presented in chapters 6 and 7. Besides the use of PEDMR, we will also present spectra recorded at different MW frequencies. This multifrequency approach has the benefit of (i) enhancing the spectral resolution at higher frequencies and (ii) allowing to separate field-dependent and field-independent line-shape contributions [264]. Therefor, PEDMR spectra have been recorded at a conventional X-band spectrometer and at a recently developed 263 GHz/12 T setup [26]. A detailed description of the experimental setups and the data-acquisition and -processing techniques used for PEDMR measurements can be found in section 4.2.

5.2 MATERIALS AND METHODS

While the results of this work concern a-Si:H in a general sense, both as a material itself and in its role as the prototype amorphous semiconductor, they will also relate to the application of a-Si:H in photovoltaic devices. In the following chapters, we will therefor also present EDMR experiments on fully processed a-Si:H solar cells. However, since this chapter serves as a starting point to understand the spin-dependent processes, the measurements presented in here have been carried out using plain undoped a-Si:H films. Thereby, we can assure that the obtained results apply to intrinsic bulk a-Si:H, allowing to compare them later on to those experiments conducted on solar-cell samples. The structure and preparation procedure of these a-Si:H film samples is summarized in section 4.1.1.

Figure 5.1a shows the room-temperature current-voltage characteristics of the a-Si:H film sample used for the X-band experiments presented in this chapter. The curve has been recorded with the sample inserted and contacted in the X-band EDMR setup. The *I-V* curves in the dark and under illumination are shown, using the same white-light source as for the EDMR experiments. Both in the dark and under illumination, the sample exhibits diode characteristics in the range of −0.5 V to 0.5 V, shifting to ohmic behavior at

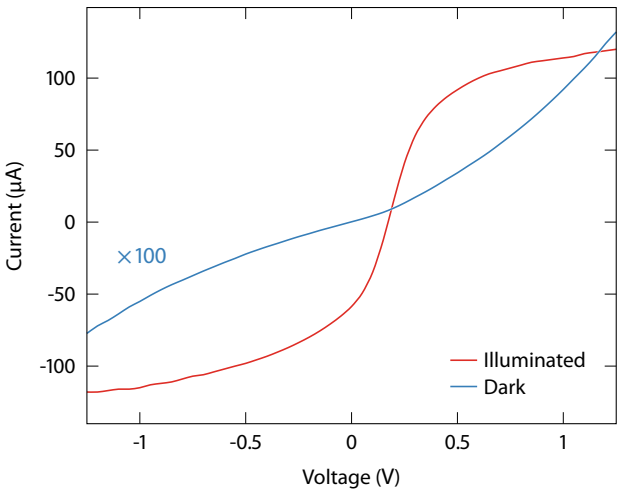

FIGURE 5.1 Current-voltage characteristics of an a-Si:H film sample investigated in this chapter. The curves were recorded with the sample mounted in the X-band EDMR setup under dark (blue) and illuminated conditions. EDMR spectra were recorded in the ohmic transport region ($V_B = -1$ V).

higher voltages. All EDMR measurements are carried out under illumination and in the ohmic regime by applying a bias voltage of 1 V. At room temperature, the photocurrent at this voltage is about 115 µA for the sample shown in fig. 5.1a. For the EDMR experiments, multiple samples of the same batch have been used. All samples, however, qualitatively showed the same *I*-*V* characteristics, with the room-temperature photocurrent (at 1 V bias) varying between 100 µA and 150 µA.

The experiments carried out in this chapter are limited to single-pulse EDMR measurements, where the transient EDMR response is detected as a function of the external magnetic field at constant MW frequency. Measurement and post-acquisition procedures are discussed in section 4.3.

5.3 MULTIFREQUENCY PULSED EDMR

Figure 5.2 shows X-band and 263 GHz PEDMR spectra recorded at $T = 10$ K (upper) and room temperature (lower), respectively. The spectra were recorded by measuring the transient photocurrent change after a single MW pulse as a function of the external magnetic field. The result is a two-dimensional time-field map, from which one-dimensional PEDMR spectra can be obtained as cross sections, either in time domain at a fixed magnetic field or in field domain at a fixed time after the MW pulse. Figure 5.2 displays magnetic-field-domain cross sections taken immediately after the MW pulse, where the maximum relative current change was detected.

5.3.1 Resonant photocurrent change

Before discussing the PEDMR spectra themselves, it is worth noting that both the absolute photocurrent I and the relative current change $\Delta I/I$ differ between spectra recorded at X-band and 263 GHz. At room temperature, the photocurrent is larger by a factor of about 3.5 for the measurement at 263 GHz compared to the X-band experiment at the same temperature, although both experiments were carried out using the same sample and biasing conditions ($V_B = -1$ V). This can, however, be explained by the different illumination methods employed in the two different setups. While the same white-light source was used in both experiments, the light-guiding onto the EDMR sample differed: At X-band, the light was coupled into the EPR resonator through an optical window using a gooseneck light guide. For the 263 GHz experiment, a single optical fiber was integrated into the probehead and positioned directly on top of the EDMR sample (see section 4.2). As a result, different illumination intensities and thus different charge-carrier generation rates are obtained at X-band and 263 GHz leading to different absolute currents at the same bias voltage. In addition, also the electrical contacts are established differently in both setups, which further complicates the comparison of absolute current values.

Besides the absolute photocurrent also the relative EDMR current change differs between X-band and 263 GHz by about an order of magnitude at equal temperatures. At $T = 10$ K, the maximum relative current change is about $9.5 \cdot 10^{-3}$ ($\Delta I \approx 53$ nA) at X-band and about $0.42 \cdot 10^{-3}$ ($\Delta I \approx 3.4$ nA) at 263 GHz. At room temperature, the maximum (absolute) values of $\Delta I/I$ are about $5.5 \cdot 10^{-6}$ ($\Delta I \approx -640$ pA) and $0.59 \cdot 10^{-6}$ ($\Delta I \approx -240$ pA) at X-band and 263 GHz, respectively. While these values are naturally also impacted by the different absolute current values, the differences in $\Delta I/I$ are certainly also a result of

the different B_1 amplitudes used in the experiments. For PEDMR experiments at X-band, a TWT amplifier with a nominal output power of 1 kW was used to supply high-power MW pulses. At the time of the experiment, the output power of the 263 GHz source was limited to 15 mW, leading the B_1 amplitudes that are by orders of magnitude lower than those obtained at X-band. Furtermore, at X-band, the EDMR sample was placed into a resonant MW cavity, which further amplifies and concentrates the B_1 field at the sample position. While MW cavities are also available for EPR experiments at 263 GHz, the available sample space in such a high-frequency resonator is by far not sufficient for placing and contacting EDMR samples. Therefor, a non-resonant probehead was used for EDMR experiments at 263 GHz (see section 4.2.2), where MWs are directly guided onto the sample as a Gaussian beam. This leads to further loss of B_1 and thus signal intensity as compared to X-band experiments.

Due to the different B_1 amplitudes, also very different MW-pulse lengths were required at X-band and 263 GHz. At X-band, pulse lengths of 208 ns and 128 ns were used at $T = 10$ K and room temperature, respectively. To set these pulse lengths, Rabi-nutation experiments were carried out prior to the EDMR measurement. From the resulting nutation frequencies, the π-pulse length required for a PEDMR measurement were read off. At 263 GHz a pulse length of 6 µs was used at all temperatures. Here, the pulse length was set by maximizing the EDMR signal, as for such long pulses, nutation experiments in order to measure B_1 and the required π-pulse length cannot be conducted.

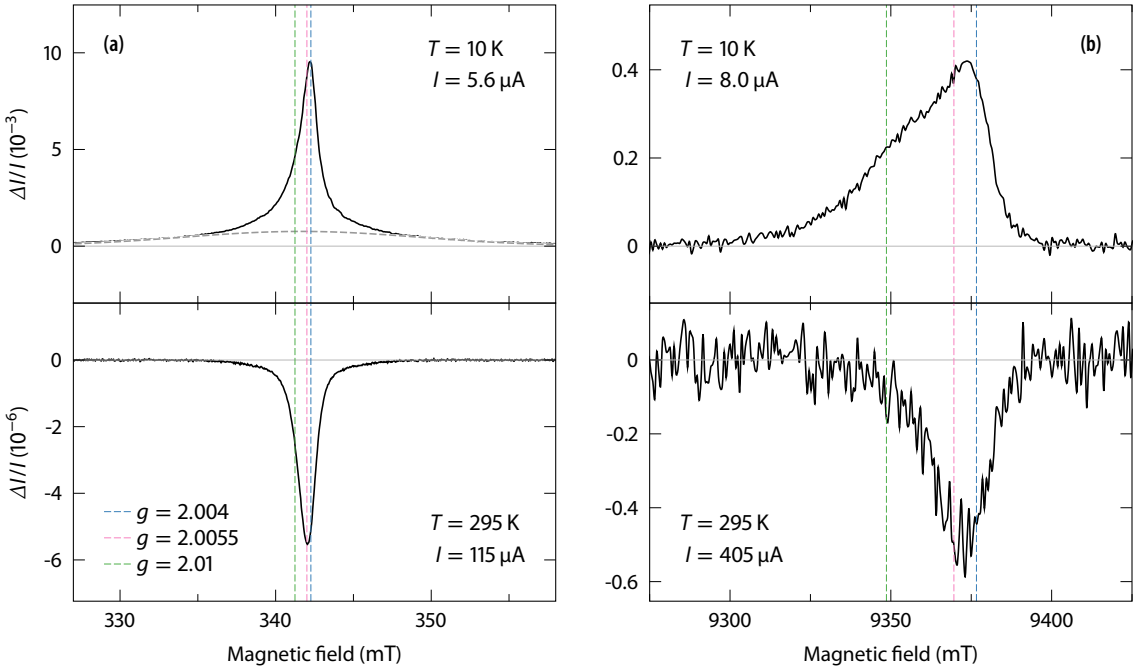

FIGURE 5.2 Field-swept pulsed EDMR spectra of a-Si:H films recorded at (a) X-band (9.6 GHz) and (b) 263 GHz at temperatures of 10 K (upper) and 295 K (lower). The spectra show the maximum relative current change after a single MW pulse. The dashed colored lines mark the expected resonance positions of CBT/VBT states (blue/green) and DB defects (magenta). The dashed gray line in fig. a marks the broad line-shape component exclusively observed at low temperatures (see text for further discussion).

5.3.2 Line shapes

The first immediate observation from fig. 5.2 is the different sign of $\Delta I/I$ at low ($T = 10$ K) and high temperature ($T = 295$ K). At low temperature, a current-enhancing ($\Delta I/I > 0$) EDMR signal is observed, while at high temperature, EDMR leads to a quenching of the current ($\Delta I/I < 0$) after the MW pulse. This observation is consistent with previous EDMR studies on a-Si:H (see summary in chapter 3). Earlier studies also reported a current-quenching EDMR signal at room temperature (see, for instance, ref. [60]), commonly interpreted to result from spin-dependent recombination of CBT electrons via DB defects (see section 3.4.1). At cryogenic temperatures, previous reports similarly found a current-enhancing EDMR signal (for example, ref. [26]). Possible interpretations include spin-dependent hopping conduction via CBT and VBT electrons and holes (see section 3.4.2). In order to test these prevailing interpretations of the EDMR spectra observed at different temperatures, it is key to identify the line-shape components resulting from different paramagnetic centers.

From fig. 5.2, it is evident that not only the signal sign, but also the line shape changes from low to high temperature. At X-band (fig. 5.2a), a narrow line ($\Delta B_0 \approx 2$ mT) is observed at both temperatures, centered at about $g = 2.005$. This resonance position is close to the g-values of electrons trapped in CBT states ($g_{\mathrm{CBT}} \approx 2.004$, blue lines in fig. 5.2) and singly occupied dangling bonds ($g_{\mathrm{DB}} = 2.0055$, red lines in fig. 5.2). Closer inspection of the two lines, however, reveals that the high-temperature line is slightly shifted and broadened towards higher g-values with respect to the low-temperature line. This is consistent with the picture of CBT electrons contributing to both EDMR signals, while a DB component being present only in the high-temperature (recombination) regime. In the latter case, one would expect a superposition of the CBT and DB resonances, leading to a broadening and a g-value shift with respect to the pure CBT resonance.

Besides the narrow central line, the low-temperature X-band spectrum contains an additional broad line feature, which is not present in the room-temperature spectrum. This feature can be approximated by a Gaussian line shape with a FWHM of about 20 mT, centered at about $g = 2.008$, as indicated by the dashed gray line in the upper plot of fig. 5.2a. A similar line contributions has also been found in earlier EDMR and ODMR experiments on a-Si:H (see section 3.4.3). Based on the unusually large line width, the resonance was associated with dipolar coupled excitonic electron-hole pairs [244]. Unambigious evidence for this assignment, however, is as yet missing.

The 263 GHz spectra further reveal pronounced asymmetric line shapes, with additional contributions at higher g-values around $g = 2.01$ (green lines). These line components are also observed in the X-band spectra, although they are more clearly visible at 263 GHz due to the higher g-value resolution. The resonance position suggests an assignment to holes trapped in VBT states, as the respective EPR resonance is known to appear at these g-values in LEPR experiments (see section 3.2.3). The presence of VBT resonances in the EDMR signals at both low and high temperature is also consistent with earlier studies. In both cases, their contribution was explained with hopping of holes through the tail states, which either leads to an increase of the photocurrent at low temperature, where hopping is expected to be the dominant transport mechanism (see sections 3.3.1 and 3.4.2), or to an enhanced CBT-DB recombination rate as the result of the enhanced hole mobility towards the recombination site (see section 3.4.1 and ref. [60]).

The direct comparison of the X-band and 263 GHz spectra shows that line-shape contributions with different magnetic-field/frequency dependencies are present. This becomes obvious when plotting the spectra on a *g*-value axis, as shown in fig. 5.3. At room temperature (fig. 5.3b), similar line shapes are observed at X-band and 263 GHz. The X-band spectrum is slightly broadened, which be explained with the presence of both field-dependent (*g*-strain) and field-indepedent (*e. g.*, lifetime broadening or unresolved HFI) broadening mechanisms. The latter has a much lower impact at 263 GHz due to the predominance of field-dependent contributions at higher magnetic fields. The spectra shown in fig. 5.3b thus demonstrate the enhanced *g*-value resolution obtained at higher MW frequency. A much stronger discrepancy between the X-band and 263 GHz line shapes is observed at low temperature (fig. 5.3a). As for the room-temperature spectra, the X-band spectrum is broadened due to field-indepedent line-width contributions. The broadening, however, is much more pronounced at low temperature. In particular, broad wings are present in the X-band, stemming from the 20 mT broad $g = 2.008$ line (red dashed line in fig. 5.3a). This broad feature is not observed in the 263 GHz spectrum, when plotted on a *g*-value axis. A close comparison of the spectra in fig. 5.3a yet reveals that the $g = 2.008$ line is observed also at 263 GHz, although with a much lower *g*-value line width (black dashed line in fig. 5.3a). This clearly indicates that the line broadening of the $g = 2.008$ component is field-independent, such that *g*-strain can be excluded as the primary broadening mechanism. On the contrary, the assignment to dipolar coupled excitonic electron-hole pairs with a certain distribution of coupling strength, as done in the past by [244] and Lips *et al.* [27], is consistent with a field-independent line width.

In summary, the comparison of X-band and 263 GHz PEDMR line shapes indicates that different spin-dependent transport mechanisms cause the EDMR signal in different temperature regimes. A current-enhancing process is observed at low temperature, whereas at a current-quenching process is found at room temperature. A visual line-shape comparison further shows that different paramagnetic centers are involved in both processes. In order to clearly identify these different species, spectral fits will be performed in the next section, using the above-discussed observations as a starting point.

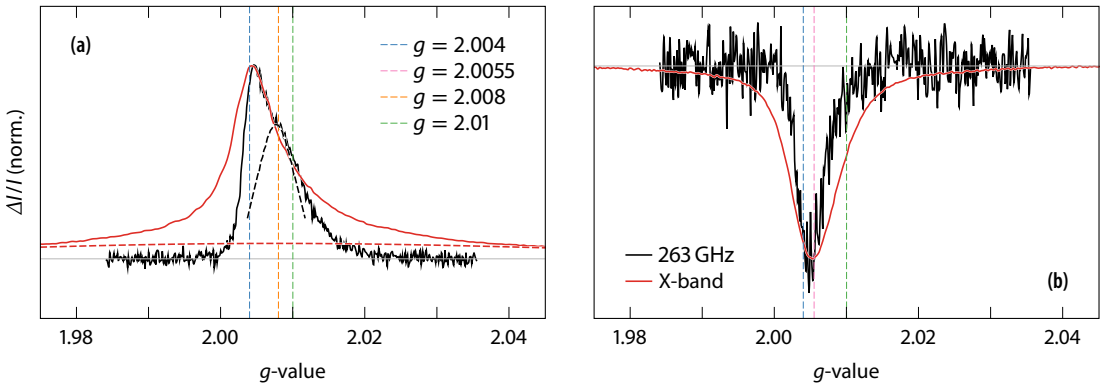

FIGURE 5.3 Pulsed EDMR spectra at (a) $T = 10$ K and (b) $T = 295$ K plotted on a *g*-value axis to illustrate the presence of field-dependent line-broadening mechanisms (*g*-strain). Black and red traces correspond to the X-band and 263 GHz spectra shown in figs. 5.2a and b, respectively. The dashed vertical lines mark the *g*-values of the observed resonance components. The dashed traces in fig. a marks the $g = 2.008$ line-shape component exhibiting a field-independent line width of about 20 mT (see text for further discussion).

5.4 SPECTRAL FITTING

Aiming to deconvolve the different line components and assign them to paramagnetic centers, we fitted the EDMR spectra shown in fig. 5.2 with simulated spectra. Therefore, we assume that the EDMR spectra can me modeled as a superposition of the EPR resonances of the paramagnetic centers identified in the previous section, namely, the resonances associated with CBT/VBT states and DB defects as well as the additional field-independently broadened $g = 2.008$ resonance. The latter we will for now label as the triplet-exciton (TE) line, based on the assignment by earlier studies to strongly dipolar coupled electron-hole pairs forming an excitonic $S = 1$ state, although a clear proof for this assumption is as yet missing. Each of the individual EPR resonances can be described by a spin Hamiltonian of the form

$$\mathcal{H} = \mu_B \boldsymbol{S}^T \boldsymbol{g} \boldsymbol{B}_0 + \sum_j \mu_N g_{N,j} \boldsymbol{I}_j^T \boldsymbol{B}_0 + h \sum_j \boldsymbol{S}^T \boldsymbol{A}_j \boldsymbol{I}_j. \tag{5.1}$$

The first term represents the electron Zeeman interaction, coupling the electron spin $\boldsymbol{S}$ to the external magnetic field $\boldsymbol{B}_0$. The second and third denote the nuclear Zeeman interaction of coupled nuclear spins $\boldsymbol{I}_j$ and the HFI that couples these nuclear spins to the electron spin via the HFI tensors $\boldsymbol{A}_j$ (see section 2.3 for details). The resulting resonances are convolved with line-broadening functions that can be either field-dependent or field-independent, yielding a simulated resonance line. These calculated lines for the individual spectral components can then be summed using weighting factors to match to simulation to the experimental EDMR spectrum.

5.4.1 Global fitting model

If, for the moment, we neglect HFIs and assume only isotropic g-values, the fit parameters required to model the EDMR spectra comprise the g-value, field-independent and -dependent line widths, as well as a weighting factor for each spectral component. Assuming three line contributions for each spectrum (CBT/VBT and DB resonances at room temperature; CBT/VBT and TE lines at $T = 10$ K), one obtains 12 fitting parameters for each spectrum (three g-values, six line-width parameters, and three weighting factors). If applied to a single spectrum, such a fit is clearly over-parametrized and will most certainly result in a best-fit spectrum that reproduces the experimental data. However, the present case offers means to substantially reduce the degrees of freedom of the fit.

The availability of EDMR spectra recorded at different MW frequencies and temperatures allows to follow a *global fitting* strategy by fitting all datasets with the same shared parameter set, instead of fitting each spectrum one at a time. Since spin-Hamiltonian parameters and line-broadening parameters do not depend on the MW frequency, the fit result is constrained to those sets of parameters that reproduce both the X-band and the 263 GHz spectra recorded at the same temperature. Global fitting of multifrequency spectra thereby allows to distinguish field-dependent and independent line-broadening mechanisms, which cannot be achieved bv fitting a single EDMR spectrum. Moreover, our fitting model assumes the presence of the CBT and VBT resonance at all temperatures (altough as the result of different spin-dependent transport processes). To our knowledge, no temperature dependencies of the CBT and VBT line shapes have been reported in previous EDMR or LEPR studies. Therefor, the fit parameters should not only be shared

amongst spectra at different MW frequencies, but also amongst spectra at different temperatures. As a result, the spin-Hamiltonian and line-broadening parameters of all four spectral components will be fit globally, leaving solely the weighting factors of the individual components to vary between the EDMR spectra at different temperatures and MW frequencies,[1] The number of fitting parameters is thereby reduced from 12 parameters per spectrum to 12 global parameters (*g*-values, *g*-strain broadenings and field-independent line widths) and 12 weighting factors for the three components per spectrum.

The degrees of freedom of the fit are further reduced by prior knowledge of a large part of the fit parameters. Especially, the EPR resonances of the DB defect and CBT/VBT states have been studied before using both EPR and/or EDMR/ODMR techniques (see chapter 3). From this earlier research, *g*-values, line broadenings and HFI parameters are in part well known and can then be either kept fixed during the fit, or at least serve as a valid starting point. These known parameters are summarized below for all four spectral components that we assume for our fitting model:

Dangling bond The DB resonance has been extensively studied in the past by both EPR and EDMR (see sections 3.2.1 and 3.4.1). Fehr *et al.* [148] determined the spin-Hamiltonian parameters in great detail using a combined approach of multifrequency EPR and DFT calculations. We thus use these parameters, comprising a rhombic *g*-tensor, an axially symmetric *A*-tensor for the HFI with ^{29}Si nuclei, *g*- and *A*-strain and a field-independent Voigtian line width to account for lifetime broadening and unresolved HFI. These parameters will be kept fixed and only the weighting factors will be fitted. The DB resonance will only be included for the room-temperature spectra.

CBT/VBT states The *g*-values of CBT and VBT states are known from earlier LEPR and EDMR/ODMR studies (see sections 3.2.3 and 3.4.1). For CBT electrons, an isotropic *g*-value of 2.0044 was found, with only little deviation between different studies. This value will thus also be excluded from the fit. The *g*-values for VBT holes reported by different groups, however, spread over a much wider range at about 2.009 to 2.015, such that we will leave this value as a fit parameter.[2] In addition, *g*-strain and line-width parameters will be included in the fit for both the CBT and the VBT line, since a systematic line-shape study that distinguishes between field-dependent and -independent broadening for these resonance is not available in the literature. As for the DB defect, Umeda *et al.* [150] found HFI with ^{29}Si nuclei for the CBT resonance as the result of a multifrequency LEPR study. This result is consistent with theoretical calculations by Ishii and Shimizu [151] (see section 3.2.3 for details). We will include their findings when simulating the CBT resonance, though without varying the HFI parameters during the fit. In order to fit the simulations to the experimental data, also *A*-strain parameters are required. Since no values are known from literature, we adopt the *A*-strain parameters from the DB defect, noting that the HFI parameters for the CBT state are very similar to the *A*-tensor reported for DBs. For the VBT resonance, HFIs were found to be negligible [150, 151] and will thus be disregarded for the simulations.

TE line While the TE resonance has been observed before in both EDMR and ODMR

[1] Note that it is tempting to assume also the same spectral weighting factors for X-band and 263 GHz spectra recorded at the same temperature. However, as described in chapter 4, different illumination intensities were used in the different experimental setups. As it is known from photoluminescence studies that transport channels in a-Si:H can strongly dependent an the charge-carrier generation rate (see section 3.3), different spectral weights at X-band and 263 GHz thus cannot be excluded.

[2] It is to be noted that several studies reported axial or rhombic *g*-tensor symmetries [26, 150]. While we will explore this possibility later on, we will assume an isotropic *g*-value here, to keep the number of fitting parameters as low as possible.

spectra of a-Si:H (see section 3.4.3), both its origin and the spin-Hamiltonian parameters are to date unknown. Previous studies reported *g*-values around 2.008, which we will use as an initial value. Stutzmann and Brandt [244] reported a Gaussian line shape, which is consistent with our findings. Besides an isotropic *g*-value, we thus also include *g*-strain, as well as a field-independent Gaussian line width into the fit. Note that this line width is purely phenomenological, since the EDMR spectra alone do not allow a clear assignment to, *e. g.*, dipolar coupled triplet excitons and a related broadening mechanism such as *D*-strain.

Besides the spin-Hamiltonian parameters, two additional field-offset parameters at X-band and 263 GHz, respectively, were included into the fit, as, unfortunately, the magnetic field was not calibrated properly at the time of the experiments. In particular, at 263 GHz, RF coils were attached to the sample holder (see section 4.2.2), which later turned out to be inadvertently made of ferromagnetic material and thus exposed the EDMR samples to a constant offset field of about 8 mT. At X-band, an NMR teslameter was used to measure the magnetic field. Nevertheless, the teslameter was positioned outside of the EPR resonator, such that a constant offset with respect to the measured field remains at the sample position. In later experiments (see, *e. g.*, chapter 6), this offset was calibrated by attaching an EPR field standard close to the EDMR sample. However, during the present experiments, such a field calibration was not carried out, such that the field-offset has to remain as a fitting parameter. This, in turn, requires at least one *g*-value parameter to be kept fixed during the fit (here, the *g*-values of the CBT and DB components).

Altogether, we obtain a total of 22 parameters that need to be adjusted to globally fit the four EDMR spectra:

- Two *g*-values (VBT and TE).
- Three *g*-strain broadening parameters (CBT, VBT and TE).
- Three field-independent line widths (CBT, VBT and TE).
- Three weighting factors per spectrum (CBT/VBT/TE at $T = 10$ K; CBT/VBT/DB at room temperature).
- Two field-offset parameters (X-band and 263 GHz).

The fitting routine was implemented in MATLAB. Simulated solid-state EPR spectra were calculated based on eq. 5.1 using the `pepper` function for powder-averaged EPR spectra from the EasySpin [43] toolbox. Global fitting was achieved by scaling all four spectra to equal amplitude and concatenating them into a single dataset. The simulated spectra were combined in the same way to achieve simultaneous fitting of all experimental spectra. The customly written fitting function is based on the `esfit` function for nonlinear least-squares fitting provided by the EasySpin library and uses a Nelder-Mead downhill-simplex algorithm.

5.4.2 Fit results

The parameter set resulting in the best fit to the experimental data is summarized in tab. 5.1. Values printed in gray refer to parameters that were kept fixed during the fit, while upright values denote fitted parameters. The resulting simulated spectra (dashed lines) are displayed in fig. 5.4 together with the experimental EDMR spectra (solid black

TABLE 5.1 Spin-Hamiltonian and line-broadening parameters obtained from globally fitting multifrequency EDMR spectra of a-Si:H recorded at $T = 10$ K and room temperature. Principal values of the *g*- and *A*-tensor are listed together with the respective strain values (FWHM of a Gaussian distribution), the latter given in parentheses. Weighting factors are fit for each spectrum individually and are given as intensity weights (integrated signal intensity), normalized to sum to unity. Values printed in gray were kept fixed during the fit, while black-colored values denote fit parameters.

	***g*-tensor**			***A*-tensor**[a] **(MHz)**		**Line width**[b] **(mT)**		**Weights**[c]			
	g_x **or** g_{iso} **(strain)**	g_y **(strain)**	g_z **(strain)**	a_{iso} **(strain)**	T **(strain)**	ΔB_0^G	ΔB_0^L	**X-band**		**263 GHz**	
								10 K	**295 K**	**10 K**	**295 K**
CBT[d]	2.0044 (0.0033)	-	-	200 (70)	40 (24)	-	1.00	0.44	0.29	0.32	0.30
VBT	2.0100 (0.0098)	-	-	-	-	-	1.20	0.15	0.14	0.37	0.14
DB[e]	2.0079 (0.0054)	2.0061 (0.0024)	2.0034 (0.0018)	190 (70)	39 (24)	0.13	0.43	-	0.57	-	0.56
TE	2.0077 (0.0036)	-	-	-	-	18.1	-	0.41	-	0.31	-

[a] Isotropic and axial component of an axially symmetric HFI tensor $\boldsymbol{A}$ (see section 2.3.2 for details).
[b] Field-independent convolutional broadening, using a Voigtian line shape with Gaussian and Lorentzian FWHM ΔB_0^G and ΔB_0^L, respectively.
[c] Integrated spectral intensities, normalized to sum to unity.
[d] Isotropic *g*-value taken from earlier EPR/EDMR studies (see ref. [17] for a summary). Hyperfine-interaction parameters are based on LEPR results by Umeda *et al.* [150] and calculations by Ishii and Shimizu [151]. *A*-strain parameters were adopted from the DB defect (see text for details).
[e] Spin-Hamiltonian parameters taken from Fehr *et al.* [148] (see text and section 3.2.1 for details).

lines). The gray lines in fig. 5.4 show the fit residuals (difference between the experimental and the fitted spectra), which are a measure for the quality of the fit. For the 263 GHz spectra, the residual amplitude is below the noise level of the experimental data. For the X-band spectra, small residuals are observed, although with negligible amplitude compared to the experimental spectra. Our fitting model thus results in a consistent set of simulated spectra that reproduces the experimental EDMR spectra.

In our fitting model, both the low-temperature and the room-temperature are a superposition of three resonance lines. In both cases, we assign two of these components to electrons and holes trapped in CBT and VBT states. At room temperature, the third resonance is the EPR signature of the DB defect, while at low temperature, the ≈20 mT broad line, which we preliminarily labeled as TE resonance. The fit results obtained for the individual spectral components are in general in good agreement with what has been reported by earlier studies. For the CBT line, the *g*-value was taken from literature and kept unchanged during the fit. Only the line-broadening parameters were fitted, yielding a field-independent Lorentzian line width of 1.0 mT and (isotropic) *g*-strain of 0.0033. Together, this results in an X-band FWHM of about 1.3 mT. For the VBT line, a *g*-value of 2.010 was found, with *g*-strain broadening of 0.0098 and a field-independent Lorentzian line width of 1.2 mT, resulting in a total X-band FWHM of about 2.4 mT. These results are in good agreement with earlier reports of the CBT and VBT resonances, studied either by LEPR or by EDMR/ODMR, such that this assignment seems reasonable for both the low- and the room-temperature EDMR spectra.

The spin-Hamiltonian parameters for the DB line were adopted from multifrequency EPR results from Fehr *et al.* [148]. Together with the CBT and VBT resonances, the combined simulated spectra are in excellent agreement with the room-temperature EDMR spectra at both X-band and 263 GHz. This is consistent with earlier EDMR studies on

a-Si:H, which identified the same three resonances as the origin of the EDMR signal (see section 3.4.1). It is interesting to compare the spectral weights of the three components found at X-band and 263 GHz (see tab. 5.1). Although the weighting factors were fitted individually for each spectrum, we find almost identical weights for both spectra. This result both supports the validity of the fitting model and suggests that the room-temperature EDMR signal is independent from the illumination conditions, which were substantially different at X-band and 263 GHz.

The fitting model for the $T = 10$ K spectra assumed the additional TE line to fit the experimental data. This line has been observed earlier in both EDMR [27, 244] and ODMR [220, 229, 233, 242, 265] studies with g-values around 2.008 and Gaussian line widths of about 20 mT. We find good agreement with these reported values, obtaining a g-value of 2.0077 and a field-independent Gaussian line width of 18 mT. The 263 GHz spectrum (upper plot in fig. 5.4b) is almost perfectly reproduced by the resulting simulated spectrum. However, the X-band simulation (fig. 5.4a) shows slight deviations from the experimental data on both sides of the central peak. This indicates that the simple model of a field-independent Gaussian line broadening does not fully reproduce the actual line shape. Such a deviation would be certainly more pronounced at X-band than at 263 GHz, where the line shape is dominated by field-dependent g-strain broadening. Besides the lower fit quality compared to the room-temperature spectra, we also find a different behavior of the spectral weights. Other than at room-temperature, where identical weights are obtained at X-band and 263 GHz, for the low-temperature spectra, different weighting factors are found: At X-band, the normalized intensity weights are 0.44/0.15/0.41 for

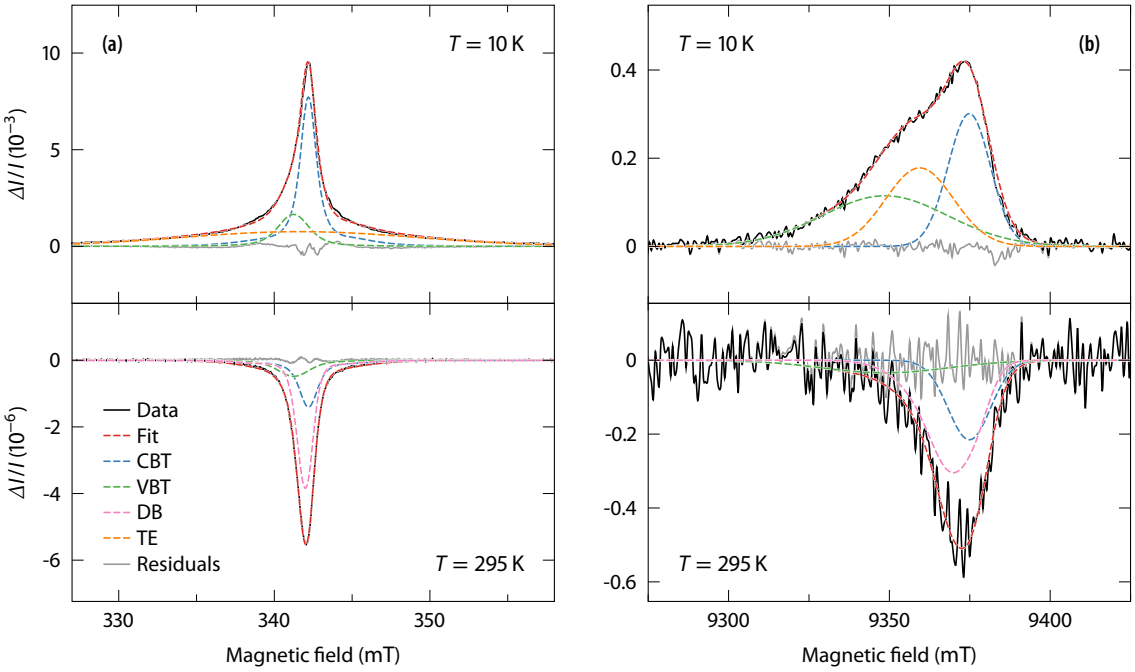

FIGURE 5.4 Simulated spectra of the (a) X-band and (b) 263 GHz PEDMR spectra of a-Si:H shown in fig. 5.2 resulting from a global simultaneous least-squares fit based on the fitting model discussed in the text. Red dashed lines mark the fit spectrum resulting as a superposition of the color-coded spectral components. The corresponding fitting parameters are given in tab. 5.1 (see text for further discussion).

the CBT/VBT/TE lines, whereas at 263 GHz, we find rougly equally distributed weights of 0.32/0.37/0.31 for the three line components. While this deviance could be an indicator of a relative change of intensity of the underlying transport mechanisms with changing experimental conditions (*e. g.*, light intensity and photocurrent), the different weight distributions may also result from an incorrect line shape of the TE line, which is in turn compensated by a change of the spectral weights.

5.4.3 Interpretation and assignment to transport processes

The room-temperature fit result, comprising the three resonances of DBs and CBT/VBT states, is consistent with earlier EDMR studies on a-Si:H. Dersch *et al.* [60] were the first to interpret the signal in terms of a spin-dependent recombination of charge carriers via DBs (see section 3.4.1). A recombination process is in accordance with the negative sign of the EDMR signal, indicating a current-decreasing process. Dersch *et al.* assumed a two-step recombination process: In a first step, an electron trapped in a CBT state tunnels into a nearby neutral (singly occupied) DB. This transition (e–D^0) is spin-dependent and explains the observation of the CBT and DB resonances. The second step, which completes the recombination cycle, is the capture of a hole into the intermediate D^- state (doubly occupied, negatively charged DB). Since this transition is not spin-dependent, Dersch *et al.* explained the presence of the VBT resonance with spin-dependent hopping of holes through the tail states towards the DB site, thereby promoting the recombination rate (see section 3.4.1 and fig. 3.5b).

This picture for spin-dependent recombination in a-Si:H satisfactorily explains the presence of all three resonances in the EDMR signal and has therefore been adopted throughout the literature. Nevertheless, it is not necessarily the only explanation for the observed signal. In fact, the spectral weights resulting from our fit to some extent contradict this recombination picture. Assuming that the spin-dependent recombination step is the initial e–D^0 transition, one would expect equal intensities of the CBT and DB resonances, since flipping either one of the two spins would induce the resonant transition. On the other hand, the intensity of the VBT line would be independent from the other two lines if the resonance originated from h–h transitions within the VBT states. From our fit, we obtain a set of intensity weights of about 0.30/0.14/0.57 for the CBT/VBT/DB lines, both for the X-band and for the 263 GHz spectrum. Certainly, the exact values are afflicted with a non-negligible degree of uncertainty, as intensity weights are very sensitive to slight changes in the line shape (*e. g.*, Gaussian or Lorentzian broadening functions). However, the fact that we obtain almost equal, independently fitted sets of weights for the X-band and 263 GHz spectra enhances the reliability of the results. Our results suggest that DB resonance is almost twice as large in intensity than the CBT line, which conflicts with the recombination picture of Dersch *et al.*

A possible alternative explanation could be that the spin-dependent recombination via DBs occurs in two different ways: Either, as proposed by Dersch *et al.*, an initial spin-dependent e–D^0 transition is followed by the capture of hole, or, vice versa, the initial step is a spin-dependent transition of a VBT hole into the neutral DB (h–D^0), completed by capturing an electron into the intermediate D^- state. In this picture, the intensities of the CBT and VBT lines would still be independent from each other, but the DB intensity would be expected to match the combined CBT and VBT line intensities, much closer to our experimental results. Our fit results thus speak for two independent spin-dependent

recombination processes of both CBT electrons and VBT holes via DB defects. Nevertheless, based on the EDMR spectrum alone, it is difficult to definitively choose between the two recombination models.

While the interpretation of the room-temperature signal in terms of spin-dependent recombination channels via DBs provides a solid explanation of the experimental data, the situation for the low-temperature case is less clear. The global fitting strategy revealed that the CBT and VBT resonances are present at both temperatures, whereas the DB line is only observed at room temperature. The positive signal sign at low temperature indicates a current-enhancing process. Since, at temperatures $T \lesssim 100\,\mathrm{K}$, charge-carrier transport in a-Si:H is dominated by hopping conduction within the band-tail states (see section 3.3.1), the observation of current-enhancing CBT and VBT resonances has commonly been assigned to spin-dependent hopping transitions *e*–*e* and *h*–*h* via the respective tail states [27, 69, 72, 77, 226].

The origin of the broad TE line, which we fitted with a simple Gaussian broadening function with a FWHM of 18 mT, remains elusive. Based on the unusually large field-independent line width, we will tentatively follow the assignment of previous studies to strongly dipolar coupled $S = 1$ states. A distribution of spin-spin distances and dipolar coupling strength can explain the observed line shapes in terms of a superposition of Pake patterns. It is tempting to assign the resonance to TEs formed by strongly coupled electron-hole pairs trapped in CBT and VBT states in close proximity, since the observed g-value is close to the arithmetic mean $(g_{\mathrm{CBT}} + g_{\mathrm{VBT}})/2 = (2.0044 + 2.0100)/2 = 2.0072$. The nature of the spin-dependent transport channel, however, remains unclear. Evidence for recombination channels of geminate triplet excitons has been obtains from photoluminescence spectrocopy [206, 210] (see section 3.3.2) and pulsed ODMR [246, 248]. Geminate-pair recombination, however, does not affect photoconductivity. Moreover, the TE line is observed as a current-enhancing signal, such that an excitonic recombination channel alone cannot explain the EDMR signal. Possible explanations include spin-dependent dissociation of strongly coupled geminate pairs or three-particle processes, *e. g.*, an Auger-recombination channel. Meier *et al.* [98] recently identified an Auger-like spin-dependent recombination process as the origin of similar EDMR signal in microcrystalline silicon (μc-Si:H). An excitonic EDMR signal has also been identified from ED-Rabi nutations on amorphous silicon nitride (a-$Si_{1-x}N_x$:H) [266]. Based on the data presented in this chapter, however, we can neither prove the excitonic nature of the TE line in a-Si:H, nor draw conclusions regarding a potentially similar origin as those $S = 1$ signals found in μc-Si:H or a-$Si_{1-x}N_x$:H. We will address this issue in chapter 6, where we present conclusive evidence for strongly coupled electron-hole pairs, based on a comprehensive PEDMR study carried out at low temperature.

A number of open question remain concerning the interpretation of the two EDMR signals observed at high and low temperature. However, the results discussed in this section clearly show that two different spin-dependent processes lead to the EDMR signals at different temperatures. In the section, we will investigate the transition between the two temperature regimes by analyzing EDMR signals recorded over the full temperature range from 10 K to room temperature.

5.5 TEMPERATURE DEPENDENCY

To understand the temperature dependency of the EDMR signal of a-Si:H, the PEDMR experiment conducted at $T = 10$ K and room temperature before was repeated at intermediate temperatures ranging from 30 K to 150 K. Due to a number of broken samples over the course of the measurements and the lack of further functioning a-Si:H EDMR film samples, the series of temperature-dependent PEDMR experiments could only be carried out at 263 GHz, such that no multifrequency data is available over the full temperature range.

5.5.1 Temperature-dependent pulsed-EDMR spectra

At each temperature, the two-dimensional time-field map was recorded by measuring the transient photocurrent change after the MW pulse as a function of the applied magnetic field. While in the previous sections we only used single field-domain slices of this two-dimensional signal for the spectral analysis, in the following we will make use of the entire time-dependent signal, aiming to seperate the different EDMR signal components based on their different dynamics. Therefor, fig. 5.5a exemplarily shows the full PEDMR signal map measured at $T = 40$ K. In fig. 5.5b, the photocurrent response at a magnetic field of 9374 mT ($g = 2.0045$) is shown, where the maximum EDMR signal is observed. This transient current signal has a positive maximum at $t = 0$ µs, immediately after the MW pulse, and a negative maximum of roughly equal amplitude at $t = 12.4$ µs, before

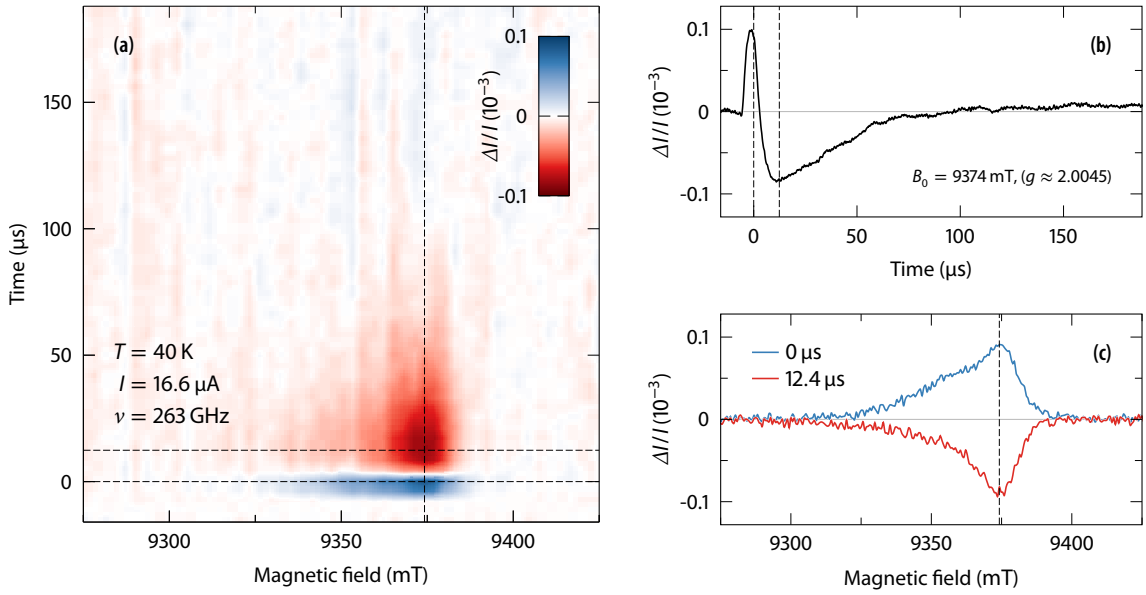

FIGURE 5.5 Field-swept PEDMR spectrum of a-Si:H recorded at a MW frequency of 263 GHz and $T = 40$ K. (a) Two-dimensional magnetic-field/time map recorded by measuring the transient current response after the MW pulse as a function of the applied magnetic field. The dashed lines mark the positions of maxima and minima, corresponding to the time- and field-domain slices shown in figs. b and c, respectively. (b) Transient photocurrent at $B_0 = 9374$ mT, where the maximum EDMR signal is observed. (c) Magnetic-field-domain slices at times $t = 0$ µs (blue) and $t = 12.4$ µs (red) after the pulse, where the maximum and mininum resonant current change is observed. Current values are relative to the absolute photocurrent ($I = 16.6$ µA).

decaying to equilibrium ($\Delta I/I = 0$). The field-domain cross sections through the signal map at these times are shown in fig. 5.5c. It is evident that the spectra corresponding to the positive (red) and negative (blue) maxima not only differ in sign, but also exhibit different line shapes. A qualitative comparison of these two spectra with the EDMR spectra at $T = 10$ K and room temperature indicates that the positive spectrum has a similar shape as the $T = 10$ K signal, while the negative signal resembles the room-temperature spectrum. Already from this visual analysis, it can be supposed that at an intermediate temperature of 40 K both spin-dependent processes coexist. Based on their different dynamics, PEDMR is able to separate the corresponding signals in the time domain.

To evaluate the EDMR signals at all intermediate temperatures, fig. 5.6 shows time- and field-domain signals at temperatures ranging from 10 K to room temperature. Instead of plotting the full signal maps, fig. 5.6a plots the integrated transient photocurrent change, obtained by integrating over the entire EDMR signal in field domain. These transients, containing the dynamics of all signal components, provide a more straightforward visualization of the temperature dependency than a comparison of the entire two-dimensional signals. At temperatures $T \leq 50$ K, the transient signals exhibit a positive maximum immediately after the MW pulse ($t = 0$ µs), followed by a negative maximum reached at times between 0.5 µs ($T = 295$ K) and 29 µs ($T = 10$ K), as marked by the red circles in fig. 5.6a. The corresponding field-domain EDMR spectra are shown in figs. 5.6b and c.

The transient signals in fig. 5.6a clearly show the transition from a current-enhancing

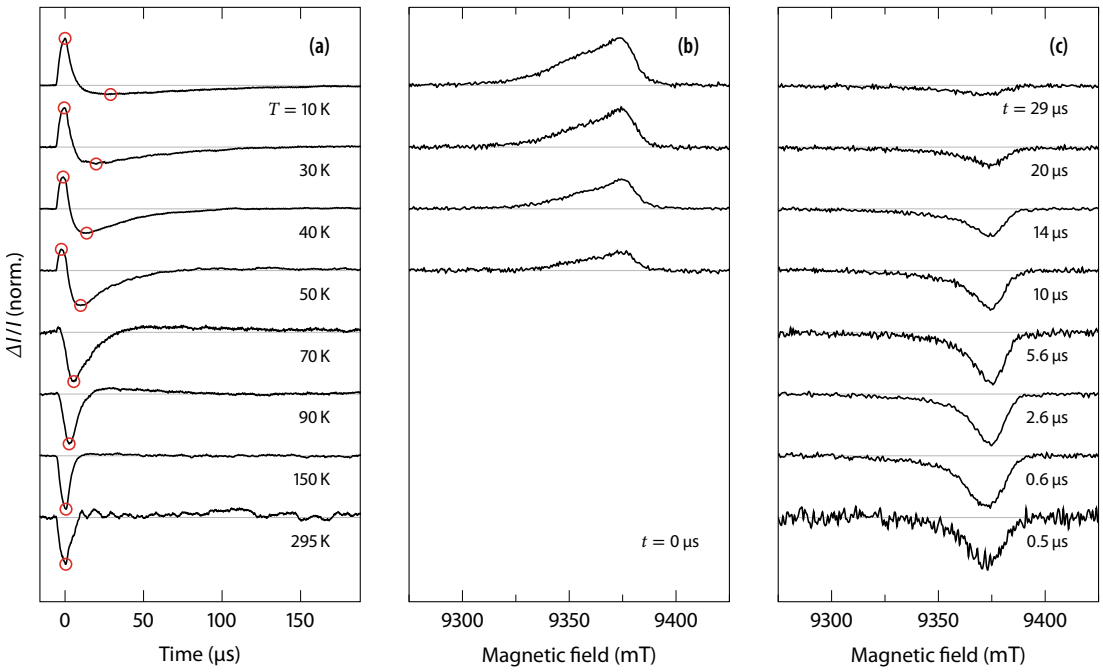

FIGURE 5.6 Temperature-dependent PEDMR spectra of a-Si:H recorded at a MW frequency of 263 GHz, recorded by measuring the transient current response after the MW pulse as a function of the applied magnetic field. (a) Integrated transient photocurrent reponse, obtained from integrating the two-dimensional signal map in magnetic-field domain. Signals are normalized to equal peak-to-peak amplitude. Red circles indicate the positive and negative maximum current changes, corresponding to the field-domain spectra shown in figs. b and c, respectively. (b) Magnetic-field-domain slices at times $t = 0$ µs after the MW pulse, where the maximum positive signal is observed. (c) Field-domain slices at times t after the pulse, as indicated, corresponding to the negative minima marked by the red circles in fig. a.

EDMR signal at $T = 10$ K to a purely current-quenching signal at $T \geq 150$ K. At temperatures $T \leq 50$ K, the initial positive current change is visible. The corresponding spectra in fig. 5.6b all exhibit a similar line shape, with a characteristic bulge on the low-field field of the peak ($B_0 \approx 9350$ mT), which, based on the fit results from section 5.4, indicate a contribution from the TE line (compare fig. 5.4b). This bulge is missing for the spectra in fig. 5.6c, corresponding to the negative maxima. Two different spin-dependent processes thus lead to the EDMR signals of a-Si:H: A current-enhancing process, dominating at low temperatures, outweighted by the current-quenching DB recombination process with increasing temperature. At intermediate temperatures ($T = 30$–50 K), where both processes appear to coexist, the positive signal decays on a faster timescale than the negative signal. Morevoer, with increasing temperature, the decay times of both signals shorten, which is evident from the transients in fig. 5.6a and the time points of the maximum negative current change listed in fig. 5.6c.

5.5.2 Time-domain spectral deconvolution

To further evaluate the temperature-dependent transition of the EDMR signal, we deconvolved the two-dimensional PEDMR signals in the time domain, by using the fit results from section 5.4. Therefor, we fitted a simulated spectrum to each field-domain slice of the signals, based on the parameters listed in tab. 5.1. Solely the spectral weights were varied, while all other parameters were kept fixed. Exemplarily, the resulting fits are shown in fig. 5.7a for selected field-domain slices of the spectrum recorded at $T = 40$ K. Repeat-

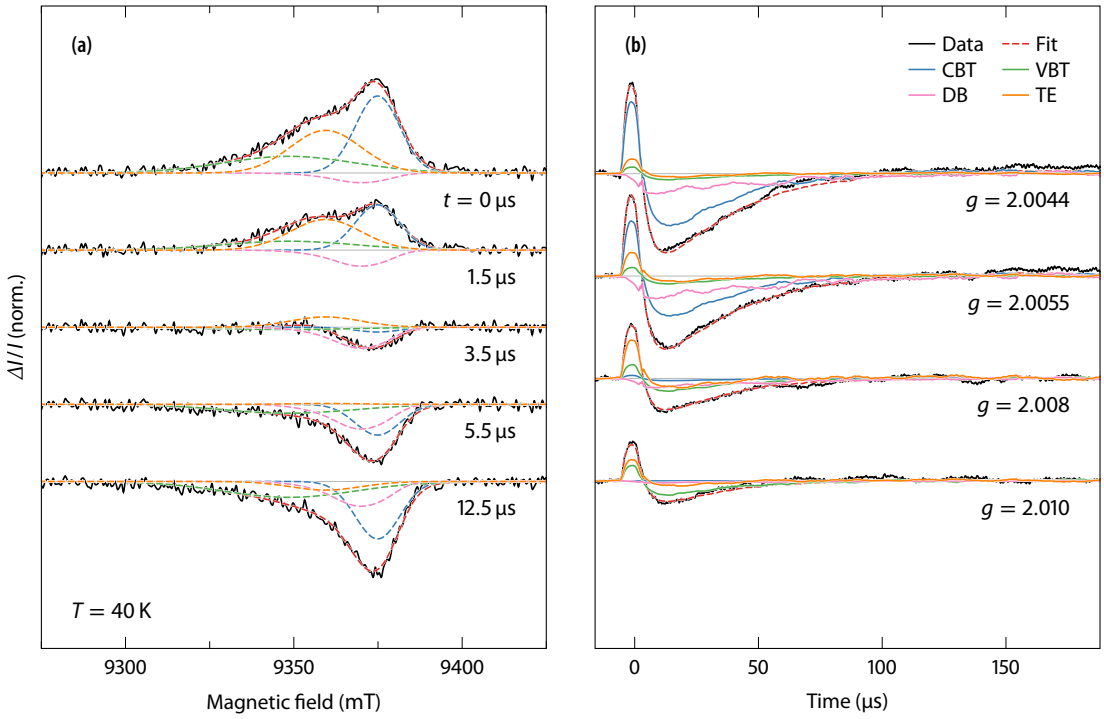

FIGURE 5.7 (a) Magnetic-field- and (b) time-domain cross sections of the $T = 40$ K two-dimensional PEDMR spectrum (fig. 5.5a) at different times t and g-values, as indicated. The dashed lines show the result of spectral least-squares fit that uses the spin-Hamiltonian parameters of tab. 5.1 and leaves only the spectral weights as fitting parameters (see text for further details).

ing this fit over the entire time range yields component-wise PEDMR transients, as shown in fig. 5.7b. This method allows to separate the time-domain signals of the overlapping spectral contributions and study their dynamics apart from each other.

Two-dimensional fits, following the above-described procedure, were carried out for all 263 GHz PEDMR spectra between $T = 10$ K and room temperature. To compare the dynamics of the different line components, fig. 5.8 plots the transients obtained by integrat-

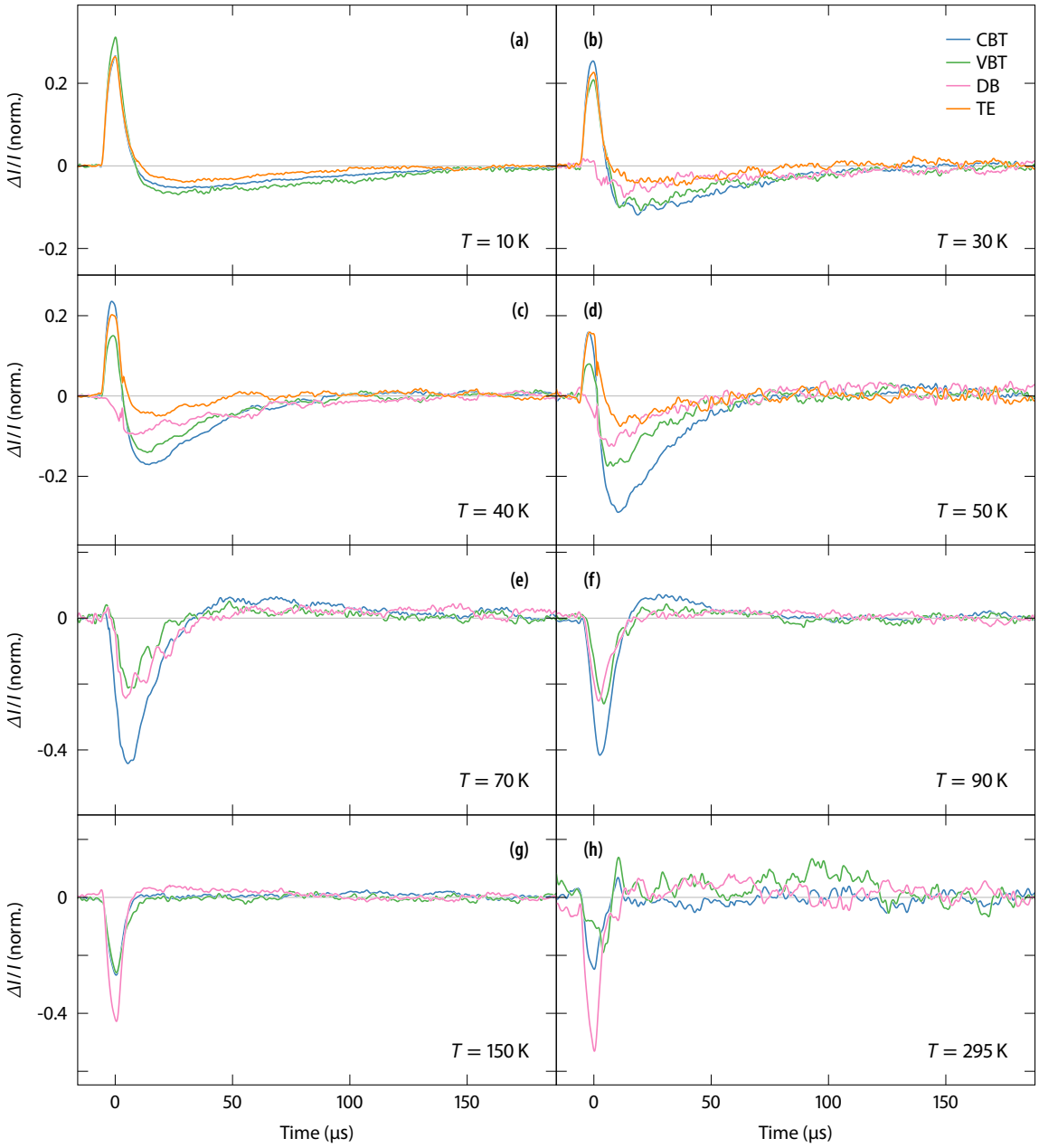

FIGURE 5.8 Time-domain deconvolution of the 263 GHz PEDMR signals as a function of temperature. The plotted transients correspond the integrated peak intensities of the different spectral components, obtained by fitting all field-domain slices with the spin-Hamiltonian parameters listed in tab. 5.1 (see text for further discussion). The transients are normalized to a summed peak-to-peak amplitude of one.

ing the simulated spectra of the individual spectral components along the magnetic-field axis. The resulting curves can be considered as the transient PEDMR signal associated with the particular resonance lines of our fitting model.

At $T = 10\,\mathrm{K}$ (fig. 5.8a), the two-dimensional PEDMR signal is a superposition of the CBT/VBT lines and the TE resonance. The deconvolved transients exhibit approximately equal amplitude, consistent with the result of the multifrequency fit. Interestingly, also the dynamics of the three resonances exhibit no perceptive difference. All three transients follow a biexponential decay with a fast positive ($\tau \leq 6\,\mu\mathrm{s}$) and a slow negative decay ($\tau \approx 50\,\mu\mathrm{s}$). Note that the fast decay might be limited by the time resolution of the current-detection system, which was set to low-pass-filter time constant of 5 µs during the experiment. While this setting was chosen to increase the SNR and enable reasonable data-acquisition times, it limits the information that can be gained by comparing absolute values of decay rates.

At high temperatures ($T \geq 150\,\mathrm{K}$, figs. 5.8g and h), the spectrum is fitted with the tail-state and the DB resonances. Again, we do not observe any marked difference between the signal dynamics. The relative intensities of the deconvolved transients reproduce an important observation, which we already made from the multifrequency fit: The intensity of DB resonance is significantly larger than the CBT and VBT intensities. As discussed above, this finding indicates that both e–D^0 and h–D^0 transitions may contribute to spin-dependent recombination.

The intermediate temperatures ($T = 30$–$90\,\mathrm{K}$, figs. 5.8b–f) represent the transition regime between low- and high-temperature transport. The TE resonance is observed up to temperatures of about 50–70 K, whereas the DB intensity gradually increases with rising temperature. Note that also the decay rates of all resonance increase with temperature. Therefor, we cannot exclude that the TEs are involved in spin-dependent transport also at higher temperature, but might not be detectable with the given time resolution.

An interesting observation is made by comparing the negative-transient intensities at intermediate temperatures ($T = 50$–$90\,\mathrm{K}$) to those in the high-temperature regime ($T = 150$–$295\,\mathrm{K}$). Whereas at high temperatures, the DB resonance exhibits the largest intensity, stronger quenching contribution are found for the CBT and VBT lines in the intermediate-temperature regime. At these temperatures, electronic transport is still dominated by hopping conduction within the tail states (see section 3.3.1). Therefor, this finding could be explained by spin-dependent hopping of both electrons and holes towards DB sites, both enhancing the recombination rate. Alternatively, a different spin-dependent recombination channel (*e. g.*, direct distant-pair recombination of CBT electrons and VBT holes) might compete with DB-mediated recombination at these temperatures, giving rise to an additional EDMR quenching signal. In the scope of this work, we did not carry out sufficient experiments in the intermediate-temperature region to fully resolve the origin of the observed intensity dependence. Despite these remaining unclarities concerning the entire temperature dependency of the EDMR signal, the results in fig. 5.8 clearly visualize the transition from low-temperature spin-dependent current enhancing to the room-temperature current-quenching recombination signal. The distinctively different line shapes at low and high temperatures and the opposing signal signs indicate that different spin-dependent transport and recombination channels dominate at different temperatures.

5.6 SUMMARY AND CONCLUSION

Using magnetic-field-/frequency- and temperature-dependent PEDMR experiments, we were able to distinguish two fundamentally different spin-dependent processes. By means of a global least-squares fitting routine, we could reproduce the experimental data with simulated spectra and thereby identify paramagnetic species involved in the current-limiting processes.

At room temperature, we assign the spin-dependent current decrease to a non-radiative recombination channel via DB defects. We find EDMR resonances of DBs as well as of electrons and holes trapped in CBT and VBT states, respectively. This observation is consistent with earlier interpretations in terms of spin-dependent tunneling of CBT electrons into neutral DBs, followed by the capture of a hole. The presence of a VBT resonance is explained by spin-dependent hopping of holes towards the recombination site, promoting the recombination rate. However, we note that also the inverse scenario, that is, an initial spin-dependent h-D^0 transition, can explain the data. Based on our findings in this chapter, we cannot finally decide on either of the two recombination mechanisms.

The current-quenching EDMR signal observed at low temperatures exhibits the EPR signatures of CBT electrons and VBT holes as well as a third broad resonance at $g = 2.0077$ with a field-independent line width of 18 mT. The CBT and VBT resonances have previously been explained with spin-dependent hopping conduction. This assignment is reasonable, considering that the current-enhancing signal is observed at temperatures $T \lesssim 50$ K, where transport in a-Si:H is dominated by tail-state hopping conduction. The broad line is tentatively assigned to dipolar coupled $S = 1$ excitons, following the argument of previous authors (see section 3.4.3). This assertion, however, cannot be conclusively proven based on the EDMR spectra alone. Further experiments are thus required to elucidate the nature of the underlying charge-transport mechanism, which will be presented in the next chapter.

The experiments presented in this chapter were conducted on undoped a-Si:H film samples. This suggests that the observed spin-dependent transport and recombination channels are intrinsic features of a-Si:H. This finding lays the basis for experiments on fully processed devices incorporating a-Si:H, and facilitate the separation of processes that, for instance, are observed at interfaces to c-Si layers in state-of-the-art heterojunction solar cells. In the next chapter, we will take our investigations one step further by studying the low-temperature process in more detail, based on PEDMR experiments on a-Si:H *pin* solar cells.

CHAPTER 6

Low-temperature transport in a-Si:H solar cells

In this chapter, we present the results of a comprehensive X-band PEDMR study, conducted on a-Si:H pin solar cells at $T = 10$ K. Using electrically detection nutation experiments and the first-time observation of a half-field resonance in the EDMR spectrum of a-Si:H, we unambiguously prove the $S = 1$ character of the $g = 2.008$ resonance. We show that the underlying paramagnetic state is a strongly dipolar and exchange coupled exciton with an average localization length of 5 Å, involved in a spin-dependent three-particle Auger-like recombination process. By complementing EDMR with transient-EPR (TREPR) experiments, we further demonstrate that light-generated triplet excitons can also be detected in the EPR spectrum of a-Si:H. Following the dynamics of the TREPR signal, allows to directly correlated excitons to the fundamental charge-separation mechanism in a-Si:H.

6.1 INTRODUCTION

The previous chapter has revealed two characteristic EDMR signals of instrinsic a-Si:H that lead to resonant quenching and enhancing of the photocurrent at room temperature and cryogenic temperatures, respectively. In this chapter, we will take a deeper look into the low-temperature signal, aiming to unravel the underlying transport process. In addition, we go a step further into the direction of real applications of a-Si:H by conducting EDMR experiments on operating *pin* solar cells.

As has become evident in the previous chapter, a thorough understanding of the electronic channels causing the EDMR signals cannot be developed solely based on the identification of paramagnetic states. More specific experiments are required, for instance, to clarify the origin of the broad $g = 2.008$ resonance and the associated transport mechanism. A broad range of experiments have arisen from the rapid evolution of PEDMR techniques over the course of the last 15 years, expanding the scope of information that can be gathered from EDMR spectroscopy. Considering the immense diversity of pulsed-EPR detection sequences and the fact that many of these experiments could potentially be translated into equivalent EDMR experiments, this development is far from being completed. A particular breakthrough was the electrical detection of Hahn spin echoes [78], which allows for a straightforward setup of new PEDMR sequences based on existing PEPR experiments (see section 2.5.7). This capability has subsequently been exploited to electrically detect spin relaxation based on echo-decay [267] and inversion-recovery [268] experiments, or to measure spin-spin interactions by ED-ELDOR [22] and ED-DEER [24] or electrically detected hyperfine spectroscopy [23, 25].

In the following, we will employ apply PEDMR toolbox to a-Si:H and thereby gain detailed insight into the charge-transport mechanisms at low temperatures. We will find that the EDMR signature of a-Si:H *pin* solar cells features the same characteristic shape

observed for the intrinsic material. We will then employ electrically detected nutation experiments to separate to resonances stemming for $S = 1/2$ doublet states and $S = 1$ triplet excitons. This is the first direct proof for an excitonic origin of the broad $g = 2.008$ resonance. In the course of these experiments, we developed a novel PEDMR detection scheme based on the phase-inverted echo-amplitude-detected nutation (PEANUT) sequence [35], well established for measuring nutation-frequency-correlated EPR spectra. Moreover, we utilize electrically detected ELDOR (ED-ELDOR) experiments to reveal the nanoscopic transport process that causes the excitonic EDMR resonance.

Finally, we will complement the PEDMR study with transient-EPR (TREPR) experiments and density-functional-theory (DFT) calculations. By means of TREPR, we will, for the first time, detect the characteristic signatures of spin-correlated electron-hole pairs and triplet excitons in the EPR spectrum of a-Si:H. We will demonstrate that these light-generated paramagnetic states are directly involved in the charge-separation mechanism of a-Si:H. *Ab-initio* DFT calculations will further provide structural models for the paramagnetic states involved in low-temperature spin-dependent transport and thereby corroborate our experimental results.

6.2 MATERIALS AND METHODS

Experimental setups as well as and the sample design and preparation procedures are summarized chapter 4. Here, we will only briefly describe the specific properties of a-Si:H *pin* solar cell samples and discuss experimental details, such as magnetic-field calibration results, relevant for the experiments present in this chapter. Other than in the previous chapter, we will employ a broad range of pulsed EDMR techniques to elucidate the origin of the low-temperature EDMR signal of a-Si:H. The experimental details and data-processing strategies for these techniques, some of which represent novel PEDMR detection schemes, will be discussed in the respective sections of this chapter.

6.2.1 Samples

Amorphous-silicon *pin* solar cells were prepared by PECVD, as described in section 4.1.1, resulting in a total batch of 18 samples. The individual samples were compared based on the current-voltage characteristics and room-temperature CWEDMR signatures. All samples exhibited qualitatively similar behavior, with slightly varying solar-cell parameters (open-circuit voltage, short-circuit current, filling factor, series and shunt resistance) and EDMR signal intensities. Based on the SNR of the EDMR signal, a single sample was selected for the EDMR measurements presented in this chapter.

Figure 6.1a shows the room-temperature current-voltage characteristics of the selected sample. We do not explicitly report solar-cell parameters, since these *I*-*V* curves have not been recorded under standard test conditions (AM1.5 illumination, 25 °C, four-point-probe connections), but with the sample inserted and contacted in the X-band EDMR setup. Nevertheless, the room-temperature *I*-*V* curve exhibit characteristic features of *pin* solar cells. Under reverse-bias conditions ($V < 0$), a photocurrent is observed under illumination ($I_{ph} \approx -45\,\mu A$). In this regime, the solar-cell current is dominated by drift, which is independent of the bias voltage. The increasing current observed with increased reverse bias, both in the dark and under illumination, is due to shunts that are presumably

induced when cutting the sample by means of laser scribing. Under low forward-bias conditions ($V \lesssim 0.6$ V), the dark current is predominantly due to charge-carrier diffusion and recombination of electrons and holes in the space-charge region. This leads to the characteristic shoulder observed in the dark *I-V* curve. At higher forward-bias voltages, charge-carrier drift outweighs diffusion due to the strong injection of electrons and holes [68, 238], giving rise to an exponential increase of the solar-cell current, both in the dark and under illumination. In this regime, the current is limited by the series resistance, both of the a-Si:H emitter and the electrical contacts.

The low-temperature *I-V* curve is shown in fig. 6.1b. Although the sample still exhibits solar-cell characteristics, the shape of the *I-V* curve is significantly different with respect to room temperature. Much lower currents are observed due to the low conductivity of a-Si:H at low temperatures (see chapter 3). Also the open-circuit voltage is decreased, as a result of the low charge-carrier density.

The EDMR experiments presented in this chapter were conducted under illumination and short-circuit ($V = 0$) or slight reverse-bias ($V > -0.3$ V) conditions. In this regime, the current is predominantly due to drift induced by the electric field over the *pin* junction. The observed photocurrents were between 0.5 µA and 3 µA. Note that the precise absolute current values at low temperatures were not reproducible after temperature changes in between different measurement series. This is potentially due to the fragile electrical contacts to the EDMR sample, which were established using silver paint. After each heating/cooling cycle (*e. g.*, heating up to room temperature and cooling back down to $T = 10$ K), the contact resistance is slightly different, such that equal measurement conditions (temperature, illumination and bias voltage) may lead to different currrents. (In fact, very fast temperature changes, *e. g.*, shock-freezing from room to liquid-helium temperature will almost certainly lead to contact breaking.) Even though absolute and relative current changes can thus not be compared quantitatively in between measurements, EDMR line shapes were unaffected by thermal cycling or replacement of electrical contacts.

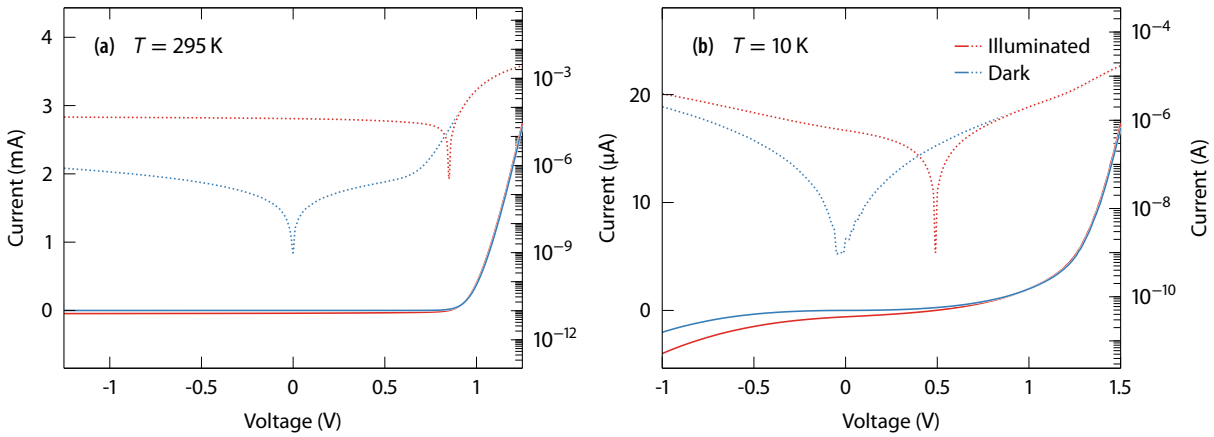

FIGURE 6.1 (a) Room-temperature and (b) low-temperature current-voltage characteristics of the a-Si:H *pin* solar-cell sample used for the EDMR experiments presented in this chapter. The curves were recorded with the sample mounted in the EDMR setup. Blue curves were measured in the dark and red curves under illumination with the same white-light source used for the EDMR experiments. Dotted lines plot the *I-V* curves on a logarithmic scale. All EDMR experiments were carried out at $T = 10$ K under illumination and short-circuit ($V = 0$) or slight reverse-bias ($V > -0.3$ V)) conditions.

6.2.2 EDMR experiments

All EDMR experiments presented in this chapter were carried out at X-band (see section 4.2.1 for details concerning the experimental setup) and $T = 10$ K. Other than in the previous chapter, the range of experiments comprises not only CW and single-pulse measurements of EDMR spectra, but also a number of more advanced PEDMR techniques, such as electrically detected nutation experiments or ED-ELDOR measurements. These techniques will be described in detail in the particular sections of this chapter.

For accurate determination of g-values and microwave-field amplitudes B_1, the amplitudes of B_0 and B_1 need to be calibrated at the position of the EDMR sample. The external magnetic field B_0 was measured during all measurements using an NMR teslameter (see section 4.2). However, this measurement was taken outside of the EPR resonator, resulting in a field offset on the order of a few Gauss with respect to the actual sample position. Therefor a small crumb of 2,2-diphenyl-1-picrylhydrazyl (DPPH) was glued onto the glass substrate, in direct vicinity of the EDMR sample. The g-value of DPPH ($g = 2.0036(2)$ [269]) was then used to calibrate the magnetic-field axis, based on a CWEPR measurement. The CWEPR spectrum of DPPH is shown in fig. 6.2a. The field offset $\Delta B_0 = B_0^{\text{measured}} - B_0^{\text{actual}}$ was extracted by least-squares fitting the experimental data with a simulated spectrum using the EasySpin [43] library. The fit parameters were ΔB_0 and the field-independent line width of a convolutional Voigtian broadening function. The resulting fit is marked by the red curve in fig. 6.2a and resulted in a field offset of 0.20(4) mT. This value was used for calibrating B_0 throughout this chapter.

Similarly, the microwave magnetic-field amplitude B_1 needs to be calibrated, in order to determine, for instance, nutation frequencies obtained from electrically detected Rabi-nutation experiments. Calibration of B_1 was achieved by recording FID-detected Rabi nutations at the center of the DPPH resonance as a function of B_1. We will discuss the procedure of Rabi-nutation measurements at this point, since a detailed description, although for the case of electrical detection, can be found in section 6.4. Nutation frequency were read off from the time-domain Rabi traces by calculating the FFT spectra. The resulting nutation frequencies are plotted in fig. 6.2b. Due to the direct proportion-

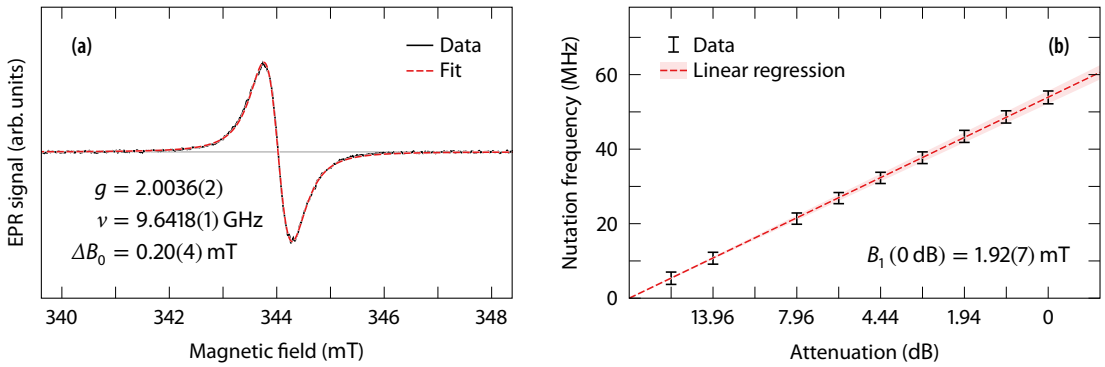

FIGURE 6.2 Calibration of B_0 and B_1 using the EPR signal of DPPH. (a) Continuous-wave EPR spectrum of DPPH. The red curve shows a simulated spectrum obtained from a least-squares fit, with a fixed isotropic g-value and a field-independent Voigtian line shape, yielding a measure for the field offset ΔB_0. (b) Nutation frequencies obtained by FID-detected Rabi nutation measurements in the center of the DPPH resonance as a function of the microwave attenuation. Linear regression yields a calibration of B_1 at 0 dB.

ality of the on-resonance nutation frequencies of $S = 1/2$ spin states to B_1 ($\Omega = \gamma B_1$), the obtained values can be used to calibrate B_1 at a given microwave power. The value of B_1 at a microwave attenuation of 0 dB was dermined by linear regression, as shown in fig. 6.2b, resulting in a value of 1.92(7) mT. Both calibration measurements were repeated several times over the course of the experiments, yielding reproducible results.

6.3 LOW-TEMPERATURE PULSED EDMR

The starting point for the study presented in this chapter is the low-temperature ($T = 10$ K) X-band PEDMR spectrum of an a-Si:H *pin* solar cell, which is shown is fig. 6.3. The two-dimensional spectrum, obtained by measuring $\Delta I(t)$ after a MW pulse of length $t_P = 40$ ns as a function of the applied magnetic field, is shown in fig. 6.3a. A maximum positive current change $\Delta I/I = 3.5\,\%$ is detected at a magnetic field of 342 mT ($g \approx 2.005$) and a time $t = 1.3$ µs after the pulse (dashed lines in fig. 6.3a). The corresponding time- and field-domain cross sections are shown in figs. 6.3b and c, respectively.

Both the transient current response and the field-domain spectrum closely resemble the equivalent PEDMR signals of undoped a-Si:H films, discussed in the previous chapter. In section 5.4, we fitted the X-band and 263 GHz spectra of a-Si:H film samples using a global multifrequency fit approach. At $T = 10$ K, the spectra could be simulated as a superposition of CBT and VBT resonances centered at $g = 2.0044$ and $g = 2.010$, respectively, as well as the additional broad triplet-exciton (TE) resonance at $g \approx 2.008$. The latter was tentatively assigned to dipolar coupled excitons, following the argument of previous authors (see section 3.4.3). Assuming the same superposition of CBT, VBT and TE lines to produce the EDMR response of a-Si:H *pin* solar cells, we used the parameters listed in tab. 5.1 to fit the spectrum shown in fig. 6.3b. Only spectral weights and a magnetic-field offset parameter, which takes into account the lack of a proper field calibration in chapter 5, were used as fit parameters. The resulting fit is included in fig. 6.3b. As in section 5.5.2, we used the individual CBT, VBT and TE line shapes obtained from the fit to deconvolve the entire PEDMR spectrum in the time domain. Therefor, we fitted each field-domain slice as a superposition of these three resonances, only leaving the amplitudes as fit parameters. The resulting integrated component-wise peak intensities are plotted in the insert of fig. 6.3c, normalized to a summed amplitude of one.

The spectral fit in fig. 6.3b is in good agreement with the experimental spectrum, although slight deviations are found on both sides of the narrow central peak, as can be seen from the residual plot (gray line in fig. 6.3b). A similar discrepancy had been found when fitting for the multifrequency fit of the a-Si:H-film spectra (compare fig. 5.4a). Since the fit residuals appear symmetric with respect to the TE line, this had been interpreted as an indicator of an incomplete fitting model, when approximating the TE line with a simple Gaussian line. The time-domain deconvolution in terms of the three fit components, shown in the insert of fig. 6.3c, exhibits different relative amplitudes for the three resonances, other than for the a-Si:H films, where we found roughly equally distributed weights (compare fig. 5.8a). However, the two-dimensional fit in section 5.5.2 was performed based on 263 GHz spectra, such that this difference may be a result of an incorrect TE line shape, leading to different relative weights at X-band and 263 GHz. Besides the different relative amplitudes, the transients associated with the three resonances, how-

ever, exhibit very similar dynamics. If scaled to equal amplitude, the traces shown in fig. 6.3c almost match each other. The same observation had been made for the respective deconvolved transients of a-Si:H films. In view of the uncertainties regarding the line shapes used for the spectral deconvolution, we can thus neither draw conclusion regarding different spin-dependent transport channels associated with the resonances, nor separate their spectra in the time domain.

When comparing the maximum resonant current changes, one notices an increased signal intensity for *pin* solar cells compared to the films. Both absolute and relative current changes at X-band are larger by factors of about ten and four, respectively. It is tempting to interpret this observation in terms of the different electronic transport properties of bulk a-Si:H and *pin* structure. However, we have already noted in section 6.2.1 that absolute photocurrents exhibit little reproducibility at low temperatures due to the strong temperature dependency of the contact resistance. Therefor, it is doubtful, how much information can be extracted from the magnitudes of $\Delta I/I$ at low temperature and we refrain from interpretations based on signal-intensity comparison.

The PEDMR spectrum of a-Si:H *pin* solar cells can be fitted with the same spectral

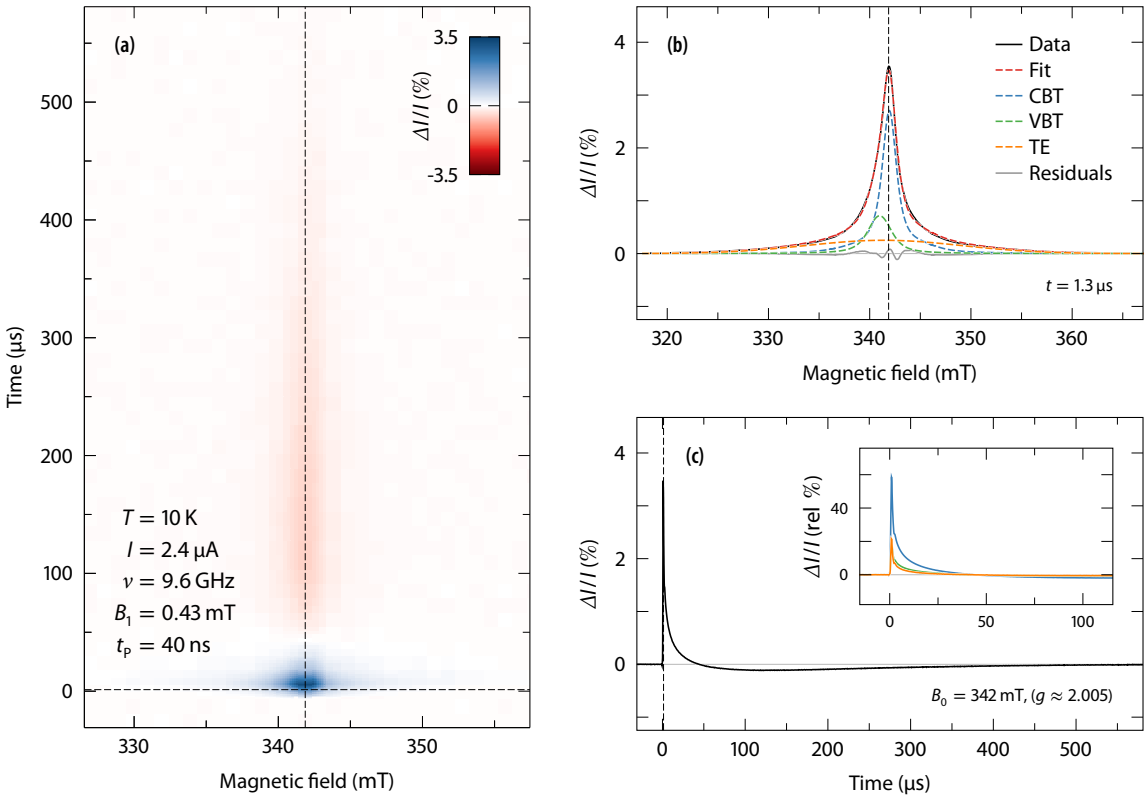

FIGURE 6.3 Low-temperature ($T = 10$ K), field-swept X-band PEDMR spectrum of an a-Si:H *pin* solar cell recorded under illumination and short-circuit conditions ($V_B = 0$ V). (a) Two-dimensional magnetic-field/time map recorded by measuring the transient current response after the MW pulse as a function of the applied magnetic field. Current values are relative to the absolute photocurrent ($I = 2.4$ µA). The dashed lines mark the positions of maxima and minima, corresponding to the time- and field-domain slices shown in figs. c and b, respectively. (b) Magnetic-field-domain slice at $t = 1.3$ µs after the pulse, where the maximum EDMR signal is observed. Dashed lines mark a least-squares fit using the results from section 5.4 (see text for discussion). (c) Transient photocurrent at $B_0 = 342$ mT. The insert shows the relative integrated fit-component intensities as a function of time.

components as the spectra of undoped a-Si:H films. We thus conclude that the same spin-dependent, current-enhancing transport mechanism causes the low-temperature EDMR signal in both types of samples. This finding allows to associate the signal with processes within the intrinsic bulk a-Si:H layer of the *pin* structure and renders strong contributions from the *p*- and *n*-doped μc-Si:H contact layers unlikely. Therefor, the interpretation of the resonance in terms of spin-dependent transport channels follows the same arguments discussed in section 5.4.3. By comparison with LEPR studies on a-Si:H (see section 3.2.3), we assign the central resonances to electrons and holes trapped in CBT and VBT states. Spin-dependent *e*–*e* and *h*–*h* hopping transitions via nearby tail states (see section 3.4.2) has prevailed as an obvious explanation throughout previous low-temperature EDMR studies [27, 69, 72, 77, 226], as hopping conduction has been identified as the dominating charge-transport mechanism at temperatures $T \lesssim 100$ K (see section 3.3.1).

The spin-dependent transport channel associated with the TE resonance, on the other hand, is yet unknown. The assignment to dipolar coupled electron-hole pairs, forming excitonic triplet states ($S = 1$), was proposed by Brandt and Stutzmann [244] based on the large field-independent line width. They explained the broad Gaussian line shape with a distribution on spin-spin distances and dipolar coupling strengths owing to the network disorder in a-Si:H. This would produce an approximate Gaussian shape instead of the well-resolved Pake pattern that is typically observed for dipolar coupled $S = 1$ states. Alternatively, Lips *et al.* [27] proposed an explanation in terms of exchange coupled *e*–*h* pairs, based on the observation that $g_{\mathrm{TE}} \approx (g_{\mathrm{CBT}} + g_{\mathrm{VBT}})/2$. A broad distribution of *e*–*h* distances would yield a distribution of *g*-values that could also explain the line shape. Note that both interpretations were solely based on the unusually large X-band line width and by excluding other broadening mechanisms such as lifetime or MW-power broadening, hyperfine interactions or *g*-tensor anisotropy [244]. Limited to CWEDMR detection, an unambigious proof of $S = 1$ triplet states, at the time, was not possible.

Modern PEDMR techniques offers a broad range of experiments that allow to gain further insight into the origin of the resonance. In the following, we will exploit these capabilities, aiming to understand the origin of the low-temperature EDMR signal and assign it to spin-dependent transport channels in a-Si:H.

6.4 ELECTRICALLY DETECTED TRANSIENT NUTATIONS

The introduction of PEDMR by Boehme and Lips [19] in 2003 paved the way for a variety of electrically detected experiments based on the coherent manipulation of spin pairs involved in a spin-dependent transport or recombination process. The basis for this is the detection of electrically detected Rabi (ED-Rabi) nutations [20, 75]. Rabi-nutation experiments allow to discriminate between different spin states—for example, $S = 1/2$ and $S = 1$ species—based on their different nutation frequencies (see sections 2.2.2 and 2.5.6). Consequently, ED-Rabi experiments are able to provide evidence for the excitonic ($S = 1$) nature of the TE resonance.

6.4.1 Electrically detected Rabi nutations

The principle of an ED-Rabi nutation experiment is sketched in fig. 6.4a. The charge ΔQ, obtained from integrating the transient current response $\Delta I(t)$ after a single MW pulse,

is recorded as a function of the pulse length t_P. As discussed in section 2.5.6, the charge ΔQ will oscillate at the Rabi-nutation frequency

$$\Omega_{ij} = \sqrt{(\alpha_{ij}\nu_1)^2 + (\nu_{ij} - \nu)^2}, \quad \text{with} \quad \alpha_{ij} = \sqrt{1 \pm \sin 2\phi}, \tag{6.1}$$

where $\nu_{ij} - \nu$ is the resonance offset between the constant MW freuency ν and the transition frequency ν_{ij} of the transition $|i\rangle \rightarrow |j\rangle$ and $\alpha_{ij}\nu_1 = \alpha_{ij}\gamma B_1/2\pi$ is the on-resonant nutation frequency. The coefficient α_{ij} corresponds to the off-diagonal entries of the spin Hamiltonian (see section 2.5.6) and depends on the mixing angle ϕ between the spin-pair partner, given by

$$\phi = \frac{1}{2}\arctan\left(\frac{J - D}{\Delta\nu}\right), \tag{6.2}$$

where J and D denote the exchange and dipolar coupling strength, respectively, and $\Delta\nu$ the Larmor-frequency separation $\Delta\nu = |\nu_a - \nu_b|$ between the two spins. For the simplest case of a weakly coupled spin-1/2 pair ($\Delta\nu \gg |J - D|$) and selective excitation of only one of the two spins ($\Delta\nu \gg \nu_1$), one obtains $\phi \rightarrow 0$ and $\alpha_{ij} = 1$, that is, a Rabi frequency $\Omega = \nu_1$, as expected for the EPR transition of a single $S = 1/2$ spin. In case of a non-selective excitation, where both spins are excited simultaneously ($\Delta\nu \ll \nu_1$), the observed nutation frequency will be the sum $\Omega = \Omega_a + \Omega_a \approx 2\nu_1$ (spin locking, see section 2.5.6).

In the case of strongly dipolar coupled spin pairs ($|D| \gg \Delta\nu$), as it has been assumed

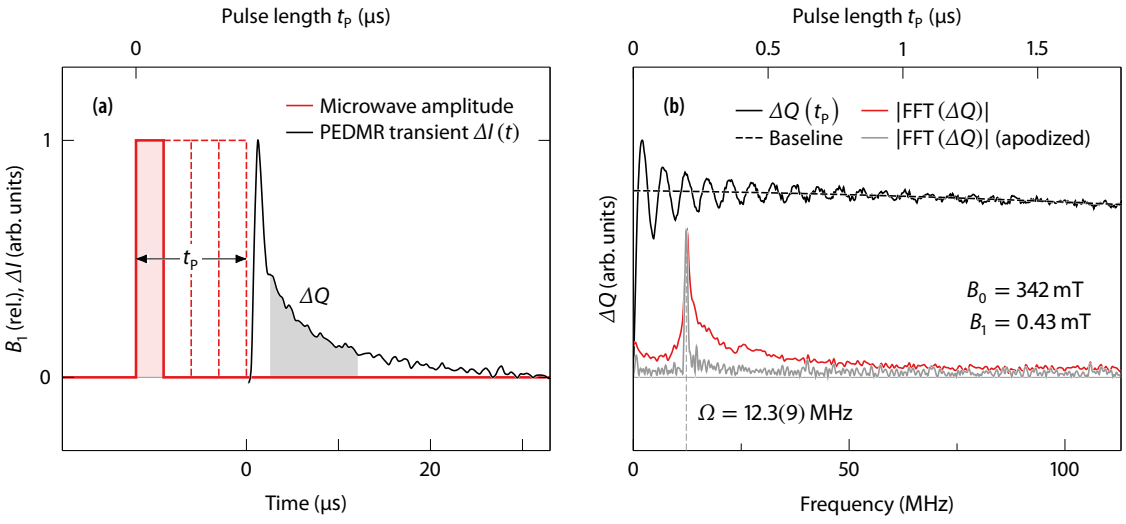

FIGURE 6.4 **(a)** Schematic illustration of an ED-Rabi nutation experiment. The resonant transient current change $\Delta I(t)$ is integrated over a constant time window after a single MW pulse, yielding a net charge ΔQ. During the pulse, spins precess about the effective magnetic field at the Rabi-nutation frequency Ω (eq. 6.1), determining the spin-pair symmetry and the resulting amplitude of ΔI at the end of the pulse. Recording ΔQ as a function of the pulse length t_P thus provides a measure of the Rabi oscillations of paramagnetic states involved in a spin-dependent transport or recombination process. **(b)** Exemplary ED-Rabi nutation trace (black) recorded as illustrated in fig. a at constant magnetic field B_0 and microwave-field amplitude B_1. The non-modulated background signal is subtracted by means of fitting a polynomial baseline (dashed line). Nutation frequencies Ω are read off from the frequency-domain FFT spectra (red). Side-bands, stemming from a broad distribution of off-resonance nutation frequencies, can be suppressed by apodization of the raw ED-Rabi trace with an appropriate window function (*e. g.*, a Hamming window, resulting in the gray FFT spectrum), allowing for a more accurate determination of nutation frequencies.

to be the origin of the broad TE line, one obtains $(1 - \sin 2\phi) \rightarrow 2$ for the dominant $|T_{\pm}\rangle \rightarrow |S\rangle$ transitions between pure triplet and singlet states. Accordingly, the expected nutation frequency is $\Omega = \sqrt{2}\nu_1$, which resembles the Rabi frequency expected for the allowed EPR transitions of an $S = 1$ state, considering that

$$\Omega(m_S,\, m_S + 1) = \sqrt{[S(S+1) - m_S(m_S+1)]\nu_1^2 + (\nu_{ij} - \nu)^2} \qquad 6.3$$

for an EPR transition between substates $|S, m_S\rangle$ and $|S, m_S + 1\rangle$ [36]. Accordingly, ED-Rabi nutation experiments allow to discrimnate between spin-dependent processes via weakly coupled spin-1/2 pairs and strongly coupled pairs, effectively forming an excitonic $S = 1$ state. Under the assumption that the narrow central peak of the a-Si:H EDMR spectrum stems from $S = 1/2$ CBT and VBT states, while the broad TE line originates from a $S = 1$ state, we measured ED-Rabi nutations at two magnetic fields B_0, where, based on our fitting model, either $S = 1/2$ or $S = 1$ resonances are expected to be on resonance (342 mT and 347 mT, respectively).

Figure 6.4b shows a single ED-Rabi trace $\Delta Q(t_P)$ measured at $B_0 = 342$ mT and a MW amplitude $B_1 = 0.43$ mT. For data analysis, the non-modulated background, which yields a strong low-frequency component in the FFT spectrum, is subtracted by fitting a polynomial baseline (dashed line in fig. 6.4b). The frequency-domain spectrum is obtained by FFT (red trace). To read off nutation frequencies, the time trace was apodized using a Hamming window function before calculating the FFT spectrum. The apodization suppresses the broad sidebands of the frequency peaks, as can be seen from the resulting FFT spectrum, shown by the gray trace in fig. 6.4b. The sidebands stem from the nutations of spins that are off-resonant, and are especially pronounced for the case of strong disorder [82], as it is the case for a-Si:H. The application of a window function thus significantly reduces the FWHM of the frequency peaks, allowing a more accurate determination of nutation frequencies.

In figs. 6.5a and b, ED-Rabi traces and FFT spectra are plotted for the two selected resonance positions. The traces were measured as a function of B_1, in order to analyze the observed nutation frequencies in terms of eq. 6.1. Already by comparing the FFT spectra recorded at equal B_1, it is evident that different nutation frequencies are observed at the two resonance fields. To compare them quantitatively, the nutation frequencies read off from the FFT spectra in figs. 6.5a and b are plotted as a function of B_1 in fig. 6.5c. On resonance, the nutation-frequency coefficient α can be obtained from a linear fit through the origin, according to eq. 6.1. Linear regression yields $\alpha = 1.03(4)$ at $B_0 = 342$ mT and $\alpha = 1.47(8)$ at $B_0 = 347$ mT.

The central part of the EDMR spectrum is thus clearly dominated by weakly coupled $S = 1/2$ pairs with $\Omega = \nu_1$. This finding is consistent with the assignment to spin-dependent hopping transport via CBT and VBT states. At $B_0 = 347$ mT, where based on our fitting model only the broad TE resonance is observed, we find $\Omega \approx \sqrt{2}\nu_1$. As discussed above, this frequency indicates strongly coupled pairs forming an excitonic state with $S = 1$. While similar results have been obtained for the similar broad resonance in ODMR, the observation of the characteristic $S = 1$ nutation frequency is the first direct proof for a contribution of excitonic states to the EDMR spectrum of a-Si:H.

Note that solely based on the nutation frequency, it is not possible to conclude on the type and the strength of the coupling within the spin-pair. Numerical simulations by

Limes *et al.* [84] have shown that a Rabi frequency $\sqrt{2}\nu_1$ will be observed both in the case of strong dipolar coupling ($|D| \gg \Delta\nu$, $J = 0$), but also if both dipolar and exchange coupling are present with either D or J being dominant ($|D - J| \gg \Delta\nu$). Only for the case of pure exchange coupling ($|J| \gg \Delta\nu$, $D = 0$), a different Rabi frequency of $2\nu_1$ would be observed. The observation of $\alpha = \sqrt{2}$ thus indicates a dipolar coupled pair, although the simultaneous presence of exchange coupling cannot be excluded.

Besides the $\sqrt{2}\nu_1$ and ν_1 components, a close look on the ED-Rabi traces recorded at $B_0 = 342$ mT (fig. 6.5a) further reveals small peaks at $2\nu_1$. For instance, this can be seen from the FFT spectrum obtained at $B_1 = 0.61$ mT, which is plotted in fig. 6.6a. Glenn *et al.* [82] provided analytical expressions to reproduce the frequency-domain Rabi spectra of weakly coupled $S = 1/2$ pairs, containing frequency components at $\Omega = 0$ (F_0), ν_1 (F_1) and $2\nu_1$ (F_2).

$$F_0(\Omega) = \left[\frac{\nu_1}{8\delta_0^2}\right] \exp\left[-\frac{\Omega^2}{2\delta_0^2}\right] K_0\left[\frac{\Omega\nu_1}{\delta_0^2}\right], \qquad \text{for } \Omega > 0, \tag{6.4a}$$

$$F_1(\Omega) = \left[\frac{\nu_1^3}{4\delta_0^2\Omega\sqrt{\Omega^2 - \nu_1^2}}\right] \exp\left[-\frac{\Omega^2 - \nu_1^2}{2\delta_0^2}\right] f\left[\frac{\nu_1^2}{2\delta_0^2}\right], \qquad \text{for } \Omega > \nu_1, \tag{6.4b}$$

$$F_2(\Omega) = \left[\frac{2\nu_1^4}{\delta_0^2\Omega^2\,(\Omega + 2\nu_1)}\right] \exp\left[-\frac{\Omega^2 - 4\nu_1^2}{4\delta_0^2}\right] G\left[\frac{(\Omega - 2\nu_1)^2}{4\delta_0^2}\right], \qquad \text{for } \Omega > 2\nu_1, \tag{6.4c}$$

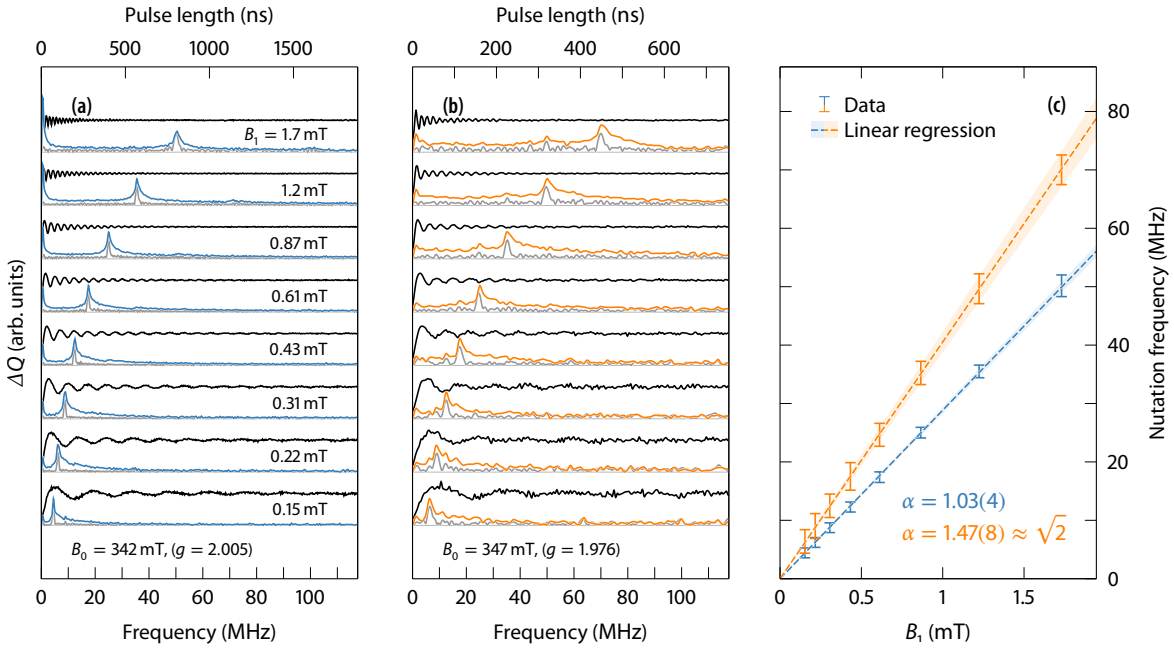

FIGURE 6.5 Electrically detected Rabi nutations measured at two different resonant positions, where EDMR signals stemming from $S = 1/2$ (blue) and $S = 1$ (orange) spin states are expected. (a, b) Baseline-corrected ED-Rabi time traces (black) and FFT magnitude spectra of the raw Rabi traces (color-coded for to the two resonance positions) and after apodization with a Hamming window (gray). Amplitudes are scaled to arbitrary units for visualization purposes. (c) Nutation frequencies, read from the FFT spectra in figs. a and b, as a function of B_1. Dashed lines show a linear-regression fit, yielding the nutation-frequency coefficients α. Shaded areas mark the confidence interval of the regression.

with

$$f(x) = \sqrt{\pi/x} - \pi \exp(x)\,\mathrm{erfc}(\sqrt{x}), \quad \text{and}$$
$$G(x) = \pi \exp(-x/2)\, I_0(x/2),$$

where δ_0 is a disorder parameter, denoting the RMS value of Larmor separations, and $I_\alpha(x)$ and $K_\alpha(x)$ are the modified Bessel functions of the first and second kind. We used these expressions to fit the frequency-domain ED-Rabi traces from fig. 6.5a, as exemplarily shown in fig. 6.6a.[1] Figure 6.6b plots the resulting amplitude ratios of the F_2 peak ($\Omega = 2\nu_1$) with respect to the F_1 peak ($\Omega = \nu_1$) as a function of B_1. Although the obtained peak ratios deviate between 5 % and 20 %—certainly also due to the low relative amplitudes of the F_2 peaks with respect to SNRs—, clearly no correlation is observed between the amplitude of the F_2 peak and B_1. Instead, the amplitude ratio F_2/F_1 appears to be be independent of B_1 with an average value of about 11(5) %, as indicated in fig. 6.6b.

This result allows to conclude on the origin of the $\Omega = 2\nu_1$ component. As discussed above, a Rabi component of twice the $S = 1/2$ frequency is commonly observed for the case of spin-locking, where both spins of a weakly coupled pair are excited simultaneously. However, in this case, the relative intensity would increase with B_1 and vanish for lower MW powers [93]. Since we observe the $2\nu_1$ component even at the lowest excitation fields, we assign its origin to exchange-coupled spin pairs. Numerical simulations by Limes *et al.* [84] predict a $2\nu_1$ component for the case of strong exchange coupled, both with and without simultaneous dipolar coupled (compare fig. 3 in ref. [84]).

In summary, ED-Rabi nutation measurements have proven the coexistence of both weakly coupled $S = 1/2$ pairs and strongly coupled excitonic $S = 1$ states leading to the EDMR signal of a-Si:H. The observation of a $\sqrt{2}\nu_1$ frequency components indicates strong dipolar coupling, while the simultaneous existence of a B_1-independent $2\nu_1$ component

[1] Note that $F = F_0 + F_1 + F_2$ only described the real parts of the FFT spectrum (see ref. [82]). Thus only the real traces, $\Re[\mathrm{FFT}(\Delta Q)]$, were used for the fits, as shown in fig. 6.6a.

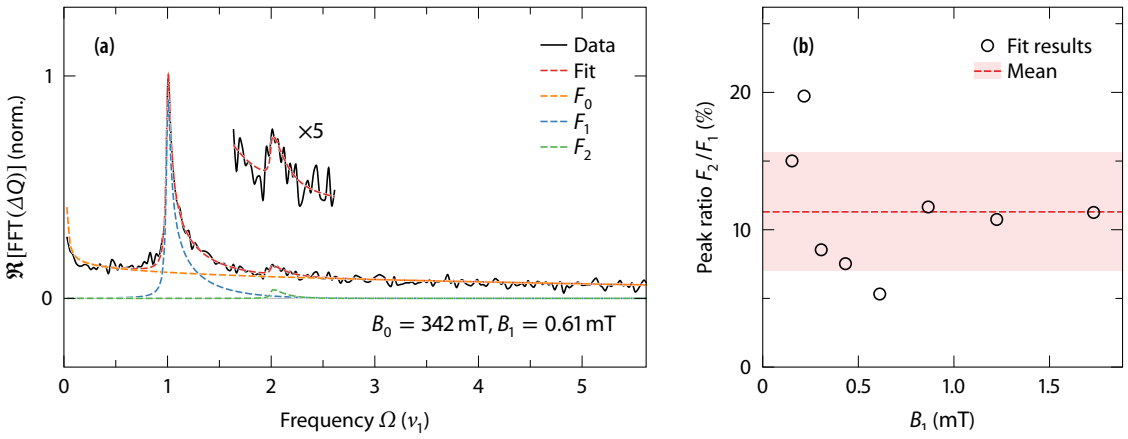

FIGURE 6.6 **(a)** Frequency spectrum of the ED-Rabi trace recorded at $B_0 = 342$ mT ($g \approx 2.005$) and $B_1 = 0.61$ mT shown in fig. 6.5a. The real part of the FFT is shown together a the result of a least-squares fit based on eq. 6.4. The red curve displays the real part of $F = F_0 + F_1 + F_2$. **(b)** Peak-amplitude ratios F_2/F_1 as a function of B_1 obtained from equivalent least-squares fits of all ED-Rabi traces shown in fig. 6.5a. The relative amplitude of the F_2 ($\Omega = 2\nu_1$) peak appears to be independent of B_1, as indicated by the arithmetic mean (dashed line and shaded area, marking the mean and standard deviation, respectively).

suggests additional strong exchange coupling as the origin of the $S = 1$ states. In the next sections, we will extend the nutation experiments into the magnetic-field domain, to finally assign these spin states to the spectral components of the EDMR line.

6.4.2 Field-resolved Rabi nutations

In the previous section, ED-Rabi nutations supplied evidence that both doublet ($S = 1/2$) and triplet ($S = 1$) states contribute to spin-dependent transport in a-Si:H. The different resonance positions where nutation frequencies $\Omega = \nu_1$ and $\Omega = \sqrt{2}\nu_1$ were detected allow to tentatively assign $S = 1$ states to the broad TE component of the EDMR spectrum. However, the strong overlap of spectral line components complicates an unambigious separation between resonances associated with different spin species.

A specific strength of pulsed magnetic-resonance techniques is the capability of disentangling overlapping signals by correlating spectral components to a second dimension, introduced by an additional experimental parameter. This second dimension can, for instance, be an electron-spin relaxation time (inversion-recovery- or echo-decay-filtered EPR), the g-value (electron-Zeeman EPR), a nuclear frequency (ENDOR-induced EPR) or an orientation dependency (anisotropy-resolved EPR). For PEDMR, we have already used the time domain to deconvolve the spectrum based on different signal dynamics (section 5.5.2). In this section, we will use the Rabi-nutation frequency to separate the EDMR spectra stemming from different spin states. For this purpose, ED-Rabi nutation experiments as a function of the magnetic field are presented. In the next section, we will then introduce a novel PEDMR detection scheme that is based on the phase-inverted echo-amplitude-detected nutation (PEANUT) experiment, used for measuring nutation-frequency-resolved EPR spectra [35].

Figure 6.7 shows the two-dimensional Rabi-nutation spectrum, recorded at a B_1-field amplitude of 0.58 mT. As in the previous section, ED-Rabi nutations were measured by recording the charge ΔQ obtained from boxcar-integrating the PEDMR transient $\Delta I(t)$ as a function of the MW pulse length t_p (see fig. 6.4). The resulting time-domain map is shown in fig. 6.7a. Note that the non-modulated background of the individual Rabi traces has been removed, as in the previous section, by subtracting a second-order polynomial baseline (see fig. 6.4b). To translate the Rabi spectrum into nutation-frequency-resolved EDMR spectra, the time-domain Rabi traces are converted into the frequency domain by calculating the FFT amplitudes. The resulting ED-Rabi nutation-frequency spectrum (fig. 6.7b) exhibits three characteristic features at distinct frequencies $\alpha = \Omega/\nu_1$ of 1, $\sqrt{2}$ and 2, as marked by the dotted lines. The EDMR spectra obtained as field-domain cross sections of fig. 6.7b at these frequencies, are plotted in figs. 6.7c–e.

The shape of the spectrum at $\Omega = \nu_1$ (fig. 6.7c), indicative of weakly coupled $S = 1/2$ pairs, will be discussed in more detail in the following section, based on the results of ED-PEANUT experiments. It will be shown there, that this line is a superposition of the resonances of CBT and VBT electrons and holes. This is indicated by the dashed lines in fig. 6.7c, marking the respective g-values. The $\Omega = \nu_1$ component can thus be assigned to CBT and VBT states.

Both the ν_1 and the $2\nu_1$ peak exhibit pronounced off-resonance parabolas, as indicated by the dashed lines in fig. 6.7b. They are due to spins excited at a resonance offset $\nu_0 - \nu$ (eq. 6.1). These parabolas, while consistent with the theoretical predictions, complicate the analysis of the nutation-frequency-correlated spectra at $\sqrt{2}\nu_1$ and $2\nu_1$, owing to the

superposition with the parabola of the ν_1 peak. This can be seen from the central overlapping features in figs. 6.7d and e. The off-resonance features can be partly suppressed by means of apodization, as shown in the previous section (fig. 6.4b). However, the choice of the window function strongly influences the shape of the resulting field-domain spectra, such that we refrained from applying a window function for the spectral analysis.

Even though the spectral shape of the spectrum at $\Omega = \sqrt{2}\nu_1$ cannot be resolved due to the overlapping signal, it is evident from fig. 6.7d that the spectrum resembles the broad shape of the TE line. The spectrum can be fitted with a Gaussian line with a FWHM of 19 mT, centered at $g = 2.008$. Comparing this to the earlier results obtained from the multifrequency fit in section 5.4 ($g_{\mathrm{TE}} = 2.0077$, $\Delta B_{\mathrm{TE}} = 18.1\,\mathrm{mT}$), shows that an almost identical line shape is found for the $\sqrt{2}\nu_1$ nutation-frequency spectrum. This allows to clearly assign the broad TE line to strongly coupled excitonic $S = 1$ states.

The feature observed observed at $\Omega = 2\nu_1$ was assigned to strongly exchange coupled to

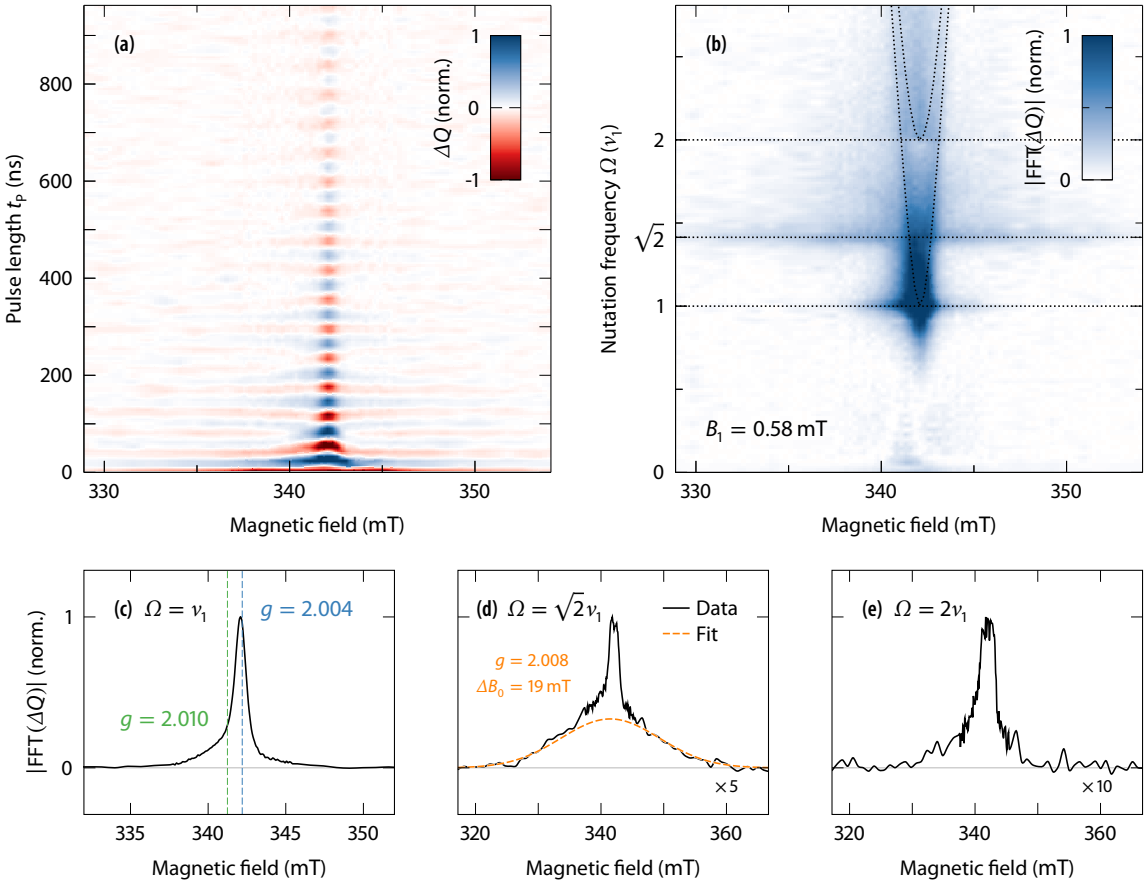

FIGURE 6.7 **(a)** Two-dimensional X-band ED-Rabi nutation spectrum measured by recording the charge ΔQ obtained from integrating the current response $\Delta I(t)$ after a single MW pulse of length t_p as a function of the applied magnetic field. **(b)** Frequency-domain amplitude spectrum, calculated from the FFTs of the time-domain Rabi traces. Both spectra are normalized to a maximum absolute amplitude of one. **(c–e)** Magnetic-field-domain ED-Rabi spectra at nutation frequencies $\Omega = \nu_1$, $\sqrt{2}\nu_1$ and $2\nu_1$, respectively. The spectra are cross sections through the two-dimensional FFT map, as indicated by the dashed lines in fig. b. For presentation purposes, the spectra in figs. d and e have been scaled, as indicated. Dashed lines in fig. c mark the expected resonance positions of CBT- and VBT-trapped electrons and holes. The dashed curve in fig. d displays the result of least-squares fit of the broad TE line with a Gaussian line shape.

pairs, due to the absence of an amplitude dependency on B_1. Owing to the strong overlap with the $\Omega = \nu_1$ off-resonance parabola, the spectral shape in fig. 6.7e cannot be analyzed. Nevertheless, the appararent narrow parabola appearing at $\Omega = 2\nu_1$ is consistent with numerically simulated nutation patterns for the case of strong exchange coupling (compare fig. 3 in ref. [84]).

By measuring field-resolved ED-Rabi nutations, we were able to split apart resonances stemming from weakly coupled $S = 1/2$ pairs and strongly coupled $S = 1$ states. Thereby, we could clearly ascribe the origin of the broad TE line to strongly coupled triplet excitons. However, the spectra in figs. 6.7c–e demonstrate a major disadvantage of the ED-Rabi detection scheme. Since nutations are recorded by changing the length of the MW pulse, the excitation bandwidth cannot be controlled during the experiment. Instead, each Rabi trace is recorded with a gradually narrowing bandwidth, which is reflected in the decay of the oscillations (although, the decay is also a result of disorder-induced incoherence). Changing B_1 instead of t_P is technically not feasible, since the high-power MW attenuator cannot be controlled on a timescale required for a Rabi-nutation experiment. The only way to decrease the excitation bandwidth in an ED-Rabi measurement is thus to decrease B_1 during the entire experiment, which, however, results in a lower SNR. An immediate consequence is the broadening of nutation-frequency-correlated spectra detected by field-resolved ED-Rabi and the strong overlap with off-resonance signals. An improved EPR detection scheme has been proposed by Stoll *et al.* [35], and is referred to as *phase-inverted echo-amplitude-detected nutation (PEANUT)*. While this method has been successfully employed to measure nutation-frequency-resolved EPR spectra, it has not yet been applied to electrically detected measurements. In the next section, we will fill this gap and carry out an ED-PEANUT experiment to measure improved nutation-frequency-correlated EDMR spectra of a-Si:H and validate the conclusions drawn from ED-Rabi experiments.

6.4.3 Electrically detected PEANUT

The pulse sequence for the PEANUT experiment is schematically shown in fig. 6.8a. In essence, the experiment is a two-pulse electron-spin echo experiment with an initial $\pi/2$ pulse of length t_P and a refocussing pulse of length T applied after a dephasing time τ, to record an echo at a time $2\tau + T$ after the initial pulse. However, the usual refocussing π pulse pulse is replaced with a high-turning-angle (HTA) nutation pulse. The HTA pulse is divided into two parts of lengths t and $T - t$ with opposite MW phases 0 and π. During time t, $\boldsymbol{B}_1$ is oriented in $+x$ direction and the spin-magnetization vector precesses about the effective field vector $\boldsymbol{B}_{\text{eff}}$ at a frequency Ω, with

$$\boldsymbol{B}_{\text{eff}} = B_1 \boldsymbol{e}_x + \left(\frac{2\pi\delta\nu_0}{\gamma}\right)\boldsymbol{e}_z \quad \text{and} \quad \Omega = \sqrt{(\alpha\nu_1)^2 + (\delta\nu_0)^2}, \tag{6.5a}$$

where $\delta\nu_0 = \nu_0 - \nu$ denotes the resonance offset. After the phase shift at time t, $\boldsymbol{B}_1$ points in $-x$ direction, such that the same precession will occur, however, about an effective field

$$\boldsymbol{B}'_{\text{eff}} = -B_1 \boldsymbol{e}_x + \left(\frac{2\pi\delta\nu_0}{\gamma}\right)\boldsymbol{e}_z. \tag{6.5b}$$

The MW-phase shift at time t results in a partial refocussing of spin packets precessing at frequencies $\Omega \neq \alpha\nu_1$, either due to resonance offsets or inhomogeneity of B_1, to a rotary

echo, which is maximum at $t = T/2$ [30, 35]. This refocussing is detected by the primary spin echo, formed at a time τ after the HTA pulse. A single PEANUT trace is detected by varying the phase-inversion time t, while keeping the pulse length T constant.

The motion of the magnetization vectors of individual spin packets during the nutation pulse is a complicated function of the initial non-equilibrium state after the evolution period τ and the ratio between $2\pi\delta\nu_0/\gamma$ and B_1, which determines the precession axis and frequency (eq. 6.5). Therefor, a visualization using Bloch-sphere trajectories does not provide much insight. However, an analytical expression for the EPR signal at time $2\tau + T$, resulting from the magnetization M_y of a given spin packet with resonance offset $\delta\nu_0$, has been given by Stoll *et al.* [35]:

$$S_y(t) \propto c_2^{\mathrm{c}} \cos\left[2\Omega\left(t - \frac{T}{2}\right)\right] + c_2^{\mathrm{s}} \sin\left[2\Omega\left(t - \frac{T}{2}\right)\right] + c_1^{\mathrm{c}} \cos(\Omega t) + c_1^{\mathrm{s}} \sin(\Omega t) + c_0. \qquad 6.6$$

The prefactors are determined by B_1 and $\delta\nu_0$, the pulse lengths t_{P} and T of the preparation and the nutation pulse, respectively, and the evolution time τ. Explicit expressions can be found in ref. [35].

The c_2 terms describe the modulation of the rotary-echo amplitude at frequency 2Ω

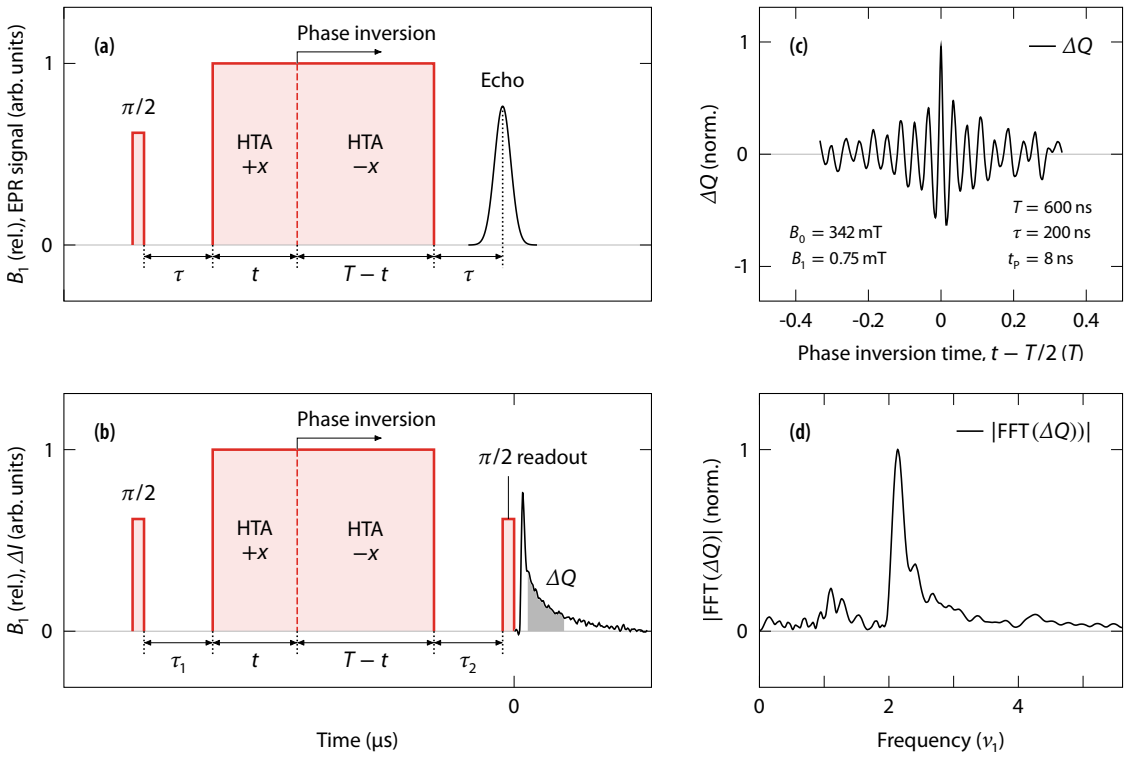

FIGURE 6.8 **(a)** Schematic illustration of the pulse sequence employed for the PEANUT experiment, according to ref. [35] (see text for discussion). **(b)** Modified ED-PEANUT sequence using an additional $\pi/2$ readout pulse to project *xy*-plane spin magnetization into spin-pair symmetry. The integrated charge ΔQ of the transient current response after the readout pulse yields a measure of the PEANUT echo amplitude. **(c)** Exemplary ED-PEANUT trace recorded at constant $B_0 = 342\,\mathrm{mT}$ ($g \approx 2.005$) by measuring ΔQ as a function of the HTA-pulse phase-inversion time t over a range $T/6 \leq t \leq 5T/6$. **(d)** Magnitude FFT spectrum of the ED-PEANUT trace shown in fig. c.

as a function of the phase-inversion time t. The doubling of the nutation frequency is a result of the phase inversion, as illustrated schematically in fig. 6.9. The constant term c_0 results from magnetization that is locked along $\boldsymbol{B}_{\text{eff}}$ and hence does not evolve during the HTA pulse. Essentially, the c_0 component is equivalent to a spin-locked echo [30]. It can be removed from the signal by subtracting the mean value from the PEANUT time trace. The c_1 components stem from magnetization that is locked along $\boldsymbol{B}_{\text{eff}}$ during either the $+x$ or $-x$ period of the HTA pulse and evolve during the other part of the pulse. Accordingly, these components exhibit the single nutation frequency Ω. However, only off-resonance spins contribute to these components ($c_1^{\text{c}} = c_1^{\text{s}} = 0$ for $\delta\nu_0 = 0$ [35]). Since the c_1 signals are maximum at the edges of the time traces ($t \to 0,\ T$), while the c_2 rotary echo is maximum at $t = T/2$, the former can be suppressed by setting a time window that records only the central part of the PEANUT trace.

An exemplary (ED-)PEANUT time trace, recorded in the range $T/6 \leq t \leq 5T/6$ is shown in fig. 6.8c. The resulting FFT spectrum in fig. 6.8d contains a small peak at the single frequency $\Omega = \nu_1$ and a larger contribution at the double frequency 2Ω, corresponding to the rotary echo of $S = 1/2$ states. A constant baseline has been subtracted from the PEANUT trace in fig. 6.8c, which cancels the c_0 term, as be seen from the FFT spectrum. The time window used for the phase-inversion times t further suppresses the c_1 components, while allowing to enhanced the SNR of the c_2 peak due to the saving of data-acquisition time required for a single PEANUT trace.

The principal advantage of the PEANUT scheme with respect to conventional Rabi-nutation experiments stems from the constant length T of the nutation pulse, which allows to control the excitation bandwidth of a PEANUT measurement. In a Rabi experiment, the length of the nutation pulse controls both the flip angle and the excitation window. For PEANUT, the frequency window for spins that contribute to the signal is set by the length of the preparation pulse t_{P}. Using different B_1 strengths for the preparation and the HTA pulse (as indicated by the different pulse amplitudes in fig. 6.8a), renders high nutation frequencies and selective narrow-band excitation possible at the same time. Further benefits include the refocussing of B_1-field inhomogeneities due to the phase inversion of the HTA pulse, and the absence of relaxational broadening, en-

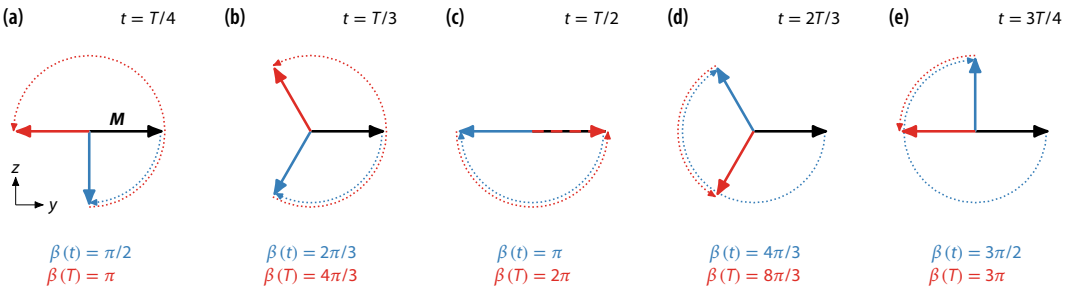

FIGURE 6.9 Schematic illustration of the motion of the magnetization vector $\boldsymbol{M}$ of a spin packet with $\delta\nu_0 = 0$ for different phase-inversion times $T - t$, using the simplified example of a PEANUT nutation pulse of length $T = 2\pi/\Omega$. After the $\pi/2$ preparation pulse, the spin system is in a non-equilibrium state, with $\boldsymbol{M}$ oriented along the y-axis (black arrow). The dotted lines indicate the trajectory of $\boldsymbol{M}$ during the $+x$ pulse of length t (blue) and the inverted $-x$ of length $T - t$ (red). The resulting orientations of $\boldsymbol{M}$ at times t and T are indicated by the blue and red arrows, corresponding to total effective flip angles $\beta(t)$ and $\beta(T)$, respectively. The doubling of $\beta(T)$ with respect to $\beta(t)$ illustrates the effective nutation frequency of 2Ω during the PEANUT nutation pulse.

hancing the resolution of PEANUT measurements [30, 35].

While the PEANUT scheme has been widely used to disentangle EPR spectra of different transitions in the nutation-frequency domain, electrically detected PEANUT have not yet been carried out. Nevertheless, as pointed out in section 2.5.7, pulse sequences for echo-detected EPR can be easily translated into equivalent EDMR excitation schemes, bearing in mind the different observables: EPR directly probes the spin magnetization in the *xy*-plane, while in EDMR, the spin-to-charge conversion is sensitive to the spin-pair symmetry in terms of singlet- and triplet-state content. To convert transversal magnetization into spin-pair symmetry, an additional $\pi/2$ "EDMR-readout" pulse is required, which projects the spin-echo coherence M_y onto the z-axis, that is, back into singlet or triplet eigenstates of the spin pair [78, 95, 268]. For the PEANUT sequence, this is illustrated in fig. 6.8b, which depicts the modified pulse sequence for detecting ED-PEANUT traces. The entire spin echo at time $\tau_2 = \tau_1$ can be detected electrically by recording the integrated charge ΔQ as a function of τ_2. The integrated echo intensity as a function of the HTA-pulse phase-inversion time t then yields the ED-PEANUT trace.

Note that the full echo-detection scheme thus required a two-dimensional experiment. Especially when adding a third dimension, as in case of field-resolved ED-PEANUT, recording the entire echo becomes too time-consuming. Thus, in practice, single-point detection is used, by solely recording ΔQ after a readout pulse at $\tau_2 = \tau_1$. The PEANUT signal is thereby only recorded on the maximum echo amplitude, which drastically reduces the data-acqusition time.

In the scope of this work, we did not explore the dependence of ED-PEANUT traces on the B_1 strength or pulse-sequence parameters T, t_p or τ. Detailed experimental and theoretical investigations concerning the parameter selection for PEANUT measurements can be found in ref. [35]. However, we employed two-dimensional field-resolved ED-PEANUT to measure enhanced nutation-frequency-correlated EDMR spectra, aiming to separate the signal contribution stemming from $S = 1/2$ pairs and $S = 1$ states by their different nutation frequencies.

6.4.4 Nutation-frequency-correlated ED-PEANUT spectra

Figure 6.10 shows the two-dimensional ED-PEANUT spectrum obtained by recording single time traces as a function of the applied magnetic field. Single ED-PEANUT traces were acquired using pulse lengths of 128 ns for the preparation and readout $\pi/2$ pulses, a dephasing time $\tau = 256$ ns and a HTA-pulse length of 1.2 µs. In addition to the ED-PEANUT sequence shown in fig. 6.8b, a two-step phase cycle ($\pm\pi/2$) is employed on the final readout pulse. This allows to limit the detection to the projected echo amplitude by cancelling both incoherent background signals and superimposed transient EDMR signals created by the individual MW pulses.

The $\pi/2$-pulse length t_p was set based on the resulting pulse bandwidth. The selected pulse length corresponds to an excitation window of about $1/t_p = 8$ MHz $\simeq 0.3$ mT. Since this a well below the line widths of the EDMR resonances, selective excitation is ensured, preventing power broadening of the obtained EDMR spectra. The corresponding B_1 amplitude was set to 0.13 mT. Since high nutation frequencies are desired to achieve optimum resolution in the frequency domain, the highest possible microwave power (attenuation 0 dB) was used for the HTA nutation pulse, yielding $B_1 = 1.92$ mT. In practice, the use of different B_1 amplitudes for different pulses within a single pulse sequence was

realized by utilizing different pulse channels of the MPFU. Sioce the high-power attenuator cannot be controlled at a sufficiently fast time scale, two sets of $\pm x$ channels were calibrated to different pulse amplitudes to match the required B_1 amplitudes (see section 4.2.1). Further, the amplitudes and phases of each set of $\pm x$ channels were carefully adjusted to equal amplitude and opposite phase to assure accurate phase inversion of the HTA pulse and correct phase and amplitude relations for phase cycling.

Compared to the single ED-PEANUT trace shown in fig. 6.8c, the time window for the phase inversion was further decreased to $T/3 \leq t \leq 2T/3$. While still comprising the central part of the PEANUT trace, where the rotary echo is detected, the overlapping single-frequency components c_1 are further suppressed. At the same time, an additional

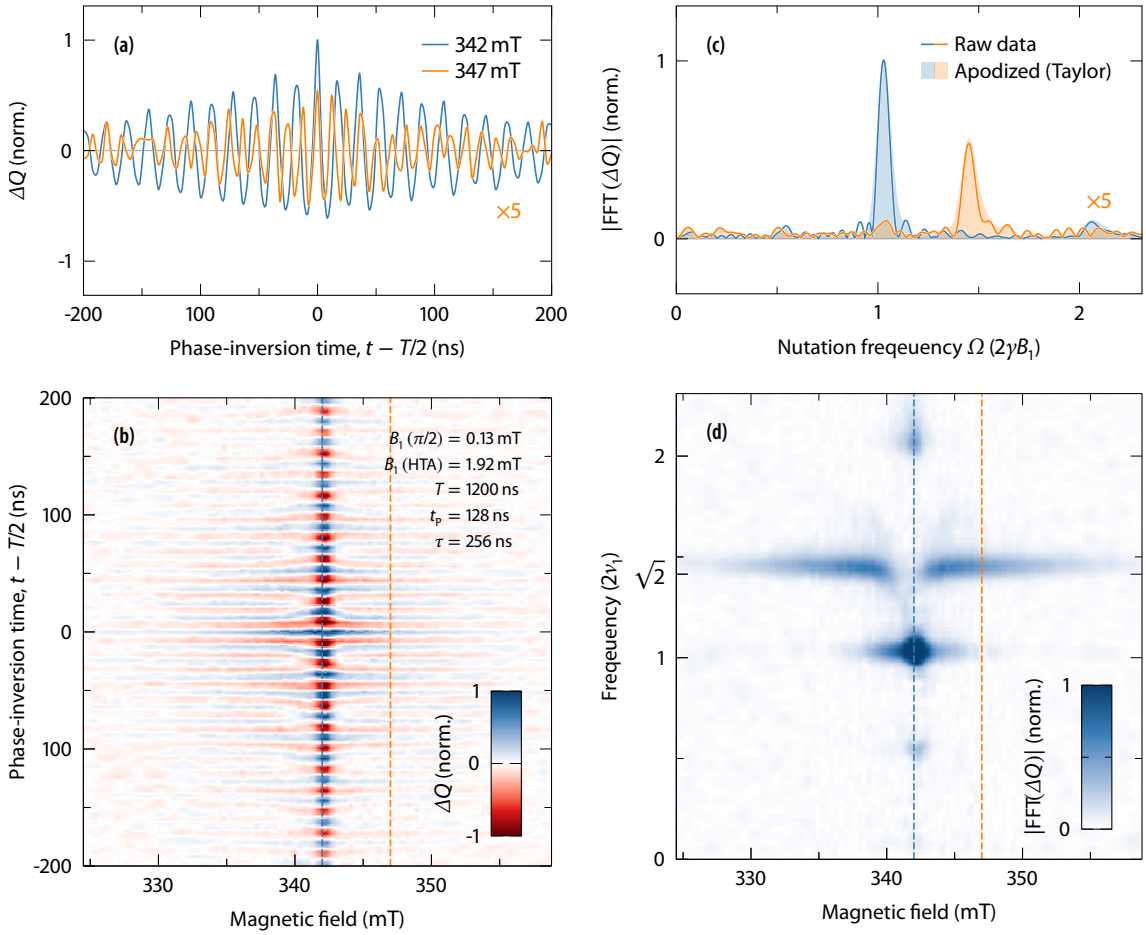

FIGURE 6.10 Magnetic-field-resolved X-band ED-PEANUT spectrum of a-Si:H, measured by recording the integrated charge ΔQ of the EDMR transient after the pulse sequence shown in fig. 6.8b. A two-step phase cycle ($\pm\pi/2$) was employed on the final readout pulse for background removal (see text for discussion). **(a, c)** Single time- and field-domain traces extracted from the two-dimensional signal maps, as indicated by the colored dashed lines in figs. b and d. **(b)** Time-domain ED-PEANUT traces, measured as a function of the magnetic field. A constant baseline has been removed by subtracting the mean value from each individual time trace (see section 6.4.3 for discussion). **(b)** Frequency-domain ED-PEANUT spectrum, obtained by calculating the FFT of each time trace from fig. b. Before the FFT, the time-domain signals were apodized using a Taylor-window function, to suppress sidelobe artifacts. The frequency-domain slices shown in fig. c compare the FFT spectra with and without signal apodization to illustrate the effect of the window function (see text for discussion). All spectra are normalized to maximum absolute amplitude of one.

saving of measurement time by a factor of two increases the SNR. A drawback of the narrowed time window is that the central double-frequency components have not fully decayed at the edges of the acquisition range (see fig. 6.10a). This produces small sidelobe artifacts in the frequency-domain PEANUT spectra. During data post-processing, these artifacts, however, can be decreased by means of apodization using an appropriate window functions. This is illustrated in fig. 6.10c, where the FFT spectra corresponding to the time traces of fig. 6.10a are shown. The solid lines plot the FFT magnitude spectra of the raw traces (after subtraction of a constant baseline), while the filled areas correspond to the FFT spectra after apodization with a Taylor window. Compared to other window functions (*e. g.*, Hann or Hamming functions), the Taylor window results in much less broadening of the mainlobe and allows to adjust the tradeoff between signal broadening and sidelobe-artifact level. As can be further seen from fig. 6.10c, a Taylor window does not affect the spectral shape and amplitudes of peaks in the frequency domain[1]—as it is the case for ED-Rabi spectra. Accordingly, apodization was used for the two-dimensional ED-PEANUT spectrum shown in fig. 6.10d, reducing the number of artifacts, which could otherwise be misinterpreted as signal peaks. For a broader phase-inversion-time range, apodization might not be required, at the cost of an increased data-acquisition time.

The field/frequency map shown in fig. 6.10d exhibit characteristic frequencies at ν_1, $2\nu_1$, $2\sqrt{2}\,\nu_1$ and $4\nu_1$. The first peak corresponds to the small residual single-frequency components (c_1) and will be neglected for the data analysis. The frequency axis in fig. 6.10d is in units of $2\nu_1$, due to the double-frequency components (c_2) forming the rotary PEANUT echo. The three remaining features can thus be assigned to nutation frequencies $\Omega = \nu_1$, $\sqrt{2}\,\nu_1$ and $2\nu_1$, respectively. These frequencies are identical to those obtained from ED-Rabi nutation measurements, though the spectral features are much better separated in the ED-PEANUT spectrum (compare fig. 6.10d to fig. 6.7b). This improved resolution is a consequence of the combination of selective excitation and high frequency resolution provided by the PEANUT sequence.

The field-domain spectra, obtained by integrating the two-dimensional signal in the frequency domain, using integration window around $\Omega = \nu_1$, $\sqrt{2}\,\nu_1$ and $2\nu_1$, are shown in fig. 6.11. The spectrum at $\Omega = \nu_1$ (fig. 6.11a) is almost identical to the respective ED-Rabi spectrum shown in fig. 6.7c. The latter is plotted in fig. 6.11a (gray line), altough it is hardly recognizable, since the spectra almost lie on top of each other. Since we assign the spectrum to $S = 1/2$ spin pairs, we fitted the line using the resonances of CBT and VBT states. Therefor, we used the spin-Hamiltonian parameters obtained from globally fitting the multifrequency EDMR spectra of a-Si:H films (see section 5.4 and tab. 5.1). We kept g-values and g-strain parameters fixed and fitted only field-independent line widths and relative spectral weights of the two resonances. Note that, as discussed in section 5.4.1 and shown in refs. [150, 151], HFI with ^{29}Si nuclei needs to be considered for the CBT resonance. Umeda *et al.* [150] found a hyperfine-coupling strength of about 200 MHz and a relative HFI intensity of about 9 % (twice the ^{29}Si natural abundancy of 4.7 at. %), which they interpreted in terms of the wavefunction of CBT-trapped electrons being spread over two silicon atoms. We thus included these HFI parameters into the fitting model. We further allowed for some variation of both the A-value and an additional A-strain parameter, since the HFIs of CBT states have been studied and determined with far less accuracy

[1] In particular, it was verified that the line shapes of the ED-PEANUT field-domain spectra discussed below (fig. 6.11) were not affected by the use of a window function.

than, for instance, the respective parameters of DB defects [148].

The result of the least-squares fit is shown in fig. 6.11a (dashed lines). The simulated spectrum almost perfectly reproduces the experimental data, although both line-width and weight parameters slightly deviate from the results of section 5.4. For the CBT resonance, we obtain a field-independent Lorentzian line width of 0.6 mT, slightly lower than the multifrequency-fit result (1.0 mT). The VBT resonance was fitted using a pseudo-Voigtian line profile with Lorentzian and Gaussian line widths of 2.6 mT and 1.8 mT, corresponding to an approximate Voigtian line width of 3.7 mT and Lorentzian and Gaussian content $\eta^{\mathrm{L}} = 0.56$ and $\eta^{\mathrm{G}} = 0.44$, respectively. Both the line width and shape are thus considerably different from what was obtained in section 5.4 ($\Delta B_0^{\mathrm{L}} = 1.2\,\mathrm{mT}$). Also the relative spectral weights of the CBT and VBT resonances slightly differ from the earlier results. However, it is to be noted that the multi-frequency fit resulted in distinctively different spectral-weight distributions for the X-band and 263 GHz spectra, indicating an incomplete fitting model. A potential reason could be the simplied model of Gaussian line shape for the TE line, affecting the fit results of the overlapping CBT and VBT. Here, ED-PEANUT separates the resonances by their nutation frequency, such that the fit results are indepedent from the TE model. Note that also the HFI parameters slightly differ from the values reported in refs. [150, 151]. However, due to the lack of sufficient data (*e. g.*, spectra recorded on a-Si:H samples of different ^{29}Si concentration), we will not put much effort into the interpretation of HFIs within the scope of this work.

Other than the $\Omega = \nu_1$ spectrum, the line shapes observed at nutation frequencies of $\sqrt{2}\nu_1$ (fig. 6.11b) and $2\nu_1$ (fig. 6.11c) clearly differ from the equivalent ED-Rabi spectra in figs. 6.7d and e. In particular, the strong off-resonance signals, superimposed on the ED-Rabi spectra, are much less pronounced in the ED-PEANUT signal. The $\sqrt{2}\nu_1$ feature exhibits a strong dip in the center of the line, which is reminiscent of the characteristic Pake-pattern predicted for the EPR resonances in the presence of dipolar coupling

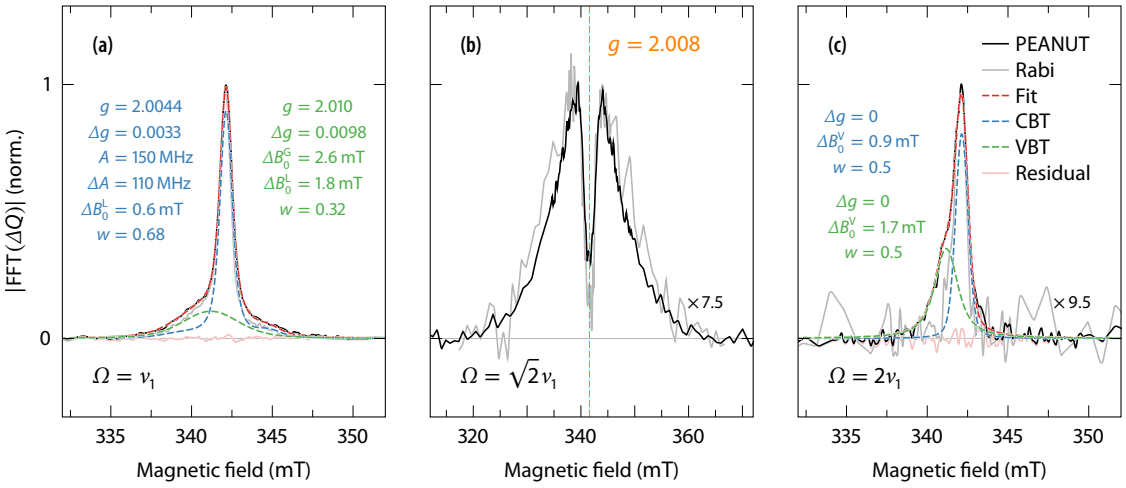

FIGURE 6.11 Magnetic-field-domain ED-PEANUT spectra at nutation frequencies (a) $\Omega = \nu_1$, (b) $\sqrt{2}\nu_1$ and (c) $2\nu_1$. The spectra were obtained by integrating the two-dimensional FFT map (fig. 6.10d) in the frequency domain, using integration windows centered about the respective nutation frequencies. The dashed curves in figs. a and c correspond the simulated spectra obtained from least-square fits based on the previously determined spin-Hamiltonian parameters of the CBT and VBT resonances (see text for discussion). For comparison, the gray lines show the corresponding ED-Rabi FFT spectra (**??**), after apodizing the time-domain signal with a Hann-window function.

(see section 2.3.3, fig. 2.4b). The observed shape strongly differs from the simple Gaussian models used to fit the line shapes of both ED-Rabi (fig. 6.7d) and PEDMR spectra. However, a similar line shape is found when applying a window function to the ED-Rabi traces, before calculating the FFT. Exemplarily, the gray line in fig. 6.7d plots the resulting Rabi spectrum after apodization using a Hann window. (Similarly, the apodized Rabi spectrum for the $2\nu_1$ feature is included in fig. 6.11c.) Apodization using a Hann function suppresses the off-resonance tails of the Rabi traces, at the tradeoff of strong broadening of the FFT peaks. While the different choices of the window function produce slightly different field-domain ED-Rabi spectra, the comparison shows that the characteristic shape is not a specific outcome of the PEANUT sequence, but indeed is a feature of the a-Si:H nutation-frequency distribution.

Interestingly, a feature of equal line shape was observed at $\Omega = \sqrt{2}\nu_1$ in field-resolved optically detected nutation experiments on a-Si:H, carried out by Lips *et al.* (figs. 8 and 9 in ref. [246]). As in our case, they found the line to be centered about $g = 2.008$—the approximate average of CBT and VBT g-values—, which led to the assignment to strongly dipolar coupled, localized electron-hole pairs trapped in the respective tail states. Assuming a distribution of Pake pattern producing the observed line shape, Lips *et al.* estimated a mean dipolar coupling from the peak separation ($\Delta\nu_{pp} = 2D$ for the Pake pattern) and obtained an average spin-pair distance of 16 Å. However, they were not able to reproduce the line shape with a simulated spectrum that assumes a distance/D-value distribution. The feature observed by Lips *et al.* led to an enhancement of the photoluminescence, such that it was assigned to a radiative recombination channel. Observing the same feature by EDMR indicates that the same $S = 1$ states are involved in both radiative recombination and spin-dependent transport.

Unfortunately, we also could not simulate the spectrum shown in fig. 6.11b. However, we note another remarkable resemblance, namely, to a numerically calculated nutation-frequency map shown by Limes *et al.* (fig. 4b in ref. [84]). They simulated the frequency-domain ED-Rabi spectrum by numerically evolving the Liouville equation for the case of simultaneous strong dipolar and exchange coupling (D, $J \gg \Delta\nu$). The simulation used a Pake distribution of D-values with $D = 80$ MHz and an exchange coupling strength $J = 300$ MHz. The resulting simulated field/frequency map exhibits features that are very similar to to the ED-PEANUT spectrum in fig. 6.10d: (i) a strong broad $\sqrt{2}\nu_1$ components; (ii) vanishing intensity and a slight decrease of the nutation frequency towards the center of the line, the latter being also found from close inspection of fig. 6.10d; (iii) narrow and weak components at $2\nu_1$ due to the strong exchange coupling. Limes *et al.* also noted the similarity to the ODMR data shown in ref. [246]. Since an equivalent simulation without inclusion of exchange coupling produced a noticeably different spectrum (fig. 2b in [84]), they concluded that the ODMR nutation pattern of a-Si:H is indicative of the simultaneous presence of dipolar and exchange coupling. Indeed this is consistent with our observations from B_1-dependent ED-Rabi nutations (section 6.4.1), where we found the $2\nu_1$ peak intensity to be independent of B_1, favoring an explanation by exchange coupling instead of spin-locking at high B_1 fields.

The line shape of the $2\nu_1$ feature is shown in fig. 6.11c. The spectrum has a maximum at about 342 mT ($g = 2.005$), similar to the $\Omega = \nu_1$ CBT/VBT feature. In addition it exhibits the same asymmetric shape stemming from the superposition of CBT and VBT resonances, although with an apparently much lower line width. Together with our pre-

vious assignment of the $2\nu_1$ feature to exchange coupling, the observed line shape could be explained by exchange-coupled electron-hole pairs trapped in the tail states. Therefor, we attempted to fit the spectrum using a superposition of CBT and VBT resonances, based on the results from fig. 6.11a. Under the assumption of coupled CBT/VBT states, however, we restricted the result to equal weights and solely fitted Voigtian line widths (*g*-strain and HFI were neglected). The resulting fit is shown in fig. 6.11c. As can be seen, the spectral shape can be reproduced with a superposition of equally weighted CBT and VBT resonances. However, the FWHM, in particular of the VBT line, is drastically reduced from a total of 4.2 mT at $\Omega = \nu_1$ to 1.7 mT at $\Omega = 2\nu_1$. For strongly exchange-coupled spin-pairs, exchange narrowing becomes an obvious explanation for the decreased line width. The obtained line shape and position thus indeed suggest an assignment of the $2\nu_1$ feature to exchange-coupled e-h pairs trapped in CBT and VBT states, respectively.

Despite the conclusions we were able to draw from the observed $\sqrt{2}\nu_1$ and $2\nu_1$ features, we must note that a detailed line-shape analysis of the spectra in figs. 6.11b and c is only of limited use. The transition moments for strongly coupled pairs have a complicated dependency on the *D* and *J* and can produce a wide range of nutation-frequency maps (compare fig. 3 in ref. [84]). A pathway towards comparing the entire map of nutation-frequency-resolved spectra to theroretical predictions requires the evolution of the spin Hamiltonian in terms of the Liouville-space formalism, as applied in refs. [79, 80, 84] for weakly and strongly coupled $S = 1/2$ pairs and in ref. [85] for coupled $S = 1/2$, $S = 1$ complexes. Although this is a straightforward approach for the analysis of individual spin pairs, it becomes computionally extensive for a disordered spin system such as a-Si:H. The combination of *g*-strain distribution and potential distributions of distances and *D* and *J* values results in a huge parameter space. A simulation for the entire spin system would be obtained as a weighted average over the evolutions of each individual spin Hamiltonian. We attempted to address this task, but unfortunately were not able to obtain satisfying results within the scope of this work.

Nevertheless, the results obtained from nutation-frequency-correlated EDMR using the ED-PEANUT detection scheme have provided valuable insight into the microscopic origin of spin-dependent transport processes in a-Si:H. A comparison of the experimental ED-PEANUT nutation spectral to numerically simulated nutation pattern indicates the presence of a spin-dependent transport channel mediated by both dipolar and exchange-coupled $S = 1$ states. The spectral position and the line width of the ED-PEANUT spectrum at $\Omega = \sqrt{2}\nu_1$ allows to clearly correlated the feature with the broad TE line, providing evidence for its excitonic nature. The additional observation of a B_1-independent $2\nu_1$ feature suggests the coexistence of dipolar and exchange coupling. Since the $2\nu_1$ spectrum resembles the resonances of CBT and VBT states, and the broad $\sqrt{2}\nu_1$ feature is centered at $g = 2.008 \approx (g_{\mathrm{CBT}} + g_{\mathrm{VBT}})/2$, we assign the TE resonance to strongly dipolar and exchange coupled electron-hole pairs trapped in their respective tail states. Both exchange [246] and dipolar coupling [244] have been proposed to explain the resonance by previous authors. Herein, we have given evidence for the validity of both assignments.

The PEANUT sequence, employed for electrical detection for the first time, has led to nutation-frequency-resolved EDMR spectra with magnetic-field and frequency resolutions superior to those obtained from conventional field-resolved ED-Rabi experiments. Electrically detected PEANUT allows to effectively adjust the excitation window for field-swept experiments, while maintaining high nutation frequencies during the high-power

nutation pulse. Moreover, B_1 inhomogeneities, which further limit the frequency resolution of ED-Rabi spectra, are partly refocussed in the PEANUT sequence. Due to these benefits, we propose ED-PEANUT as the method of choice for measuring nutation-frequency-resolved EDMR spectra.

6.5 HALF-FIELD RESONANCE

Electrically detected nutation experiments have proven the existence of a spin-dependent transport channel stemming from strongly dipolar- and exchange-coupled excitons. In the previous section, we assigned these states to strongly coupled *e*-*h* pairs trapped in CBT and VBT states. Strong dipolar coupling and the presence of simultaneous exchange coupling indicates the electron and hole to be trapped in tail states located in close proximity. The dipolar-coupling strength D is determined by the spin-spin distance r, and can thus provide a measure for the localization of the excitons. Previous authors estimated an average exciton size of about 5 Å, based on the line width of the TE resonance, assuming a distribution of Pake pattern. In this section, we will use the observation of a half-field resonance to determine the distributions of D and r more accurately.

As discussed in section 2.3.3, strong dipolar coupling induces small but non-negligible transition moments between the $m_S = \pm 1$ states (T_+, T_-) of the triplet manifold. These normally forbidden $\Delta m_S = \pm 2$ transitions become weakly allowed in the presence of dipolar coupling, which introduces off-diagonal elements in the spin Hamiltonian that mix the T_+ and T_- states [48]. Consequently, the appearance of the resulting half-field resonance ($g \approx 4$) can serve as a strong indicator of dipolar coupled $S = 1$ states.

In fact, a resonance at $g \approx 4$ has been observed in ODMR spectra of a-Si:H already in the late 1980s [242, 245, 265]. At the time, this was the first direct proof for an excitonic spin-dependent recombination process. On the contrary, the half-field resonance has as yet not been observed in EDMR spectra of a-Si:H, which led to the conclusion that the broad $g = 2.008$ features observed in ODMR and EDMR originate from different spin states [17]. In this work, we have for the first time identified a half-field signal in both CW and PEDMR spectra of a-Si:H. This observation provides further evidence for a spin-dependent transport channel via dipolar coupled triplet excitons and, in addition, allows to measure the coupling strength (D) by means of ED-Rabi nutation experiments carried out on the half-field resonance.

6.5.1 EDMR signal at half field

Figure 6.12 shows CW (black) and pulsed EDMR (red) spectra recorded at full and half field. In both spectra a resonance centered at $B_0 \approx 171\,\mathrm{mT}$ ($g \approx 4.03$) is found, enlarged in the inserts in figs. 6.12a and b. Compared to the full-field resonance the signal has a relative amplitude of about 2 %. This small amplitude may explain why the EDMR half-field resonance has not been observed previously, especially since earlier studies were carried out at higher temperatures ($T \approx 150\,\mathrm{K}$), where the SNR is much lower than at cryogenic temperatures.

As discussed in section 2.3.3, the position of the half-field resonance (B_{min}) can serve as a measure for D [48]:

$$B_{\mathrm{min}} = \frac{h\nu}{2g\mu_{\mathrm{B}}}\sqrt{1-\frac{4}{3}\left(\frac{D^*}{\nu}\right)^2}, \quad \text{where } D^* = \sqrt{D^2+3E^2}. \tag{6.7}$$

At the MW frequency of 9.6487 GHz used for recording the CWEDMR half-field spectrum, we find a zero-crossing at 171.24(10) mT (fig. 6.12a). According to eq. 6.7 (assuming an axially symmetric D-tensor with $E = 0$), one obtains $D = 580(80)$ MHz, where the error includes both the field-calibration and the B_{min} read-off uncertainty. For $E = 0$ and point-dipole approximation, the D-value can be used directly to estimate the spin-spin distance r_{AB} between strongly coupled spins A and B, according to

$$D = \frac{3}{2}\frac{\mu_0 g_{\mathrm{A}} g_{\mathrm{B}} \mu_{\mathrm{B}}^2}{4\pi h}\frac{1}{r_{\mathrm{ab}}^3}, \quad \text{or} \quad D/\mathrm{MHz} \approx \frac{77.8\cdot 10^3}{(r_{\mathrm{AB}}/\text{Å})^3}, \quad \text{for } g_{\mathrm{A,B}} = g_e. \tag{6.8}$$

Using eq. 6.8 we obtain a spin-pair distance of 5.1(3) Å. Note that this result is in close proximity to what has been derived in the early EDMR and ODMR studies by assuming a distribution of Pake doublets yielding the broad TE line shape. Based on the observed line width ($\Delta B_0 = \mu_0 g \mu_{\mathrm{B}}/4\pi r^3$), spin-spin distances between 4 Å and 5 Å have been estimated from both EDMR [244] and ODMR [243, 245].

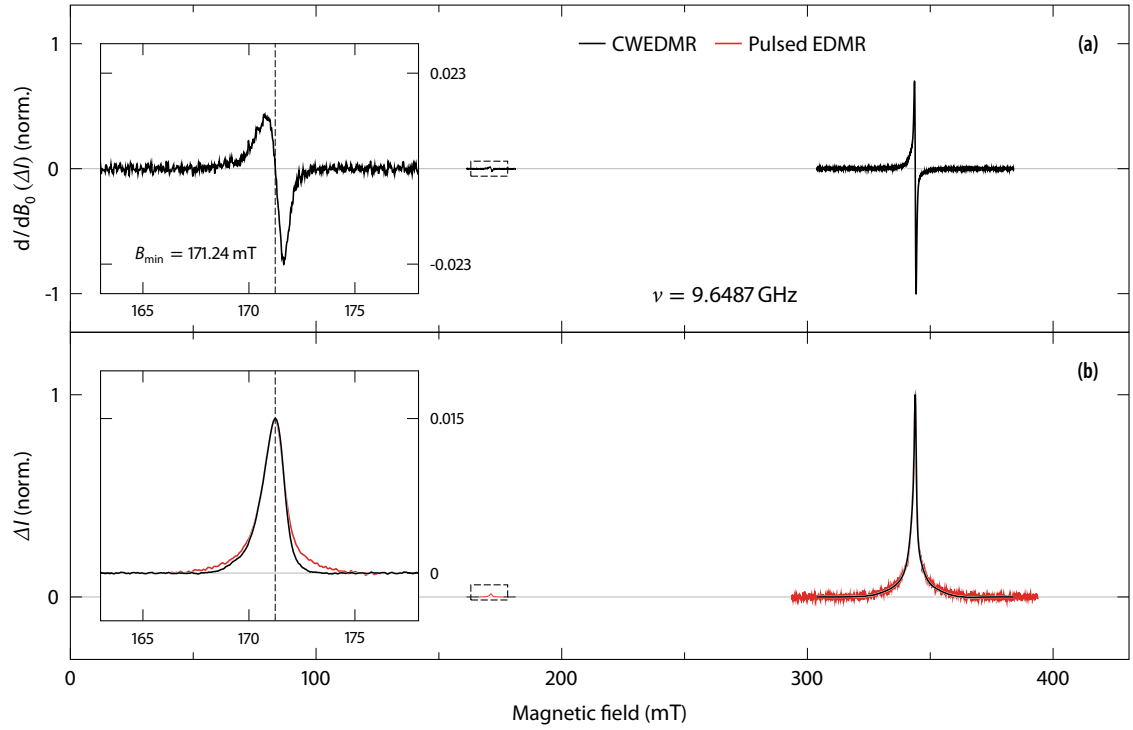

FIGURE 6.12 (a) Continuous-wave and (b) pulsed EDMR spectra recorded at full ($g \approx 2$) and half field ($g \approx 4$). The spectra are normalized to a maximum absolute full-field amplitude of one. The inserts are magnified views of the half-field resonance. Red traces in fig. b correspond to the PEDMR spectra, while the black traces show the integrated CWEDMR signal, scaled to equal amplitude.

The half-field resonance exhibits an asymmetric line shape with a sharper edge at the high-field side and a broader wing towards the low-field side. In addition, the insert in fig. 6.12b, where the integrated CWEDMR signal and the PEDMR signal (scaled to equal amplitude) are shown, indicates a broadening of the PEDMR line shape. The latter can, however, be attributed to MW-power broadening, since the PEDMR spectrum was recorded at the maximum available B_1-field (0 dB $\simeq$ 1.92 mT). For the analysis of the line shape, we will thus only use the CWEDMR spectrum. As shown in section 2.3.3 (fig. 2.4), an asymmtric line shape is predicted theoretically for the half-field resonance, according to the two field positions B_{min} and B_{max}. However, this asymmetry should be mirror-inverted to the observed shape, as the maximum of the line is found at B_{min}. Moreover, the difference between B_{max} and B_{min} is only about 0.1 mT for $D = 580$ MHz and can only have a minor influence on the line shape. Other obvious explanations such as g-tensor anisotropy, a rhombic D-tensor ($E > 0$) or the the influence of additional exchange coupling can also be excluded as explanations, since none of these effects—although potentially present—leads to a line shape that is as asymmetric as observed experimentally. The only remaining explanation for the observed line shape is an asymmetric distribution of D-values. According to eq. 6.7, the D-value strongly influences the position of the half-field resonance. Assuming a disorder-induced Gaussian distribution of exciton distances leads to a corresponding D-value distribution that is asymmetrically weighted towards higher D, as shown in fig. 6.13a, resulting from the $1/r^3$ dependency of D (eq. 6.8). Larger D-values shift the half-field resonance towards lower magnetic fields (eq. 6.7), which is consistent with the asymetrically broadened line shape.

To test this hypothesis, we performed a least-squares fit of the CWEDMR half-field signal, assuming an isotropic g-value of 2.0077 (g_{TE} from the multifrequency-fit results of section 5.4) and a Gaussian distribution of exciton distances with FWHM Δr, centered about $\bar{r}$. At each iteration, the individual half-field spectra were calculated for a set of 101 distances, equally spread over a range $\bar{r} \pm 1.5\,\Delta r$, and then summed using the respective Gaussian weights. The individual spectra were calculated using the EasySpin [43] library and eq. 6.8 to calculate D as a function of r. The fit parameters were $\bar{r}$ and Δr, as well as the line width of a field-independent Voigtian convolutional broadening function and a linear scaling factor. The fitting routine was implemented in MATLAB using a trust-region-reflective algorithm.

The shape of the half-field resonance is very sensitive to both $\bar{r}$ and Δr. In order to assess the confidence level of the obtained fit parameters, the fit was iterated using numerical bootstrap resampling, as described in section 4.4.2. A bootstrap population of $N = 1000$ data traces was generated and the least-squares regression was repeated for each sample, yielding a distribution of fit parameters and spectra. Fitting errors were estimated from the respective standard deviations of the bootstrap distribution.

The r and D distributions and the simulated half-field spectrum obtained from the fit are shown in figs. 6.13a and b. The shaded areas mark the 95 % confidence intervals of the respective bootstrap-population results. From the fit, we obtain a Gaussian distribution of spin-spin distances with a mean value $\bar{r} = 5.3(2)$ Å and a FWHM $\Delta r = 1.6(5)$ Å. Note that the uncertainties include both the fitting errors derived from the bootstrap distributions ($\Delta\,[\bar{r}]_{\mathrm{fit}} = 0.06$ Å and $\Delta\,[\Delta r]_{\mathrm{fit}} = 0.3$ Å) and the propagated uncertainties stemming from magnetic-field calibration and an estimated error of the g-value ($\Delta\,[g_{\mathrm{TE}}] \approx 0.0005$). The resulting mean of the asymmetric D-value distribution takes a value of $\overline{D} = 590(80)$ MHz

(red dotted line in fig. 6.13a). To illustrate the formation of the half-field spectrum as superposition of spectra based on the distributions of r and D, fig. 6.13c shows individual spectra at selected values of r, weighted according to the distributions shown in fig. 6.13a.

The simulated half-field spectrum shows excellent aggrement with the experimental line shape. This supports the assumption of normally distributed exciton sizes, especially regarding the lack of other explanations for the pronounced asymmetric line shape. We hence conclude that the TEs responsible for the EDMR signal have an average spin-spin distance of 5.3(2) Å, normally distributed with a FWHM of 1.6(5) Å. The determined exciton size matches earlier estimations based on the full-field line width. Considering the average a-Si bond length of 2.35 Å [102], our result suggests a localization of the TEs over two to three atomic sites. In the next section, we will confirm our findings by directly measuring the dipolar coupling strength.

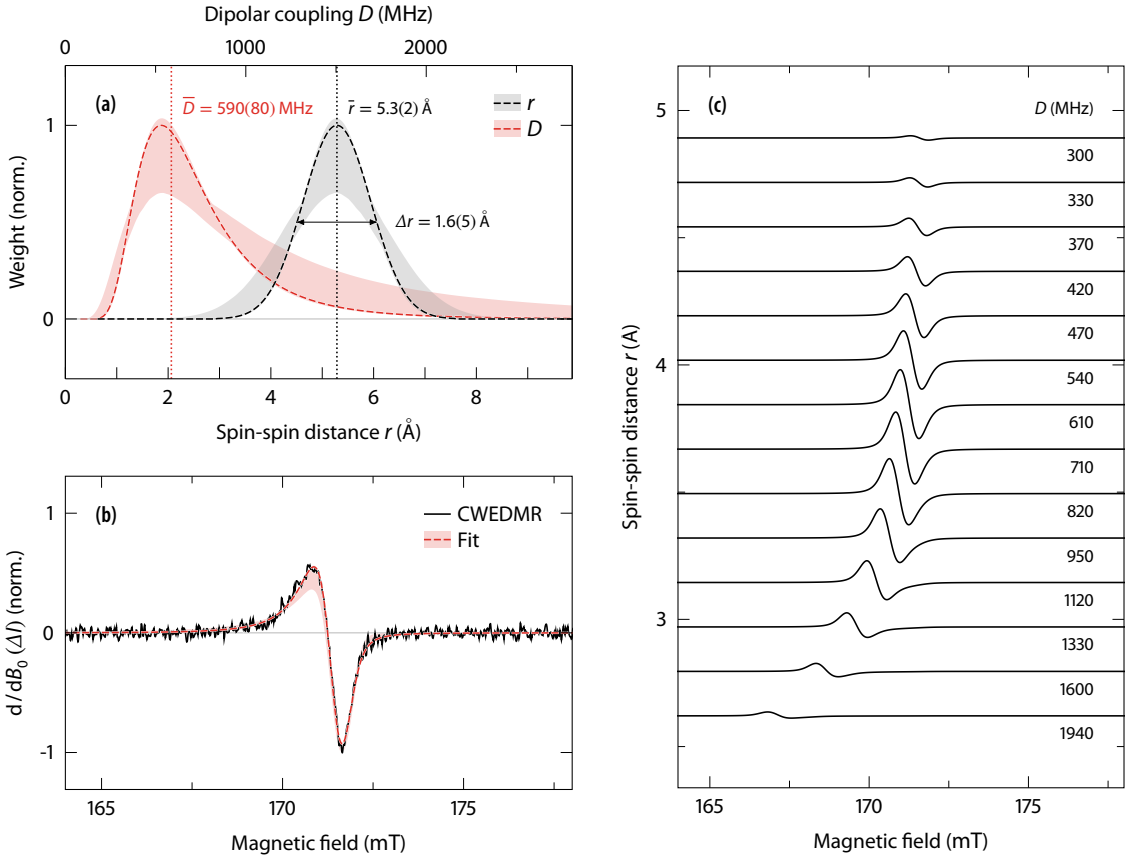

FIGURE 6.13 Spectral fit of the CWEDMR half-field resonance assuming dipolar coupled $S = 1$ triplets ($g = 2.0077$) with a Gaussian distribution of spin-spin distances r. (a) Distributions of r and D obtained from the least-squares fit (dashed lines), normalized to an amplitude of one. The shaded areas mark the 95 % confidence of the distributions, estimated by means of bootstrap resampling. (b) Experimental and simulated half-field spectrum, based on the distributions shown in fig. a. The spectrum is a superposition of the half-resonances calculated for a set of 101 distances, equal spread over a range $\bar{r} \pm 1.5\,\Delta r$, weighted according to the Gaussian distribution. Each individual spectrum is convolved with a Voigtian broadening function with a FWHM of 0.7 mT. (c) Half-field resonances for selected values of r, weighted according to the distribution shown in fig. a.

6.5.2 ED-Rabi nutations

The observation of an electrically detected half-field resonance unambigiously proves the presence of a spin-dependent transport channel via dipolar coupled $S = 1$ states. Based on the spectral simulation carried out in the previous section, we were able to estimate the spin-spin distance of the exciton and the associate D-value. In addition, the existence of a half-field resonance allows for a direct measurement of the dipolar coupling strength by means of an ED-Rabi nutation experiment.

Keevers *et al.* [85] have calculated the transition moment of the $\Delta m_S = \pm 2$ transition using a second-order expansion of the time-averaged spin Hamiltonian. Using this approach, they were able to show that the half-field Rabi-nutation frequency is directly proportional to the D-value of the exciton, according to

$$\Omega(\theta) \propto \Omega_{\mathrm{H}} \sin(2\theta), \quad \text{with } \Omega_{\mathrm{H}} = \frac{B_1}{B_0} D, \tag{6.9}$$

where the angle θ denotes the orientation of $\boldsymbol{B}_0$ with respect to the molecular frame. For the half-field nutation frequency of the entire spin ensemble, one needs to integrate eq. 6.9 over all possible orientations θ. Based on eq. 6.9, D can thus be quantified by recording ED-Rabi nutations at the half-field resonance as a function of the MW field strength B_1. At constant B_0, D can be read off from the slope of a linear regression of the measured nutation frequencies Ω with respect to B_1. In this way, Baker *et al.* [96] employed half-field ED-Rabi measurements to determine the dipolar coupling strength of $S = 1$ states within

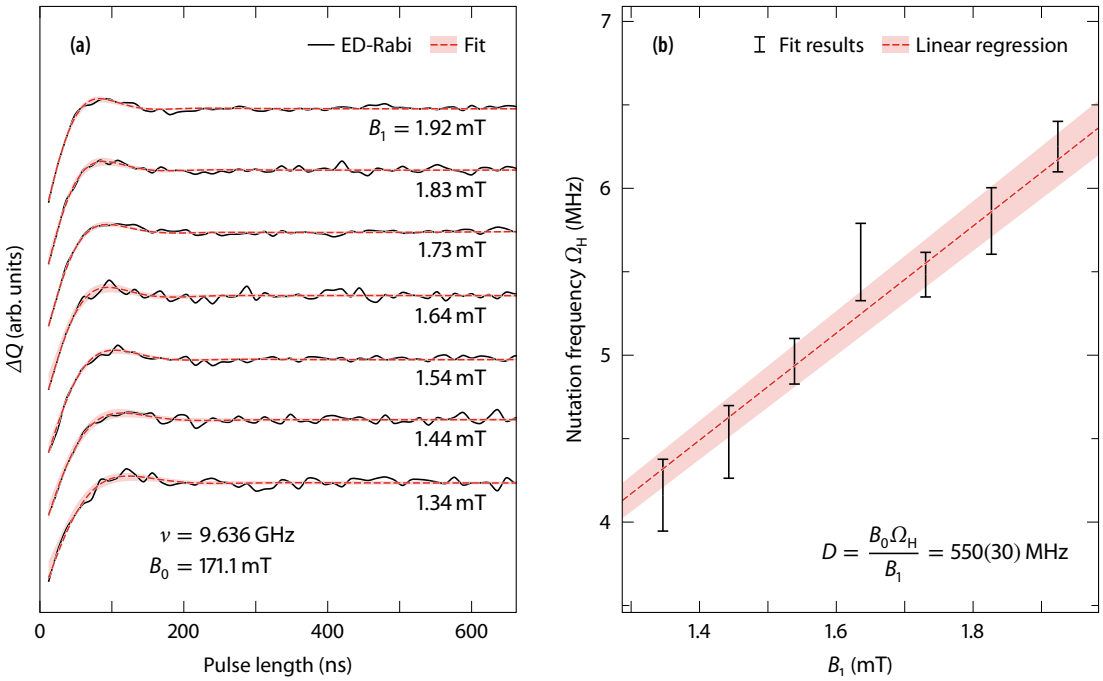

FIGURE 6.14 (a) Electrically detected Rabi nutations recorded at $g \approx 4.03$, at the center of the half-field resonance, as a function of B_1. Black traces show the experimental traces after subtraction of a second-order polynomial baseline. Red traces and shaded areas mark the result and confidence interval of a least-squares fit according to eq. 6.10. (b) Nutation frequencies Ω_H obtained from the least-squares fit of the ED-Rabi traces. Fitting errors were estimated from the standard deviation of the bootstrap population (see fig. 6.15). The D-value is obtained from linear regression.

triplet-exciton/polaron complexes in . We followed the same approach and recorded ED-Rabi nutations with B_0 adjusted to the center of the half-field resonance. The measurements were carried out as described in section 6.4.1. The resulting time-domain traces of the integrated charge ΔQ as a function of the MW pulse length are shown in fig. 6.14a, recorded at different B_1 strengths as indicated.

Strongly damped oscillations are observed, modulated only for about one nutation period. This strong damping is, however, not surprising as, according to eq. 6.9, not only B_1 inhomogeneity but also a distribution of D-values and the powder average over all angles θ leads to a broad nutation-frequency distribution that smears out the nutation trace. To determine the half-field nutation frequencies Ω_H, the Rabi traces were fitted with a damped powder-averaged oscillation function of the form

$$\Delta Q(t_P) \propto \exp\left[-t_P/\tau_{inh}\right] \cdot \int_0^{\pi} \cos\left[\Omega_H\, t_P \sin(2\theta)\right] \sin\theta \, d\theta, \qquad 6.10$$

which is based on eq. 6.9. The integration over all orientations θ includes the weighting factor $\sin\theta$, assuming equally distributed orientations on the unit sphere. The damping factor with time constant τ_{inh} takes into account both B_1 inhomogeneity and damping due to a distribution of D-values. The fitting parameters of this model are Ω_H and τ_{inh} as well as a linear scaling factor. In addition, a second-order polynomial baseline has been included into the fit. The resulting fits are plotted with red dashed lines in fig. 6.14a. Baselines have already been subtracted from both the data and the fit traces.

Due to the low SNR of the ED-Rabi traces with respect to the oscillation amplitude, we evaluated the fitting error using bootstrap resampling, as discussed in the previous section and explained in section 4.4.2. For each Rabi trace, $N = 1000$ bootstrap iterations were performed to evaluate the errors of the obtained nutation frequencies Ω_H. The shaded areas in fig. 6.14a mark the 95 % confidence interval of the resultant fitted Rabi traces over the bootstrap population. Note that also the baseline fit was included into the boot-

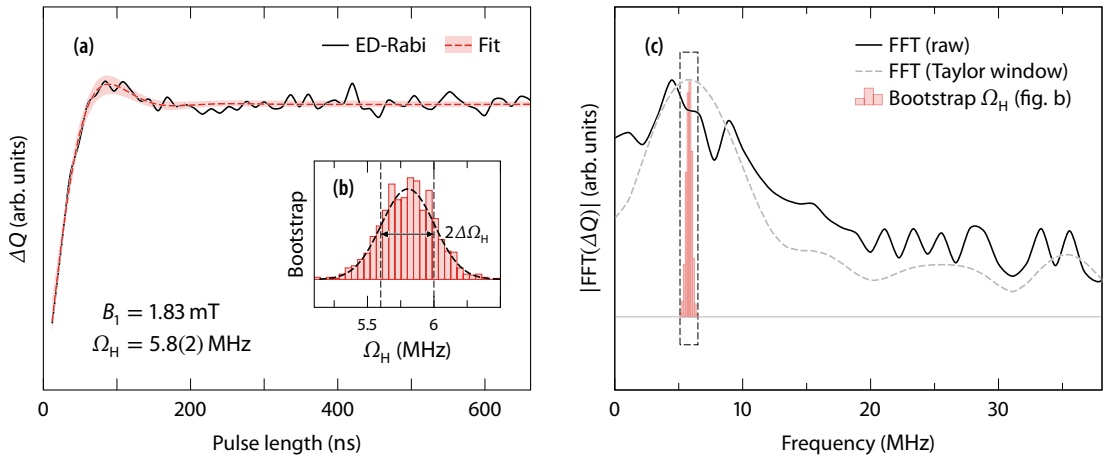

FIGURE 6.15 (a) Enlarged view of the half-field ED-Rabi nutation recorded at $B_1 = 1.83$ mT. The experimental trace (black) and the fitted curve match those shown in fig. 6.14a. (b) Histogram of the fit-parameter distribution Ω_H over the bootstrap distribution. The dashed curve shows a normal distribution with FWHM $= 2\Delta\Omega_H\sqrt{2\ln 2}$. (c) Comparison of the FFT spectrum calculated from the time-domain ED-Rabi trace shown in fig. a and the distribution of nutation frequencies Ω_H obtained from the least-squares fit (see text for discussion).

strap. The error margin of the baseline has been included into the confidence intervals shown in fig. 6.14a. Exemplarily, fig. 6.15a shows a magnified plot of the ED-Rabi trace and the fit result for the measurement at $B_1 = 1.83\,\mathrm{mT}$. In addition, the insert (fig. 6.15b) plots a histogram of the bootstrap nutation-frequency distribution. From the standard deviation, the fitting error of Ω_H is estimated, yielding $\Omega_H = 5.8(2)\,\mathrm{MHz}$.[1] Figure 6.15c also shows the frequency-domain Rabi spectrum calculated by means of FFT of the time-domain trace in fig. 6.15a. The frequency peak at Ω_H is clearly visible, especially when applying apodization using a window function before calculating the FFT. However, the nutation frequency cannot be read off accurately from the FFT spectrum due to the broad peak width. We will thus use the results obtained from the least-squares fit for the data analysis. Nevertheless the comparison of the bootstrap histogram with the FFT spectrum in fig. 6.15c confirms that the frequency peak is centered about the same frequency Ω_H obtained from the fit.

In fig. 6.14b, the nutation frequencies Ω_H are plotted as a function of B_1. According to eq. 6.9, the slope of a linear fit through the origin provides the dipolar coupling strength. The result of the linear regression is marked by the red shaded area in fig. 6.14b, yielding $D = 550(30)\,\mathrm{MHz}$. The uncertainty includes both fitting and nutation-frequency errors and the experimental uncertainties of B_1 and B_0 arising from field calibration and fluctuation during the measurement. The result matches the average D-value obtained from the spectral fit of the half-field resonance in the previous section, providing support for the fitting model.

In conclusion, we have for the first time observed an electrically detected half-field resonance of a-Si:H, unambiguously proven the presence of a spin-dependent transport channel via dipolar coupled $S = 1$ states. By means of spectrally fitting the CWEDMR half-field signal and ED-Rabi nutation experiments at half field, we were able to estimate the dipolar coupling strength and the underlying spin-spin distance distribution of the excitons. This combined approach, yielding consistent results from both methods, strengthens the reliability of the results. We find a Gaussian distribution of spin-spin distances with an average distance of 5.3(2) Å and a FWHM of 1.6(5) Å, corresponding to roughly two to three a-Si bond lengths. This distribution leads to a mean dipolar coupling strength of 590(80) MHz, consistent with the value of 550(30) MHz measured from B_1-dependent ED-Rabi nutations.

6.6 DENSITY-FUNCTIONAL-THEORY CALCULATIONS

Based on the experimental results presented so far, we have identified three paramagnetic species that are involved in low-temperature spin-dependent transport in a-Si:H. Electrically detected nutation experiments have identified spectral contributions stemming from $S = 1/2$ doublet and $S = 1$ triplet states. The $S = 1/2$ signature comprises the resonances of CBT- and VBT-trapped electrons and holes, with g-values of 2.0044 and 2.010, respectively. The $S = 1$ resonance has been assigned to strongly dipolar and exchange coupled electron-hole pairs forming a triplet exciton. From the multifrequency fit in chapter 5, we found a g-value of 2.0077. From the observed half-field resonance, we

[1] Note that the bootstrap results in a normal distribution with FWHM $= 2\sqrt{2\ln(2)}$, as illustrated by the dashed Gauss profile in fig. 6.15b. This symmetric distribution confirms that there is no systematic error in the fitting model, which would lead to a biasing of the bootstrap distribution.

TABLE 6.1 Calculated (DFT) and experimental *g*- and *D*-tensor principal values of delocalized conduction-band- (CBT) and valence-band-tail (VBT) states and localized triplet excitons (TEs). Both the results of this work and of selected earlier studies are listed. The TE state has been modeled as by relaxing an unperturbed superposition of a CBT-trapped electron and a VBT-trapped hole. DFT calculations have been performed by the group of Uwe Gerstmann at the University of Paderborn.

	Source	g_x (or g_{iso})	g_y	g_z	$\bar{g}$	D (MHz)
CBT	DFT (George *et al.* [240])	2.0046	2.0046	2.0038	2.0044	
	EDMR (this work)	2.0044			2.0044	
	LEPR (Umeda *et al.* [149, 150])	2.004			2.004	
VBT	DFT (this work)	2.0047	2.0124	2.0140	2.0104	
	EDMR (this work)	2.010			2.010	
	EDMR (Akhtar *et al.* [26])	2.006	2.009	2.015	2.010	
	LEPR (Umeda *et al.* [149, 150])	2.005	2.012	2.019	2.004	
TE	DFT (this work)	2.0051	2.0070	2.0083	2.0069	614
	EDMR (this work)	2.0077			2.0077	550(30)

determined a *D*-value of 550(30) MHz and a mean exciton spin-spin distance of 5.3(2) Å, normally distributed with a FWHM of 1.6(5) Å. To further validate these results and translate them into structural models on an atomic scale, we complemented our experiments with *ab-initio* density-functional-theory (DFT) calculations. These calculations were performed by the group of Uwe Gerstmann at the University of Paderborn within the framework of a project collaboration.

The combination of EPR experiments and DFT model calculations has already been successfully employed to study the DB defect in a-Si:H [148]. The same approach has been used for EDMR experiments on a-Si:H/c-Si heterojunctions [240]. In this study, both DB defects at the interface and CBT states in the a-Si:H layer could be identified to contribute to spin-dependent recombination. Both DB and CBT could be modeled by DFT calculations, yielding excellent agreement between theory and experiment. For the CBT state, an almost isotropic *g*-tensor with $g = 2.0044$ was calculated (see tab. 6.1), assuming an only 1 nm thick a-Si:H layer in the heterostructure. With increasing thickness, the *g*-tensor can be expected to be purely isotropic [240]. The resulting spin-magnetization density is shown in fig. 6.16a, indicating strong delocalization with the a-Si:H network. This calculated result matches the *g*-value of CBT states that has been observed experimentally by LEPR and EDMR/ODMR, both in earlier studies and in this work, confirming the involvement of CBT-trapped electrons into spin-dependent transport and recombination.

Following the success of complementary EPR/EDMR and DFT investigations on a-Si:H, we have extended the DFT calculations also to VBT-trapped holes. Based on the common model for CBT and VBT states in terms of weak bonding sites caused by disorder-induced distortions in the a-Si network (see section 3.2.3), VBT states are modeled as a delocalized excess hole centered at a distorted four-fold coordinated Si bonding site (in similarity to a CBT state, which is modeled as an excess electron trapped at a disorder-induced weak-bonding site). The *g*-tensor was calculated from first principles, using the gauge-including projector-augmented plane-wave (GI-PAW) approach [270], which is implemented in the QUANTUM ESPRESSO package [271]. A detailed description of the calculation procedure can be found in ref. [240].

As for the CBT electron, modeling of a VBT hole results in a delocalized state, centered at a distorted four-fold coordinated Si bonding site, as shown in fig. 6.16b. However,

the calculated g-tensor has strong rhombic symmetry, with principal values $g_x = 2.0047$, $g_y = 2.0124$ and $g_z = 2.0140$. The average g-value, $\bar{g} = 2.0104$, is in excellent agreement with our experimental results, as obtained both from multifrequency EDMR in chapter 5 and from the $S = 1/2$ nutation-frequency-correlated EDMR spectra in section 6.4. In our fitting models, however, we assumed an isotropic g-value, primarily to limit the fit-parameter space. The X-band spectrum will only be slightly changed when including an anisotropic g-tensor. On the contrary, the impact of g-tensor anisotropy on the 263 GHz spectrum is much stronger. Due to the strong overlap with the CBT and TE lines, however, the VBT resonance cannot be isolated, in order to unambiguously determine a potential g-tensor anisotropy. We found that including g-tensor anisotropy into the simulations still produces good fit results, while slightly changing the relative spectral weights and broadening parameters. Akhtar *et al.* [26] included a rhombic g-tensor into a fitting model for low-temperature ($T = 5$ K) X-band and 263 GHz EDMR spectra and reported principal g-values that are in good agreement with the DFT calculations. Similar values were also derived by Umeda *et al.* [149, 150] from multifrequency LEPR on a-Si:H (see also section 3.2.3). On this basis, we can overall conclude that the calculated VBT model is consistent with experimental data. The DFT model thus corroborates our assignment to a transport channel involving delocalized VBT-trapped holes.

Recently, the PAW formalism has been extended to enable DFT calculations of D-tensors of high-spin centers [272]. Based on this approach, D-values were calculated for defect states in diamond and polymorphs of silicon carbide, which were in good agreement with experimentally obtained values [272]. In the scope of this work, the novel algorithm has been applied to calculate a model for the TE state in a-Si:H. Based on the observed g-value, which is approximately equal to the arithmetic mean of the CBT and VBT g-values, the TE state was modeled as an unperturbed superposition of a CBT-trapped electron and a VBT-trapped hole. Relaxation of this structure leads to the spin-magnetization density shown in fig. 6.16c. Note that a large share of magnetization is localized within one to two Si bonding sites. This is consistent with the exciton-radius distribution derived from the EDMR half-field resonance. The calculated g-tensor exhibits rhombic anisotropy (see tab. 6.1), resulting from the anisotropic VBT state. The average g-value, $\bar{g} = 2.0069$, is consistent with our experimental results. The calculated TE structure results in a D-value of 614 MHz, in excellent agreement with the D-value we estimated from a least-squares fit of the half-field resonance ($D = 590(80)$ MHz) and

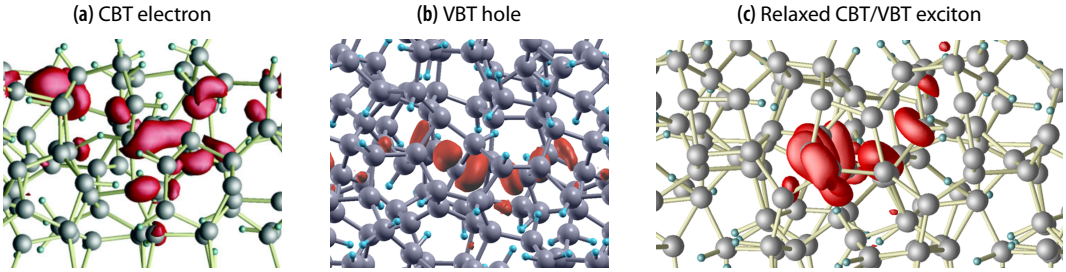

FIGURE 6.16 Spin-magnetization density (red) calculated from DFT for (a) conduction-band-tail (CBT) and (b) valence-band-tail states (VBT), and (c) a triplet exciton TE formed by an strongly dipolar coupled pair of a CBT electron and a VBT hole. Large and small spheres mark Si and H atoms, respectively. All graphics have been prepared by the group of Uwe Gerstmann at the University of Paderborn.

from ED-Rabi nutations at half field ($D = 550(30)$ MHz). This consistency between experiment and theory clearly substantiates our model for TEs in a-Si:H, as being formed strongly coupled *e-h* pairs trapped in tail states in direct proximity.

Complementing the EDMR investigations with DFT calculations has provided strong support for assigning low-temperature spin-dependent transport to immobile electrons and holes trapped in tail states, either as separated delocalized $S = 1/2$ states or as strongly coupled, localized $S = 1$ excitons. Before adressing the nature of the associated transport channels in section 6.8, the following section will present transient-EPR experiments, demonstrating that the same paramagnetic states can be detected also by EPR.

6.7 TRANSIENT EPR

Transient EPR detects light-induced paramagnetic states by recording the time-resolved EPR signal after a laser-flash excitation. The technique is ideally suited to study short-lived light-induced states and has been successfully employed to investigate, for instance, charge-conversion via photoinduced charge-transfer states [273–275] or strongly coupled TE complexes [276, 277] in organic photovoltaic materials. In this section, we apply TREPR to a-Si:H powder samples at low temperatures ($T \leq 80$ K). We will thereby present evidence for both weakly coupled spin-correlated electron-hole pairs and photoinduced TEs. From the dynamics of the TREPR spectrum, we will further be able to gain insight into the impact of these states on charge separation in a-Si:H, and correlate the TREPR signals with the spin-dependent transport channels probed by EDMR.

Unlike in PEPR, continuous MW irradiation is applied to the spin system, while measuring the transient EPR signal at constant MW frequency and magnetic field as a function of time. In contrast to conventional CWEPR, the signal is directly detected without the use of phase-sensitive detection (*e. g.*, based on magnetic-field or MW-frequency modulation). Time-resolved EPR spectra are obtained by carrying out field-swept TREPR, yielding two-dimensional signal maps. Comprehensive details concerning instrumentation, methodology and applications of TREPR can be found in EPR textbooks or recent reviews (see, for example, ref. [259]). A brief description of the experimental setup can be found in section 4.2. We applied TREPR to powder samples prepared from undoped a-Si:H films, which were deposited using PECVD as described in refs. [163, 253] and summarized in section 4.1. Samples of different electronic quality due to varying deposition conditions and light exposure were examined, to evaluate a potential correlation of the observed states with, for instance, sample morphology or defect density.

6.7.1 Transient-EPR signal of a-Si:H

Figure 6.17 shows the two-dimensional TREPR signal of an undoped a-Si:H powder sample at $T = 80$ K. The dominant signal is a broad feature, covering a magnetic-field range of more than 60 mT. The spectrum reaches maximum intensity at about $t = 0.8$ µs after the laser flash and fully decays within 3 µs. The characteristic line shape with both emissive (E) and absorptive (A) features (see fig. 6.17b) is typical of spin-polarized triplet states [259, 275–278]. Non-Boltzmann populations of the triplet sublevels give rise to $\Delta m_S = \pm 1$ transitions, which either absorb or emit a MW photon. This polarization pattern reflected by the TREPR signature can be used to determine the formation mecha-

nism of the photo-excited triplet states [275, 277, 278]. The observed EA polarization pattern is indicative of triplet states generated by intersystem crossing (ISC) from an excited singlet precursor state. In this case, the spin polarization is solely governed by the selective population of the zero-field triplet sublevels, which depends on the symmetries of the singlet and triplet wavefunctions. The resulting sublevel populations in presence of a magnetic field depend on the orientation of the D-tensor principal axes with respect to the magnetic-field vector (see section 2.3.3). The powder pattern, averaging over all orientations, then exhibits a characteristic EEEAAA (or AAAEEE) sequence, resulting from the three canonical orientations [259, 278]. Other triplet-formation mechanisms, such as, for instance, recombination of spin-correlated radical pairs, directly populate the high-field triplet manifold, producing polarization patterns that cannot be obtained from ISC-generated triplets (*e. g.*, AEEAAE or EAAEEA) [275, 278]. Therefor, we assign the broad TREPR signal observed in fig. 6.17 to TEs formed by ISC of the geminate, photo-excited singlet excitons.

The assignment to light-generated TEs is supported by an increase of the TREPR signal intensity with increasing light intensity (laser-pulse energy E_L). This is illustrated in fig. 6.17c, where the field-domain TREPR signal at $t = 0.8$ µs is shown as a function of E_L. Other experimental conditions were kept constant (temperature, laser wavelength, MW frequency and power, resonator coupling and sample position). A clear light dependency of the TE resonance is observed.

The line width of the TREPR signal ($\Delta B_{pp} \approx 16$ mT) is comparable to the line width of the TE resonance measured with EDMR. It thus seems natural to assume that the same states cause both signals. Therefor, we simulated the TREPR signal of ISC-generated TEs based on the spin-spin-distance and D-value distribution determined from the EDMR half-field signal (fig. 6.13). The resulting simulated spectra are shown in fig. 6.18a, scaled to

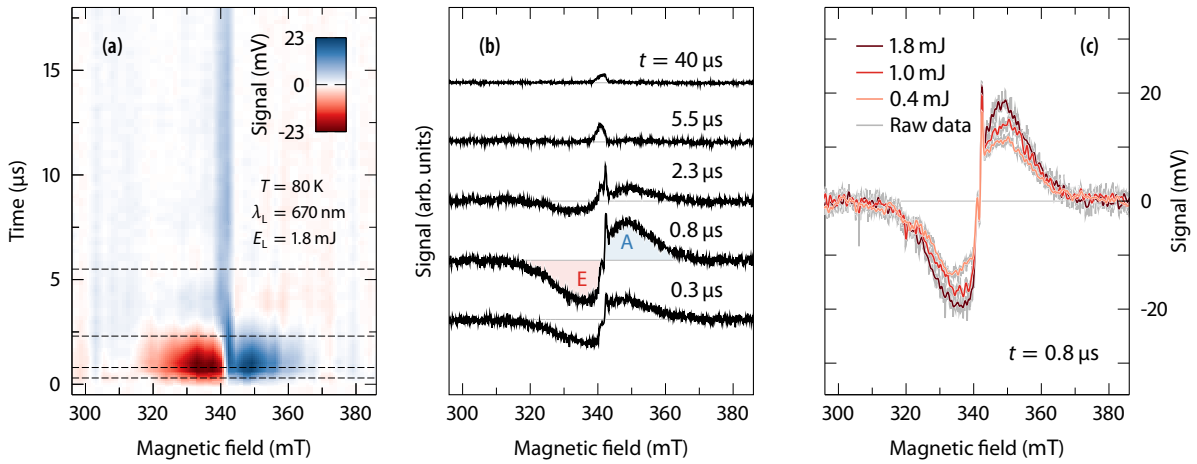

FIGURE 6.17 (a) Field-swept transient EPR spectrum of undoped a-Si:H at $T = 80$ K. The spectrum was measured by directly recording the time-resolved EPR signal after a laser flash of wavelength $\lambda_L = 670$ nm and laser-pulse energy $E_L = 1.8$ mJ as a function of the external magnetic field. (b) Selected field-domain slices at different times after the laser flash, as indicated by the dashed lines in fig. a. Emissive (negative) and absorptive (positive) signal components are exemplarily marked by the shaded areas. (c) Light-intensity dependence of the TREPR signal. The field-domain slice at $t = 0.8$ µs after the laser flash is shown for three different laser-pulse energies. For better visual comparability, the colored traces have been smoothed by means of a digital fourth-order Butterworth low-pass filter.

match the amplitude of the TREPR field-domain slices. Excellent agreement is observed between simulation and experiment, suggesting that the same photo-generated TEs that are probed by TREPR indeed cause the spin-dependent transport channel responsible for the EDMR signal.

In the central part of the spectrum, additional signals are superimposed onto the TE resonance. This can be seen from the residual spectra between the three TREPR slices and the TE simulation, which are shown in fig. 6.18b. At short times after the laser flash ($t < 2\,\mu s$), the residual spectrum exhibits an EAEA polarization pattern. We will not attempt to explicitly analyze the line shape, since already a slight change of $\bar{r}$ or Δr in the TE simulation strongly influences the residual line shape. However, the characteristic shape of the signal, in particular, the presence of both absorptive and emissive line components, is an unambiguous fingerprint of spin-correlated pairs. Similar TREPR line shapes have been reported for organic semiconductors, such as polymer/fullerene blends, and were assigned to charge-transfer (CT) states formed by spin-correlated polaron pairs [273, 275, 279]. Due to the non-thermal spin polarization, the signal unequivocally originates from a geminate electron-hole pair. Based on the centering of the line at about $g = 2.008$, that is, the arithmetic mean of CBT and VBT g-values, we assign the signal to weakly coupled

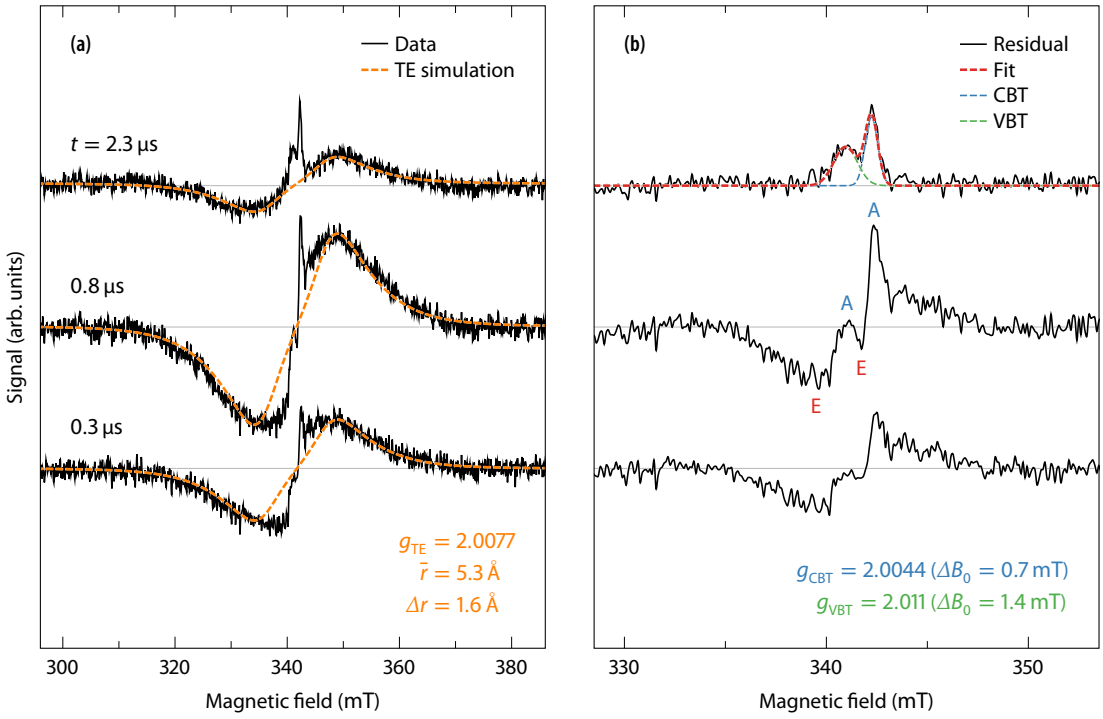

FIGURE 6.18 Spectral simulations of the TREPR signal of a-Si:H. **(a)** Field-domain slices from fig. 6.17b, featuring the broad triplet resonance. Simulations of the TE resonance, based on the result obtained from the half-field resonance (fig. 6.13), have been carried out using the EasySpin [43] library. Only a linear scaling factor has been adjusted by least-squares fitting to the experimental data. **(b)** Residual spectra of the slices shown in fig. a, obtained by subtracting the simulated TE spectrum from the experimental TREPR traces. For times $t < 2\,\mu s$, the characteristic polarization pattern of weakly coupled spin-correlated radical pairs (EAEA) is observed. The purely absorptive signal at larger times (upper trace), was least-squares fitted with a set of two Gaussian lines. The resulting g-values and line widths are consistent with the line shapes of CBT- and VBT-trapped electrons and holes. Note that the magnetic-field range shown in fig. b has been narrowed with respect to fig. a.

light-generated *e*-*h*-pairs that have been trapped in spatially correlated tail states before being able to fully dissociate from the geminate pair.

At times $t > 2\,\mu s$, the shape of the signal that is superimposed onto the TE resonance changes and a purely absorptive feature is observed (upper trace in fig. 6.18b). We fitted this spectrum with a spectral simulation, assuming the simple model of two Gaussian lines with isotropic *g*-values. The resulting fit is shown by the dashed lines in fig. 6.18b and results in *g*-values resembling the resonances of CBT and VBT states. This signal can thus be assigned to trapped electrons and holes that have fully escaped the geminate coupled pair. These signatures of separated charge carriers are likewise observed in LEPR spectra of a-Si:H, as discussed in section 3.2.3.

The above results suggest that TREPR directly probes the charge-separation mechanism in a-Si:H. The observed signals are consistent with the findings from PC, PL and QFRS studies summarized in section 3.3. Photo-excited excitons are created in a singlet state, due to the singlet ground state of doubly occupied states in thermal equilibrium. After excitation into the extended band states, electron and hole relax down towards the mobility edges (rapid thermalization) and into the tail states. After thermalization, geminate pairs exist as spatially correlated weakly coupled excitons, giving rise to the observed TREPR signature. Dissociation leads to separated charge carriers that are observed in both TREPR and LEPR when they are trapped in CBT or VBT states. Moreover, geminate pairs are observed as strongly coupled TEs that form from the excited singlet exciton by ISC. Due to the similarity to the charge-separation process via CT complexes proped by TREPR in organic photovoltaic materials [273, 275], we adopt the term *charge-transfer exciton* for the spin-correlated *e*-*h*-pair in a-Si:H.

Both the signatures of spin-correlated coupled pairs and TEs are observed by TREPR. Likewise, QFRS revealed lifetime peaks $\tau_S \approx 3\,\mu s$ and $\tau_T \approx 1\,ms$, assigned to geminate-pair recombination of SEs and TEs [206, 210] (see section 3.3.2). Radiative recombination of geminate coupled pairs thus counteracts efficient charge separation in a-Si:H. Aoki *et al.* [206, 213–215] identified another long-lived lifetime peak $\tau_D = 0.1$–$160\,s$, which they assigned to radiative recombination of distant pairs. This is consistent with our observation of a TREPR signature of separated electrons and holes trapped in CBT and VBT states. These states exhibit a much longer transient spin lifetime than the coupled states, which is in agreement with the longer lifetime τ_D found from QFRS.[1] By proving the existence of both weakly and strongly coupled excitonic states as well as uncoupled transient paramagnetic species, our TREPR provides support for the conclusions drawn from QFRS. By means of TREPR, we were able to directly follow the charge-separation process in a-Si:H on a microsecond time scale and thereby elucidate the conversion from light-generated excitons to separated electrons and holes contributing to photoconductivity.

6.7.2 Temperature dependency

In section 5.5, temperature-dependent EDMR spectra of a-Si:H films were presented, which illustrated the transition from the low-temperature current-enhancing signal, featuring the TE resonance, towards the room-temperature quenching signal, assigned to spin-dependent recombination via DB defects. The enhancing signal was clearly identi-

[1] Note that we cannot directly compare PL lifetimes to the transient spin lifetimes observed in TREPR measurements. Spin lifetimes include effects such as relaxation, while QFRS solely probes the population dynamics. Recombination lifetimes, however, set an upper bound of the spin lifetimes in TREPR measurements.

fied at temperatures $T \leq 50$ K, while at $T \geq 150$ K only the quenching signal was observed. At intermediate temperatures, a superposition of both signals, separated by their different dynamics, was found. The TREPR signal discussed in the previous section was recorded at $T = 80$ K. The observation of a TE signal at this temperature is hence consistent with the results of section 5.5 and allows for the conclusion that the same states are detected by EDMR and TREPR. We repeated the TREPR measurement at higher and lower temperatures to further test the correlation between EDMR and TREPR signals.

Figure 6.19 shows TREPR of the same a-Si:H powder sample, recorded at $T = 10$ K and 120 K. Both spectra were acquired under the same conditions as the $T = 80$ K spectrum shown in fig. 6.17 (laser adjustment, wavelength and power, MW power, sample positioning and resonator coupling). At $T = 10$ K (fig. 6.19a), a strong TE resonance is evident—comparable to what was observed at 80 K. At $T = 120$ K (fig. 6.19b), by constrast, only a

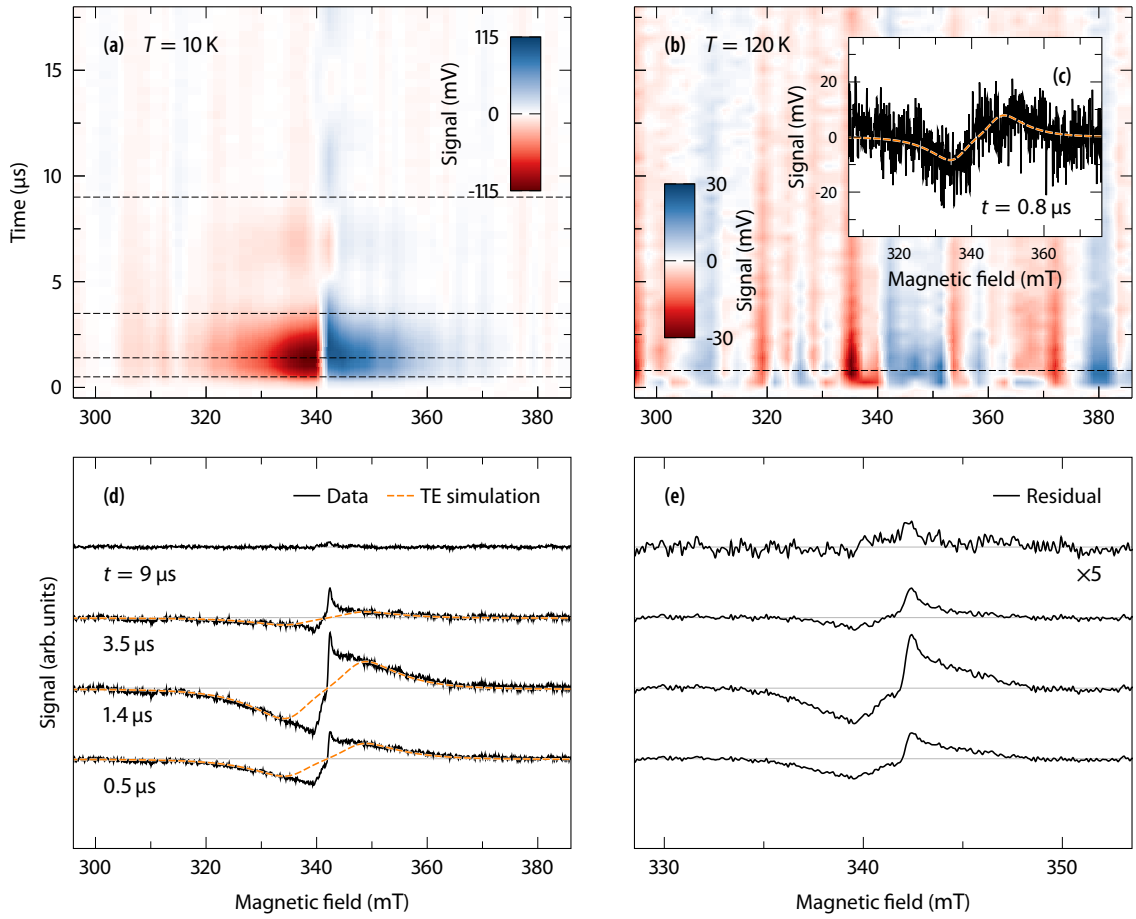

FIGURE 6.19 Temperature dependency of the TREPR signal of a-Si:H. (a, b) Two-dimensional TREPR recorded at $T = 10$ K and 120 K. Both spectra were recorded of the same sample and under the same experimental conditions as the measurements discussed in section 6.7.1 ($\lambda_L = 670$ nm, $E_L = 1.8$ mJ, MW attenuation 35 dB). (c, d) Magnetic-field domain cross section at different times t after the laser flash (dashed lines in figs. a and b). The dashed orange curves show the simulated resonance of ISC-generated TEs, based on the results of section 6.5. (e) Residual spectra obtained by subtracting the simulated TE resonance from the traces shown in fig. d. Similar line shapes are observed at $T = 80$ K (fig. 6.18b), although the resonance assigned to separated electrons and holes (upper trace) exhibits a significantly reduced relative intensity (note the scaling by a factor of five).

very weak TE can be observed, as shown in fig. 6.19c, where the magnetic-field-domain cross section at $t = 0.8\,\mu s$ after the laser flash is shown. At higher temperatures (150 K, 295 K), no TREPR signal was observed. This temperature dependency thus appears to correlate with the low-temperature EDMR signal, lending support to the assumption that the same TE states are detected by both methods.

Single field-domain slices at $T = 10$ K are shown in fig. 6.19d, extracted from the two-dimensional signal as indicated by the dashed lines in fig. 6.19a. As in the previous section, we simulated the TE resonance based on the exciton-distance distribution determined from the EDMR half-field resonance ($\bar{r} = 4.6$ Å, $\Delta r = 1.4$ Å), and scaled the resulting spectrum to the field-domain TREPR traces. The residual spectra between the experimental data and the TE simulation are shown in fig. 6.19e. The line shape of the TE resonance appears unchanged with respect to the 80 K measurement. The residual spectra between 0.5 µs and 3.5 µs also resemble the previously observed shape, indicative of spin-correlated weakly coupled CT excitons. The relative intensity with respect to the TE resonance, though, has increased, compared to the 80 K signal. On the contrary, the resonance stemming from uncoupled thermalized electrons and holes is merely visible. This can, however, be explained by the decreased charge-carrier mobility at lower temperatures. Due to the lack of thermal energy, hopping transport between tail states is predominantly limited to energy-loss hopping. Therefor, dissociation of the geminate exciton becomes less probable, yielding a lower concentration of mobile, uncoupled electrons and holes and, resultingly, a lower photoconductivity. In this respect, the differences between the TREPR signals at $T = 80$ K and 10 K are consistent with earlier PC studies of a-Si:H (see section 3.3.1).

6.7.3 Transient Torrey nutations

A useful observation becomes apparent when taking a closer look at the single time-domain TREPR traces, recorded at $T = 10$ K. In fig. 6.20a, the TREPR signals at magnetic fields $B_0 = 342$ mT ($g \approx 2.004$) and 347 mT ($g \approx 1.978$) are plotted, including the entire data-aquisition interval. An oscillation of the TREPR signal is evident, suggesting the observation of transient nutations due to the exposure to continuous MW irradiation. These so-called *Torrey oscillations* [280–283] are a common byproduct of TREPR signals that appear if the nutation frequency exceeds the spin-spin relaxation rates ($1/T_1$, $1/T_2$). They can be used either as a measure of B_1 or to separate TREPR spectra stemming from different paramagnetic species, not only by their dynamics, but also by their potentially different nutation frequencies (similar to the approach we used in section 6.4 when carrying out field-resolved ED-Rabi or -PEANUT experiments).

The magnetic-field positions of the slices shown in fig. 6.20a were selected according to the maxima of either the narrow central signals (weakly coupled CT states and separated localized electrons and holes) or the broad TE resonance. Already from the time-domain traces, it is evident that the two signals exhibit different nutation frequencies. This becomes even more apparent from fig. 6.20b, where the respective FFT magnitude spectra are shown.[1] To derive the transient nutation frequencies Ω, the FFT spectra were fitted with a simple Gaussian model, as shown by the dashed lines in fig. 6.20b. This yields fre-

[1] Note that an exponential baseline has been fitted and subtracted from the FFT spectra shown in fig. 6.20b. Owing to the low MW power and the resultingly low nutation frequencies, the FFT peaks are superimposed by the strong zero-frequency peak, comprising non-modulated signal components. Negative FFT magnitudes in figs. 6.20b–d are thus a result of an imperfect baseline correction.

quencies $\Omega = 0.13(4)$ MHz at $B_0 = 342$ mT and $\Omega = 0.19(4)$ MHz at $B_0 = 347$ mT, where the given uncertainties correspond to the HWHM of the peaks. During the TREPR experiment, unfortunately, no calibration of B_1 has been conducted. However, based on the assignment of the central narrow resonances to either weakly coupled or uncoupled $S = 1/2$ states, such that $\Omega_S = \gamma B_1$, we estimate $B_1 = 4.7(13)\,\mu$T, consistent with the low MW power applied during the experiment (MW-power attenuation of 38 dB). For the ratio between the two nutation frequencies, we obtain $\Omega_T/\Omega_S = 1.47(54) \approx \sqrt{2}$. Therefor, Ω_T represents the expected nutation frequency of $S = 1$ triplet states.

Figure 6.20c shows the baseline-corrected FFT spectrum for the entire magnetic-field range. Field-domain cross sections at the closest frequencies to Ω_S and Ω_T are shown in fig. 6.20d. Negative (red) FFT magnitudes are residual artifacts stemming from the exponential baseline correction in the frequency domain. Due to these artifacts, we will not attempt to quantitatively evaluate the nutation-frequency-resolved TREPR spectra. Nevertheless, the two-dimensional FFT spectrum clearly illustrates the presence of $S = 1/2$ and $S = 1$ species. Moreover, a striking similarity between the TREPR nutation-frequency

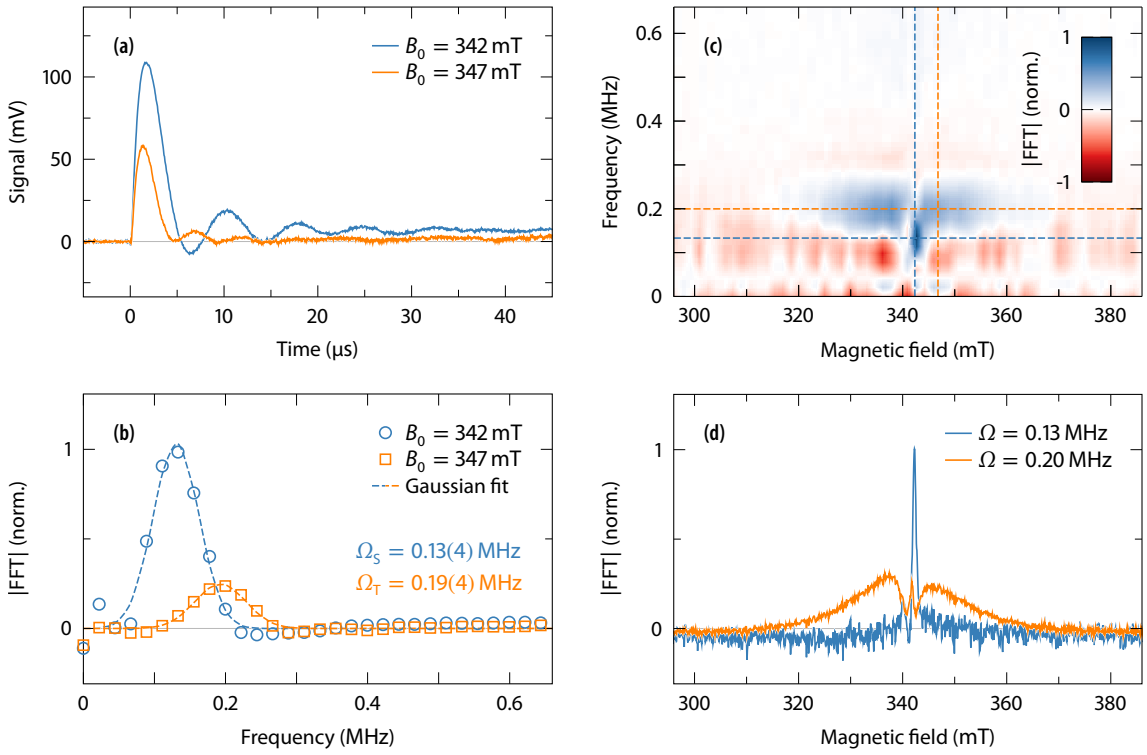

FIGURE 6.20 Transient Torrey oscillations observed in the $T = 10$ K TREPR spectrum of a-Si:H. **(a)** Time-domain TREPR signals extracted from fig. 6.19a at two fixed magnetic-field positions. Both traces exhibit transient oscillations at different nutation frequencies Ω. **(b)** Frequency-domain spectra obtained by calculating the FFT of the traces shown in fig. a. An exponential baseline has been subtracted from the FFT magnitude spectra to allow for an identification of the low-frequency nutation peaks. The dashed lines show the result of least-squares fits with Gaussian line shapes, used to read off nutation frequencies. The ratio $\Omega_T/\Omega_S = 1.47(54) \approx \sqrt{2}$ resembles the expected ratio between the nutation frequencies of $S = 1$ and $S = 1/2$ species. **(c)** Two-dimensional FFT spectrum of the field-resolved transient nutations. A remarkable similarity to the electrically detected nutation-frequency maps presented in section 6.4 becomes immediately evident. **(d)** Field-domain nutation-frequency-resolved magnitude spectra, extracted at the nutation frequencies of $S = 1/2$ and $S = 1$ states, as indicated by the dashed lines in fig. c.

TABLE 6.2 Deposition conditions and material properties of a-Si:H powder samplesused for comparing the TREPR signals as a function of the structural and electronic material quality. Samples labeled A–E were prepared at Delft Technical University, as described in ref. [163]. The first, unlabeled sample has been used for the TREPR measurements discussed in the previous sections and was prepared at Forschungszentrum Jülich, according to ref. [253].

Sample	Label [a]	m (mg)	R $[H_2]/[SiH_4]$	P_{RF} (W)	r_D (Å/s)	p (mbar)	Porosity [b]	n_S [c] ($1/cm^3$)
	09B502I	68	9	N/A	N/A	N/A	N/A	N/A
A	M3610	10	0	3.1	1.8	0.7	low	$6 \cdot 10^{15}$
B	A6725	11	0	3.6	2.8	0.7	medium	$1 \cdot 10^{16}$
C	A6729	11	0	10	7.2	1	high	$9 \cdot 10^{16}$
D [d]	A6709	4	50	10	1.8	8	low	$3 \cdot 10^{16}$
E [d]	M3621	11	10	3.1	1.0	2	low	$3 \cdot 10^{16}$

[a] Internal sample label, specified for future reference.
[b] Porosity refers to the density of nanosized voids, measured by Fourier-transform infrared (FTIR) spectroscopy from the ratio of high and low hydrogen stretching modes (HSM, 2090 1/cm and LSM, 2000 1/cm), as described in refs. [255, 256].
[c] Spin concentrations, measured by quantitative EPR (see section 2.1) of the DB-defect resonance. For the light-soaked sample D, quantitative EPR measurements were repeated before and after recording the TREPR spectrum, yielding similar results.
[d] Light-soaked samples, which were illuminated for 400 h under an AM1.5 solar simulator at $T = 50$ °C.

map and the electrically detected nutation pattern, obtained from ED-Rabi and -PEANUT experiments, is observed (compare fig. 6.10). This further supports the assumption of the same paramagnetic species being detected by both EPR and EDMR.

6.7.4 Comparison of different a-Si:H samples

Transient-EPR experiments revealed the presence of both weakly and strongly bound light-generated excitons, affecting charge separation in a-Si:H. The correlation between TREPR and EDMR signatures further suggests that the paramagnetic species detected by EPR also induce the spin-dependent transport channels that cause resonant photocurrent changes. To examine whether these states are universal properties of a-Si:H or specific to material properties, we recorded TREPR signals of a-Si:H samples of differing morphology and electronic quality induced by different preparation conditions.[1]

All a-Si:H powder samples prepared by RF-PECVD, as described in ref. [163]. Deposition conditions were chosen such that a significant variation of the electronic quality and the nanoscopic morphology is assured between different samples. Therefor, the hydrogen/silane gas-flow-rate ratio $R = [H_2]/[SiH_4]$, the RF power density P_{RF}, determining the deposition rate r_D, and the pressure p were varied during deposition. An increased silane dillution R is known to produce a-Si:H with enhanced light-soaking stablity [284, 285], while a higher deposition rate increases the porosity by introducing nanosized voids, yielding a higher defect density and a reduced light-soaking stability [163, 255, 256, 286]. Furthermore, a-Si:H processed at high pressure has been found to exhibit an increased bandgap and enhanced light-soaking stability, resulting in high open-circuit voltages and efficiencies when used as an absorber layer in solar-cell devices [256, 287]. The deposition conditions for the measured samples are summarized in tab. 6.2.

The TREPR signals obtained from samples A–C, measured under equal conditions (laser wavelength $\lambda_L = 670$ nm and pulse energy $E_L = 1.3(2)$ mJ, MW-power attenuation of 35 dB and temperature $T = 80$ K), are shown in figs. 6.21a–c. All samples show the

[1] Transient EPR spectra presented in the previous sections are from the same intrinsic a-Si:H powder sample, prepared at Forschungszentrum Jülich, as described in ref. [253]. Spectra discussed in this section were provided by the group of M. Zeman at the Delft University of Technology. Comparing samples prepared at different research centers corroborates the universal nature of our findings.

characteristic signatures of strongly bound TEs, weakly coupled CT excitons and dissociated electrons and holes. Figure 6.21d shows the non-resonant background signals of all three samples, which have been subtracted from the TREPR spectra. These background signals, following the laser flash, arise due to dielectric heating of both the MW resonator and the sample, which is reflected in a change of the resonator impedance and quality factor. At comparable laser-pulse intensities, the amplitude of the background signal thus provides an indicator for the sample conductivity. As expected, we observe the highest background signal for sample A, which exhibits a low density of nanostructural voids and the lowest DB-defect density, while the lowest background signal is observed for sample C, which features the highest defect density and nanostructural quality.

For a comparison of TREPR signal intensities, single time- and field-domain slices of the three samples are shown in figs. 6.21e–g. The resonances of TEs and weakly coupled CT states exhibit almost equal intensities for all three samples (figs. 6.21f and g). Only at $B_0 = 342$ mT, where the resonance of dissociated electrons and holes is observed, a significantly lower signal intensity is observed for sample C (fig. 6.21e). This can be explained by a decrease of the charge-carrier density due to enhanced recombination via DB defects, as the DB density of sample C is by an order of magnitude larger than for the other two samples (see tab. 6.2). Note that the variation of SNRs (figs. 6.21a–c) can be attributed to

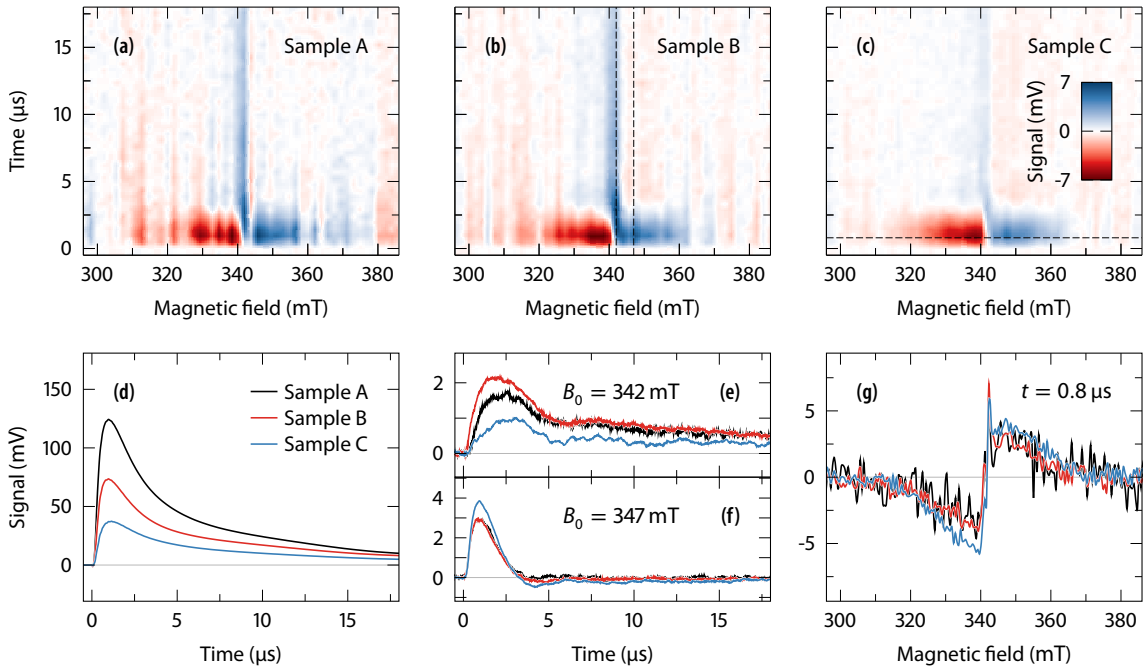

FIGURE 6.21 Comparison of the TREPR spectra and signal intensities of instrinsic a-Si:H samples with varying structural and electronic properties. (a–c) Transient-EPR spectra of samples A–C (compare tab. 6.2). The samples were measured as deposited, *i. e.*, without application of light-soaking. All spectra were recorded under comparable experimental conditions ($T = 80$ K, $\lambda_L = 670$ nm, $E_L = 1.3(2)$ mJ, MW attenuation 35 dB). (d) Non-resonant background signals, arising as a result of dielectric sample heating. These baselines have been subtracted from the TREPR signals, but serve as an indicator of the sample conductivity. (e, f) Time-domain TREPR signal at magnetic-field positions corresponding to the maximum amplitude of either the uncoupled electron/hole or the TE resonance. (g) Field-domain cross sections at a fixed time $t = 0.8$ µs after the laser pulse, where the TE resonance is maximum. Despite the distinctively different sample morphologies and conductivities, an almost equal intensity and shape of the TE signal is observed.

the different amplitudes of the subtracted background signals, causing varying strengths of residuals remaining from an imperfect background subtraction.

In fig. 6.22, analogous TREPR spectra of samples D and E are shown. These samples have been light-soaked for 400 h under an AM1.5 sun simulator, previous to the TREPR experiments. For both samples, light-soaking led to an increase of the DB spin density (from $n_S = 1 \cdot 10^{16}$ to $3 \cdot 10^{16}\,1/\mathrm{cm}^3$ for sample D, and from $2 \cdot 10^{15}$ to $3 \cdot 10^{16}\,1/\mathrm{cm}^3$ for sample E), as determined by quantitative EPR. This light-induced degradation is a result of the creation of metastable defects due to the Staebler-Wronski effect (SWE), although the responsible microscopic mechanism is not understood yet, even after 40 years of extensive research (see section 3.2.2). Note that sample D has been prepared under high pressure ($p = 8$ mbar) and from highly H_2-diluted silane ($R = 50$), both known to produce a-Si:H that makes for highly efficient solar-cell absorbers with enhanced light-soaking stability [256, 287]. This explains the stronger relative increase of the DB density of sample E.

Both signals feature the same characteristic shape and dynamics found for the as-deposited samples. Slightly different intensities are observed for the resonances of separated electrons and holes (fig. 6.22c) and for the TE signal (figs. 6.22d and e). However, regarding the different sample masses ($m_D = 4$ mg, $m_E = 11$ mg) and slightly differing light intensities during the aquisition of both spectra ($E_L^D = 0.6$ mJ, $E_L^E = 0.8$ mJ), we cannot decide whether the different intensities are related to actual sample properties. A systematic comparison of as-deposited and light-soaked samples is yet to be done.

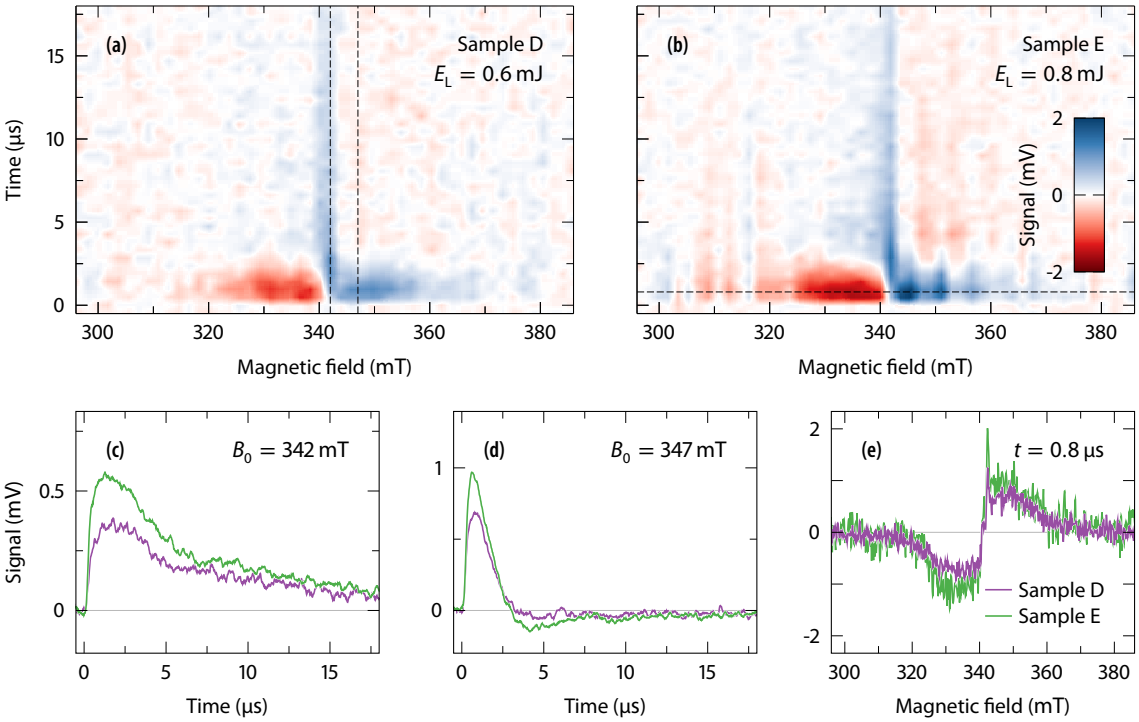

FIGURE 6.22 Transient EPR spectra of light-soaked samples D and E, recorded at $T = 80$ K after a laser flash of energy E_L and wavelength $\lambda_L = 670$ nm. (a, b) Two-dimensional signals, (c, d) time-domain and (e) field-domain traces exhibit similar line shapes as observed for the as-deposited samples in fig. 6.21 (section 6.7.1). An unambiguous comparison of absolute signal intensities is not possible due to the different sample size ($m_D = 4$ mg, $m_E = 11$ mg) and slightly different light intensities.

6.7.5 Conclusion

Using TREPR, we were able to prove the existence of strongly and weakly coupled excitonic states in instrinic a-Si:H, forming after light excitation of geminate *e-h* pairs. The time resolution of TREPR allowed to follow the charge-separation process in a-Si:H on a microsecond time scale. Comparable signal intensities were found in as-depsited and light-soaked samples of varying morphology, defect density and light-soaking stability, resulting from distinctively different preparation conditions. This suggests that excitonic states are a universal feature of a-Si:H, which is consistent with an assignment to the intrinsic charge-separation mechanism of a-Si:H.

From these findings, the central role of the observed CT excitons for the yield of free charge carriers that contribute to electronic transport has become evident. Backreaction of the geminate singlet exciton into a strongly dipolar coupled TE via ISC is identified as a mechanism that interferes with efficient charge dissociation. Comparison to the line shapes of EDMR and ODMR signatures of TEs indicates that the same states are observed. In ODMR, the TE resonance is due to spin-dependent radiative recombination [233, 242, 243, 246, 265], identifying TE formation as a major loss channel of geminate pairs. This is supported by the observation of distinct recombination lifetimes by QFRS, which were assigned to singlet and triplet excitons [206, 210]. It is tempting to assign these recombination channels to the CT and TE states identified by TREPR.

Turning back to the EDMR results presented in this chapter, we have shown that the line shape of the TREPR signal is in excellent agreement with the TE distance distribution derived from the EDMR half-field resonance. Moreover, transient Torrey oscillations revealed a nutation-frequency-resolved TREPR spectrum, almost identical to the nutation-frequency maps obtained from ED-Rabi and -PEANUT experiments. This clearly suggests that the transport channel probed by EDMR is mediated by the same TEs. The mechanism that causes the resonant photocurrent change, however, is still to be uncovered. We will adress this issue in the following section, where we employ electrically detected double-resonance techniques to prove the existence of a three-particle Auger-like recombination process that gives rise to the EDMR signal.

6.8 ELECTRICALLY DETECTED ELDOR

The shape of the TREPR resonance, exhibiting both emissive and absorptive features, provides a clear identification of spin-polarized TEs, created from a geminate light-excited singlet exciton via ISC. The correlation between EDMR and EPR line shapes suggests that the same light-generated excitons cause the spin-dependent transport channel probed by EDMR. From the similarity between electrically (section 6.4) and optically (ref. [246]) nutation measurements, we further conclude that the same TEs also provide the radiative recombination channel causing the ODMR signal. However, as already mentioned earlier, geminate recombination does not affect photoconductivity, as charge carriers contributing to the photocurrent must necessarily have escaped the photo-excited pair. An additional spin-dependent transport or recombination channel must thus be present to explain the EDMR signal.

Two possible scenarios arise that could explain a current-enhancing EDMR signal originating from geminate TEs: (i) spin-dependent dissociation of the geminate TE, yielding

separated electrons and holes, which can contribute to the photocurrent; or (ii) spin-dependent non-radiative recombination of the TE, involving an additional bound charge carriers, which is released in a three-particle Auger-like recombination process. Similar processes have recently been identified in organic semiconductors [96, 288] and μc-Si:H [98]. Moreover, combined PC and PL studies on a-Si:H indicate the presence of a non-radiative Auger-recombination channel at low temperatures, due to a quenching of the PL at temperatures $T < 50$ K [173, 191] (see section 3.3.1). Obvious canditates to be involved in such a three-particle process are electrons or holes trapped in CBT or VBT states in close proximity to the exciton.

Based on the experimental data presented until now, we cannot decide between either spin-dependent dissociation or a three-particle recombination process. The method of choice to investigate interactions between weakly coupled spins and thus identify a potential three-particle process is *electrically detected ELDOR (ED-ELDOR)* [22, 289]. Note that ED-ELDOR is not to be confused with the pulsed ELDOR experiment, also referred to as *double electron-electron resonance (DEER)*, which is well known from EPR [34]. Electrically detected ELDOR qualitatively detects couplings between electron spins involved in a spin-dependent transport or recombination process, while PELDOR quantitatively measures dipolar coupling strengths between interacting paramagnetic states.

The ED-ELDOR sequence has been employed to demonstrate the existence of spin-dependent recombination channels betweeen phosphorus-donor and Si/SiO_2 interface states [22], as well as oxygen-vacanvy complexes [289] in phosphorus-doped silicon. Moreover, ED-ELDOR has recently been used to prove the existence of a spin-dependent three-particle Auger-recombination channel involving $S = 1$ excitons and $S = 1/2$ CBT states in μc-Si:H [98]. We will use the same approach to probe the existence of a three-particle process involving both TEs and $S = 1/2$ electrons or holes in a-Si:H.

6.8.1 Experiment and data evaluation

The principle of the ED-ELDOR experiment is schematically illustrated in fig. 6.23a. The experiment is carried out at constant magnetic field B_0 and employs a pump-probe pulse sequence using two different MW frequencies to selectively excite transitions of the interacting spin species. A pump pulse of length t_P (red) is applied at a MW frequency ν_P, which is resonant with the first spin species (A). After a time interval T, a three-pulse spin-echo-detection sequence (blue), comprising a final $\pi/2$ read-out pulse, is applied at a MW frequency ν, resonant with the second spin species (B). During the pump pulse, spins A perform a Rabi nutation at a frequency $\Omega_P = \alpha_P \nu_{1,P}$, affecting the spin-pair symmetry of coupled pairs A–B. If a coupling exists between spins A and B, the spin-pair symmetry prior to the detection sequence determines the spin-echo amplitude. Carrying out the experiment as a function of t_P will then result in an echo amplitude that oscillates at frequency Ω_P, reflecting the Rabi nutations performed by spins A.

In ED-ELDOR experiments, it is crucial to ensure selective excitation of A and B spins during pump and probe phases. In case of overlapping excitation windows, pump and probe pulses excite the same spin species, preventing an unambiguous interperation of the resulting ED-ELDOR traces. Figure 6.23b depicts the pump and probe frequencies selected with respect to the PEDMR spectrum. Under the assumption of a three-particle process involving TEs and CBT- or VBT-trapped electrons or holes, the ED-ELDOR experiment was carried out by pumping on the central narrow EDMR peak, assigned to

$S = 1/2$ CBT and VBT states, and probing on the broad TE resonance, far off the resonances of $S = 1/2$ states. Red and blue traces in fig. 6.23b indicate the excitation profiles of pump ($g \approx 2.005$) and probe ($g \approx 1.971$) π pulses, approximated by Gaussian B_1 distributions. The shaded areas mark the regions of homogeneous excitation of widths $1/t_P$ and $1/t_{Probe}$, respectively. Pump and probe frequencies were spread apart about 170 MHz, ensuring sufficiently separated excitation windows. The maximum frequency separation of pump and probe positions is limited by the bandwidth of the MW cavity. During the experiment, the resonator Q-value was about 250 (measured by recording the resonator tuning picture), yielding a resonator bandwidth of about 40 MHz, centered about the pumping frequency $\nu_P = 9.644$ GHz. Although the resonator bandwidth is significantly lower than the pump-probe frequency difference, we still found sufficient MW amplitude B_1 at the probe frequency ν. Note that different B_1 strengths were set for pump and probe pulses, by using different channels of the pulse-forming unit, aiming to achieve maximum pumping efficiency and detection selectivity at the same time.

Despite the straightforward approach of the ED-ELDOR sequence, careful data acquisition and post-processing is required to deduce reliable results from the experiment. One needs to ensure that the recorded integrated charge ΔQ indeed reflects the amplitude of the potentially modulated spin echo. This is particularly crucial in ED-ELDOR since the signal stemming from the spin echo of spins B is superimposed by an ED-Rabi-nutation signal of spin A. The initial pump pulse induces an EDMR transient oscillating at frequency Ω_P due to the variation of the pulse length t_P (gray trace[1] in fig. 6.23a). The integrated charge ΔQ will thus contain both the ED-Rabi signal of spins A and the spin-

[1]Note the different time scales of pulses and EDMR signals in fig. 6.23a. Pulse lengths are on a ns time scale, while EDMR responses decay within µs or even ms. The ED-Rabi background is thus recorded at full amplitude together with the ED-ELDOR spin-echo signal.

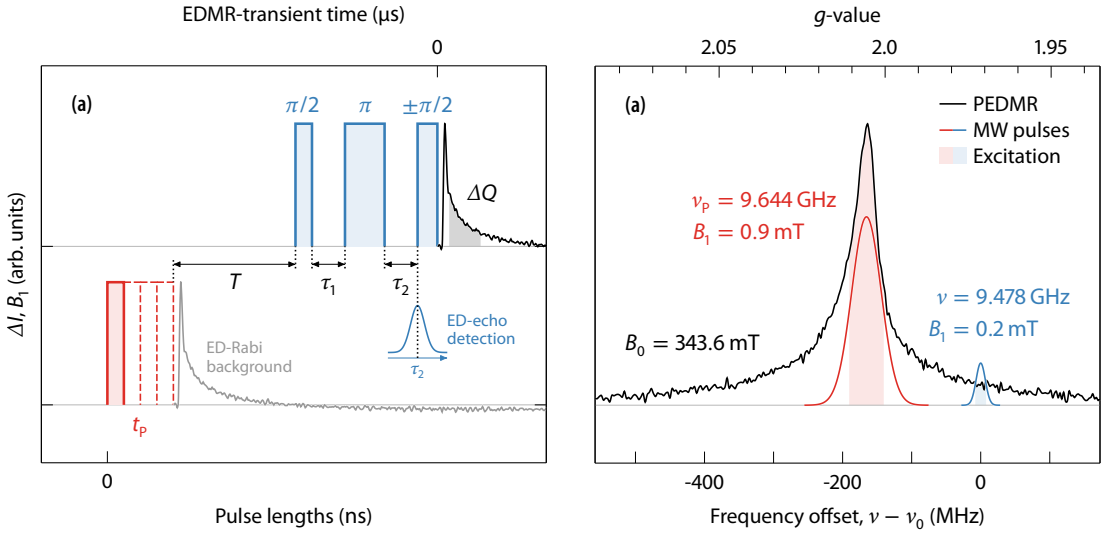

FIGURE 6.23 (a) Pulse sequence employed for an ED-ELDOR experiment. The frequency ν_P of the lower MW pulse of length t_P (red) is resonant with spins A. The upper ED-echo sequence at frequency ν matches the resonance of spins B. If a coupling exists between spins A and B, the spin-echo amplitude will be a function of the pump-pulse length t_P. (b) X-band PEDMR spectrum of a-Si:H, plotted as a function of the Larmor-frequency offset with respect to the detection frequency ν. The shaded areas mark the excitation bandwidths of pump and probe π pulses. The frequency difference needs to be sufficiently large to ensure selective pump and probe excitation windows. In the present case, the pump pulse excites $S = 1/2$ spins, while echo detection is selective the $S = 1$ exciton states.

echo signal of spins B. In presence of a coupling between the spin species, both signals are modulated with the same nutation frequency Ω_P. To remove the ED-Rabi background signal, a two-step $\pm\pi/2$ phase cycle is applied to the final read-out pulse. This results in opposing signs of the electrically detected spin echo [78] (∓ 1 for total flip angles 2π or π during the three-pulse echo sequence). Both the ED-Rabi background as well as other EDMR and non-coherent background signals will be unaffected by the phase of the read-out pulse. Subtraction of the $+\pi/2$ from the $-\pi/2$ cycle yields an echo amplitude with the sign equal to the PEDMR spectrum, while background signals are cancelled out [78, 289].

In practice, we found that phase cycling only partly removes unwanted background signals. Slight variations in temperature, illumination intensity, photocurrent and MW power in between phase cycles and small amplitude mismatches between the different channels of the pulse-forming unit result in small residuals remaining from the superimposed currents, which cannot be avoided. Unfortunately, the amplitude of the remaining background signals is still of the same order of magnitude as the ED-ELDOR-induced echo modulation. Other than, for instance, in ED-PEANUT, where we used single-point detection of ΔQ to monitor the rotary-echo amplitude, ED-ELDOR thus requires to record the entire spin echo, in order to separate echo and background signals by means of a two-dimensional baseline-correction procedure. Recording the spin echo is achieved by means of echo tomography, where ΔQ is recorded as a function of the read-out pulse position τ_2 (see section 2.5.7). Therefor, ED-ELDOR is necessarily a two-dimensional experiment that records ΔQ as a function of t_P and τ_2.

The two-dimensional ED-ELDOR signal is shown in fig. 6.24a, recorded at constant magnetic field ($B_0 = 343.6$ mT) and pump-/probe-pulse frequencies and amplitudes given in fig. 6.23b. A constant waiting time $T = 500$ ns between pump pulse and probe sequence and a dephasing time $\tau_1 = 100$ ns was used. The pulse lengths of the $\pi/2$ and π detection pulses were set to 32 ns and 64 ns, while the B_1 strength of the detection channels was adjusted accordingly to match the corresponding nutation frequency of resonant $S = 1$ states. An electrically detected spin echo is observed, centered at $\tau_2 = \tau_1 = 100$ ns (fig. 6.24d). Moreover, an oscillation along the t_P dimension is found (fig. 6.24c), with a first minimum at $t_P = 20$ ns, corresponding to the approximate π-pulse length expected for $S = 1/2$ states at the given pump-pulse B_1. The stepwise two-dimensional baseline-removal procedure required to separate this oscillation into ED-ELDOR and ED-Rabi background signals is illustrated column-wise in fig. 6.24.

Basically, the baseline correction follows the same approach used for subtracting incoherent background signals from two-dimensional PEDMR spectra (see section 4.3.2). In a first step, a linear baseline is fitted and subtracted along the t_P dimension (fig. 6.24c). The resulting baseline is shown in fig. 6.24b. This baseline comprises the non-modulated signal (both spin echo and superimposed non-modulated EDMR transients). In the second step, conversely, a linear baseline is subtracted from the remaining modulated traces along the τ_2 dimension (figs. 6.24e–h). This baseline corresponds to the modulated background signal, that is, the ED-Rabi nutation of spins A ($S = 1/2$ states) excited by the pump pulse. The remaining signal after these two baseline-removal steps contains only the modulated spin echo (figs. 6.24i–l). As an illustration, we fitted the individual echo traces with Gaussian lines centered at $\tau_2 = 100$ ns (red curves in figs. 6.24k and l). The resulting two-dimensional fit is shown in fig. 6.24j and clearly exposes the modulation of the spin-echo intensity. The superposition of the ED-ELDOR signal with both mod-

ulated and unmodulated background signal is evident from fig. 6.24. This stresses the importance of carefully recording the entire echo signal when carrying out ED-ELDOR experiment. Uncovering the ED-ELDOR signal from the superimposed background signals corroborates the reliability of our results.

6.8.2 ED-ELDOR results

Figure 6.25a shows the fully processed ED-ELDOR trace (blue), corresponding to the modulated echo intensity, which is obtained by integrating fig. 6.24i along the τ_2 axis. The ED-echo intensity is modulated with a frequency of 25(2) MHz, read off from the FFT spectrum (fig. 6.25b). This frequency is identical to the nutation frequency determined from an ED-Rabi experiment at the pump position at equal B_0, ν and B_1) (red traces in figs. 6.25a and b). This comparison shows that the observed echo-modulaton frequency corresponds to the Rabi-nutation frequency of $S = 1/2$ states ($\Omega = \nu_1$). With the echo-

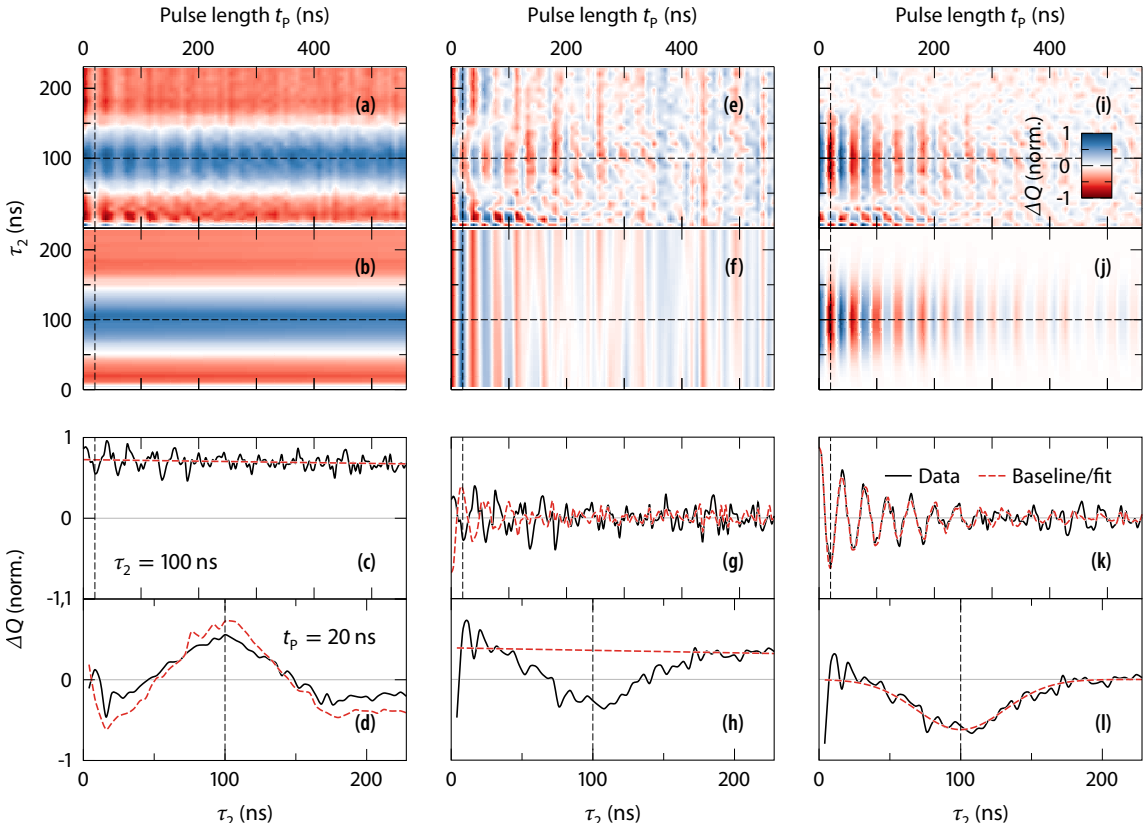

FIGURE 6.24 Illustration of the baseline-removal procedure used to separate the modulated ED-ELDOR spin-echo signal from coherent and non-coherent background signals. (a) Raw two-dimensional ED-ELDOR signal recorded by measuring ΔQ as a function of the pump-pulse length t_P and the read-out pulse position τ_2. (b) Non-modulated background signal obtained by linear fits along the t_P dimension. (c, d) Single slices taken from figs. a and b, as indicated by the dashed lines, at $\tau_2 = \tau_1 = 100$ ns, where the echo amplitude is maximum, and $t_P = 20$ ns, corresponding to the π-pulse length of the pump pulse. (e–h) Second baseline-removal step along the τ_2 dimension. A linear baseline is fitted to the edges of the echo traces (fig. h), yielding the baseline shown in fig. f. This signal corresponds to the superimposed ED-Rabi nutation of the EDMR response following the pump pulse. (i–l) Background-corrected ED-ELDOR signal containing only the modulated spin-echo intensity. The red curves in figs. k and l correspond to a fit of the echo traces with a Gaussian line centered about $\tau_2 = 100$ ns. The two-dimensional result of these fits is shown in fig. j.

detection sequence being selective to the TE resonance, the observed modulation clearly indicates a coupling between TEs and $S = 1/2$ states.

Maximum echo intensity is observed for zero pump-pulse length. In this case, the experiment corresponds to a normal ED-echo experiment on the TE resonance. The total flip angle during the echo sequence is π, such that the final TE state after the echo sequence is effectively the same state that would have been obtained by a single-pulse EDMR experiment.[1] For a coupled three-particle system that is initially in a quartet state, a flip of either the $S = 1$ or the $S = 1/2$ spin leads to an increased doublet content (see section 2.5.8). As a result, the transition rate between the two states will be enhanced, resulting in a positive echo for a current-enhancing process. For a pump pulse with flip angle π ($t_P = 20$ ns), both the $S = 1/2$ and the $S = 1$ state are flipped. This, in turn, reduces the doublet content of the three-spin system with respect to only exciting the $S = 1$ manifold. Consequently, the echo intensity is quenched, which is exactly what is observed in fig. 6.25a.

To verify our findings, we repeated the ED-ELDOR experiment with interchanged pump and probe positions. Therefor, we changed the magnetic field, such that the pump

[1]This is due to the chosen phase cycle, which *subtracts* the $+\pi/2$ (total flip angle 2π, quenching echo) from the $-\pi/2$ cycle (flip angle π, enhancing echo).

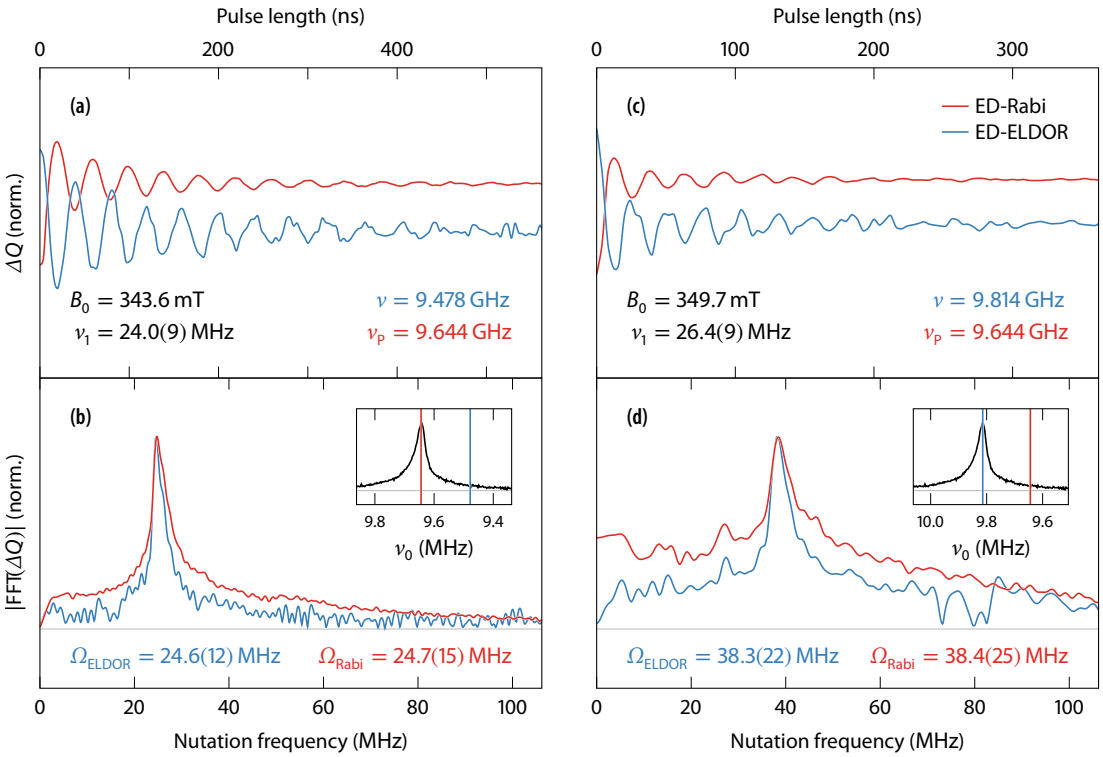

FIGURE 6.25 **(a)** Time-domain ED-ELDOR trace (blue), obtained by integrating the modulated spin echo along τ_2 (figs. 6.24i–l). The red trace shows the result of an ED-Rabi measurement at the pump position ($\nu = 9.644$ GHz) at equal B_1 strength ($B_1 = 0.9$ mT). **(b)** Frequency-domain FFT spectra of the ED-ELDOR and ED-Rabi traces. The ED-echo amplitude, detected on the TE resonance, is modulated with the Rabi-frequency of $S = 1/2$ states excited by the pump pulse. **(c, d)** Results of an equivalent ED-ELDOR experiments with reversed pump and probe positions, as indicated by the inserts in figs. b and d. The same baseline-removal procedure (fig. 6.24) has been applied to the ED-ELDOR signal. The spin echo of $S = 1/2$ states is modulated with the nutation frequency of $S = 1$ triplet states ($\Omega = \sqrt{2}\nu_1$). The experiment provides clear evidence for a spin-spin coupling between $S = 1$ excitons and $S = 1/2$ states (either CBT electrons or VBT holes).

frequency becomes resonant with the TE resonance. The probe frequency was then adjusted to match the resonance of $S = 1/2$ states (see insert in fig. 6.25d). The equivalent time- and frequency-domain ED-ELDOR and ED-Rabi traces are shown in figs. 6.25c and d, respectively. As expected, we find the echo intensity, detected on $S = 1/2$ states, to be modulated with the $S = 1$ nutation frequency ($\Omega = \sqrt{2}\nu_1$). Being able to detecting an ED-ELDOR signal in both pump/probe configurations affirms the conclusion that a coupling exists between TEs and $S = 1/2$ species.

In the above discussion, we intentionally did not specify the $S = 1/2$ coupling partner. The strong overlap between the resonances of CBT electrons and VBT holes does not allow to differentiate, which of the two potential states is coupled to the exciton. An obvious experiment to resolve this issue would be a magnetic-field-resolved ED-ELDOR measurement. From the relative FFT amplitudes under different resonance conditions, one might be able to conclude on the coupling partner. Since a single ED-ELDOR trace already requires a two-dimensional measurement, field-swept ED-ELDOR would have to be carried out in three dimensions. Such an experiment would, on the one hand, be time-consuming, as even the constant-field traces shown in this section already required data-acquisition times of more than ten hours. On the other hand, field-resolved ED-ELDOR measurements would also be technically demanding. In order to assure meaningful data, one would have to carefully readjust either the pump or the probe frequency when changing B_0, while keeping B_1 strengths unchanged. In the scope of this work, such a measurement has not been realized. Therefor, we can only conclude that TEs are involved in a three-particle process with either CBT electrons or VBT holes (or both).

6.8.3 Three-particle transport process

By providing evidence for a spin-spin coupling between TEs and CBT electrons and/or VBT holes, we have shown that the excitonic EDMR signal originates from a three-particle spin-dependent transport process. We propose an Auger-like recombination mechanism, as sketched in fig. 6.26. Photo-induced geminate excitons are generated in an excited singlet state (fig. 6.26a). After thermalization into the tail states, the electron-hole pair may

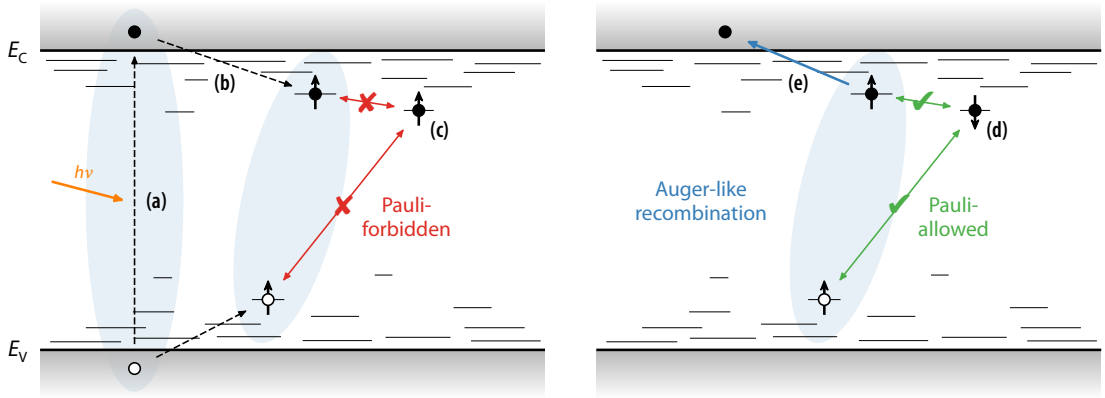

FIGURE 6.26 Illustration of a spin-dependent Auger-like three-particle recombination process, which can explain the current-enhancing EDMR signal associated with $S = 1$ triplet excitons. Filled and open circles mark negatively and positively charged electrons and holes, respectively. See text for further explanations.

be separated via the formation of an intermediate CT state, as shown by TREPR in section 6.7. Alternatively, the singlet exciton can back-react into a strongly coupled localized TE state by means of ISC (fig. 6.26b). The TE may recombine radiatively, which would not result in an EDMR signal, but could be observed by photoluminescence and ODMR. If the TE is located in proximity to a CBT electron or a VBT hole, a coupled three-spin complex can form. Transitions between the $S = 1/2$ state and the exciton will be spin-dependent, according to the Pauli-exclusion principle (fig. 6.26c). If the three-spin system forms a total quartet state (for example, a $|T_+ \uparrow\rangle$ state, as shown in fig. 6.26c), electronic transitions will be Pauli-blocked. Flipping either the triplet spins or the $S = 1/2$ spin increases the doublet content of the three-spin state ($|T_+ \downarrow\rangle$ in fig. 6.26d), and transitions between the three states become Pauli-allowed.

A number of scenarios could give rise to a current-enhancing EDMR signal. We believe that the most probable mechanism is a spin-dependent Auger-recombination process, illustrated on the right-hand side of fig. 6.26. Spin-manipulation by EPR enables *e-h* and *e-e* transitions between the TE and, for instance, the coupled CBT electron.[1] In a non-radiative *e-h* recombination process, the excess energy released by the recombination event is transferred to the remaining electron. The latter is thereby excited into the conduction band and leads to a resonant current increase (fig. 6.26e). Different pathways exist for a spin-dependent Auger-recombination channel between the three spins:

- Direct recombination of the CBT electron and the TE hole, releasing the TE electron, as shown in fig. 6.26e. The transition rate depends on the doublet content of the total three-spin state.
- Spin-dependent tunneling of the CBT electron into the CBT state of the exciton, followed by a recombination with the hole, yielding the same result.
- Recombination of the TE due to an increased ISC rate into a singlet state after a resonant spin transition $|T_\pm\rangle \rightarrow |T_0\rangle$. In this case, the excess energy would be transferred to the weakly coupled CBT electron (or VBT hole).
- Enhanced triplet-exciton recombination after a resonant spin flip of the coupled CBT electron. The mixing of states between the weakly coupled CBT spin and the TE spins can give rise to spin flip-flop processes. A resonant flip of the CBT electron can thus also induce transitions between the triplet manifold, finally increasing the ISC-mediated exciton-recombination probability.

While we cannot decide on the precise microscopic mechanism, all scenarios result in the same final state, that is, an excess charge carrier being released into the conduction or valence band, where it can contribute to photoconductivity. The result is a spin-dependent current enhancement that causes a positive EDMR signal, as observed experimentally.

Alternative explanations for a current-enhancing process via the coupled three-spin state include spin-dependent tunneling of the CBT/VBT spin through the TE site, or spin-dependent dissociation of the weakly coupled spin from the exciton. However, there are a couple of reasons that favor the Auger-recombination picture. First of all, we have already noted the close similarity between the TE signatures observed in EDMR and ODMR, clearly suggesting that the same states are observed by both methods. The pres-

[1] In fig. 6.26, we exemplarily illustrate the proposed transport process for a CBT electron coupled to the exciton. An equivalent Auger-recombination process could occur between a three-spin system formed by a TE and a VBT hole.

ence of an ODMR signal proves the existence of a spin-dependent TE recombination channel. In this case, the excess energy is released by emission of a photon, giving rise to spin-dependent photoluminescence. Such a radiative TE recombination channel has also been identified from QFRS experiments (see section 3.3.2). The presence of competing radiative and non-radiative recombination at low temperature has already been concluded from early photoconductivity and -luminescence measurements on a-Si:H (see section 3.3.1). At temperatures $T < 50$ K, a decrease of the photoluminescence was observed and assigned to a non-radiative Auger-recombination channel [173, 191, 193]. The reported temperature regime is consistent with the observed spin-dependent TE-mediated process, providing further support for the Auger-recombination model.

A final question remains regarding the contributions of the CBT and VBT resonances to the EDMR signal. Previous studies have assigned the current-enhancing signals at low temperature with spin-dependent hopping (see section 3.4.2). The above discussion, however, shows that current-enhancing CBT and/or VBT resonances can also be caused by a three-particle recombination process. This shows that the interpretation of the low-temperature CBT and VBT resonances is ambiguous. Interestingly, we found no marked differences on the signal dynamics, when deconvolving the PEDMR signals of both a-Si:H films (section 5.5.2) and *pin* solar cells (section 6.3) in the time domain. This further indicates that CBT/VBT states and TEs are involved in the same spin-dependent transport process. Our results thus suggest that a large share of the CBT/VBT resonances originates from electrons and holes that are trapped at TE sites and are involved in spin-dependent Auger recombination. Nevertheless, we cannot exclude the simultaneous presence of spin-dependent hopping channels.

6.9 SUMMARY AND CONCLUSION

In this chapter, we have studied charge transport via paramagnetic states in a-Si:H at low temperatures by means of PEDMR and TREPR spectroscopy. We have proven the presence of light-generated strongly coupled excitonic states, which give rise to both EDMR and EPR signals. Based on the similar line shapes of EDMR and TREPR resonances, we conclude that the same TE states are detected by both methods. These TEs further appear to be an instrinsic property of a-Si:H and play a central role in the fundamental charge-separation process.

For EDMR, clear evidence for an excitonic nature is provided by the characteristic nutation frequency of $\sqrt{2}\nu_1$ and the first-time observation of an electrically detected half-field resonance. Based on magnetic-field- and MW-power-dependent nutation experiments, the TE resonance can be assigned to strongly dipolar- and exchange-coupled electron-hole pairs. From the line shape of the half-field EDMR signal, we estimate a mean electron-hole distance of 5.3(2) Å, which is in excellent agreement with the dipolar coupling strength of 550(30) MHz determined from ED-Rabi-nutation measurements at half field. The excitons are thus strongly localized, expanding over only two to three Si bond lengths. Microscopically, we assign the TEs to an electron-hole pair trapped in CBT and VBT states in close proximity. This model is supported by DFT calculations, which leads to g-values and dipolar coupling strengths that are in excellent agreement with our experimental data. The spin-dependent current-enhancing process associated with TEs

is described in terms of a three-particle Auger-like recombination process. Experimental proof for the involvement of a third spin is provided by ED-ELDOR measurements. The third spin can either be a CBT electron or a VBT hole trapped in vicinity and weakly coupled to the TE. Both resonances are clearly identified at their characteristic $S = 1/2$ nutation frequency by means of field-resolved electrically detected nutation experiments. Whether CBT and VBT states are also involved in spin-dependent hopping transitions cannot be unambigiously answered based on the experimental data.

Transient-EPR spectra of undoped a-Si:H exhibit characteristic resonances of TEs as well as weakly coupled spin-correlated electron-hole pairs and thermalized electrons and holes. By comparing the TREPR signatures of a-Si:H samples with different structural and electronic properties (morphology, defect density, light degradation), we could show that these resonances are universal properties of a-Si:H. The TE line shape can be reproduced assuming the same exciton-distance distribution derived from the EDMR signal. Moreover, we observed transient Torrey oscillations that produce a nutation-frequency map similar to the one obtained from ED-PEANUT measurements. This suggests that the same TEs are detected by EPR and EDMR, The existence of a TREPR signal clearly indicates that the TEs are geminate, that is, electron-hole pairs created by the same photon. The dynamics of the TREPR signal allows to correlate the states to the charge-separation mechanism in a-Si:H at low temperatures. After light excitation of singlet excitons, weakly coupled spin-correlated charge-transfer states form. Electrons and holes can only contribute to conductivity after dissociation of the CT state. By means of intersystem crossing, excited singlet excitons can also back-react to strongly coupled, localized TEs, impeding the separation of electrons and holes.

Our EDMR results have shown that TEs provide a non-radiative Auger-recombination channel. In addition, ODMR measurements on a-Si:H have revealed excitonic radiative recombination channels (see section 3.4.3). As for EDMR in this work, ODMR measurements have detected a half-field resonance, providing evidence for $S = 1$ triplet states [242, 243, 245]. Moreover, pulsed-ODMR nutation measurements have produced magnetic-field/nutation-frequency maps that are strikingly similar to our EDMR results [246–248]. We thus conclude that radiative TE recombination occurs via the same geminate excitons observed in EDMR and TREPR.

Radiative excitonic recombination channels have also been identified by photoluminescence experiments (see section 3.3.2). Characteristic lifetimes were identified by QFRS that are independent of the charge-carrier-generation rate, which is indicative of radiative geminate-pair recombination [193, 208–212]. These lifetime peaks were assigned to singlet and triplet excitons. It seems natural to assume that these PL lifetime peaks correspond to the same excitons measured by EDMR/ODMR and TREPR. Clearly proving this correlation, however, remains a challenging task. The lifetimes measured by QFRS cannot directly be compared to those detected by EDMR or TREPR. Transient-EPR signal dynamics are not only determined by recombination lifetimes, but also by spin relaxation. The dynamics of PEDMR signals are complicated functions of recombination and dissociation rates and can also not be directly related to QFRS lifetimes. Nevertheless, the similarity between the EDMR/ODMR signals and the TREPR line strongly suggests that both radiative and non-radiative spin-dependent exciton recombination originates from geminate pairs, which renders a common origin of all excitonic recombination channels in a-Si:H very probable.

The experimental techniques applied in the course of this chapter have illustrated the capability of modern PEDMR techniques to unravel the microscopic nature of electronic tranport channels via localized paramagnetic states based on their spin dependency. This methodology is not limited to a-Si:H, but can be used to elucidate the physical mechanisms of charge-carrier transport and recombination in any organic or inorganic material that exhibits spin-dependent electronic transitions. In particular, the novel ED-PEANUT detection scheme presented in this chapter may help to identify paramagnetic species involved in spin-depedendent transitions.

CHAPTER 7

Charge-carrier recombination at room temperature

After evaluating the spin-dependent transport channels in a-Si:H at low temperatures, this final experimental chapter presents preliminary results obtained on a-Si:H at room temperature. We show multifrequency PEDMR spectra and ED-Rabi nutations of a-Si:H pin solar cells, which allow to narrow down the spin-dependent DB-related recombination channel to transitions between weakly coupled neutral DBs and electrons that are either directly captured from the conduction band or trapped in vicinity to the DB defect.

7.1 INTRODUCTION

The EDMR experiments of chapter 5 revealed two temperature regimes of spin-dependent transport and recombination in a-Si:H. At low temperatures, a current-enhancing signal is observed, which has been studied in great detail in the previous chapter. With increasing temperature, a current-quenching EDMR signal becomes visible, which is dominating for temperatures $T \gtrsim 70$ K. This signal has commonly been assigned to spin-dependent recombination via DB defects. Non-radiative recombination via DBs has already been identified as the major loss channel for light-generated charge carriers in a-Si:H from early photoconductivity and -luminescence studies [192]. In addition, DB defects are known to be closely related to the light-induced degradation of a-Si:H (see section 3.2.2). As a result, the DB defect in a-Si:H has been amongst the most thoroughly studied paramagnetic centers in amorphous solids within the last fifty years. Despite this extensive research, many question concerning the nanoscopic structure of DBs, their relation to the SWE and their role as recombination centers still remain unanswered.

One of these anbiguities concerns the physical mechanism of DB-related recombination. The associated EDMR signal at $g \approx 2.005$ has been interpreted in terms of the capture of electrons trapped in the band tails by neutral DBs, followed by the capture of a hole to complete the recombination cycle. The additional presence of a VBT resonance has been explained by spin-dependent diffusion of holes in the valence-band tail towards the DB, enhancing the recombination rate [60] (see section 3.4.1). Although this model has been widely accepted [27, 61, 72, 225] and is consistent with the spectral contributions to the EDMR signal, alternative models for DB-related recombination have been proposed that can also explain the experimental data.

Under sub-bandgap illumination, a g-value shift from $g = 2.0050$ to $g = 2.0062$ has been observed [241], indicating an increased contribution of VBT holes. This has been explained with a shift of the dominant recombination mechanism from transitions towards tunneling of holes into neutral dangling bonds, followed by the capture of an electron [17]. The presence of both e-D^0 and h-D^0 transitions could also explain the results

of our multifrequency EDMR study of a-Si:H films in chapter 5. For a spin-dependent e-D^0 transition, one would expect equal spectral intensities of the resulting CBT and DB resonances. However, we found that the relative intensity of the DB resonance is much larger than the intensity of the CBT line and is rather close to the combined CBT and VBT íntensity. Alternatively, direct capture of electrons from the extended conduction band into neutral DBs has been proposed as the dominant recombination mechanism at room temperature [113, 238]. This model is supported by a shift of the g-value from about $g = 2.0050$ at intermediate temperatures (100–150 K) towards the pure DB g-value ($g = 2.0055$) at room temperature [290]. We observed a similar effect in chapter 5, where we found a significant increase of the relative DB-resonance intensity for temperatures $T \geq 150$ K. Direct capture also appears reasonable based on the temperature dependency of electronic transport in a-Si:H. Whereas at low temperatures, transport predominantly occurs within the tail states, increasing the thermal energy more and more shifts the transport path into the extended states for $T \gtrsim 100$ K (see section 3.3.1).

Solely based on the EDMR line shape, it is not possible to verify either of the different microscopic models. However, as demonstrated in the previous chapter, modern PEDMR techniques allow to directly identify coupling partners involved in spin-dependent pair processes based on electrically detected nutation experiments. Such measurements, conducted at room temperature, are presented in this chapter, aiming to approach one of the central unanswered questions regarding electronic transport in a-Si:H, that is, the microscopic nature of the most prominent recombination process.

7.2 MATERIALS AND METHODS

The experiments presented in this chapter have been carried out on an a-Si:H *pin* solar cell of the same type as used in the previous chapter. The sample structure and preparation procedure is summarized in section 4.1.1. Figure 7.1 shows the dark current-voltage

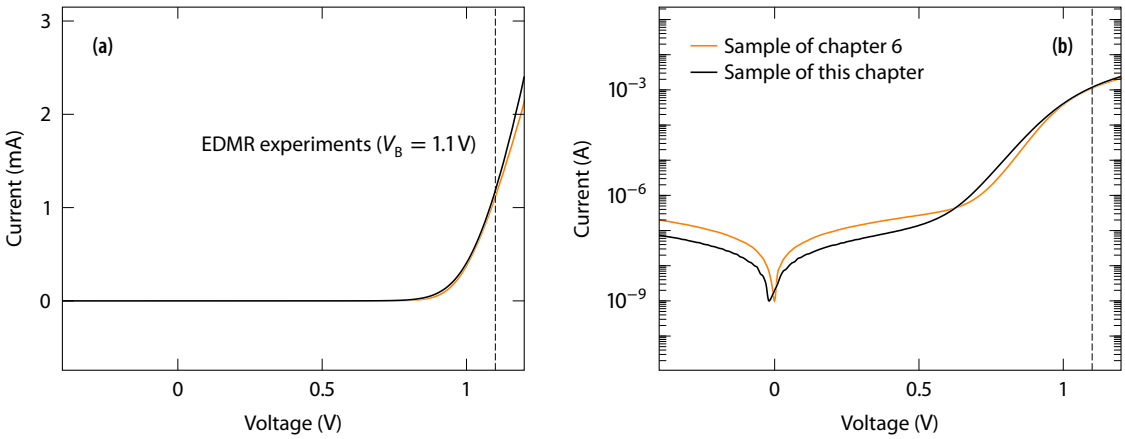

FIGURE 7.1 Room-temperature dark current-voltage characteristics of the a-Si:H *pin* solar cell studied in this chapter, plotted on (a) a linear and (b) a logarithmic current scale. The curve was recorded with the sample inserted into the X-band EDMR setup. For comparison, the orange lines plot the dark *I-V* curve of the sample investigated in chapter 6, which was of the same batch of EDMR samples. The EDMR experiments presented in this chapter were conducted in the dark under forward-bias conditions (V_B = 1.1 V), as indicated by the dashed lines.

characteristics of the sample used for the measurements discussed in this chapter. For the sake of comparison, the figure also includes the dark *I-V* curve of the *pin* solar cell investigated in the previous chapter, which was of the same sample batch.

Qualitatively, both samples exhibit similar *I-V* characteristics, such that we will not repeat the discussion of the different voltage regimes that can be identified from the dark *I-V* curve (see section 6.2.1). The EDMR experiments presented in this chapter were carried out in the dark under strong forward-bias conditions ($V_B = 1.1\,V$). In this regime, earlier EDMR studies on a-Si:H *pin* solar cells have revealed that electronic transport in the intrinsic a-Si:H layer is predominantly caused by drift of charge carriers along an internal electric field that is determined by the strong injection of charge carriers [68, 238]. The current is limited by the series resistance of the device, which is increased by an enhanced recombination rate. Therefor, in this regime, strong current-quenching EDMR signals are typically observed, yielding high SNRs [238].

EDMR experiments were conducted at X-band and 263 GHz, using the setups described in section 4.2. As for the low-temperature EDMR measurements discussed in the previous chapter (see section 6.2.2), a small crumb of DPPH ($g = 2.0036(2)$ [269]) was attached on the sample substrate, directly next to the solar cell, and used for magnetic-field (B_0) and MW-field-stength (B_1) calibration by means of CWEPR and Rabi-nutation measurements, respectively. Unfortunately, field-calibration could only be conducted at X-band. At 263 GHz, the required EPR measurements could not be performed owing to an instrument failure after the EDMR experiment. The magnetic-field offset thus has to remain as a fitting parameter. At X-band, the calibration resulted in a magnetic-field error of 0.07 mT and a maximum B_1 strength (0 dB MW attenuation) of 1.61(4) mT.[1]

7.3 RESULTS AND DISCUSSION

In chapter 5, we recorded multifrequency PEDMR spectra of undoped a-Si:H films and used a global least-squares fitting strategy to disentangle the different resonance contributions. Here, we followed the same approach by carrying out multifrequency PEDMR on a *pin* solar cell at X-band and 263 GHz. In a second step, we conducted ED-Rabi-nutation experiments to identify coupled spins involved in the spin-dependent recombination step. Note that the results presented in this chapter have to be considered as preliminary, since they refer to ongoing research.

7.3.1 Multifrequency pulsed EDMR on *pin* solar cells

Figure 7.2 shows room-temperature X-band and 263 GHz field-swept PEDMR spectra, recorded in the dark and under 1.1 V forward-bias conditions. A current-quenching signal is observed, consistent with previous EDMR studies of a-Si:H *pin* solar cells under similar conditions [68, 238].

Both the X-band and the 263 GHz spectrum exhibit a similar shape as the corresponding room-temperature spectra of a-Si:H films (fig. 5.2). Therefor, we carried out a spectral least-squares fit, assuming the same superposition of DB and CBT/VBT resonances.

[1] Note that B_1 is slightly lower at room temperature than at cryogenic temperatures due to a lower resonator Q.

Again, we will follow a global fitting approach by calculating and fitting spectral simulations, using a single parameter set, to both spectra at once. To reduce the degrees of freedom, we did not fit any g-value, but used the values from our DFT models (section 6.6), and only fitted line-broadening parameters and spectral weights. As a result, we started from the following parameter set:

Dangling bond As in section 5.4, we use the rhombic g-tensor and an axially symmetric A-tensor for the HFI with ^{29}Si nuclei, determined by Fehr *et al.* [148] from multifrequency EPR (see section 3.2.1). Only the spectral weight was varied during the fit.

CBT state The DFT model shown in section 6.6 resulted in an almost isotropic g-value. This value was calculated based on modeling an a-Si:H/c-Si heterojunction, assuming an only 1 nm thick a-Si:H layer. For bulk a-Si:H, it can be assumed that the g-tensor becomes purely isotropic [240]. We thus set an isotropic g-value of $g = 2.0044$, which is consistent with experimental results, both of this work and previous studies. In addition, we used the g-strain parameter that was determined in section 5.4 ($\Delta g = 0.0033$). As already discussed in sections 3.2.3 and 5.4.1, HFI with ^{29}Si nuclei needs to be taken into account for the CBT resonance. An axially symmetric A-tensor was assumed, based on LEPR results of Umeda *et al.* [150] and theoretical calculations by Ishii and Shimizu [151]. As in section 5.4, A-strain parameters were adopted from the DB defect, due to the lack of literature values. The fitting parameters for the CBT resonance comprised only the spectral weight and a field-independent convolutional Lorentzian line width.

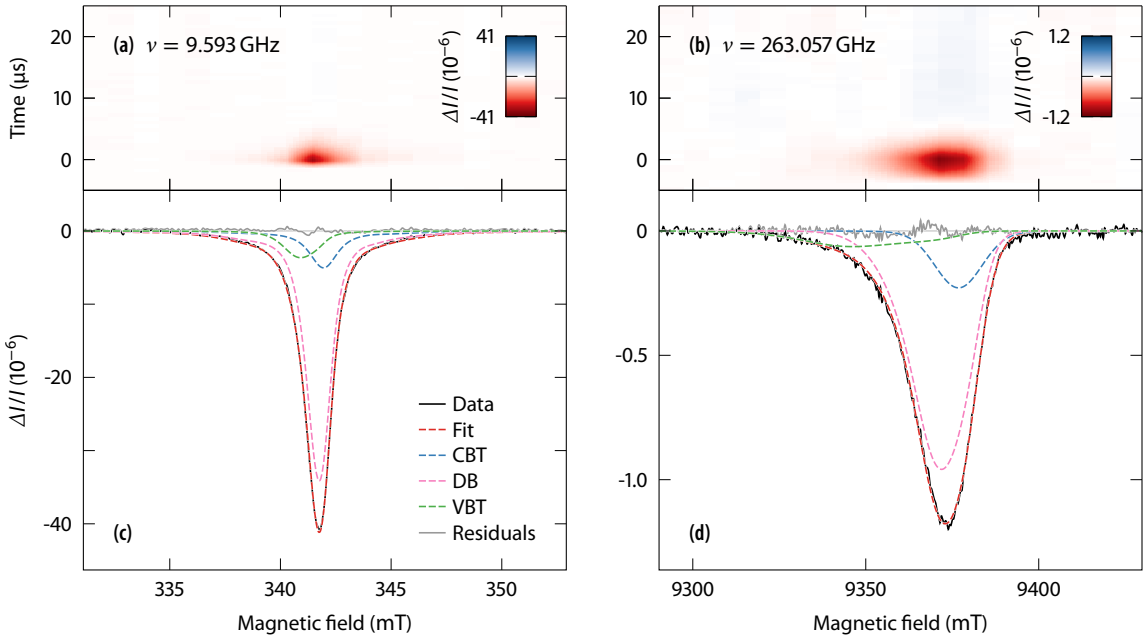

FIGURE 7.2 Room-temperature ($T = 295$ K) field-swept PEDMR spectra of an a-Si:H *pin* solar cell recorded at (a, c) X-band and (b, d) mm-waveband under dark, forward-bias ($V_B = 1.1$ V) conditions. Figures a and b show the two-dimensional PEDMR spectrum, recorded by measuring the transient current response after the MW pulse as a function of the external magnetic field. Figures c and d correspond to the field-domain cross sections immediately after the MW pulse ($t = 0$), where the maximum relative current change is observed. The dashed lines show the result of a spectral least-squares fit, assuming a superposition of DB and CBT/VBT resonances (see text for discussion).

TABLE 7.1 Spin-Hamiltonian and line-broadening parameters obtained from globally fitting the room-temperature X-band and 263 GHz PEDMR spectra of a-Si:H *pin* solar cells. Principal values of the *g*- and *A*-tensor are listed together with the respective strain values (FWHM of a Gaussian distribution), the latter given in parentheses. Values printed in gray were kept fixed during the fit, while black-colored values denote fit parameters.

	g-tensor			*A*-tensor (MHz)		Line width [a] (mT)		Weight [b]
	g_x or g_{iso} (strain)	g_y (strain)	g_z (strain)	a_{iso} (strain)	T (strain)	ΔB_0^G	ΔB_0^L	
CBT	2.0044 (0.0033)	-	-	200 (70)	40 (24)	-	0.87	0.15
VBT	2.0140 (0.0086)	2.0124 (0.0039)	2.0047 (0.0025)	-	-	-	0.27	0.10
DB	2.0079 (0.0054)	2.0061 (0.0024)	2.0034 (0.0018)	190 (70)	39 (24)	0.13	0.43	0.75

[a] Field-independent convolutional broadening using a Voigtian line shape with Gaussian and Lorentzian FWHM ΔB_0^G and ΔB_0^L, respectively. An additional Lorentzian line-broadening function ($\Delta B_0^L = 0.4$ mT) was applied to the X-band spectrum to account for MW-power broadening.
[b] Integrated spectral intensities normalized to sum to unity. Fitting errors are in the order of 30–40 %.

VBT state DFT model calculation of VBT holes revealed a rhombic *g*-tensor anisotropy. This result is consistent with earlier experimental results obtained from both EPR [149, 150] and EDMR [26]. In the previous chapters, we did not take *g*-tensor anisotropy into account, but assumed an isotropic *g*-value of 2.01, which is, however, in excellent agreement with the average *g*-value obtained from the DFT model. Here, we used the calculated *g*-tensor and only fit *g*-strain parameters. Hyperfine interactions were not considered, since they were found to be negligible for the VBT resonance [150, 151]. The fitting parameters for the VBT resonance were thus the *g*-strain parameters, a field-independent Lorentzian line width and the spectral weight.

In addition to the component-wise line-broadening and weighting parameters, a field-offset parameter for the uncalibrated magnetic-field axis of the 263 GHz spectrum, and a global convolutional Lorentzian line-broadening for the X-band spectrum, which accounts for MW-power broadening, were required. Note that we only used a single set of spectral weights for both the X-band and the 263 GHz spectrum. This constraint significantly reduces the degrees of freedom and is reasonably justified by the fact that we found equal weight distributions for the multifrequency room-temperature spectra of a-Si:H films in section 5.4.[1] The fitting routine was implemented in MATLAB using the EasySpin toolbox [43] for simulating solid-state powder-EPR spectra. The fit function is based on the `esfit` method provided by EasySpin and uses a Nelder-Mead downhill-simplex algorithm for non-linear least-squares optimization.

The parameter set obtained from the fit is listed in tab. 7.1. The resulting simulated X-band and 263 GHz spectra are included in figs. 7.2c and d, respectively. Note that we do not explicitly state error margins of the fitted parameters. Precise estimations are not possible without the use of numerical procedures such as bootstrapping (see section 4.4.2), which become extensively time-consuming for multi-parameter spectral simulations. By varying the starting parameters and altering the fitting model (*e. g.*, by varying the line-

[1] To allow for a more granular fitting model, which also takes into account a potential frequency/field dependence of the spectral contributions of DB and CBT/VBT resonances, further EDMR spectra at additional excitation frequencies are required. Moreover, frequencies below X-band would also enable a more explicit characterization of the field-independent line broadenings. Such experiments have already been initiated and will allow for an improved line-shape analysis in the near future.

broadening functions or by replacing the rhombic VBT g-tensor by an isotropic g-value), we found variations of the line-broadening and weighting parameters on the order of 30–40 %, while obtaining simulations that were all in good agreement with the experimental spectra.

Despite these fairly large error margins, the fit qualitatively produced a stable result, concerning the relative distribution of spectral weights: We generally observed a convergence of the fit towards a significantly larger weight of the DB resonance compared to the CBT and VBT components. The same observation was already made in chapter 5 for the EDMR signal of a-Si:H films at temperatures above 150 K. Previous authors similarly reported a g-value shift from $g = 2.0050$ to $g = 2.0055$ with increasing temperature [290], indicating a weighting towards to pure DB resonance. This result does not appear consistent with a spin-dependent recombination model based on either an e-D^0 or an h-D^0 transition, followed by the (spin-independent) capture of a hole or an electron, respectively. For both cases, one would expect equal contributions of both spin-pair constituents. Lips *et al.* [290] explained the g-value shift based on a rate-equation model, considering the effect of different DB and CBT spin-lattice relaxation times (T_1) on the EDMR signature of the e-D^0 transition: Whereas the T_1 relaxation of DBs exhibits only a slight temperature dependency, T_1 changes by orders of magnitudes for tail-state electrons and holes [150, 291]. As a result, the contribution of the CBT resonance is diminished with increasing temperature. As already stated in chapter 5 and section 7.1, an alternative explanation could be a coexistence of spin-dependent e-D^0 and h-D^0 recombination channels. In addition, direct capture of electrons from the conduction band could explain the increased DB content at room temperature. A transition from tunneling of tail states into defects towards direct capture has also been proposed to explained a similar temperature dependency of the EDMR line shape of μc-Si:H *pin* solar cells [238, 292].

To narrow down the possible explanations for the observed EDMR line shape at room temperature, it is inevitable to identify the coupling partners of the spin-pair underlying the electronic transition. Pulsed EDMR techniques provide this capability. Particularly useful information can be obtained, when varying the MW power in a PEDMR experiment, as shown in the following.

7.3.2 Microwave-power-dependent EDMR spectra

Figure 7.3 shows X-band PEDMR spectra recorded as a function of the MW-field amplitude B_1. The lengths of the MW pulses were adjusted to match the π-pulse lengths of $S = 1/2$ states. As a result, pulse lengths varied between 136 ns at $B_1 = 0.13$ mT (uppermost spectrum) and 18 ns at $B_1 = 1.02$ mT (bottommost spectrum), corresponding to excitation bandwidths of about 0.3 mT and 2.0 mT, respectively. Note that the spectrum at $B_1 = 0.13$ mT corresponds to the same X-band spectrum that was analyzed in the previous section. For reference, the fit result of fig. 7.2c is thus included in fig. 7.3c.

At low MW powers ($B_1 \lesssim 0.4$ mT), the spectrum consists of a single peak that becomes slightly broadened with increasing B_1 (MW-power broadening). At higher MW powers ($B_1 \gtrsim 0.5$ mT), a dip appears in the center of the spectrum. This dip is characteristic for spin-locking conditions [92], which occur if the two spin-pair constituents involved in the spin-dependent transition are excited simultaneously (see section 2.5.6). In this case, the singlet and triplet content remains unchanged, since the total spin-pair-state density is only shifted between the triplet eigenstates $|T_+\rangle$, $|T_0\rangle$ and $|T_-\rangle$ [88, 293, 294].

Spin-dependent transitions can still occur due to an increased intersystem-crossing rate between the $|T_0\rangle$ and $|S\rangle$ state (see section 7.3.3). However, the overall transition rate decreases under spin-locking conditions, such that the EDMR signal becomes quenched, resulting in the characteristic dip [92].

In fig. 7.3c, vertical lines are included that mark the average g-values of DB defects ($g = 2.0055$), CBT electrons ($g = 2.0044$) and VBT holes ($g = 2.0104$), according to the fitting model described in the previous section. A close comparison with the center position of the dip indicates an alignment with the center of the DB resonance. This observation is consistent with our findings from the previous section, indicating a dominant distribution of DB defects. Note, however, that conclusions based on the dip position need to be drawn with care. Taking into account field-calibration, read-off and MW-frequency uncertainties, we find the center of the dip at a magnetic field of 341.75(12) mT (marked by the shaded area in fig. 7.3c), corresponding to $g = 2.0056(7)$. Considering the error margin, the dip is consistent with both the pure DB g-value, and the average value $g = 2.0050$ that would be expected for spin locking of a coupled CBT/DB pair. Under the assumption that spin locking is the origin of the dip, we can conclude that either e-D^0 tunneling transitions or direct capture of charge carriers into DB defects cause the spin-dependent recombination channel. On the contrary, h-D^0 transitions seem less likely, as spin locking would be expected to appear at maximum overlap of the VBT and DB resonances at $g \approx 2.008$.

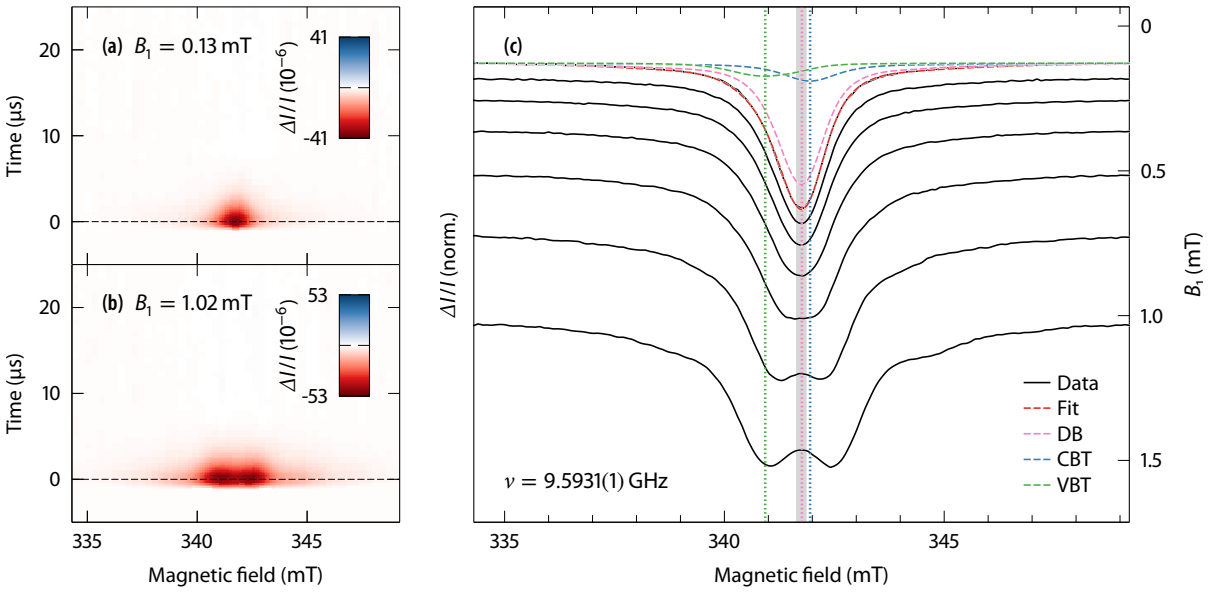

FIGURE 7.3 Dependence of the X-band PEDMR spectrum on the MW-field amplitude B_1. **(a, b)** Dark-current forward-bias PEDMR signals at low and high B_1 as indicated. **(c)** Field-domain cross sections through the two-dimensional PEDMR signal maps, taken immediately after the MW pulse ($t = 0$), as indicated by the dashed lines in figs. a and b. All spectra are normalized to equal amplitude and plotted such that the baselines indicate the value of B_1. The dashed curves show the spectral fit result from fig. 7.2c. Vertical dotted lines mark the mean g-values of DBs ($g = 2.0055$), CBT electrons ($g = 2.0044$) and VBT holes ($g = 2.0104$). The shaded gray area marks the center of the characteristic dip ($B_0 = 341.75(12)$ mT), which emerges at high B_1 and serves as an indicator for spin locking of a coupled spin pair due to simultaneous excitation, taken into the account read-off and magnetic-field-calibration uncertainties (see text for discussion).

While the change of the PEDMR line shape as a function of B_1 serves as an indicator of spin-locking conditions, more direct evidence can be obtained from ED-Rabi-nutation measurements (see section 2.5.6). Spin locking should result in a characteristic $\Omega = 2\nu_1$ nutation-frequency component, also referred to as Rabi-beating [19, 21, 92, 295]. Such room-temperature ED-Rabi experiments are presented in the next section.

7.3.3 Room-temperature ED-Rabi nutations

Figure 7.4a shows ED-Rabi-nutation traces, recorded by measuring the integrated charge ΔQ after a single MW pulse as a function the pulse length t_P (see sections 2.5.6 and 6.4.1). All traces were measured at fixed MW frequency and magnetic field ($g \approx 2.0055$), under variation of the MW-field amplitude B_1. The resulting frequency-domain FFT spectra are shown in fig. 7.4b. At low MW powers ($B_1 \lesssim 0.4$ mT), a single Rabi-frequency components is observed. Linear regression of the nutation frequencies, read off from the peak positions in the FFT spectra, yields a nutation-frequency coefficient $\alpha = \Omega/\nu_1 = 1.0(1)$, where $\nu_1 = g\mu_B B_1/h$ is the precession frequency of $S = 1/2$ spins about the MW-field vector $\boldsymbol{B}_1$. This characteristic nutation frequency accordingly stems from a spin-dependent transition involving weakly coupled $S = 1/2$ spin pairs (see section 2.5.6).

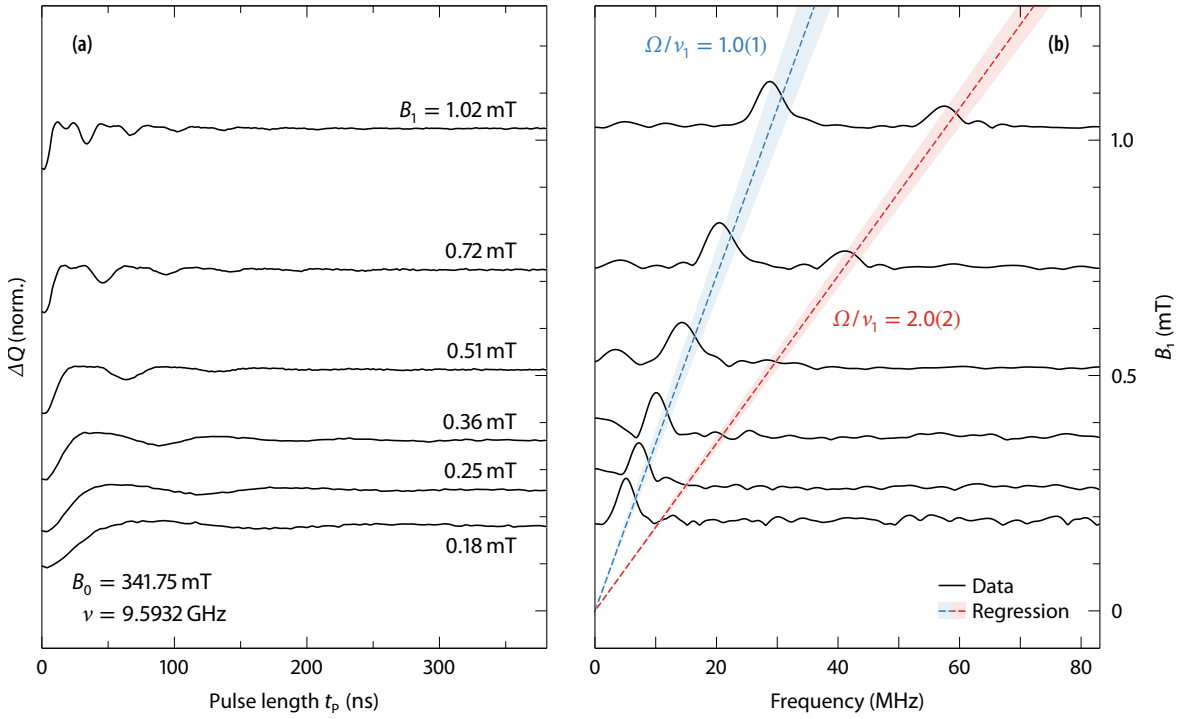

FIGURE 7.4 Room-temperature X-band ED-Rabi nutations as a function of the MW-field amplitude B_1, recorded at the center of the EDMR resonance ($g \approx 2.0055$). (a) Time-domain ED-Rabi traces, measured by recording the integrated charge ΔQ of the transient dark-current change ΔI as a function of the MW-pulse length t_P. A polynomial baseline was subtracted from the raw data traces (see section 6.4.1). (b) Frequency-domain spectra, obtained by calculating the FFT magnitude of the traces shown in fig. a, after apodization with a Hamming window function. Note that both time- and frequency-domain traces are normalized to equal amplitude and plotted such that the baselines indicate the particular value of B_1 on the right-hand y-axis. The dashed lines in fig. b correspond to linear-regression fits of the B_1-dependent frequency peaks observed in the FFT spectra, yielding Rabi-nutation frequencies $\Omega = \nu_1$ (blue) and $\Omega = 2\nu_1$ (red).

With increasing MW power ($B_1 \gtrsim 0.5\,\mathrm{mT}$), an additional frequency peak emerges in the FFT spectra in fig. 7.4b. In the time-domain traces, this additional frequency component becomes visible as a characteristic beating (uppermost trace in fig. 7.4a). Linear regression of the FFT-peak positions results in a nutation-frequency coefficient $\alpha = 2.0(2)$, that is, a doubling of the $S = 1/2$ Rabi frequency. In section 6.4.1, we also observed such a double-frequency component in low-temperature ED-Rabi spectra of a-Si:H and assigned it to strongly exchange-coupled spin pairs. However, in that case, we found a $\Omega = 2\nu_1$ component that did not evince any marked B_1 dependence. On the contrary, the double-frequency peak in fig. 7.4b clearly appears only at high MW powers and increases monotonically with B_1. This unambiguously identifies the origin of the room-temperature beating-component as spin locking.

Under spin-locking conditions, the paired spins are excited simultaneously due to the increased excitation bandwidth. As discussed above, this results in a total spin-pair population that is only shifted between the sublevels of the triplet manifold, with transition frequencies $\Omega = 2\nu_1$ (see section 6.4.1). Although the spin-pair symmetry, in terms of singlet and triplet content, is thus not directly affected by EPR, spin-dependent electronic transitions can still occur due to intersystem crossing (ISC). If the $|T_0\rangle$ and $|S\rangle$ are mixed, for instance, as a result of hyperfine interactions of the paired spins with neighbouring nuclear spins of ^{1}H or ^{29}Si nuclei, triplet population is shifted into the singlet state by means of ISC [88, 92]. Consequently, the singlet content oscillates at frequency $\Omega = 2\nu_1$, giving rise to spin-dependent current changes.

By comparing figs. 7.3 and 7.4, it immediately becomes apparent that the $\boldsymbol{B}_1$ dependency of the ED-Rabi spin-locking component coincides with the appearance of the dip in the PEDMR spectrum. This correlation clearly shows that the feature is indeed caused by spin locking. Based on this result, we can narrow down the spin-dependent recombination channel in a-Si:H to either direct capture of charge-carriers from the extended band states into DB defects or tunneling transitions between CBT-trapped electrons and neutral DBs. To further corroborate this finding, we measured ED-Rabi nutations as a function of the external magnetic field. Such nutation-frequency-correlated EDMR experiments have already provided in-depth insight into the microscopic nature of low-temperature spin-dependent transitions in a-Si:H in the previous chapter.

Figures 7.5a and b show field-resolved ED-Rabi spectra at low ($B_1 = 0.26\,\mathrm{mT}$) and high ($B_1 = 1.02\,\mathrm{mT}$) MW power. Both spectra contain features at nutation frequencies $\Omega = \nu_1$, that is, the expected nutation frequency of weakly coupled $S = 1/2$ spin pairs. The high-B_1 spectrum in fig. 7.5b further shows a spin-locking component at $\Omega = 2\nu_1$. Both features exhibit characteristic parabolas, which are due to off-resonant spin excitations (see section 2.5.6). Magnetic-field-domain EDMR spectra associated with a particular Rabi-nutation frequency can be obtained as cross sections through the two-dimensional field/frequency map (see sections 6.4.2 and 6.4.4). Such spectra are shown for the single- and double-frequency components in figs. 7.5c and 7.5d, respectively.

The field-resolved ED-Rabi spectrum at $\Omega = \nu_1$ (fig. 7.5c) resembles the line shape of the low-power PEDMR spectrum discussed in section 7.3.1. The PEDMR spectrum appears slightly broadened, which can be attributed to MW-power broadening. Since at low MW power only the $\Omega = \nu_1$ is observed, the spin-dependent recombination process clearly occurs via weakly coupled $S = 1/2$ pairs. The $\Omega = 2\nu_1$ peak, emerging at high B_1 (fig. 7.5d), is a narrow unstructured line that can be fitted with a simple Gaussian line,

centered at $g = 2.0052(5)$. This finding corroborates our previous conclusion and excludes VBT holes as coupling partners of the spin-locked pair. The confidence interval of the g-value (comprising both an estimated fitting error and the magnetic-field/MW-frequency uncertainties), however, does not allow to differentiate between $g = 2.0055$ and $g = 2.0050$, that is, the g-values of the pure DB resonance and the averaged g-value that would be expected for a CBT/DB spin pair. Purely based on the shape and position of the spin-locking signal, it is thus not possible to draw further conclusions regarding the nature of the recombination mechanism.

As discussed above, both direct capture of electrons from the conduction band and e-D^0 tunneling transitions have been proposed as spin-dependent DB-related recombination channels. Direct capture has been identified as the dominant room-temperature recombination mechanism in μc-Si:H [238, 292]. A qualitative model for direct capture in terms of a spin-dependent Shockley-Read-Hall recombination process has been provided by Rong *et al.* [296]. In this model, electron capture leads to an excited charged DB state D^{-*}, which can be either in a singlet or a triplet state. Relaxation to the ground

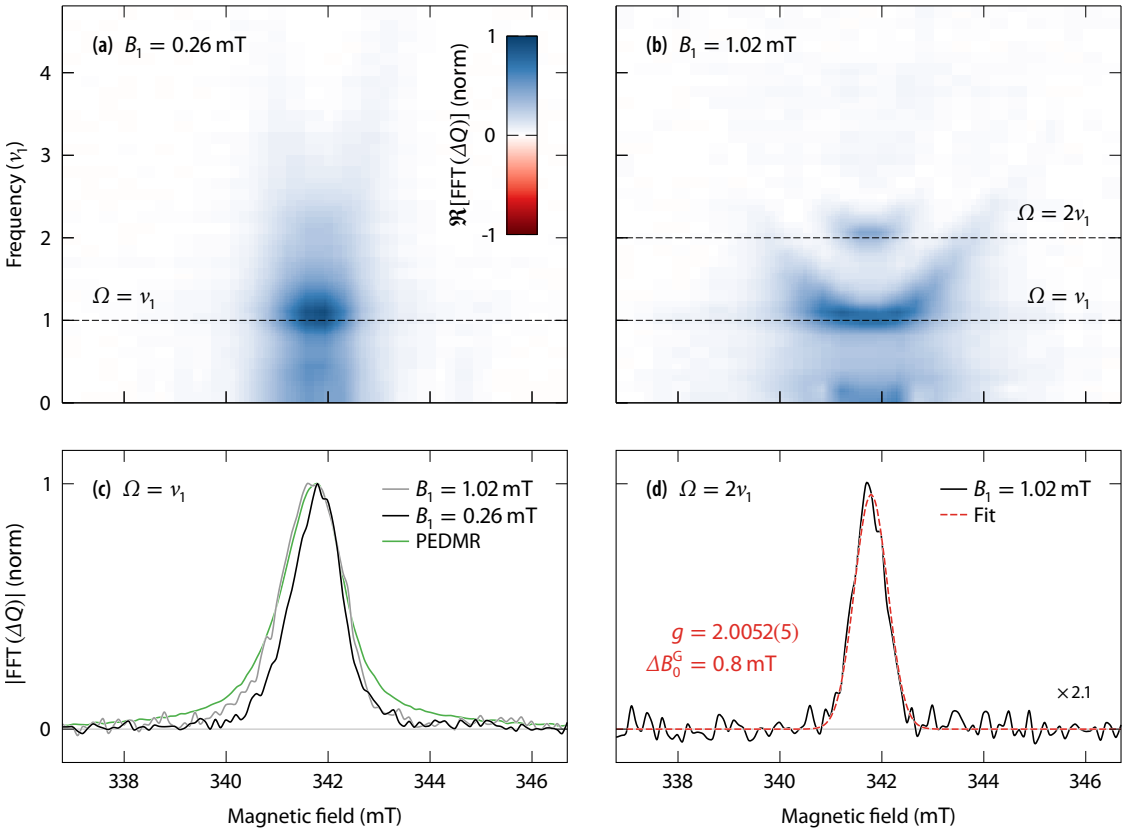

FIGURE 7.5 Field-swept X-band room-temperature ED-Rabi nutations of an a-Si:H *pin* solar cell. **(a, b)** Two-dimensional magnetic-field/nutation-frequency maps, obtained by calculating FFT (real part) of the time-domain ED-Rabi traces, recorded as a function of the external magnetic field at two distinct MW-power settings. **(c, d)** Nutation-frequency-resolved PEDMR spectra, corresponding to cross sections through the ED-Rabi field/frequency maps at nutation frequencies $\Omega = \nu_1$ and $\Omega = 2\nu_1$, respectively. Note that a Hamming-window function has been applied to the ED-Rabi time traces, before calculating the spectra in figs. c and d, in order to suppress off-resonance parabolas (see section 6.4). For reference, the green curve in fig. c plots the PEDMR spectra of fig. 7.2c. The red, dashed curve in fig. d shows the result of a spectral least-squares fit, assuming a simple Gaussian line shape.

state D^- of the charged DB, from where the recombination cycle can be completed by the caption of a hole, will thus be spin-dependent. Manipulation of the D^{-*} spin state by EPR thus causes the EDMR signal originating from a direct-capture process. Due to the spatial overlap of spins in the exited D^{-*} state, however, the spin pair will be strongly coupled. This was shown for the case of μc-Si:H by Boehme and Lips [292] and utilized to identify the direct-capture mechanism. We have not found any marked indicator of strong spin-spin coupling in the room-temperature ED-Rabi spectra of a-Si:H. For strong dipolar coupling, one would expect a characteristic nutation frequency $\Omega = \sqrt{2}\nu_1$, as observed at low temperature in the previous chapter. For strong exchange coupling, a B_1-independent $2\nu_1$ frequency component would be observed (see section 6.4). We could clearly assign the double-frequency component to B_1-dependent spin locking. Based on the absence of strong spin-spin coupling, it appears more likely that room-temperature spin-dependent recombination in a-Si:H is due to e-D^0 tunneling transitions. The predominance of the DB resonance in the PEDMR spectrum can be explained by different temperature dependencies of the spin-lattice relaxation times, as discussed in section 7.3.1.

7.4 SUMMARY AND CONCLUSION

In this chapter, we have presented room-temperature PEDMR experiments on a-Si:H *pin* solar cells, seeking to understand the mechanism of spin-dependent DB-related recombination. We have shown that the current-quenching room-temperature PEDMR spectrum is dominated by the DB-defect resonance, with additional small contributions of CBT- and VBT-trapped electrons and holes. Based on ED-Rabi-nutation experiments, a spin-dependent transition via weakly coupled $S = 1/2$ spin pairs could be identified, which is further corroborated by the presence of spin locking under strong MW excitation. From the resonance position of the spin-locking signal, we were able to exclude spin-dependent tunneling of VBT holes into DB defects as the dominant recombination channel. A direct-capture mechanism further seems improbable due to the absence of strong spin-spin coupling. As a result, we conclude that the spin-dependent recombination channel giving rise to the room-temperature EDMR signal is based on tunneling of CBT-trapped electrons into neutral DB defects. This is consistent with early models derived from CWEDMR experiments [60].

It is to be noted that the results presented in this chapter have to be considered as preliminary, as they are part of ongoing research. In collaboration with the group of C. Boehme (University of Utah), a wider range of multifrequency EDMR experiments have recently been conducted, covering excitation frequencies between 50 MHz and 263 GHz. These experiments will help to derive more granular and reliable spin-Hamiltonian parameters based on a global multifrequency fitting approach. Based on these results, the assignment to spin-dependent e-D^0 tunneling needs to be reevaluated. In addition, an explanation for the strong relative DB-resonance intensity, leading to a g-value shift with increasing temperature, needs to found. As discussed in section 7.3.1 and proposed by Lips *et al.* [290], different temperature dependencies of the spin-lattice relaxation times of CBT electrons and DB defects may cause a shift of the relative line contributions. Temperature-dependent electrically detected relaxation measurements [267, 268, 297] may help to support this hypothesis.

Although a final conclusion regarding the microscopic mechanism of spin-dependent room-temperature recombination cannot yet be drawn from the experiments presented in this chapter, the results have once more demonstrated the strength of PEDMR to directly probe paired spin states involved in spin-dependent electronic transitions. A comprehensive answer to the open questions concerning DB-related recombination in a-Si:H can thus be expected from future experiments that exploit this capability.

CHAPTER 8

Summary and conclusion

In this work, the microscopic nature of charge-transport and -recombination mechanisms in a-Si:H were studied using PEDMR spectroscopy. Current-limiting transport channels via paramagnetic states could be identified in both intrinsic a-Si:H films and fully processed a-Si:H solar cells. By employing the powerful toolbox of modern PEDMR techniques in conjunction with TREPR and *ab-initio* DFT calculations, we were able to gain in-depth insights into the impact of disorder-induced localized states on electronic-transport properties of a-Si:H. In the following, the results and conclusions of chapters 5 to 7 are briefly summarized and set into context of previous research on a-Si:H, which has been discussed in chapter 3.

In chapter 5, we employed multifrequency PEDMR on undoped a-Si:H films to disentangle the different spin-dependent processes observed at different temperatures. We identified a current-enhancing process at low temperatures ($T < 50$ K) and a current-quenching process at temperatures above 150 K. Based on a global multifrequency spectral fit, the high-temperature signal could be assigned to spin-dependent recombination via DB defects, whereas the low-temperature signal exhibited the characteristic resonances of electrons and holes trapped in CBT and VBT states, as well as a third field-independently broadened line at $g = 2.0077$. This line had formerly been observed in EDMR spectra of a-Si:H and had been tentatively assigned to triplet excitons based on the unusually large field-independent line width of about 20 mT.

The excitonic nature of the low-temperature EDMR signal could, for the first time, be unequivocally proven in chapter 6, were we presented a comprehensive study of the low-temperature PEDMR signal of a-Si:H *pin* solar cells. By combining PEDMR with TREPR spectroscopy, we could demonstrate that light-generated TE states form from geminate electron-hole pairs. Based on the observed *g*-value and the complementation with DFT model calculations, we were able to assign the TE states to a strongly coupled *e*-*h*-pair trapped in CBT and VBT states in direct proximity. Evidence for strong dipolar and exchange coupling was found. We could further determine the exciton size to an average *e*-*h* distance of 5.3(2) Å. This result not only confirms earlier estimations, but is also in excellent agreement with the dipolar-coupling strength calculated from our DFT model. Based on our finding that the excitonic TREPR resonance is observed in a-Si:H samples with a wide range of structural and electronic properties, we conclude that the existence of these states is a universal feature of a-Si:H.

Triplet excitons in a-Si:H have also been observed in ODMR studies by a number of groups, as discussed in chapter 3. Based on the similarities between PEDMR and PODMR signatures, we believe that the same TEs lead to spin-dependent current and luminescence changes. The ODMR signal can be explained with radiative TE recom-

bination. The current-enhancing EDMR signal could be assigned to a spin-dependent non-radiative Auger-like recombination channel. We have provided clear evidence for such a three-particle process by means of ED-ELDOR experiments. Triplet-exciton recombination thus provides an important loss channel of geminate pairs in a-Si:H, counteracting efficient separation of light-generated charge carriers. This central role of TEs during the charge-separation process in a-Si:H is further corroborated by our TREPR experiments, which allowed to follow the charge-separation mechanism of light-generated excitons on a microsecond time scale. We found the first direct experimental evidence of spin-correlated *e*-*h*-pairs forming after light excitation. We interpret these states as charge-transfer states (in analogy to CT states found in organic semiconductors), which can either dissociate into separated charges or form strongly coupled TEs by means of ISC. Radiative or non-radiative recombination of these excitons thus finally decreases the yield of light-generated charge carriers that can contribute to photoconductivity.

The picture that has emerged from this low-temperature EDMR/EPR study is also consistent with earlier findings from photoluminescence and -conductivity studies on a-Si:H (chapter 3). Radiative recombination channels of geminate singlet and triplet excitons have been identified by means of QFRS. The associated characteristic PL lifetimes have been observed at temperatures $T \lesssim 100\,\mathrm{K}$, which coincides with the temperature regime where we found the TE signature in TREPR spectra. Moreover, PL and PC measurements at low temperatures indicated the presence of a non-radiative Auger-recombination channel, competing with radiative geminate-pair recombination. This is in excellent agreement with the three-particle Auger-recombination process that can describe the observed spin-dependent TE-mediated current enhancement, which was detect in the exact same temperature regime.

At low temperatures, the transport in a-Si:H is dominated by hopping conduction of electrons and holes via their respective tail states, as was concluded from the low-temperature dependencies of PC and PL on temperature, electric field and charge-carrier generation rate (see section 3.3.1). Earlier studies have therefor assigned the current-enhancing low-temperature EDMR signals associated with CBT and VBT states to spin-dependent hopping transitions. However, we have shown that the same signals can also originate from the observed three-particle process. We can thus not finally decide whether spin-dependent hopping is directly observed in the low-temperature EDMR signal of a-Si:H. Theoretical models of hopping conduction are, however, consistent with the observed temperature dependence of the EDMR signal. Such models (see, *e. g.*, refs. [198, 199]) predict a transport path that is moved more and more towards the mobility edges with increasing temperature. This results in a strong increase of the conductivity at temperatures $T \gtrsim 60\,\mathrm{K}$ until the transport path is entirely shifted into the extended band states for temperatures above approximately 100 K. At these intermediate temperatures, we observe a transition from the low-temperature current-enhancing TE signal towards the current-quenching recombination signal, as was shown in chapter 5. This is in agreement with the simultaneous quenching of the PL intensity that is commonly observed at these temperatures, indicating the predominating influence of non-radiative recombination channels competing with geminate-pair recombination.

The investigation of the room-temperature EDMR signal of a-Si:H solar cells in chapter 7 has shown that the dominant non-radiative recombination process at high temperatures is recombination via mid-gap DB defects, as it had been already concluded from

earlier EDMR studies as well as our results in chapter 5. A spectral fit of the multifrequency EDMR signals of both a-Si:H films and solar cells comprises the EPR signatures of DB defects and CBT-/VBT-trapped electrons and holes. Earlier studies have interpreted the presence of these resonance in terms of a spin-dependent *e*-DB transition, followed by the capture of a hole to complete the recombination. The observation of a VBT resonance was explained by spin-dependent hopping of holes towards the recombination site, thereby increasing the recombination rate. An alternative explanation would be a spin-dependent *h*-DB transition, followed by the capture of an electron. In chapter 5, we concluded from the relative signal intensities of DB, CBT and VBT resonances that probably both mechanisms are present. However, in chapter 7 we could prove this assumption wrong, based on the observation of room-temperature ED-Rabi nutations. With increasing MW power, we detected spin locking, which provided direct experimental evidence for a spin-dependent recombination process via weakly coupled paired spins. Based on the *g*-value of the spin-locking signal ($g \approx 2.005$), we were able to exclude a spin-dependent *h*-DB transition.

Unfortunately, the resolution at X-band did not allow to resolve the small *g*-value differences between DB and CBT resonances, such that we could not finally decide whether the above-described model of spin-dependent *e*-DB tunneling or a direct-capture mechanism causes the room-temperature EDMR signal. Based on the absence of strong spin-spin coupling, we believe that recombination of CBT-trapped electrons is more likely than direct capture of charge carriers from the extended band states. However, further experiments are required to reach a final conclusion. Such experiments include electrically detected spin-relaxation measurements, a wider range of multifrequency EDMR experiments, and electrically detected nutation experiments at higher MW-excitation frequencies, offering an increased *g*-value resolution. High-frequency ED-Rabi experiments were not conducted in the scope of this work, but have recently come into reach due to a MW-power upgrade of our 263 GHz/9.4 T EPR/EDMR setup. Moreover, room-temperature multifrequency EDMR experiments at MW frequencies between 50 MHz and 263 GHz have recently been conducted in collaboration with the group of C. Boehme (University of Utah), and will be included into the analysis in the near future. Based on these experiments, we expect to come up with a final microscopic model for non-radiative DB-mediated recombination, which provides a major charge-carrier loss channel that strongly influences the electronic performance of a-Si:H-based devices.

Future work is also required to develop a comprehensive understanding for the temperature dependency of spin-dependent transport and recombination in a-Si:H. Based on the temperature-dependent spectral deconvolution of 263 GHz EDMR signals in chapter 5, we observed strongly deviating temperature dependencies of the current-quenching resonances associated with CBT/VBT states and DB defects. Within this work, we did not acquire sufficient data at intermediate temperatures to corroborate and interpret this observation. Future multifrequency PEDMR experiments can help to gain a better understanding of the temperature dependency of recombination channels in a-Si:H.

Finally, the excitonic states that were identified in this work may trigger further investigations using both EDMR and EPR spectroscopy. The temperature dependency of the TE resonance cannot be fully understood based on the data presented in this thesis. Most of the experiments in chapter 6 were conducted at cryogenic temperatures ($T = 10$ K). In the temperature-dependent measurements in chapter 5, we observed a TE line at tem-

peratures up to about 50 K. Earlier studies that were based on CWEDMR experiments reported the presence of a broad $g = 2.008$ line at temperatures around 150 K (see section 3.4.3). This discrepancy may be due to different detection bandwidths of pulsed and CWEDMR. A systematic combined temperature-dependent pulsed/CWEDMR study is required, possibly also as a function of structural and electronic material properties, to resolve this issue. Furthermore, a potential correlation between light-induced degradation and TEs may be evaluated in the future. Triplet excitons have been proposed as a potential precursor state in the so-called bond-breaking model for the SWE [11, 244]. Interestingly, non-radiative Auger recombination of excitons, also referred to as exciton-polaron annihilation, has been identified to cause the long-term degradation of blue phosphorescent OLEDs [298–300]. Noting the many similarities between transport and recombination mechanisms in organic and inorganic semiconductors, it is worth investigating whether the Auger-like TE recombination process identified in this work might also be related to the SWE. Developing a consistent model for light-induced degradation of a-Si:H, which has not yet been understood on a microscopic level, even after more than fourty years of active research, would be a valuable contribution to the research field of a-Si:H.

The results of this work have shed light upon a number of open questions regarding the microscopic nature of transport and recombination processes in a-Si:H. In particular, the role of geminate excitons in the separation process of light-generated charge carriers has been studied in great detail. The findings of this thesis may help to disentangle transport and recombination channels in multilayer a-Si:H-based devices, such as, for instance, heterojunction a-Si/c-Si solar cells. Considering the role of a-Si:H as a model-like amorphous semiconductor, our results also contribute to the general understanding of disordered solids. Nevertheless, a plethora of questions concerning structural and electronic properties of a-Si:H remains unanswered. Research on a-Si:H can thus be expected to keep progressing in the future. The methodology applied in this thesis has demonstrated that EDMR and EPR spectroscopy can be valuable tools to support this development.

Bibliography

[1] P. J. MOHR, B. N. TAYLOR, D. B. NEWELL: CODATA recommended values of the fundamental physical constants: 2010. *Rev. Mod. Phys.* **84** (4): 1527–1605 (2012).

[2] R. A. STREET, W. S. WONG, T. NG, R. LUJAN: Amorphous silicon thin film transistor image sensors. *Philos. Mag.* **89** (28–30): 2687–2697 (2009).

[3] K. YOSHIKAWA, H. KAWASAKI, W. YOSHIDA, T. IRIE, K. KONISHI, K. NAKANO, T. UTO, D. ADACHI, M. KANEMATSU, H. UZU, K. YAMAMOTO: Silicon heterojunction solar cell with interdigitated back contacts for a photoconversion efficiency over 26 %. *Nat. Energy* **2**: 17032 (2017).

[4] D. L. STAEBLER, C. R. WRONSKI: Reversible conductivity changes in discharge-produced amorphous Si. *Appl. Phys. Lett.* **31** (4): 292–294 (1977).

[5] D. L. STAEBLER, C. R. WRONSKI: Optically induced conductivity changes in discharge-produced hydrogenated amorphous silicon. *J. Appl. Phys.* **51** (6): 3262–3268 (1980).

[6] M. M. J. TREACY, K. B. BORISENKO: The local structure of amorphous silicon. *Science* **335** (6071): 950–953 (2012).

[7] P. W. ANDERSON: Absence of diffusion in certain random lattices. *Phys. Rev.* **109** (5): 1492–1505 (1958).

[8] M. H. BRODSKY, R. S. TITLE: Electron spin resonance in amorphous silicon, germanium and silicon carbide. *Phys. Rev. Lett.* **23** (11): 581–584 (1969).

[9] Z. Z. DITINA, L. P. STRAKHOV, H. H. HELMS: Paramagnetic centers in evaporated silicon films. *Sov. Phys.-Semicond.* **2**: 1006–1007 (1969).

[10] H. DERSCH, J. STUKE, J. BEICHLER: Light-induced dangling bonds in hydrogenated amorphous silicon. *Appl. Phys. Lett.* **38** (6): 456–458 (1981).

[11] M. STUTZMANN, W. B. JACKSON, C. C. TSAI: Light-induced metastable defects in hydrogenated amorphous silicon: A systematic study. *Phys. Rev. B* **32** (1): 23–47 (1985).

[12] S. T. PANTELIDES: Defects in amorphous silicon: A new perspective. *Phys. Rev. Lett.* **57** (23): 2979–2982 (1986).

[13] J. C. PHILIPS: Comment on "Defects in amorphous silicon: A new perspective". *Phys. Rev. Lett.* **58** (26): 2824 (1987); S. T. PANTELIDES: Pantelides responds. *Phys. Rev. Lett.* **58** (26): 2825 (1987).

[14] M. STUTZMANN, D. K. BIEGELSEN: Dangling or floating bonds in amorphous silicon? *Phys. Rev. Lett.* **60** (16): 1682 (1988); S. T. PANTELIDES: Pantelides replies. *Phys. Rev. Lett.* **60** (16): 1683 (1988).

[15] T. UMEDA, S. YAMASAKI, J. ISOYA, H. TANAKA: Electron-spin-resonance center of dangling bonds in undoped a-Si:H. *Phys. Rev. B* **59** (7): 4849–4857 (1999).

[16] I. SOLOMON, D. K. BIEGELSEN, J. C. KNIGHTS: Spin-dependent photoconductivity in *n*-type and *p*-type amorphous silicon. *Solid State Commun.* **22** (8): 505–508 (1977).

[17] M. STUTZMANN, M. S. BRANDT, M. W. BAYERL: Spin-dependent processes in amorphous and microcrystalline silicon: A survey. *J. Non-Cryst. Solids* **266** (1): 1–22 (2000).

[18] C. BOEHME, P. KANSCHAT, K. LIPS: Time domain measurement of spin-dependent recombination: A novel defect spectroscopy method. *Nucl. Instrum. Methods Phys. Res., Sect. B* **186** (1): 30–35 (2002).

[19] C. BOEHME, K. LIPS: Theory of time-domain measurement of spin-dependent recombination with pulsed electrically detected magnetic resonance. *Phys. Rev. B* **68** (24): 245105 (2003).

[20] C. BOEHME, K. LIPS: The ultra-sensitive electrical detection of spin-Rabi oscillations at paramagnetic defects. *Phys. B* **376–377**: 930–935 (2006).

[21] W. J. BAKER, D. R. MCCAMEY, K. J. VAN SCHOOTEN, J. M. LUPTON, C. BOEHME: Differentiation between polaron-pair and triplet-exciton polaron spin-dependent mechanisms in organic light-emitting diodes by coherent spin beating. *Phys. Rev. B* **84** (16): 165205 (2011).

[22] F. HOEHNE, H. HUEBL, B. GALLER, M. STUTZMANN, M. S. BRANDT: Spin-dependent recombination between phosphorus donors in silicon and Si/SiO_2 interface states investigated with pulsed electrically detected electron double resonance. *Phys. Rev. Lett.* **104** (4): 046402 (2010).

[23] M. FEHR, J. BEHRENDS, S. HAAS, B. RECH, K. LIPS, A. SCHNEGG: Electrical detection of electron-spin-echo envelope modulations in thin-film silicon solar cells. *Phys. Rev. B* **84** (19): 193202 (2011).

[24] M. SUCKERT, F. HOEHNE, L. DREHER, M. KUENZL, H. HUEBL, M. STUTZMANN, M. S. BRANDT: Electrically detected double electron–electron resonance: Exchange interaction of ^{31}P donors and P_{b0} defects at the Si/SiO_2 interface. *Mol. Phys.* **111** (18–19): 2690–2695 (2013).

[25] F. HOEHNE, L. DREHER, H. HUEBL, M. STUTZMANN, M. S. BRANDT: Electrical detection of coherent nuclear spin oscillations in phosphorus-doped silicon using pulsed ENDOR. *Phys. Rev. Lett.* **106** (18): 187601(4) (2011).

[26] W. AKHTAR, A. SCHNEGG, S. VEBER, C. MEIER, M. FEHR, K. LIPS: CW and pulsed electrically detected magnetic resonance spectroscopy at 263 GHz/12 T on operating amorphous silicon solar cells. *J. Magn. Reson.* **257**: 94–101 (2015).

[27] K. LIPS, S. SCHÜTTE, W. FUHS: Microwave-induced resonant changes in transport and recombination in hydrogenated amorphous silicon. *Philos. Mag. B* **65** (5): 945–959 (1992).

[28] IEEE AEROSPACE & ELECTRONIC SYSTEMS SOCIETY: IEEE standard letter designations for radar-frequency bands. *IEEE Standards* **521-2002**: (2003).

[29] J. W. STONER, D. SZYMANSKI, S. S. EATON, R. W. QUINE, G. A. RINARD, G. R. EATON: Direct-detected rapid-scan EPR at 250 MHz. *J. Magn. Reson.* **170** (1): 127–135 (2004).

[30] A. SCHWEIGER, G. JESCHKE: Principles of pulse electron paramagnetic resonance (Oxford: Oxford University Press, 2001).

[31] G. FEHER: Sensitivity considerations in microwave paramagnetic resonance absorption techniques. *Bell Syst. Tech. J.* **36** (2): 449–484 (1957).

[32] J. R. HARMER: Hyperfine spectroscopy: ENDOR. *eMagRes* **5** (4): 1493–1514 (2016).

[33] S. VAN DOORSLAER: Hyperfine spectroscopy: ESEEM. *eMagRes* **6** (1): 51–70 (2017).

[34] G. JESCHKE: Dipolar spectroscopy: Double-resonance methods. *eMagRes* **5** (3): 1459–1476 (2016).

[35] S. STOLL, G. JESCHKE, M. WILLER, A. SCHWEIGER: Nutation-frequency correlated EPR spectroscopy: The PEANUT experiment. *J. Magn. Reson.* **130** (1): 86–96 (1998).

[36] A. V. ASTASHKIN, A. SCHWEIGER: Electron-spin transient nutation: A new approach to simplify the interpretation of ESR spectra. *Chem. Phys. Lett.* **174** (6): 595–602 (1990).

[37] F. BLOCH, A. SIEGERT: Magnetic resonance for nonrotating fields. *Phys. Rev.* **57** (6): 522–527 (1940).

[38] E. L. HAHN: Spin echoes. *Phys. Rev.* **80** (4): 580–594 (1950).

[39] S. STOLL: Pulse EPR. *eMagRes* **6** (1): 23–38 (2017).

[40] A. ABRAGAM, M. H. L. PRYCE: Theory of the nuclear hyperfine structure of paramagnetic resonance spectra in crystals. *Proc. R. Soc. London, Sec. A* **205** (1080): 135–153 (1951).

[41] N. M. ATHERTON: Principles of electron spin resonance (Chichester: Ellis Horwood and PTR Prentice Hall, 1993).

[42] J. A. WEIL, J. R. BOLTON: Electron paramagnetic resonance: Elementary theory and practical applications, 2nd ed. (Hoboken, NJ: Wiley-Interscience, 2007).

[43] S. STOLL, A. SCHWEIGER: EasySpin, a comprehensive software package for spectral simulation and analysis in EPR. *J. Magn. Reson.* **178** (1): 42–55 (2006).

[44] M. STUTZMANN, J. STUKE: Paramagnetic states in doped amorphous silicon and germanium. *Solid State Commun.* **47** (8): 635–639 (1983).

[45] M. BENNATI: EPR interactions: Hyperfine couplings. *eMagRes* **6** (2): 271–282 (2017).

[46] M. FEHR, P. SIMON, T. SONTHEIMER, C. LEENDERTZ, B. GORKA, A. SCHNEGG, B. RECH, K. LIPS: Influence of deep defects on device performance of thin-film polycrystalline silicon solar cells. *Appl. Phys. Lett.* **101** (12): 123904 (2012).

[47] D. GOLDFARB: ELDOR-detected NMR. *eMagRes* **6** (1): 101–114 (2017).

[48] J. H. VAN DER WAALS, M. S. DE GROOT: Paramagnetic resonance in phosphorescent aromatic hydrocarbons. I: Naphthalene. *Mol. Phys.* **2** (4): 333–340 (1959); M. S. DE GROOT, J. H. VAN DER WAALS: II: Determination of zero-field splitting from solution spectra. *Mol. Phys.* **3** (2): 190–200 (1960).

[49] G. JESCHKE: Determination of the nanostructure of polymer materials by electron paramagnetic resonance spectroscopy. *Macromol. Rapid Commun.* **23** (4): 227–246 (2002).

[50] E. J. L. MCINNES, D. COLLISON: EPR interactions: Coupled spins. *eMagRes* **5** (3): 1445–1458 (2016).

[51] J. M. ELZERMAN, R. HANSON, L. H. WILLEMS VAN BEVEREN, B. WITKAMP, L. M. K. VANDERSYPEN, L. P. KOUWENHOVEN: Single-shot readout of an individual electron spin in a quantum dot. *Nature* **430**: 431–435 (2004).

[52] D. R. MCCAMEY, H. HUEBL, M. S. BRANDT, W. D. HUTCHISON, J. C. MCCALLUM, R. G. CLARK, A. R. HAMILTON: Electrically detected magnetic resonance in ion-implanted Si:P nanostructures. *Appl. Phys. Lett.* **89** (18): 182115 (2006).

[53] J. SCHMIDT, I. SOLOMON: Modulation de la photoconductivité dans le silicium à basse température par résonance magnétique électronique des impuretés peu profondes. *C. R. Seances Acad. Sci., Ser. B* **263**: 169–172 (1966).

[54] R. MAXWELL, A. HONIG: Neutral-impurity scattering experiments in silicon with highly spin-polarized electrons. *Phys. Rev. Lett.* **17** (4): 188–190 (1966).

[55] T. HIROSE, H. YOSHIOKA, K. HORAI: Conduction increase of reduced rutile with the saturation of electron spin resonance. *J. Phys. Soc. Jpn.* **21** (3): 559 (1966).

[56] D. J. LÉPINE, J. J. PREJEAN. *Proc. Int. Conf. Phys. Semicond.* **9**: 805–807 (1970); D. J. LÉPINE: Spin-dependent recombination on silicon surface. *Phys. Rev. B* **6** (2): 436–441 (1972).

[57] I. SOLOMON: Spin-dependent recombination in a silicon p-n junction. *Solid State Commun.* **20** (3): 215–217 (1976).

[58] G. MENDZ, J. MILLER, D. HANEMAN: Photoconductive resonance in silicon: Theory and experiment. *Phys. Rev. B* **20** (12): 5246–5251 (1979).

[59] D. KAPLAN, I. SOLOMON, N. F. MOTT: Explanation of large spin-dependent recombination effect in semiconductors. *J. Phys., Lett.* **39** (4): 51–55 (1978).

[60] H. DERSCH, L. SCHWEITZER, J. STUKE: Recombination processes in a-Si:H: spin-depedendent photoconductivity. *Phys. Rev. B* **28** (8): 4678–4684 (1983).

[61] K. LIPS, W. FUHS: Spin-dependent transport and recombination in a-Si:H. *J. Non-Cryst. Solids* **137/138**: 255–258 (1991).

[62] B. STICH, S. GREULICH-WEBER, J.-M. SPAETH: Electrical detection of electron paramagnetic resonance: New possibilities for the study of point defects. *J. Appl. Phys.* **77** (4): 1546–1553 (1995).

[63] P. KANSCHAT, K. LIPS, W. FUHS: Identification of non-radiative recombination paths in microcrystalline silicon (μc-Si:H). *J. Non-Cryst. Solids* **266–269**: 524–528 (2000).

[64] I. HIROMITSU, Y. KAIMORI, T. ITO: Photovoltaic effect and electrically detected electron spin resonance of a H_2-phthalocyanine/C_{60} heterojunction. *Solid State Commun.* **104** (9): 511–515 (1997).

[65] T. EICKELKAMP, S. ROTH, M. MEHRING: Electrically detected magnetic resonance in photoexcited fullerenes. *Mol. Phys.* **95** (5): 967–972 (1998).

[66] I. HIROMITSU, Y. KAIMORI, M. KITANO, T. ITO: Spin-dependent recombination of photoinduced carriers in phthalocyanine/C_{60} heterojunctions. *Phys. Rev. B* **59** (2151–2163): (1999).

[67] K. P. HOMEWOOD, B. C. CAVENETT, W. E. SPEAR, P.G. LE COMBER: Spin effects in p^+-i-n^+ a-Si:H cells; photovoltaic detected magnetic resonance (PDMR). *J. Phys. C: Solid State Phys.* **16** (13): L427–L432 (1983).

[68] K. LIPS, W. FUHS: Transport and recombination in amorphous p-i-n-type solar cells studied by electrically detected magnetic resonance. *J. Appl. Phys.* **74** (6): 3993–3999 (1993).

[69] R. MÜLLER, P. KANSCHAT, S. VON AICHBERGER, K. LIPS, W. FUHS: Identification of transport and recombination paths in homo- and heterojunction silicon solar cells by electrically detected magnetic resonance. *J. Non-Cryst. Solids* **266–269** (2): 1124–1128 (2000).

[70] F. C. RONG, G. J. GERARDI, W. R. BUCHWALD, E. H. POINDEXTER, M. T. UMLOR, D. J. KEEBLE, W. L. WARREN: Electrically detected magnetic resonance of a transition metal related recombination center in Si p–n diodes. *Appl. Phys. Lett.* **60** (5): 610–612 (1992).

[71] C. LERNER, K. LIPS, W. FUHS: Spin-dependent processes in a-Si:H Schottky barrier diodes. *J. Non-Cryst. Solids* **227-230** (B): 1177–1181 (1998).

[72] G. KAWACHI, C. F. O. GRAEFF, M. S. BRANDT, M. STUTZMANN: Carrier transport in amourphous silicon-based thin-film transistors studied by spin-dependent transport. *Phys. Rev. B* **54** (11): 7957–7964 (1996).

[73] C. BOEHME, K. LIPS: Time domain measurement of spin-dependent recombination. *Appl. Phys. Lett.* **79** (26): 4363–4365 (2001).

[74] C. BOEHME, K. LIPS: Spin-dependent recombination: An electronic readout mechanism for solid state quantum computers. *Phys. Status Solidi B* **233** (3): 427–435 (2002).

[75] C. BOEHME, K. LIPS: Electrical detection of spin coherence in silicon. *Phys. Rev. Lett.* **91** (24): (2003).

[76] C. BOEHME, K. LIPS: The investigation of charge carrier recombination and hopping transport with pulsed electrically detected magnetic resonance techniques. In: *Charge transport in disordered solids with applications in electronics*, ed. by S. Baranovski (Chichester: John Wiley & Sons, Ltd., 2006).

[77] C. BOEHME, J. BEHRENDS, K. VON MAYDELL, M. SCHMIDT, K. LIPS: Investigation of hopping transport in *n*-a-Si:H/c-Si solar cells with pulsed electrically detected magnetic resonance. *J. Non-Cryst. Solids* **352** (9–20): 1113–1116 (2006).

[78] H. HUEBL, F. HOEHNE, B. GROLIK, A. R. STEGNER, M. STUTZMANN, M. S. BRANDT: Spin echoes in the charge transport through phosphorus donors in silicon. *Phys. Rev. Lett.* **100** (17): 177602 (2008).

[79] V. RAJEVAC, C. BOEHME, C. MICHEL, A. GLIESCHE, K. LIPS, S. D. BARANOVSKII, P. THOMAS: Transport and recombination through weakly coupled localized spin pairs in semiconductors during coherent spin excitation. *Phys. Rev. B* **74** (24): 245206 (2006).

[80] A. GLIESCHE, C. MICHEL, V. RAJEVAC, K. LIPS, S. D. BARANOVSKII, F. GEBHARD, C. BOEHME: Effect of exchange coupling on coherently controlled spin-dependent transition rates. *Phys. Rev. B* **77** (24): 245206 (2008).

[81] C. MICHEL, A. GLIESCHE, S. D. BARANOVSKII, K. LIPS, F. GEBHARD, C. BOEHME: Influence of disorder on electrically and optically detected electron spin nutation. *Phys. Rev. B* **79** (5): 052201 (2009).

[82] R. GLENN, W. J. BAKER, C. BOEHME, M. E. RAIKH: Analytical description of spin-Rabi oscillation controlled electronic transitions rates between weakly coupled pairs of paramagnetic states with $S = 1/2$. *Phys. Rev. B* **87** (15): 155208 (2013).

[83] R. GLENN, M. E. LIMES, B. SAAM, C. BOEHME, M. E. RAIKH: Analytical study of spin-dependent transition rates within pairs of dipolar and strongly exchange coupled spins with $s = 1/2$ during magnetic resonant excitation. *Phys. Rev. B* **87** (16): 165205 (2013).

[84] M. E. LIMES, J. WANG, W. J. BAKER, S.-Y. LEE, B. SAAM, C. BOEHME: Numerical study of spin-dependent transition rates within pairs of dipolar and exchange coupled spins with $s = 1/2$ during magnetic resonant excitation. *Phys. Rev. B* **87** (16): 165204 (2013).

[85] T. L. KEEVERS, W. J. BAKER, D. R. MCCAMEY: Theory of exciton-polaron complexes in pulsed electrically detected magnetic resonance. *Phys. Rev. B* **91** (20): 205206 (2015).

[86] R. HABERKORN, W. DIETZ: Theory of spin-dependent recombination in semiconductors. *Solid State Commun.* **35** (6): 505–508 (1980).

[87] A. G. REDFIELD: On the theory of relaxation processes. *IBM J. Res. Dev.* **1** (1): 19–31 (1957).

[88] J. BEHRENDS: "Spin-dependent transport and recombination in solar cells studied by pulse electrically detected magnetic resonance". Thesis. 2009.

[89] D. EPHRON, M. R. BEASLEY, H. BAHLOULI, K. A. MATVEEV: Correlated hopping through thin disordered insulators. *Phys. Rev. B* **49** (4): 2989–2992 (1994).

[90] J. STUKE: Recent results on hydrogenated amorphous silicon. *Annu. Rev. Mater. Sci.* **15**: 79–102 (1985).

[91] K. J. VAN SCHOOTEN, D. L. BAIRD, M. E. LIMES, J. M. LUPTON, C. BOEHME: Probing long-range carrier-pair spin–spin interactions in a conjugated polymer by detuning of electrically detected spin beating. *Nat. Commun.* **6**: (2014).

[92] J. BEHRENDS, A. SCHNEGG, K. LIPS, E. A. THOMSEN, A. K. PANDEY, I. D. W. SAMUEL, D. J. KEEBLE: Bipolaron formation inorganic solar cells observed by pulsed electrically detected magnetic resonance. *Phys. Rev. Lett.* **105** (17): 176601 (2010).

[93] C. MEIER, J. BEHRENDS, R. BITTL: Electrical detection of Rabi oscillations in microcrystalline silicon thin-film solar cells. *Mol. Phys.* **111** (18–19): 2683–2689 (2013).

[94] D. R. MCCAMEY, K. J. VAN SCHOOTEN, W. J. BAKER, S.-Y. LEE, S.-Y. PAIK, J. M. LUPTON, C. BOEHME: Hyperfine-field mediated spin beating in electrostatically bound charge carrier pairs. *Phys. Rev. Lett.* **104** (1): 017601 (2010).

[95] L. CHILDRESS, M. V. GURUDEV DUTT, J. M. TAYLOR, A. S. ZIBROV, F. JELEZKO, J. WRACHTRUP, P. R. HEMMER, M. D. LUKIN: Coherent dynamics of coupled electron and nuclear spin qubits in diamond. *Science* **314** (5797): 281–285 (2006).

[96] W. J. BAKER, T. L. KEEVERS, C. BOEHME, D. R. MCCAMEY: Using coherent dynamics to quantify spin coupling with triplet-exciton/polaron complexes in organic dipoles. *Phys. Rev. B* **92** (4): 041201 (2015).

[97] A. V. BELOLIPETSKIY, O. B. GUSEV, A. P. DMITRIEV, E. I. TERUKOV, I. N. YASSIEVICH: Trions in silicon nanocrystals in an amorphous hydrogenated silicon matrix. *Semiconductors* **48** (2): 235–238 (2014).

[98] C. MEIER, C. TEUTLOFF, J. BEHRENDS, R. BITTL, O. ASTAKHOV, K. LIPS: Triplet excitons as sensitive spin probes for structure analysis of extended defects in microcrystalline silicon. *Phys. Rev. B* **94** (4): 045302 (2016).

[99] R. A. STREET: Hydrogenated amourphous silicon (Cambridge: Cambridge University Press, 1991).

[100] K. WINER: Defects in hydrogenated amorphous silicon. *Annu. Rev. Mater. Sci.* **21**: 1–21 (1991).

[101] W. FUHS: Hydrogenated amorphous silicon: material properties and device applications. In: *Charge transport in disordered solids with applications in electronics*, ed. by S. Baranovski (Chichester: John Wiley & Sons, Ltd., 2006).

[102] K. LAAZIRI, S. KYCIA, S. ROORDA, M. CHICOINE, J. L. ROBERTSON, J. WANG, S. C. MOOS: High resolution radial distribution function of pure amorphous silicon. *Phys. Rev. Lett.* **82** (17): 3460–3463 (1999).

[103] W. H. ZACHARIASEN: The atomic arrangement in glass. *J. Am. Chem. Soc.* **54** (10): 3841–3851 (1932).

[104] D. E. POLK: Structural model for amorphous silicon and germanium. *J. Non-Cryst. Solids* **5** (5): 365–376 (1971).

[105] J. DONG, D. A. DRABOLD: Atomistic structure of band-tail states in amorphous silicon. *Phys. Rev. Lett.* **80** (9): 1928–1931 (1998).

[106] N. F. MOTT: Electrons in disordered structures. *Adv. Phys.* **16** (61): 49–144 (1967).

[107] W. PAUL, D. A. ANDERSON: Properties of amorphous hydrogenated silicon, with special emphasis on preparation by sputtering. *Sol. Energy Mater. Sol. Cells* **5** (3): 229–316 (1981).

[108] R. C. CHITTICK, J. H. ALEXANDER, H. F. STERLING: The preparation and properties of amorphous silicon. *J. Electrochem. Soc.* **116** (1): 77–81 (1969).

[109] A. J. LEWIS, G. A. N. CONNELL, W. PAUL, J. PAWLIK, R. TEMKIN: Hydrogen incorporation in amorphous germanium. *AIP Conf. Proc.* **20**: 27–33 (1974).

[110] W. E. SPEAR, P. G. LE COMBER: Substitutional doping of amorphous silicon. *Solid State Commun.* **17** (9): 1193–1196 (1975).

[111] D. E. CARLSON, C. R. WRONSKI: Amorphous silicon solar cell. *Appl. Phys. Lett.* **28** (11): 671–673 (1976).

[112] P. G. LE COMBER, W. E. SPEAR, A. GHAITH: Amorphous-silicon field-effect device and possible application. *Electron. Lett.* **15** (6): 179–181 (1979).

[113] S. OLIBET, E. VALLAT-SAUVAIN, C. BALLIF: Model for a-Si:H/c-Si interface recombination based on the amphoteric nature of silicon dangling bonds. *Phys. Rev. B* **76** (3): 035326 (2007).

[114] S. DE WOLF, C. BALLIF, M. KONDO: Kinetics of a-Si:H bulk defect and a-Si:H/c-Si interface-state reduction. *Phys. Rev. B* **85** (11): 113302 (2012).

[115] J. STUKE: ESR in amorphous germanium and silicon. In: *Proceedings of the 7th International Conference on Amorphous and Liquid Semiconductors*, ed. by W. E. Spear (Edinburgh: University of Edinburgh, 1977).

[116] S. HASEGAWA, T. KASAJIMA, T. SHIMIZU: Doping and annealing effects on ESR in chemically vapor deposited amorphous silicon. *Solid State Commun.* **29** (1): 13–16 (1979).

[117] H. DERSCH, J. STUKE, J. BEICHLER: Electron spin resonance of doped glow-discharge amorphous silicon. *Phys. Status Solidi B* **105** (1): 265–274 (1981).

[118] S. HASEGAWA, T. KASAJIMA, T. SHIMIZU: E.S.R. in doped CVD amorphous silicon films. *Philos. Mag. B* **43** (1): 149–156 (1981).

[119] J. C. KNIGHTS, D. K. BIEGELSEN, I. SOLOMON: Optically induced electron spin resonance in doped amorphous silicon. *Solid State Commun.* **22** (2): 133–137 (1977).

[120] J. R. PAWLIK, W. PAUL: EPR and photo-EPR in doped and undoped amorphous Si and Ge. In: *Proceedings of the 7th International Conference on Amorphous and Liquid Semiconductors*, ed. by W. E. Spear (Edinburgh: University of Edinburgh, 1977).

[121] A. FRIEDERICH, D. KAPLAN: Light-induced E.S.R. in amorphous silicon. *J. Electron. Mater.* **8** (2): 79–85 (1979).

[122] R. A. STREET, D. K. BIEGELSEN: Luminescence and ESR studies of defects in hydrogenated amorphous silicon. *Solid State Commun.* **33** (12): 1159–1162 (1980).

[123] R. A. STREET, D. K. BIEGELSEN: Explanation of light induced ESR in a-Si:H: Dangling bonds with a positive correlation energy. *J. Non-Cryst. Solids* **35–36**: 651–656 (1980).

[124] G. K. WALTERS, T. L. ESTLE: Paramagnetic resonance of defects introduced near the surface of solids by mechanical damage. *J. Appl. Phys.* **32** (10): 1854–1859 (1961).

[125] D. HANEMAN: Electron paramagnetic resonance from clean single-crystal cleavage surfaces of silicon. *Phys. Rev.* **170** (3): 705–719 (1968); D. HANEMAN, M. F. CHUNG, A. TALONI: Comparison of thermal behavior of vacuum-crushed, air-crushed, and mechanically polished silicon surfaces by electron paramagnetic resonance. *Phys. Rev.* **170** (3): 719–723 (1968).

[126] D. K. BIEGELSEN, M. STUTZMANN: Hyperfine studies of dangling bonds in amorphous silicon. *Phys. Rev. B* **33** (5): 3006–3011 (1986).

[127] M. STUTZMANN, D. K. BIEGELSEN: Microscopic nature of coordination defects in amorphous silicon. *Phys. Rev. B* **40** (14): 9834–9840 (1989).

[128] G. D. WATKINS, J. W. CORBETT: Defects in irradiated silicon. I. Electron spin resonance on the Si−A center. *Phys. Rev.* **121** (4): 1001–1014 (1961).

[129] P. A. FEDDERS, A. E. CARLSSON: Energy levels and charge distributions of nonideal dangling and floating bonds in amorphous Si. *Phys. Rev. B* **39** (2): 1134–1139 (1989).

[130] R. BISWAS, C. Z. WANG, C. T. CHAN, K. M. HO, C. M. SOUKOULIS: Electronic structure of dangling and floating bonds in amorphous silicon. *Phys. Rev. Lett.* **63** (14): 1491–1494 (1989).

[131] K. L. BROWER: ^{29}Si hyperfine structure of unpaired spins at the Si/SiO_2 interface. *Appl. Phys. Lett.* **43** (12): 1111–1113 (1983).

[132] N. ISHII, T. SHIMIZU: Origin of the ESR signal with $g = 2.0055$ in amorphous silicon. *Phys. Rev. B* **42** (15): 9697–9700 (1990).

[133] P. W. ANDERSON: Model for the electronic structure of amorphous semiconductors. *Phys. Rev. Lett.* **34** (15): 953–955 (1975).

[134] K. SHIMAKAWA, A. KOLOBOV, S. R. ELLIOT: Photoinduced effects and metastability in amorphous semiconductors and insulators. *Adv. Phys.* **44** (6): 475–588 (1995).

[135] R. A. STREET, N. F. MOTT: States in gap in glassy semiconductors. *Phys. Rev. Lett.* **35** (19): 1293–1296 (1975).

[136] M. KASTNER, D. ADLER, H. FRITZSCHE: Valence-alternation model for localized gap states in lone-pair semiconductors. *Phys. Rev. Lett.* **37** (22): 1504–1507 (1976).

[137] J. D. COHEN, J. P. HARBISON, K. W. WECHT: Identification of the dangling-bond state within the mobility gap of a-Si:H by depletion-width-modulated ESR spectroscopy. *Phys. Rev. Lett.* **48** (2): 109–112 (1982).

[138] J.-K. LEE, E. A. SCHIFF: Modulated electron-spin-resonance measurements and defect correlation energies in amorphous silicon. *Phys. Rev. Lett.* **68** (19): 2972–2975 (1992).

[139] K. MORIGAKI: Spin-dependent radiative and nonradiative recombinations in hydrogenated amorphous silicon: Optically detected magnetic resonance. *J. Phys. Soc. Jpn.* **50** (7): 2279–2287 (1981).

[140] D. ADLER: Origin of the photo-induced changes in hydrogenated amorphous silicon. *Sol. Cells* **9** (1-2): 133–148 (1983).

[141] T. SHIMIZU, H. KIDOH, A. MORIMOTO, M. KUMEDA: Nature of localized states in hydrogenated Si-based amorphous semiconductor films elucidated from LESR and CPM. *Jpn. J. Appl. Phys., Part 1* **28** (4): 586–592 (1989).

[142] J. RISTEIN, J. HAUTALA, P. C. TAYLOR: Excitation-energy dependence of optically induced ESR in a-Si:H. *Phys. Rev. B* **40** (1): 88–92 (1989).

[143] S. YAMASAKI, H. OKUSHI, A. MATSUDA, H. TANAKA, J. ISOYA: Origin of optically induced electron-spin resonance in hydrogenated amorphous silicon. *Phys. Rev. Lett.* **65** (6): 756–759 (1990).

[144] J. HAUTALA, J. D. COHEN: ESR studies on a-Si:H: Evidence for charged defects and safe hole traps. *J. Non-Cryst. Solids* **164–166** (1): 371–374 (1993).

[145] N. ORITA, T. MATSUMURA, H. KATAYAMA-YOSHIDA: Mechanism of Staebler-Wronski effect: Negative effective-U and positive effective-U nature of the bistable dangling-bonds in a-Si, a-Si:H and c-Si by ab initio molecular-dynamics simulation. *J. Non-Cryst. Solids* **198–200** (1): 347–350 (1996).

[146] N. ISHII, M. KUMEDA, T. SHIMIZU: The effects of H and F on the ESR signals in a-Si:H. *Jpn. J. Appl. Phys., Part 2* **21**(2): L92–L94 (1982).

[147] M. S. BRANDT, M. W. BAYERL, M. STUTZMANN, C. F. O. GRAEFF: Electrically detected magnetic resonance of a-Si:H at low magnetic fields: The influence of hydrogen on the dangling bond resonance. *J. Non-Cryst. Solids* **227–230**: 343–347 (1998).

[148] M. FEHR, A. SCHNEGG, B. RECH, K. LIPS, O. ASTAKHOV, F. FINGER, G. PFANNER, C. FREYSOLDT, J. NEUGEBAUER, R. BITTL, C. TEUTLOFF: Combined multifrequency EPR and DFT study of dangling bonds in a-Si:H. *Phys. Rev. B* **84**(24): 245203 (2011); M. FEHR, A. SCHNEGG, B. RECH, K. LIPS, O. ASTAKHOV, F. FINGER, C. FREYSOLDT, R. BITTL, C. TEUTLOFF: Dangling bonds in amorphous silicon investigated by multifrequency EPR. *J. Non-Cryst. Solids* **358**(17): 2067–2070 (2012).

[149] T. UMEDA, S. YAMASAKI, J. ISOYA, A. MATSUDA, K. TANAKA: Electronic structure of band-tail electrons in a-Si:H. *Phys. Rev. Lett.* **77**(22): 4600–4603 (1996).

[150] T. UMEDA, S. YAMASAKI, J. ISOYA, K. TANAKA: Microscopic origin of light-induced ESR centers in undoped hydrogenated amorphous silicon. *Phys. Rev. B* **62**(23): 15702–15710 (2000).

[151] N. ISHII, T. SHIMIZU: Cluster-model calculations of hyperfine coupling constants of dangling bond and weak bond in a-Si:H. *Solid State Commun.* **102**(9): 647–651 (1997).

[152] H. FRITZSCHE: Development in understanding and controlling the Staebler-Wronski effect in a-Si:H. *Annu. Rev. Mater. Res.* **31**: 47–79 (2001).

[153] D. E. CARLSON: Hydrogenated microvoids and light-induced degradation of amorphous-silicon solar cells. *Appl. Phys. A: Mater. Sci. Process.* **41**(4): 305–309 (1986).

[154] K. MORIGAKI: Microscopic mechanism for the photo-creation of dangling bonds in a-Si:H. *Jpn. J. Appl. Phys., Part 1* **27**(2): 163–168 (1988).

[155] W. B. JACKSON: Role of hydrogen complexes in the metastability of hydrogenated amorphous silicon. *Phys. Rev. B* **41**(14): 10257(R) (1990).

[156] S. B. ZHANG, W. B. JACKSON, D. J. CHADI: Diatomic-hydrogen-complex dissociation: A microscopic model for metastable defect generation in Si. *Phys. Rev. Lett.* **65**(20): 2575–2578 (1990).

[157] M. STUTZMANN: Microscopic aspects of the Staebler-Wronski effect. *Mater. Res. Soc. Symp. Proc.* **467**: 37–48 (1997).

[158] H. M. BRANZ: Hydrogen collision model: Quantitative description of metastability in amorphous silicon. *Phys. Rev. B* **59**(8): 5498–5512 (1999).

[159] C. LONGEAUD, D. ROY, O. SAADANE: Role of interstitial hydrogen and voids in light-induced metastable defect formation in hydrogenated amorphous silicon: A model. *Phys. Rev. B* **65**(8): 085206 (2002).

[160] M. J. POWELL: Microscopic mechanisms for creation and removal of metastable dangling bonds in hydrogenated amorphous silicon. *Phys. Rev. B* **66**(15): 155212 (2002).

[161] K. LIPS, M. FEHR, J. BEHRENDS: Electron-spin resonance in hydrogenated amorphous silicon. In: *Advanced characterization techniques for thin film solar cells*, ed. by D. Abou-Ras, T. Kirchartz, U. Rau (Weinheim: Wiley-VCH, 2011).

[162] M. FEHR, A. SCHNEGG, B. RECH, O. ASTAKHOV, F. FINGER, R. BITTL, C. TEUTLOFF, K. LIPS: Metastable defect formation at microvoids identified as a source of light-induced degradation in a-Si:H. *Phys. Rev. Lett.* **112**(6): 066403 (2014).

[163] J. MELSKENS, A. SCHNEGG, A. BALDANSUREN, K. LIPS, M. P. PLOKKER, S. W. H. EIJT, H. SCHUT, M. FISCHER, M. ZEMAN, A. H. M. SMETS: Structural and electrical properties of metastable defects in hydrogenated amorphous silicon. *Phys. Rev. B* **91**(24): 245207 (2015).

[164] H. M. BRANZ, M. SILVER: Potential fluctuations due to inhomogeneity in hydrogenated amorphous silicon and the resulting charged dangling-bond defects. *Phys. Rev. B* **42**(12): 7420–7428 (1990).

[165] S. YAMASAKI, S. KURODA, J. ISOYA, K. TANAKA: ^{1}H-ENDOR-detected ESR spectra of P- and B-dopes a-Si:H. *J. Non-Cryst. Solids* **97/98**: 691–694 (1987).

[166] K. TAKEDA, K. SHIRAISHI, M. FUJIKI, M. KONDO, K. MORIGAKI: Photocreated metastable states in polysilanes. *Phys. Rev. B* **50**(8): 5171–5179 (1994).

[167] D. ENGEMANN, R. FISCHER: Radiative recombination in amorphous silicon. In: *Proceedings of the 5th internal conference on amorphous and liquid semiconductors*, ed. by J. Stuke, W. Brenig (London: Taylor & Francis, 1974).

[168] D. ENGEMANN, R. FISCHER: Radiative and non-radiative recombination in amorphous silicon. *AIP Conf. Proc.* **31**(1): 37–43 (1976); D. ENGEMANN, R. FISCHER: Photoluminescence in amorphous silicon. *Phys. Status Solidi B* **79**(1): 195–202 (1977).

[169] T. S. NASHASHIBI, I. G. AUSTIN, T. M. SEARLE: Photoluminescence in pure and doped amorphous silicon. *Philos. Mag. A* **35**(3): 831–835 (1977).

[170] J. I. PANKOVE, D. E. CARLSON: Luminescence of hydrogenated amorphous silicon. In: *Proceedings of the 7th International Conference on Amorphous and Liquid Semiconductors*, ed. by W. E. Spear (Edinburgh: University of Edinburgh, 1977); J. I. PANKOVE, D. E. CARLSON: Photoluminescence of hydrogenated amorphous silicon. *Appl. Phys. Lett.* **31**(7): 450–451 (1977).

[171] R. A. STREET: Phonon interactions in the luminescence of amorphous silicon. *Philos. Mag. B* **37**(1): 35–42 (1978).

[172] C. TSANG, R. A. STREET: Luminescence decay in glow-discharge deposited amorphous silicon. *Philos. Mag. B* **37**(5): 601–608 (1978).

[173] W. REHM, R. FISCHER: Fast radiationless recombination in amorphous silicon. *Phys. Status Solidi A* **94**(2): 595–602 (1979).

[174] M. A. PAESLER, W. PAUL: Photoluminescence in sputtered amorphous silicon-hydrogen alloys. *Philos. Mag. B* **41**(4): 393–417 (1980); R. W. COLLINS, M. A. PAESLER, W. PAUL: The temperature dependence of photoluminescence in a-Si:H alloys. *Solid State Commun.* **34**(10): 833–836 (1980).

[175] R. A. STREET: Recombination in a-Si:H: Defect luminescence. *Phys. Rev. B* **21**(12): 5775–5784 (1980).

[176] R. A. STREET: Luminescence and recombination in hydrogenated amorphous silicon. *Adv. Phys.* **30**(5): 593–676 (1981).

[177] C. TSANG, R. A. STREET: Recombination in plasma-deposited amorphous Si:H. Luminescence decay. *Phys. Rev. B* **19**(6): 3027–3040 (1979).

[178] D. G. THOMAS, J. J. HOPFIELD, W. M. AUGUSTYNIAK: Kinetics of radiative recombination at randomly distributed donors and acceptors. *Phys. Rev.* **150**(1A): A202–A220 (1965).

[179] J. SINGH, K. SHIMAKAWA: Advances in amorphous semiconductors (Boca Raton: CRC Press, 2003).

[180] J. TAUC: Photoinduced absorption in amorphous silicon. In: *Festkörperprobleme 22*, ed. by P. Grosse (Berlin, Heidelberg: Springer, 1982).

[181] A. V. V. NAMPOOTHIRI, S. L. DEXHEIMER: Femtosecond far-infrared studies of photoconductivity in a-Si:H and a-SiGe:H. *Mater. Res. Soc. Symp. Proc.* **808**: A5.9 (2004).

[182] L. ONSAGER: Initial recombination of ions. *Phys. Rev.* **54**(8): 554–557 (1938).

[183] J. NOOLANDI, K. M. HONG, R. A. STREET: Theory of radiative recombination by diffusion and tunnelling in amorphous Si:H. *J. Non-Cryst. Solids* **35/36**(2): 669–674 (1980); J. NOOLANDI, K. M. HONG, R. A. STREET: A geminate recombination model for photoluminescence decay in plasma-deposited amorphous Si:H. *Solid State Commun.* **34**(1): 45–48 (1980).

[184] R. A. STREET, D. K. BIEGELSEN: Distribution of recombination lifetimes in amorphous silicon. *Solid State Commun.* **44**(4): 501–505 (1982).

[185] D. J. DUNSTAN: Kinetics of distant-pair recombination I. Amorphous silicon luminescence at low temperature. *Philos. Mag. B* **46**(6): 579–594 (1982); D. J. DUNSTAN: Kinetics of distant-pair recombination II. Tunnelling non-radiative recombination. *Philos. Mag. B* **49**(2): 191–213 (1984); D. J. DUNSTAN: Kinetics of distant-pair recombination III. Bias illumination and frequency-resolved spectroscopy. *Philos. Mag. B* **52**(2): 111–119 (1985).

[186] R. C. CHITTICK: Properties of glow-discharge deposited amorphous germanium and silicon. *J. Non-Cryst. Solids* **3**(3): 255–270 (1970).

[187] J. E. FISCHER, T. M. DONOVAN: Optical and photoelectric properties of amorphous silicon. *J. Non-Cryst. Solids* **8–10**: 202–208 (1972); J. E. FISCHER: Photoelectric properties of amorphous silicon and germanium films. *Thin Solid Films* **17**(2): 223–229 (1973).

[188] R. J. LOVELAND, W. E. SPEAR, A. AL-SHARBATY: Photoconductivity and absorption in amorphous Si. *J. Non-Cryst. Solids* **13**(1): 55–68 (1973); W. E. SPEAR, R. J. LOVELAND, A. AL-SHARBATY: The temperature dependence of photoconductivity in a-Si. *J. Non-Cryst. Solids* **15**(3): 410–422 (1974).

[189] D. A. ANDERSON, W. E. SPEAR: Photoconductivity and recombination in doped amorphous silicon. *Philos. Mag. B* **36** (3): 695–712 (1977).

[190] M. HOHEISEL, R. CARIUS, W. FUHS: Low temperature photoconductivity in a-Si:H films. *J. Non-Cryst. Solids* **59/60** (1): 457–460 (1983).

[191] R. A. STREET: Recombination in a-Si:H: Auger effects and nongeminate recombination. *Phys. Rev. B* **23** (2): 861–868 (1981).

[192] R. A. STREET, J. C. KNIGHTS, D. K. BIEGELSEN: Luminescence studies of plasma-deposited hydrogenated silicon. *Phys. Rev. B* **18** (4): 1880–1891 (1978).

[193] S. AMBROS, R. CARIUS, H. WAGNER: Lifetime distribution in a-Si:H: Geminate-, nongeminate- and auger-processes. *J. Non-Cryst. Solids* **137/138** (1): 555–558 (1991).

[194] H. FRITZSCHE: Low temperature electronic transport in non-crystalline semiconductors. *J. Non-Cryst. Solids* **114** (1): 1–6 (1989).

[195] H. FRITZSCHE, B.-G. YOON, D.-Z. CHI, M. Q. TRAN: Some observations on the photoconductivity of amorphous semiconductors. *J. Non-Cryst. Solids* **141**: 123–132 (1992).

[196] M. HOHEISEL, R. CARIUS, W. FUHS: Photoconductivity and photoluminescence of a-Si:H at low temperature. *J. Non-Cryst. Solids* **63** (3): 313–319 (1984).

[197] W. E. SPEAR, C. S. CLOUDE: Interpretation of the low-temperature photoconductivity in a-Si. *Philos. Mag. Lett.* **55** (6): 271–276 (1987).

[198] B. I. SHKLOVSKII, H. FRITZSCHE, S. D. BARANOVSKII: Electronic transport and recombination in amorphous semiconductors at low temperatures. *Phys. Rev. Lett.* **62** (25): 2989–2992 (1989).

[199] B. I. SHKLOVSKII, E. I. LEVIN, H. FRITZSCHE, S. D. BARANOVSKII: Hopping photoconductivity in amorphous semiconductors: Dependence on temperature, electric field and frequency. In: *Advances in Disordered Semiconductors, Volume 3: Transport, Correlation and Structural Defects*, ed. by H. Fritzsche (Singapore: World Scientific, 1990).

[200] R. STACHOWITZ, W. FUHS, K. JAHN: Low-temperature transport and recombination in a-Si:H. *Philos. Mag. B* **62** (1): 5–18 (1990).

[201] S. D. BARANOVSKII, P. THOMAS, G. J. ADRIAENSSENS: The concept of transport energy and its application to steady-state photoconductivity in amorphous silicon. *J. Non-Cryst. Solids* **190** (3): 283–287 (1995).

[202] B. CLEVE, B. HARTENSTEIN, S. D. BARANOVSKII, M. SCHEIDLER, P. THOMAS, H. BAESSLER: High-field hopping transport in band tails of disordered semiconductors. *Phys. Rev. B* **51** (23): 16705–16713 (1995).

[203] D. J. DUNSTAN, S. DEPINNA, B. C. CAVENETT: A direct determination of the lifetime distribution of the 1.4 eV luminescence of a-Si:H. *J. Phys. C: Solid State Phys.* **15** (13): L425–L429 (1982).

[204] S. P. DEPINNA, D. J. DUNSTAN: Frequency-resolved spectroscopy and its application to the analysis of recombination in semiconductors. *Philos. Mag. B* **50** (5): 579–597 (1984).

[205] M. BORT, W. FUHS, S. LIEDTKE, R. STACHOWITZ, R. CARIUS: Geminate recombination in a-Si:H. *Philos. Mag. Lett.* **64** (4): 227–233 (1991).

[206] T. AOKI, T. SHIMIZU, D. SAITO, K. IKEDA: Mechanism of photoluminescence in hydrogenated amorphous silicon determined by wide-band quadrature frequency-resolved spectroscopy (QFRS). *J. Optoelectron. Adv. Mater.* **7** (1): 137–144 (2005).

[207] F. BOULITROP, D. J. DUNSTAN: Temperature dependence of carrier lifetimes in a-Si:H. *J. Non-Cryst. Solids* **77/78** (1): 663–666 (1985).

[208] T. M. SEARLE, M. HOPKINSON, M. EDMEADES, S. KALEM, I. G. AUSTIN, R. A. GIBSON: Recombination in a-Si:H based materials: Evidence for two slow radiative processes. In: *Disordered Semiconductors*, ed. by M. A. Kastner, G. A. Thomas, S. R. Ovshinsky (New York, London: Plenum Press, 1987).

[209] R. STACHOWITZ, M. SCHUBERT, W. FUHS: Nonradiative recombination and its influence on the lifetime distribution in amorphous silicon (a-Si:H. *Phys. Rev. B* **52** (15): 10906–10914 (1995).

[210] R. STACHOWITZ, M. SCHUBERT, W. FUHS: Non-radiative distant pair recombination in amorphous silicon. *J. Non-Cryst. Solids* **227**: 190–196 (1998).

[211] T. AOKI, S. KOMEDOORI, S. KOBAYASHI, C. FUJIHASHI, A. GANJOO, K. SHIMAKAWA: Photoluminescence lifetime distribution of a-Si:H and a-Ge:H expanded to nanosecond region using wide-band frequency-resolved spectroscopy. *J. Non-Cryst. Solids* **299–302** (1): 642–647 (2002).

[212] T. AOKI: Nanosecond QFRS study of photoluminescence in amorphous semiconductors. *J. Mater. Sci.: Mater. Electron.* **14** (10–12): 697–701 (2003).

[213] T. AOKI, T. SHIMIZU, S. KOMEDOORI, S. KOBAYASHI, K. SHIMAKAWA: Coexistence of geminate and non-geminate recombination in a-Si:H and a-Ge:H observed by quadrature frequency resolved spectroscopy. *J. Non-Cryst. Solids* **338–340**: 456–459 (2004).

[214] T. AOKI, K. IKEDA, S. KOBAYASHI, K. SHIMAKAWA: Recombination kinetics of very-long-lived photoluminescence decay in a-Si:H correlated with light-induced spin densities. *Philos. Mag. Lett.* **86** (3): (2006).

[215] T. AOKI, K. IKEDA, N. OHRUI, S. KOBAYASHI, K. SHIMAKAWA: Photoluminescence lifetime studies of a-Si:H and a-SiN:H. *J. Optoelectron. Adv. Mater.* **9** (1): 70–76 (2007).

[216] N. ISHII, M. KURIHARA, T. AOKI, K. SHIMAKAWA, J. SINGH: Photoluminescence in high-quality a-Ge:H. *J. Non-Cryst. Solids* **266-269** (2): 721–725 (2000).

[217] T. AOKI, S. KOMEDOORI, S. KOBAYASHI, T. SHIMIZU, A. GANJOO, K. SHIMAKAWA: Photoluminescence lifetime distributions of chalcogenide glasses obtained by wide-band frequency resolved spectroscopy. *J. Non-Cryst. Solids* **326/327**: 273–278 (2003).

[218] T. AOKI, D. SAITO, K. IKEDA, S. KOBAYASHI, K. SHIMAKAWA: Radiative recombination processes in chalcogenide glasses deduced by lifetime measurements over 11 decades. *J. Optoelectron. Adv. Mater.* **7** (4): 1749–1757 (2005).

[219] E. I. LEVIN, S. MARIANER, B. I. SHKLOVSKII: Photoluminescence of amorphous silicon at low temperatures: Computer simulation. *Phys. Rev. B* **45** (11): 5906–5918 (1992).

[220] D. K. BIEGELSEN, J. C. KNIGHTS, R. A. STREET, C. TSANG, R. M. WHITE: Spin dependent luminescence in hydrogenated amorphous silicon. *Philos. Mag. B* **37** (4): 477–488 (1978).

[221] K. MORIGAKI, D. J. DUNSTAN, B. C. CAVENETT, P. DAWSON, J. E. NICHOLLS: Optically detected electron spin resonance in amorphous silicon. *Solid State Commun.* **26** (12): 981–985 (1978).

[222] E. A. SCHIFF: Spin polarization effects in the photoconductivity of a-Si:H. *AIP Conf. Proc.* **73** (1): 233–237 (1981).

[223] N. KISHIMOTO, K. MORIGAKI, K. MURAKAMI: Conductivity change due to electron-spin resonance in amorphous Si-Au system. *J. Phys. Soc. Jpn.* **50** (6): 1970–1977 (1981).

[224] R. A. STREET: Spin-dependent photoconductivity in undoped a-Si:H. *Philos. Mag. B* **46** (3): 273–278 (1982).

[225] M. S. BRANDT, M. STUTZMANN: Spin-dependent conductivity in amorphous hydrogenated silicon. *Phys. Rev. B* **43** (6): 5184–5187 (1991).

[226] W. BRONNER, J. P. KLEIDER, R. BRÜGGEMANN, P. ROCA I CABARROCAS, D. MENCARAGLIA, M. MEHRING: Comparison of transport and defects properties in hydrogenated polymorphous and amorphous silicon. *J. Non-Cryst. Solids* **299–302** (1): 551–555 (2002).

[227] S. P. DEPINNA, B. C. CAVENETT, T. M. SEARLE, I. G. AUSTIN: Optically detected magnetic resonance (ODMR) in a-Si. *J. Phys. Colloques* **42** (C4): 323–326 (1981).

[228] K. MORIGAKI, Y. SANO, I. HIRABAYASHI: Radiative and nonradiative recombination processes in hydrogenated amorphous silicon as elucidated by optically detected magnetic resonance. *Solid State Commun.* **39** (9): 947–951 (1981).

[229] S. DEPINNA, B. C. CAVENETT, I. G. AUSTIN, T. M. SEARLE, M. J. THOMPSON, J. ALLISON, P.G. LE COMBER: Characterization of radiative recombination in amorphous silicon by optically detected magnetic resonance: Part I. *Philos. Mag. B* **46** (5): 473–500 (1982); S. DEPINNA, B. C. CAVENETT, T. M. SEARLE, I. G. AUSTIN: Characterization of radiative recombination in amorphous silicon by optically detected magnetic resonance: Part II. *Philos. Mag. B* **46** (5): 501–513 (1982).

[230] S. P. DEPINNA, B. C. CAVENETT: Time-resolved ODMR in a-Si:H by frequency response spectroscopy (FRS). *J. Phys. C: Solid State Phys.* **15** (14): L489–L493 (1982).

[231] R. A. STREET, D. K. BIEGELSEN, J. ZESCH: Spin-dependent recombination at dangling bonds in a-Si:H. *Phys. Rev. B* **25** (6): 4334–4337 (1982).

[232] R. A. STREET: Recombination in a-Si:H: Spin-dependent effects. *Phys. Rev. B* **26** (7): 3588–3604 (1982).

[233] F. BOULITROP: Recombination processes in a-Si:H: A study by optically detected magnetic resonance. *Phys. Rev. B* **28** (11): 6192–6208 (1983).

[234] M. YOSHIDA, K. MORIGAKI: Time-resolved optically detected magnetic resonance in a-Si:H. *J. Non-Cryst. Solids* **77/78**: 619–622 (1985).

[235] S. LIEDTKE, W. FUHS: Optically detected magnetic resonance (ODMR) in a-Si:H. *J. Non-Cryst. Solids* **137/138**: 583–586 (1991).

[236] W. FUHS, K. LIPS: Recombination in a-Si:H films and pin-structures studied by electrically detected magnetic resonance (EDMR). *J. Non-Cryst. Solids* **164–166** (1): 541–546 (1993).

[237] K. LIPS, M. BLOCK, W. FUHS, C. LERNER: Degradation of a-Si:H *p-i-n* solar cells studied by electrically detected magnetic resonance. *J. Non-Cryst. Solids* **164–166** (2): 697–700 (1993).

[238] K. LIPS, C. BOEHME, W. FUHS: Recombination in silicon thin-film solar cells: A study of electrically detected magnetic resonance. *IEE Proc., Part G: Circuits, Devices Syst.* **150** (4): 309–315 (2003).

[239] J. BEHRENDS, K. LIPS, C. BOEHME: Observation of precursor pair formation of recombining charge carriers. *Phys. Rev. B* **80** (4): 045207 (2009).

[240] B. M. GEORGE, J. BEHRENDS, A. SCHNEGG, T. F. SCHULZE, M. FEHR, L. KORTE, B. RECH, K. LIPS, M. ROHRMÜLLER, E. RAULS, W. G. SCHMIDT, U. GERSTMANN: Atomic structure of interface states at silicon heterojunction solar cells. *Phys. Rev. Lett.* **110** (13): 136803 (2013).

[241] M. S. BRANDT, M. STUTZMANN: Spin-dependent photoconductivity as a function of wavelength: A test for the constant photocurrent method in a-Si:H. *J. Non-Cryst. Solids* **164–166** (1): 547–550 (1993).

[242] M. YOSHIDA, K. MORIGAKI: Triplet exciton recombination in a-Si:H as elucidated by optically detected magnetic resonance experiments. *Philos. Mag. B* **54** (2): (1986).

[243] M. YOSHIDA, K. MORIGAKI: Triplet exciton recombination in silicon-based amorphous semiconductors. *J. Non-Cryst. Solids* **97/98**: 579–582 (1987).

[244] M. S. BRANDT, M. STUTZMANN: Excitons and light-induced degradation of amorphous hydrogenated silicon. *Appl. Phys. Lett.* **58** (15): 1620–1622 (1991); M. STUTZMANN, M. S. BRANDT: Excitonic states in hydrogenated amorphous silicon. *J. Non-Cryst. Solids* **141** (1–3): 97–105 (1992).

[245] M. S. BRANDT, M. STUTZMANN: Triplet excitons in porous silicon and siloxene. *Solid State Commun.* **93** (6): 473–477 (1995).

[246] K. LIPS, C. BOEHME, T. EHARA: The impact of the electron spin on charge carrier recombination: The example of amorphous silicon. *J. Optoelectron. Adv. Mater.* **7** (1): 13–24 (2005).

[247] W. FUHS: Recombination and transport through localized states in hydrogenated amorphous and microcrystalline silicon. *J. Non-Cryst. Solids* **354** (19–25): 2067–2078 (2008).

[248] T. W. HERRING, S.-Y. LEE, D. R. MCCAMEY, P. C. TAYLOR, K. LIPS, J. HU, F. ZHU, A. MADAN, C. BOEHME: Experimental discrimination of geminate and non-geminate recombination in a-Si:H. *Phys. Rev. B* **79** (19): 195205 (2009).

[249] S. PHILIPPS, W. WARMUTH: Photovoltaics report (Freiburg: Fraunhofer Institute for Solar Energy Systems, 2018).

[250] M. A. GREEN, Y. HISHIKAWA, E. D. DUNLOP, D. H. LEVI, J. HOHL-EBINGER, M. YOSHITA, A. W. Y. HO-BAILLIE: Solar cell efficiency tables (version 53). *Prog. Photovolt: Res. Appl.* **27** (1): 3–12 (2019).

[251] A. B. DJURIŠIĆ, F. LIU, A. M. C. NG, Q. DONG, M. K. WONG, A. NG, C. SURYA: Stability issues of the next generation solar cells. *Phys. Status Solidi RRL* **10** (4): 281–299 (2016).

[252] M. TAGUCHI, K. KAWAMOTO, S. TSUGE, T. BABA, H. SAKATA, M. MORIZANE, K. UCHIHASHI, N. NAKAMURA, S. KIYAMA, O. OOTA: HIT™ cells—high-efficiency crystalline Si cells with novel structure. *Prog. Photovolt: Res. Appl.* **8** (5): 503–513 (2000).

[253] L. H. XIAO, O. ASTAKHOV, F. FINGER: Silicon thin film powder samples for electron spin resonance investigations: Role of substrate and preparation procedure. *Jpn. J. Appl. Phys.* **50** (7): 071301 (2011).

[254] S. HAAS, A. GORDIJN, H. STIEBIG: High speed laser processing for monolithical series connection of silicon thin-film modules. *Prog. Photovolt: Res. Appl.* **16** (3): 195–203 (2008).

[255] J. MELSKENS, A. H. M. SMETS, S. W. H. EIJT, H. SCHUT, E. BRÜCK, M. ZEMAN: The nanostructural analysis of hydrogenated silicon films based on positron annihilation studies. *J. Non-Cryst. Solids* **358** (17): 2015–2018 (2012).

[256] M. STUCKELBERGER, M. DESPEISSE, G. BUGNON, J. W. SCHÜTTAUF, F. J. HAUG, C. BALLIF: Comparison of amorphous silicon absorber materials: Light-induced degradation and solar cell efficiency. *J. Appl. Phys.* **114** (15): 154509 (2013).

[257] I. GROMOV, M. MAIXNER, I. PRISECARU, K. BAUER, J. SCHULTE, A. TAVERNIER, D. SCHMALBEIN, P. HÖFER, P. VONLANTHEN, J. HINDERER, A. BÄR, T. WÜTHRICH, P. MOCK, D. ECKERT, O. SCHETT, R. JEKER: Novel mm-wave EPR spectrometer ELEXSYS 7th series: Design and performance. *Bruker SpinReport* 15–23 (2015).

[258] S.-Y. LEE, S.-Y. PAIK, D. R. MCCAMEY, C. BOEHME: Modulation frequency dependence of continuous-wave optically/electrically detected magnetic resonance. *Phys. Rev. B* **86** (11): 115204 (2012).

[259] S. WEBER: Transient EPR. *eMagRes* **6** (2): 255–277 (2017).

[260] S. WEBER, C. W. M. KAY, H. MÖGLING, K. MÖBIUS, K. HITOMI, T. TODO: Photoactivation of the flavin cofactor in Xenopus laevis (6–4) photolyase: Observation of a transient tyrosyl radical by time-resolved electron paramagnetic resonance. *Proc. Natl. Acad. Sci. U. S. A.* **99** (3): 1319–1322 (2002).

[261] B. EFRON: Bootstrap methods: Another look at the jackknife. *Ann. Statist.* **7** (1): 1–26 (1979).

[262] A. C. DAVISON, D. V. HINKLEY: Bootstrap methods and their application (Cambridge: Cambridge University Press, 1997).

[263] J. BEHRENDS, A. SCHNEGG, M. FEHR, A. LAMBERTZ, S. HAAS, F. FINGER, B. RECH, K. LIPS: Electrical detection of electron spin resonance in microcrystalline silicon pin solar cells. *Philos. Mag.* **89** (28–30): 2655–2676 (2009).

[264] C. MEIER, J. BEHRENDS, C. TEUTLOFF, O. ASTAKHOV, A. SCHNEGG, K. LIPS, R. BITTL: Multi-frequency EDMR applied to microcrystalline thin-film silicon solar cells. *J. Magn. Reson.* **234**: 1–9 (2013).

[265] K. MORIGAKI, M. YOSHIDA: Triplet exciton recombination in a-Si:H. *J. Non-Cryst. Solids* **90** (1–3): 139–146 (1987).

[266] S.-Y. LEE, S.-Y. PAIK, D. R. MCCAMEY, J. HU, F. ZHU, A. MADAN: Spin-dependent processes in amorphous silicon-rich silicon-nitride. *Appl. Phys. Lett.* **97** (19): 192104 (2010).

[267] G. W. MORLEY, D. R. MCCAMEY, H. A. SEIPEL, L.-C. BRUNEL, J. VAN TOL, C. BOEHME: Long-lived spin coherence in silicon with an electrical spin trap readout. *Phys. Rev. Lett.* **101** (20): 207602 (2008).

[268] D. R. MCCAMEY, C. BOEHME, G. W. MORLEY, J. VAN TOL: Electrically detected spin echoes of donor nuclei in silicon. *Phys. Rev. B* **85** (7): 073201 (2012).

[269] J. KRZYSTEK, A. SIENKIEWICZ, L. PARDI, L.-C. BRUNEL: DPPH as a standard for high-field EPR. *J. Magn. Reson.* **125** (1): 207–211 (1997).

[270] C. J. PICKARD, F. MAURI: First-principles theory of the EPR *g* tensor in solids: Defects in quartz. *Phys. Rev. Lett.* **88** (8): 086403 (2002).

[271] P. GIANNOZZI, S. BARONI, N. BONINI, M. CALANDRA, R. CAR, C. CAVAZZONI, D. CERESOLI, G. L. CHIAROTTI, M. COCOCCIONI, I. DABO, A. DAL CORSO, S. DE GIRONCOLI, S. FABRIS, G. FRATESI, R. GEBAUER, U. GERSTMANN, C. GOUGOUSSIS, A. KOKALJ, M. LAZZERI, L. MARTIN-SAMOS, N. MARZARI, F. MAURI, R. MAZZARELLO, S. PAOLINI, A. PASQUARELLO, L. PAULATTO, C. SBRACCIA, S. SCANDOLO, G. SCLAUZERO, A. P. SEITSONEN, A. SMOGUNOV, P. UMARI, R. M. WENTZCOVITCH: QUANTUM ESPRESSO: a modular and open-source software project for quantum simulations of materials. *Journal of Physics: Condensed Matter* **21** (39): 395502 (2009).

[272] T. BIKTAGIROV, W. G. SCHMIDT, U. GERSTMANN: Calculation of spin-spin zero-field splitting within periodic boundary conditions: Towards all-electron accuracy. *Phys. Rev. B* **97** (11): 115135 (2018).

[273] J. BEHRENDS, A. SPERLICH, A. SCHNEGG, T. BISKUP, C. TEUTLOFF, K. LIPS, V. DYAKONOV, R. BITTL: Direct detection of photoinduced charge transfer complexes in polymer fullerene blends. *Phys. Rev. B* **85** (12): 125206 (2012).

[274] Y. KOBORI, R. NOJI, S. TSUGANEZAWA: Initial molecular photocurrent: Nanostructure and motion of weakly bound charge-separated state in organic photovoltaic interface. *J. Phys. Chem. C* **117** (4): 1589–1599 (2013).

[275] F. KRAFFERT, R. STEYRLEUTHNER, S. ALBRECHT, D. NEHER, M. C. SCHARBER, R. BITTL, J. BEHRENDS: Charge separation in PCPDTBT:PCBM blends from an EPR perspective. *J. Phys. Chem. C* **118** (49): 28482–28493 (2014).

[276] T. BISKUP, M. SOMMER, S. REIN, D. L. MEYER, M. KOHLSTÄDT, U. WÜRFEL, S. WEBER: Ordering of PCDTBT revealed by time-resolved electron paramagnetic resonance spectroscopy of its triplet excitons. *Angew. Chem., Int. Ed.* **54** (26): 7707–7710 (2015).

[277] L. R. WEISS, S. L. BAYLISS, F. KRAFFERT, K. J. THORLEY, J. E. ANTHONY, R. BITTL, R. H. FRIEND, A. RAO, N. C. GREENHAM, J. BEHRENDS: Strongly exchange-coupled triplet pairs in an organic semiconductor. *Nat. Phys.* **13**: 176–181 (2017).

[278] S. RICHERT, C. E. TAIT, C. R. TIMMEL: Delocalisation of photoexcited triplet states probed by transient EPR and hyperfine spectroscopy. *J. Magn. Reson.* **280**: 103–116 (2017).

[279] F. KRAFFERT, R. STEYRLEUTHNER, C. MEIER, R. BITTL, J. BEHRENDS: Transient electrically detected magnetic resonance spectroscopy applied to organic solar cells. *Appl. Phys. Lett.* **107** (4): 043302 (2015).

[280] H. C. TORREY: Transient nutations in nuclear magnetic resonance. *Phys. Rev.* **76** (8): 1059–1068 (1949).

[281] P. W. ATKINS, A. J. DOBBS, K. A. MCLAUCHLAN: Transient nutations in electron spin resonance. *Chem. Phys. Lett.* **25** (1): 105–107 (1974).

[282] G. KOTHE, S. WEBER, R. BITTL, E. OHMES, M. C. THURNAUER, J. R. NORRIS: Transient EPR of light-induced radical pairs in plant photosystem I: Observation of quantum beats. *Chem. Phys. Lett.* **186** (6): 474–480 (1991).

[283] M. GIERER, A. VAN DER EST, D. STEHLIK: Transient EPR of weakly coupled spin-correlated radical pairs in photosynthetic reaction centres: Increase spectral resolution from nutation analysis. *Chem. Phys. Lett.* **186** (2): 238–247 (1991).

[284] J. YANG, X. XU, S. GUHA: Stability studies of hydrogenated amorphous silicon alloy solar cells prepared with hydrogen dilution. *Mater. Res. Soc. Symp. Proc.* **336**: 687–692 (1994).

[285] L. YANG, L.-F. CHEN: The effect of H_2 dilution on the stability of a-Si:H based solar cells. *Mater. Res. Soc. Symp. Proc.* **336**: 669–674 (1994).

[286] E. BHATTACHARYA, A. H. MAHAN: Microstructure and the light-induced metastability in hydrogenated amorphous silicon. *Appl. Phys. Lett.* **52** (19): 1587–1589 (1988).

[287] M. FISCHER, H. TAN, J. MELSKENS, R. VASUDEVAN, M. ZEMAN, A. H. M. SMETS: High pressure processing of hydrogenated amorphous silicon solar cells: Relation between nanostructure and high open-circuit voltage. *Appl. Phys. Lett.* **106** (4): 043905 (2015).

[288] P. JANSSEN, M. COX, S. H. W. WOUTERS, M. KEMERINK, M. M. WIENK, B. KOOPMANS: Tuning organic magnetoresistance in polymer-fullerene blends by controlling spin reaction pathways. *Nat. Commun.* **4**: 2286 (2013).

[289] D. P. FRANKE, F. HOEHNE, L. S. VLASENKO, K. M. ITOH, M. S. BRANDT: Spin-dependent recombination involving oxygen-vacancy complexes in silicon. *Phys. Rev. B* **89** (19): 195207 (2014).

[290] K. LIPS, C. LERNER, W. FUHS: Semiclassical model of electrically detected magnetic resonance in undoped a-Si:H. *J. Non-Cryst. Solids* **198–200**: 267–270 (1996).

[291] M. STUTZMANN, D. K. BIEGELSEN: Electron-spin-lattice relaxation in amorphous silicon and germanium. *Phys. Rev. B* **28** (11): 6256–6261 (1983).

[292] C. BOEHME, K. LIPS: The nature of dangling bond recombination in µc-Si:H. *J. Non-Cryst. Solids* **338–340**: 434–439 (2004).

[293] Y. ARAKI, K. MAEDA, H. MURAI: Observation of two-spin controlling of a radical pair by pulsed irradiation of microwave monitored by absorption detected magnetic resonance. *Chem. Phys. Lett.* **332** (5): 515–520 (2000).

[294] V. R. GORELIK, K. MAEDA, H. YASHIRO, H. MURAI: Microwave-induced quantum beats in micellized radical pairs under spin-locking conditions. *J. Phys. Chem. A* **105** (34): 8011–8017 (2001).

[295] D. R. MCCAMEY, S.-Y. LEE, S.-Y. PAIK, J. M. LUPTON, C. BOEHME: Spin-dependent dynamics of polaron pairs in organic semiconductors. *Phys. Rev. B* **82** (12): 125206 (2010).

[296] F. C. RONG, W. R. BUCHWALD, E. H. POINDEXTER, W. L. WARREN, D. J. KEEBLE: Spin-dependent Shockley-read recombination of electrons and holes in indirect-band-gap semiconductor *p-n* junction diodes. *Solid-State Electronics* **34** (8): 835–841 (1991).

[297] S.-Y. PAIK, S.-Y. LEE, W. J. BAKER, D. R. MCCAMEY, C. BOEHME: T_1 and T_2 spin relaxation time limitations of phosphorous donor electrons near crystalline silicon to silicon dioxide interface defects. *Phys. Rev. B* **81** (7): 075214 (2010).

[298] N. C. GIEBINK, B. W. D'ANDRADE, M. S. WEAVER, P. B. MACKENZIE, J. J. BROWN, M. E. THOMPSON, S. R. FORREST: Intrinsic luminance loss in phosphorescent small-molecule organic light emitting devices due to bimolecular annihilation reactions. *J. Appl. Phys.* **103** (4): 044509 (2008).

[299] S. R. FORREST: Excitons and the lifetime of organic semiconductor devices. *Philos. Trans. R. Soc., A* **373** (2044): 20140320 (2015).

[300] S. KIM, H. J. BAE, S. PARK, W- KIM, J. KIM, J. S. KIM, Y. JUNG, S. SUL, S.-G. IHN, C. NOH, S. KIM, Y. YOU: Degradation of blue-phosphorescent organic light-emitting devices involves exciton-induced generation of polaron pair within emitting layers. *Nat. Commun.* **9** (1): 1211 (2018).

Acknowledgements

Abschließend möchte ich mich bei all denen bedanken, die mich auf unterschiedlichste Art und Weise bei dieser Arbeit unterstützt haben:

Klaus Lips, zu aller erst, für die Gelegenheit zur Promotion und zur wissenschaftlichen Arbeit am HZB. Vielen Dank für dein Vertrauen in meine Arbeit, die großzügige Freiheit bei der Auswahl meiner Forschungsschwerpunkte, dein offenes Ohr und die vielen wissenschaftlichen Anregungen.

Alexander Schnegg möchte ich ganz besonders danken für die intensive Betreuung während der letzten Jahre, viele motivierende Gespräche und die offene und unkomplizierte Arbeitsatmosphäre. Ohne dich wäre diese Arbeit nicht möglich gewesen.

Jan Behrends für die Zweitbegutachtung dieser Dissertation. Außerdem danke ich dir und *Felix Kraffert* für die gemeinsamen transienten EPR Messungen, die wesentlich zum Verständnis der Tieftemperaturprozesse beigetragen haben.

Matthias Fehr, *Waseem Akhtar* und *Joscha Nehrkorn* für viele hilfreiche Tipps bei meinem Einstieg in die EPR/EDMR-Spektroskopie.

Meinen Bürokollegen *Silvio Künstner* und *Joscha Nehrkorn* für die nette Arbeitsatmosphäre. Außerdem auch allen anderen Mitgliedern der EPR-Gruppe für die angenehme Zeit sowie viele wissenschaftliche Diskussionen und Hilfestellungen.

Den Mitarbeitern des Instituts für Nanospektroskopie sowie des Instituts für Silizium-Photovoltaik am HZB. Insbesondere *Andreas von Kozierowski*, *Thomas Lußky* and *Martin Muske* für viele technische Hilfestellungen, sowie *Jutta Proszak* und *Marion Krusche* für die Hilfe in organisatorischen Fragen.

Friedhelm Finger und *Oleksandr Asthakhov* vom Forschungszentrum Jülich, sowie *Jimmy Melskens* und *Arno Smets* von der Technischen Universität Delft für die Präparation von EPR- und EDMR-Proben.

Uwe Gerstmann und *Timur Biktagirov* für die Durchführung von DFT-Rechnungen sowie wertvolle Diskussionen in Rahmen der Zusammenarbeit bei der Analyse von Defektzentren in amorphem Silizium.

Zu guter Letzt danke ich meiner Familie für den Rückhalt und die unendliche Unterstützung während meines Studiums und meiner Promotion, die mir diese Arbeit erst ermöglicht haben. Ganz besonders danke ich Daniela für die viele liebevolle Aufbauarbeit und Unterstützung. Euer Beitrag zu dieser Arbeit ist nicht in Worte zu fassen.

Publications and conferences

The results presented in this thesis, in particular, chapters 6 and 7 are in preparation to be published in a peer-reviewed journal. The following articles have been published, but are not directly related to this thesis:

- W. RIEDEL, L. THUM, **J. MÖSER**, V. FLEISCHER, U. SIMON, K. SIEMENSMEYER, A. SCHNEGG, R. SCHOMÄCKER, T. RISSE, K.-P. DINSE: Magnetic properties of reduced and reoxidized Mn–Na_2WO_4/$Si)_2$: A catalyst for oxidative coupling of methane (OCM). *J. Ohys. Chem.* **122**(39): 22605–-22614 (2018).
- **J. MÖSER**, K. LIPS, M. TSEYTLIN, M. TSEYTLIN, G. R. EATON, S. S. EATON, A. SCHNEGG: Using rapid-scan EPR to improve the detection limit of quantitative EPR by more than one order of magnitude. *J. Magn. Reson.* **281**: 17–25 (2017).
- H. JIA, R. ROA, S. ANGIOLETTI-UBERTI, K. HENZLER, A. OTT, X. LIN, **J. MÖSER**, Z. KOCHOVSKI, A. SCHNEGG, J. DZUBIELLA, M. BALLAUF, Y. LIU: Thermosensitive Cu_2O-PNIPAM core-shell nanoreactors with tunable photocatalytic activity. *J. Mater. Chem. A* **4**(24): 9677–9684 (2016).

In addition, several results, both of this thesis and of additional projects, have been presented at national and international conferences in the form of poster presentations or oral contributions (selection):

- **J. MÖSER**, J. BEHRENDS, A. SCHNEGG, K. LIPS: Exciton-induced transport in amorphous silicon studied by pulsed electrically detected magnetic resonance. *40th FGMR Annual Meeting & DFG SPP 1601 Meeting*, Leipzig, Germany (2018). Talk.
- **J. MÖSER**, J. BEHRENDS, A. SCHNEGG, K. LIPS: Excitonic transport in amorphous silicon studied by pulsed electrically detected magnetic resonance. *Young Researcher's Workshop of the DFG SPP 1601*, Schmitten, Germany (2018). Talk.
- **J. MÖSER**, A. SCHNEGG, W. AKHTAR, S. VEBER, K. LIPS: Combined high- and low-frequency EDMR for solar-cell applications. *Annual Meeting of the DFG SPP 1601*, Hirschegg, Austria (2016). Talk.
- **J. MÖSER**, K. LIPS, B. RECH, A. SCHNEGG: Improving the detection limit of quantitative EPR on silicon dangling bond defects by rapid scan EPR. *GDCh FGMR Annual Meeting & Joint Discussion Meeting of the German and British Magnetic Resonance Societies*, Darmstadt, Germany (2015). Poster, awarded with one of three conference-wide poster prize.
- **J. MÖSER**, A. SCHNEGG, B. RECH, K. LIPS: Sensitive detection of defects in thin-film silicon materials by rapid scan EPR. *Schulich Symposium: Modern Electron Spin Resonance—New Methodologies and New Applications*, Haifa, Israel (2015). Talk.

Erklärung

Ich erkläre hiermit, dass ich diese im Fachbereich Physik der Freien Universität Berlin zur Promotionsprüfung eingereichte Dissertation selbstständigt verfasst und ausschließlich unter Verwendung der angegebenen Hilfsmittel angefertigt habe. Alle wörtlich oder inhaltlich übernommenen Textstellen sowie übernommene oder reproduzierte Grafiken sind als solche gekennzeichnet.

Außerdem versichere ich, dass ich die vorgelegte Dissertation nur in diesem und keinem anderen Promotionsverfahren eingereicht habe und, dass diesem Promotionsverfahren keine endgültig gescheiterten Promotionsverfahren vorausgegangen sind.

Ort, Datum

Jannik Möser